The Analysis of Weak Rock Using the Pressuremeter

Jacob Dafni

A thesis submitted in partial fulfillment
of the requirements for the degree of

Master of Science in Civil Engineering

University of Washington

2013

Committee:

Pedro Arduino, Chair

Joseph Wartman

Program Authorized to Offer Degree:
Civil and Environmental Engineering

University of Washington

Abstract

The Analysis of Weak Rock Using the Pressuremeter

Jacob Dafni

Chair of the Supervisory Committee:
Research Advisor Pedro Arduino
Civil and Environmental Engineering

The pressuremeter is a versatile *in situ* testing instrument capable of testing a large range of materials from very soft clay to weak rock. Due to limitations of other testing devices, the pressuremeter is one of the few instruments capable of capturing stiffness and strength properties of weak rock. However, data collected is only useful if the material tested is properly modeled and desirable material properties can be obtained. While constitutive models with various flows rules have been developed for pressuremeter analysis in soil, less research has been directed at model development for pressuremeter tests in weak rock. The result is pressuremeter data collected in rock is typically analyzed using models designed for soil. The aim of this study was to explore constitutive rock models for development into a pressuremeter framework. Three models were considered, with two of those three implemented for pressuremeter analysis. A Mohr-Coulomb model with a tensile cutoff developed by Haberfield [10] and a Hoek-Brown model initiated by Yang *et al* in [23] and further developed by the author were implemented and calibrated against a data set of pressuremeter tests from 5 project test sites including a total of 115 pressuremeter tests in a number of different rock formations. Development of a multiscale damage model established by Kondo *et al* [8] was explored. However, this model requires further development to be used for pressuremeter data analysis.

TABLE OF CONTENTS

Page

LIST OF FIGURES

Figure Number Page

LIST OF TABLES

Table Number Page

ACKNOWLEDGMENTS

First and foremost, I would like to thank all my former colleagues at In Situ Engineering without whom this thesis would not have been possible. I would like to thank owner and President Keith Brown for giving me the opportunity to do some amazing work early in my career, previous partial owner and in many ways pressuremeter master expert, Dr. John Hughes for providing guidance and breaking me into pressuremeter analysis, former coworker Chris Nowak for tireless hours put in collecting data and showing me the ropes for performing pressuremeter tests in the field, former coworker Joel Witthus for helping upgrade the pressuremeter software and systems and the late Larry Bailey for always being prepared and helping us be ready for every job - you will be missed. I would like to extend another thanks to In Situ Engineering for providing me with this amazing data set to play with as part of my thesis work.

Another key player is my advisor Dr. Pedro Arduino, who provided guidance in many ways as well as many useful insights and lessons for material modeling. I would also like to thank him for his incredible patience. There were many times where this thesis work was set down for other priorities, but Pedro never gave up on me.

Finally, I would like to thank all my friends and family for their love and support throughout this process - my mother Janet, father Brian, step father Dave, sisters Daneel, Jess and Melany and of course my lady Brook. Thank you very much to all. I did it!

Chapter 1

INTRODUCTION

The pressuremeter is one of the most versatile *in situ* testing instruments used in the field of geotechnical engineering; capable of data collection in materials ranging from very soft clay to weak rock. Dependant upon the type of pressuremeter used and the manner in which the test is performed, a large number of soil parameters can be obtained from a pressuremeter (PM) test. Refer to Tables 1.1 and 1.2 on the next page, adopted from Clarke (1995) after Robertson (1986) and Wroth (1984). Among them, the most common parameters that are determined from a PM test are shear modulus, G, which can then be correlated to Young's modulus, E, undrained shear strength S_u, friction angle ϕ', and the *in situ* horizontal shear stress σ_{ho}. Accurately defining these parameters can lead to more reliable and efficient shallow and deep foundation, tunnel, earth anchor and excavation design. For this reason it is imperative to continue the advancement of pressuremeter instrumentation as well as the development and improvement of accurate constitutive models for analysis of pressuremeter data.

The focus of this study is the interpretation of pressuremeter data obtained in weak rock. Due to the limitations in testing capabilities for weak rock, the pressuremeter is one of few and probably the most appropriate *in situ* test for estimating rock modulus [17] that is also capable of capturing strength properties. Although the pressuremeter is highly capable of testing weak rock, data collected is only useful if the material tested is properly modeled and desirable material properties are obtained. Many constitutive models have been developed to analyze different soil types, but less research has been directed toward the behavior of rock subjected to pressuremeter loading. Complicating factors, such as propagating cracks, discontinuities, tensile strength, and brittle behavior have attenuated the development of weak rock models. A result of this is that tests performed in weak rock are often analyzed using models designed to interpret soil. The goal of this research is accomplished by reviewing previous models developed for PM analysis and exploring constitutive models for weak rock. This information is used to develop an alternative cavity expansion rock model which is calibrated against a large pressuremeter data set and subsequently compared to applicable previous models (in particular that by Haberfield (1987)). The data analyzed was collected from five different sites throughout the United states and in other regions of the world in weak, weathered and sometimes highly fractured material. The instrumentation deployed was a pre-bored pressuremeter fitted with cavity displacement and pressure sensors.

Table 1.1: Applicability of the Pressuremeter (adopted from Clarke; adjusted by author)

Device	Ground Type						
	Hard Rock	Soft Rock	Gravel	Sand	Silt	Clay	Peat
PBP	A	A	B	B	B	A	B
SBP	-	A	-	B	A	A	A
PIP	-	-	-	B	A	A	B
Cone PIP	-	-	-	A	A	A	A

Applicability: A-high; B-moderate; C-low; -not.

Table 1.2: Usefulness of the Pressuremeter (adopted from Clarke (1995); adjusted by author)

Device	Parameters												
	Soil	Profile	u	ϕ'	S_u	D_r	m_v	c_v	k	G	σ_h	OCR	$\sigma - \epsilon$
PBP	B	B	-	C	B	C	B	C	-	B	C	C	C
SBP	B	B	A	A	A	A	A	A	B	A	A	A	A
PIP	A	B	B	C	B	C	C	A	B	A	C	C	C
Cone PIP	C	B	B	C	B	C	C	A	B	A	C	C	C

Applicability: A-high; B-moderate; C-low; -not.

Before the research performed for this thesis is presented, the author will first provide background information on pressuremeter development, instrumentation and testing. The author will also provide a brief description of the data analyzed and a working definition of weak rock. This chapter then concludes with an outline of the thesis.

1.1 Background

The pressuremeter is a cylindrical probe with a flexible membrane that is inserted into the ground and expanded radially against a borehole wall to measure the displacement obtained given a certain pressure applied (refer to Figure 1.1)). The resulting data obtained is a stress-strain curve, where the pressure applied (radial stress) is plotted against circumferential (Δ radius/initial radius), or volumetric strain. Both strain-controlled tests and stress-controlled tests are possible dependant on the equipment and setup used. Four main categories of pressuremeters exist as shown in Tables 1.1 and 1.2: pre-bored pressuremeter (PBP), self-boring pressuremeter (SBP), push-in pressuremeter (PIP) and cone PIP, of which the focus of this study will be the pre-bored pressuremeter. It should be noted that within any one category a number of instrument configurations exist.

1.1.1 Development of the Pressuremeter Instrumentation and Interpretation

The idea of a pressuremeter was first developed by Kogler in 1933, but major development of the instrument did not occur until Louis Mẽnard began his work at the University of Illinois in the 1950s. Mẽnard developed and patented what is known as the Mẽnard pressuremeter in 1957, one of the most widely used types of pressuremeter today [7]. Also during the 1950s in Japan, Fukuoka was researching laterally loaded piles and independently developed a pressuremeter for the OYO Corporation. The Mẽnard pressuremeter is a pre-bored pressuremeter with expansion induced by a controlled volume of water fed into the pressuremeter cavity via an umbilical cable that extends to the ground surface. Volumetric strain and pressure are recorded as the test proceeds. In 1980 Hughes and Irvin developed the high pressure dilatometer manufactured in Cambridge, England, not to be confused with the later developed Marchetti dilatometer. The instrument is equipped with a pressure cell and three or six displacement sensors placed equidistant around the center of

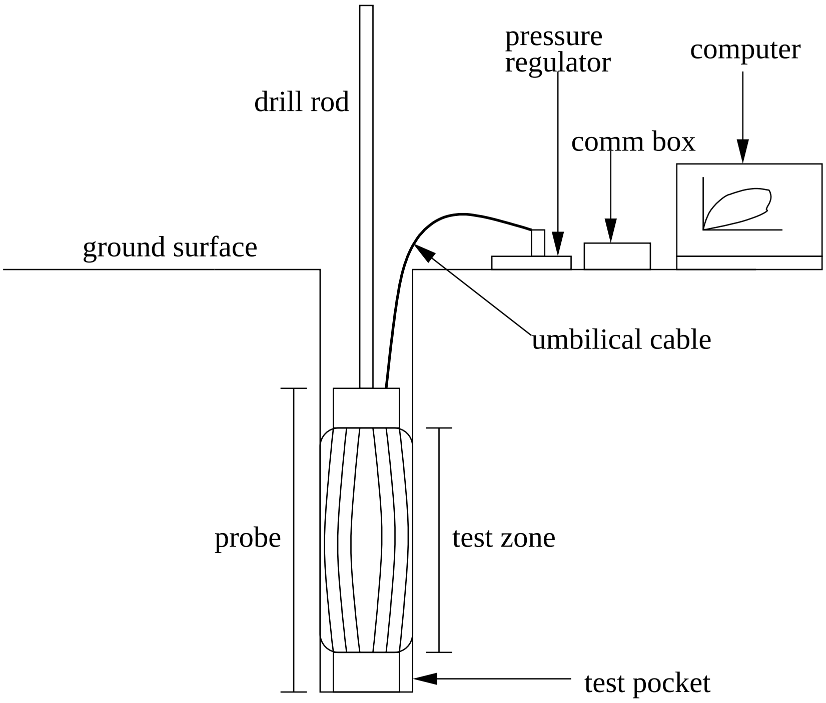

Figure 1.1: Pressuremeter Test Setup

the expanding zone of the instrument. Previously analog and now digital signals from the pressure cell and strain gauges are processed by a computer board within the instrument and then sent to the surface via an umbilical cable attached to the instrument. At the surface the signals are interpreted by computer software and a plot of pressure versus cavity strain is created. Data analyzed for this research was collected with instruments developed by Hughes (Cambridge type) and will be described in greater detail later.

The advancement of the pressuremeter has subsequently led to the development of a number of material models to analyze the data collected. However, the theory of cavity expansion existed prior to the creation of the pressuremeter, originally developed by Lamẽ in 1852. The interpretation techniques for the pressuremeter have often been developed for a specific material and focus on either drained or undrained analysis. In this regard, materials analyzed are usually viewed as either purely cohesive materials or purely frictional materials. Table 1.3 briefly summarizes the history of model progression. The more common

Table 1.3: Theoretical Interpretation of a Pressuremeter Test (after Clarke (1995))

Lamẽ (1852)	Linear elastic material
Bishop *et al.* (1945)	Cohesive material
Mẽnard (1957d) Vesic (1972)	Frictional cohesive material
Gibson and Anderson (1961) Windle and Wroth (1977a) Jefferies (1988) Houlsby and Withers (1988)	Linear elastic perfectly plastic material with no volume changes
Denby (1978) Ferreira and Robertson (1992)	Non-linear elastic perfectly plastic material with no volume changes
Prẽvost and Hoeg (1975)	Elastic-plastic with strain hardening or softening with no volume changes
Ladanyi (1963a) Vesic (1972) Hughes *et al.* (1977) Robertson and Hughes (1986) Houlsby *et al.* (1986)	Linear elastic perfectly plastic material with volume changes
Palmer (1972)	Cohesive material with no volume changes
Manassero (1989)	Cohesionless material with volume changes

models used in practice today are those developed by Gibson and Anderson (1961), Palmer (1972) and Jefferies (1988) for cohesive materials; Hughes (1977) and Manassero (1989) for frictional materials. These models will be described in more detail in the following chapter. It should be noted that models developed by Rocha (1966), Ladayni (1976) and Haberfield (1987) are not included in Table 1.3, but will also discussed in the next chapter.

1.1.2 Pressuremeter Instrumentation and Typical Data Collected

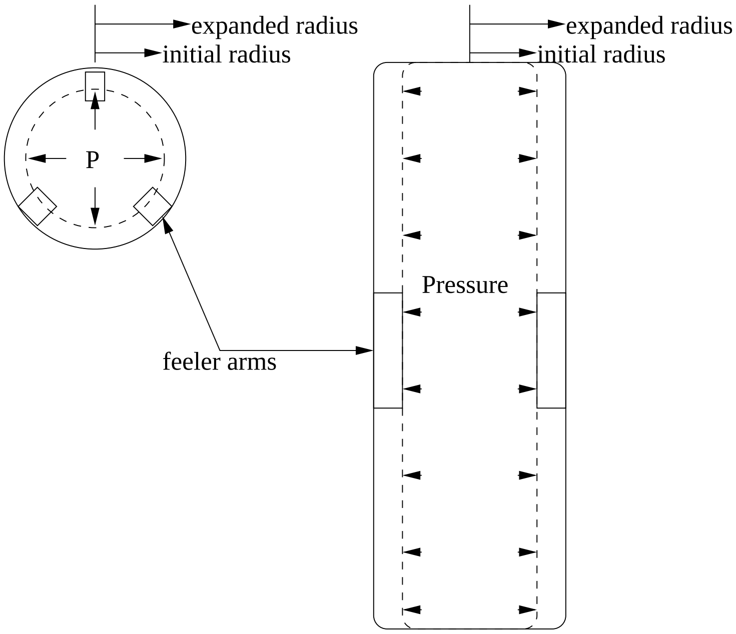

Figure 1.2: Pressuremeter Expansion (Cross Section)

As previously mentioned, a number of different types of pressuremeters exist. The focus of this study revolves around data collected using a pre-bored monocell pressuremeter of the Cambridge type; the description that follows will be applicable to this type of pressuremeter. The Cambridge style pre-bored pressuremeter developed by Hughes consists of a cylindrical probe with three displacement sensors and a pressure sensor. The three displacement sensors, spaced 120 degrees apart, are comprised of feeler arms equipped with strain gauges that measure the movement of the inside of a rubber membrane as it expands laterally (refer to Figure 1.2). The rubber membrane encloses the electronics of the instrument and is locked down on either end of the instrument via a threaded coupling mechanism to avoid pressure loss during a test. The strain gauges and pressure sensor both feed information to a computer board within the instrument. Electronic cables run from the computer board up an umbilical cable to the surface. The umbilical cable serves two purposes: i) protection for the electronic cables running from the instrument to the surface and ii) feeds pressurized air or oil to the instrument during a test. The information sent to the surface is processed by a communication box, which sends information to a computer for interpretation by data collection software. The software allows the operator to observe a live stress-strain curve while performing a test. The flow of air or oil is controlled by the operator using a regulator at the surface, which hooks into the umbilical cable. Prior to installation for a test, the instrument is also fitted with a shield to protect the membrane, consisting of a series of metal strips that allow for free movement of the instrument. This style pressuremeter is approximately 2.5 feet (.76 meters) long and 3 inches (7.6 cms) in diameter. The portion that expands during a test is approximately 18 inches (45.7 cms) long (deemed the 'test zone' in Figure 1.1).

The testing process involves employing drillers to create test pockets (refer to Figure 1.1) at different locations of interest for a particular engineering project. Often multiple boreholes will be selected to perform pressuremeter testing and a number of depth locations are assigned. At a given borehole location, the driller will ream out a hole of larger diameter (typically 4-6 inches (10.1-15.2 cm)) to a depth just above the location of the desired test pocket. A test pocket is then drilled out using a 2-15/16 inch tricone bit or NQ core barrel, which is typically used in a rock. The term NQ is the size designation for the core barrel used; NQ rod has an outside diameter of approximately 2.75 inches (7 cms) and cuts a hole approximately 3 inches in diameter. Depending upon conditions, usually a 5-6 foot (1.5-1.8 meter) test pocket is drilled. The pressuremeter is then lowered into the test pocket as far as possible; ground conditions may be such that the pressuremeter is stopped short due to sloughing or inhibiting rock or gravel fragments which cease the advancement of the instrument. After testing this location, the instrument is raised 18 inches and another test is performed in the same test pocket (if possible). The second test serves multiple purposes:

i) if one test is of poor quality due to a washed out area in the test pocket, the second may provide useful data, ii) if both tests are good quality and in the same material, confirmation of the material properties can be gained during the modeling process, and iii) if both tests are good quality and in different materials, the properties of both materials are captured (in the case of highly variable material or interbedded zones). The process described above is then repeated at the next testing location.

During a test, the flow of air or oil into the instrument is controlled by the PM operator. The judgement of the operator is crucial in collecting data. Depending upon what parameters are desired, the test may be performed in a different fashion. The main goal, however, is to deform the surrounding material sufficiently so that material yield or failure has occurred if such pressures are within the achievable range of the instrument (typical ranges are 0-20 MPa or approximately 0-2,900 psi). During the process a series of unload-reload loops are also performed to determine the shear modulus of the material. Of course, considerations for disturbance due to drilling action, the size of the pocket relative to the instrument and the possibility of damaging the instrument are of concern as well.

An example of a test performed in rock-like material is given in Figure 1.3. The test commences at point A and the pressure is gradually increased until the initiation of the first unload-reload loop at point B. From this portion of the test, the in situ stress and initial shear modulus can be determined, the details of which will be discussed later. It should, however, be noted that the portion of the test between points A and B is prone to disturbance from drilling action. Evidence of disturbance is present in this test as illustrated by the irregular shape of the initial loading curve.

Beyond point B, the material is unloaded and upon reloading, the curve takes on a shape more indicative of an initial loading curve without the presence of disturbance. The pressuremeter is then incrementally loaded until point C.

Between points C and D, the pressure is held constant for three minutes in order to capture the movement of the surrounding material under a constant load; this is deemed a ‘creep test’.

Immediately following the creep test, the pressuremeter is again unloaded between points D and E, and then reloaded from points E to F forming an unload-reload loop. It is from

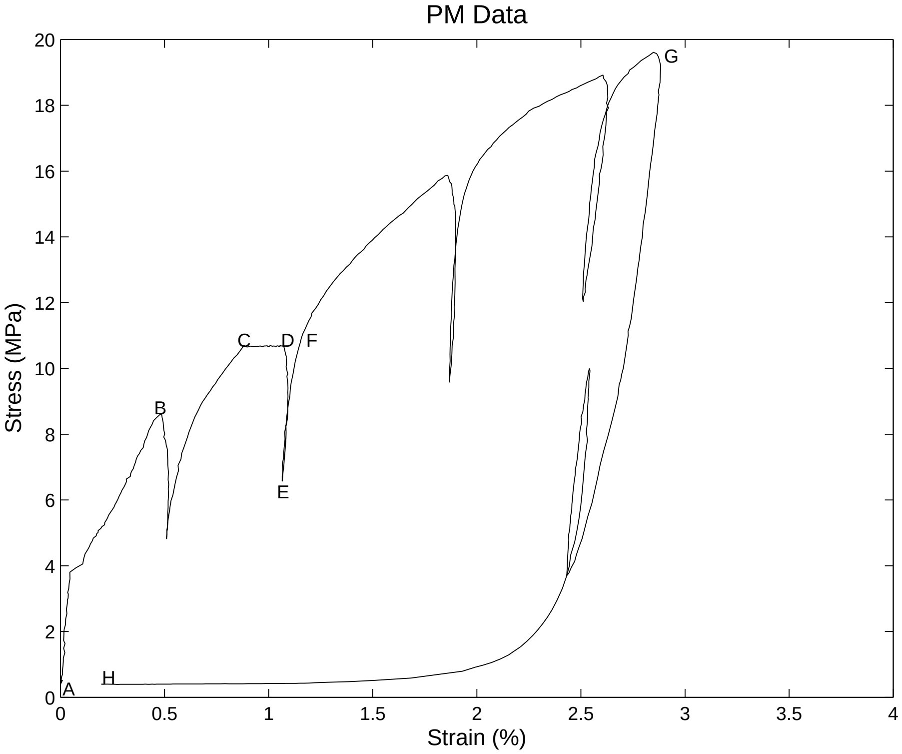

Figure 1.3: Example of Pressuremeter Test in Rock

this loop that the shear modulus of the material can be determined. The initial portion of the slope can also be used for determining the shear modulus, but lower modulus values are often obtained due to the drilling disturbance and stress relief. As the loading is increased further, a series of unload-reload loops is performed. Parallel loops indicate a consistent shear modulus value that can be reported with confidence. In the case where loops are not parallel, this is indicative of disturbance or that a strain-hardening or strain-softening material is present.

The loading is again increased further until the final unloading is commenced at point G. Although yield has occurred in this test, it's worth noting that the test was terminated as a result of the pressure limitations of the instrument. Typically, a test in soil will be terminated due to the strain capacity of the instrument and it is often the goal to reach a material strain of 10%.

During the unloading, a reload-unload loop is performed in order to gain more information about the material shear modulus. At point H, the pressuremeter is almost completely deflated. The rapid collapse of the membrane prior to point H is a result of the static pore water pressure present in the surrounding formation. Once the pressure inside the membrane is reduced below the static pore pressure, the membrane is quickly forced back towards the instrument body.

The overall shape of the loading and unloading curve can both be modeled for strength properties provided that sufficient yield has occurred. Such details of the analysis process will be further discussed in the following chapters of this thesis.

1.1.3 Weak Rock Data and Definition

It is important to establish a working definition of the material modeled in this research project. Therefore a classification scheme separating soil and rock, that accounts for the general strength of rock must be established. A parameter that is commonly used to describe rock strength is the unconfined compressive strength, also known as the uniaxial compressive strength (σ_c). A scheme that considers these qualities, adopted by [17] after Meigh and Wolski (1979), has been reproduced in Figure 1.4 and provides a straightforward working definition. However, it should be noted that this chart does not consider the effects of discontinuities and rock structure, which should be accounted for [17]. Nevertheless, it does provide a scale of measure and generally, weak to moderately weak rock has an axial compressive strength in the range of 1 - 12.5 MPa.

The data set analyzed in thesis consists of 115 pressuremeter tests in a number of rock types including: limestone, siltstone, sandstone, gruss, shale, mudstone, meta-welded tuff and a cemented cobble, gravel matrix. Through modeling and background information, it was determined that uniaxial compressive strength of the data collected typically ranged from 4.5 - 50 MPa, with data from one site (in meta-welded tuff) in the range of 70 - 120 MPa. With the exclusion of the tests in meta-welded tuff, which would be defined as strong rock, the majority of the data varied between weak to moderately strong rock. The data collected in the meta-welded tuff allowed for easier model calibration and provided a good

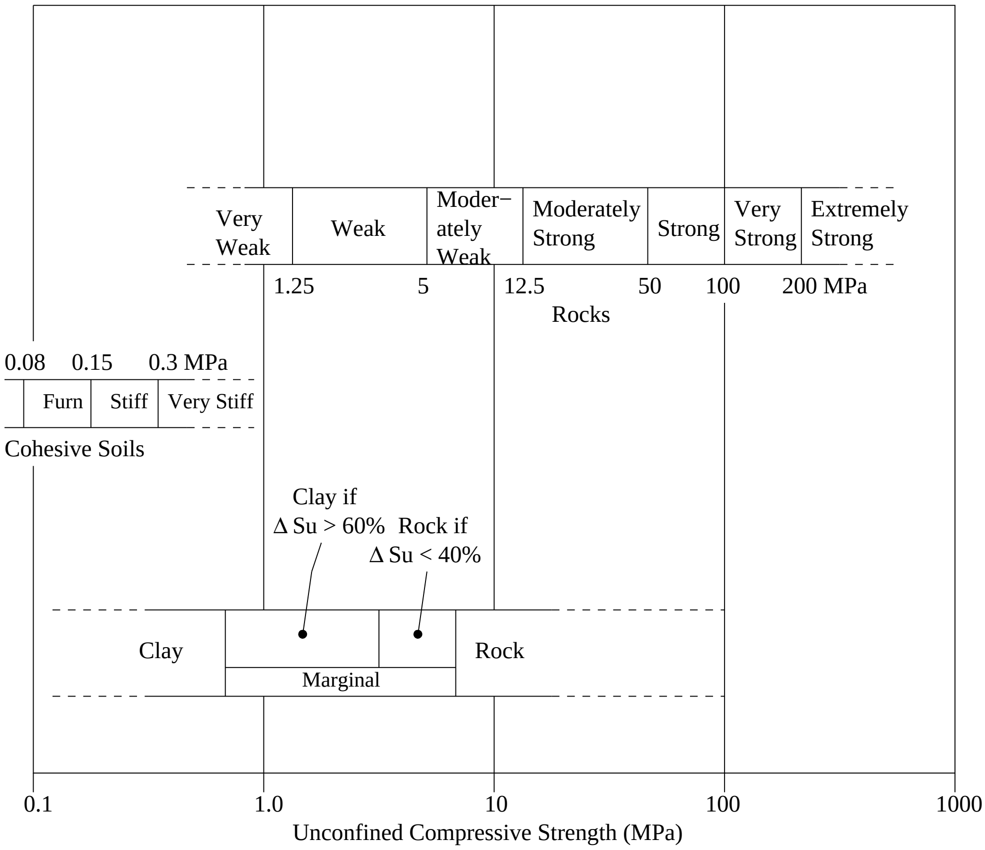

Figure 1.4: Scale of Strengths for classifying rock (adopted from [17] after Meigh and Wolski (1979))

basis for comparison to the weaker rock formations. It should also be stressed that the tuff is only considered strong rock in an intact state.

1.2 Thesis Outline

As described above, the purpose of this study is to explore constitutive models for weak rock using cavity expansion theory to analyze pressuremeter data. A Hoek-Brown model is developed and used to interpret pressuremeter data from the five sites mentioned. The equivalent strength values determined through the Hoek-Brown analysis are compared to the strength parameters found analyzing the same data set using a Mohr-Coulomb model with a tensile cutoff developed by Haberfield (1987). A third constitutive model with a double yield criterion considering crack propagation is also investigated for possible future use in analyzing pressuremeter data. The thesis will be organized and presented as follows:

- Chapter 2 provides a literature review of previous pressuremeter models developed. Theory is presented covering both elastic and inelastic (plastic) deformation using a cavity expansion framework. The validity of the models for use in weak rock analysis is then discussed.

- Chapter 3 goes into the development of the Hoek-Brown model and also provides further detail of the model developed by Haberfield. Validation of the models is provided and a parametric analysis of the two models is presented and discussed. Finally, the framework of a third constitutive model is outlined.

- Chapter 4 presents details of data interpretation and the pressuremeter data set analyzed. Some sample results of the data analysis for both the Hoek-Brown and Mohr-Coulomb model are presented and discussed.

- Chapter 5 discusses the performance of the models and concluding thoughts on strength and weaknesses of the models. A framework for possible future work is also presented.

- Appendix A provides plots of all the data analyzed by the Hoek-Brown model. Input parameters and other pertinent information is provided for the five test sites in which data was collected.

Chapter 2

CAVITY EXPANSION THEORY FOR PRESSUREMETER ANALYSIS

The different models developed to analyze pressuremeter data have all spawned from the same theory of cavity expansion developed originally by Lamẽ in 1852 for a linear elastic material. When solving a cavity expansion problem there are two different approaches which can be utilized; either a constitutive model for the soil or rock is used to derive a cavity expansion curve or a cavity expansion curve is developed using a mathematical function or flow rule, and parameters are derived by applying a constitutive model to the function. The second method is often applied to develop new pressuremeter models and is known as an inverse cavity expansion method [24]. Both methods produce an idealized pressuremeter stress-strain curve which can be used to determine stress and displacement fields. Adjustment of key parameters affecting the shape of the cavity expansion curve is required until a 'best fit' to the recorded data is accomplished. In order to properly develop a new model or adapt a constitutive model for use in pressuremeter analysis, first an understanding of cavity expansion theory and a review of some of the existing models is required.

Before presenting the existing models, it is important to first consider the basic assumptions used in the model development. The assumptions true to most pressuremeter models are as follows:

- The material tested is homogeneous
- The material behaves isotropically
- Axial symmetry is valid
- The material deforms as a right cylinder and thus deforms in plane strain
- Loading and strain rate effects are negligible
- No significant disturbance occurs prior to the start of a test
- The material follows a unique stress-strain law

Along with the above assumptions, it is generally accepted that small strain theory is applicable, which remains valid until higher strain and dilation angles are reached [7]. Dependant upon the material tested, a drained analysis assuming volume change or an undrained analysis assuming no volume change is often applied. Although a drained analysis is more likely appropriate in modeling weak rock, solutions for both types of analysis will be presented in this chapter. Flow rules and yield criterion adopted will be included in the discussion of each model.

It should be noted that the purpose of this chapter is to provide a general overview of some of the principals of cavity expansion and it's application to the pressuremeter. Some of the pressuremeter models currently adopted and pertinent equations are provided. However, a more detailed description of model development and formulation is given in Chapter 3, specifically for the models explored for analyzing weak rock that are the focus of this thesis.

2.1 Cavity Expansion in an Elastic Medium [7][10][24]

During a pressuremeter test, as pressure is applied, the material will initially deform in an elastic manner. The solution for an expanding right cylinder in an infinite elastic material can be determined by utilizing boundary conditions related to conditions of stress or displacement. Both solutions will be presented here. From these results, a method for determining the shear modulus, G, will also be revealed. It should be recognized that the following solutions are in cylindrical coordinates with vertical stress, σ_z, radial stress, σ_r and circumferential stress σ_θ acting as the principal stresses. It follows that ϵ_z, ϵ_r and ϵ_θ are the principal strains.

2.1.1 Solution using Displacement Boundary Conditions

For a given element of soil, dr, located at a distance r, in an axisymmetric system the equation for equilibrium in terms of radial and hoop stress is as follows:

$$\frac{d\sigma_r}{dr} + \frac{\sigma_r - \sigma_\theta}{r} = 0 \tag{2.1}$$

where σ_r and σ_θ are stresses in the radial and circumferential directions respectively and r is the radius from the neutral axis, an example of which is given in Figure 2.1. The kinematic

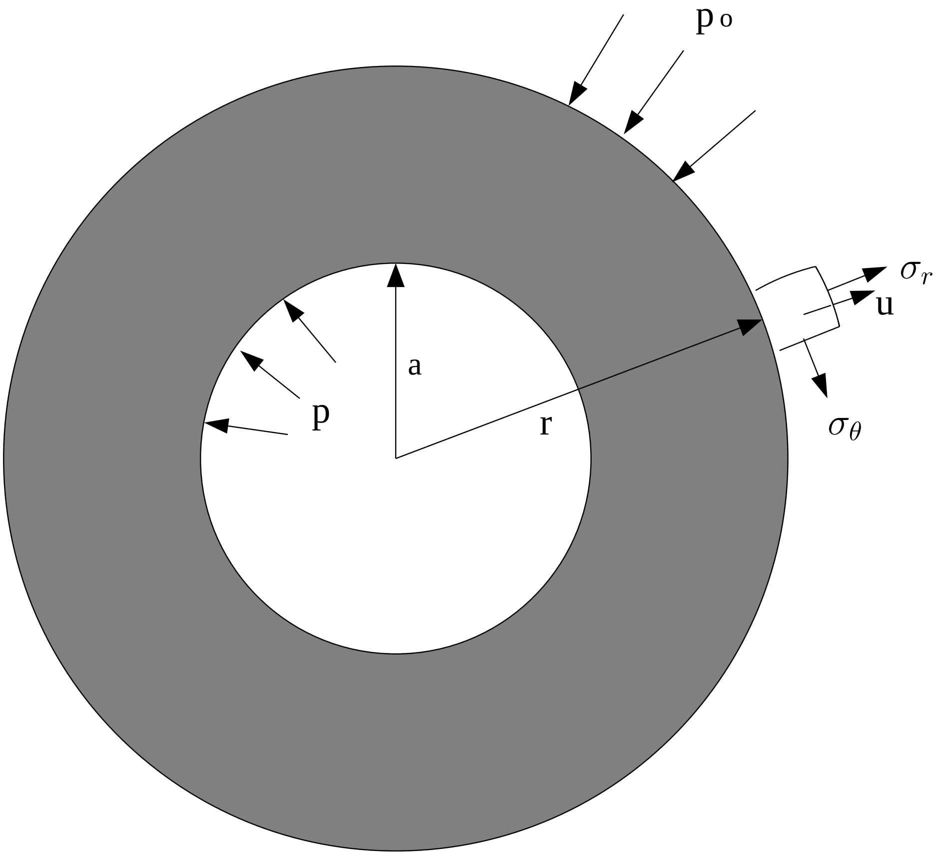

Figure 2.1: Cross Section of an Expanding Cylindrical Cavity

relations for an expanding cylindrical cavity are:

$$\epsilon_\theta = \frac{u}{r} \tag{2.2}$$

and

$$\epsilon_r = \frac{du}{dr} \tag{2.3}$$

where u is displacement in the radial direction. The cavity strain directly measured during a pressuremeter test can be related to the radius of the expanding cavity as follows:

$$\epsilon_c = \frac{a - a_o}{a_o} \tag{2.4}$$

where a is the radius or the inner cavity (pressuremeter cavity) and a_o is the initial inner cavity radius. It can be noted that cavity strain as defined in Equation (2.4) is a measure of circumferential strain. If the material is assumed to be isotropic and behave in a linear elastic manner, Hooke's Law can be used to define the constitutive relations between stress and strain for the axisymmetric case as follows:

$$E\epsilon_r = \sigma_r - \nu(\sigma_\theta + \sigma_z) \tag{2.5}$$

$$E\epsilon_\theta = \sigma_\theta - \nu(\sigma_r + \sigma_z) \tag{2.6}$$

$$E\epsilon_z = \sigma_z - \nu(\sigma_\theta + \sigma_r) \tag{2.7}$$

where E is the elastic modulus and ν is Poisson's ratio. If it is recognized that the strain in the vertical direction is zero (plain strain assumption), then the above equations can be rearranged yielding:

$$\epsilon_r = \frac{1-\nu^2}{E}\left(\sigma_r - \frac{\nu}{1-\nu}\sigma_\theta\right) \tag{2.8}$$

$$\epsilon_\theta = \frac{1-\nu^2}{E}\left(\sigma_\theta - \frac{\nu}{1-\nu}\sigma_r\right) \tag{2.9}$$

For a homogeneous, isotropic, linear elastic material (as assumed here) Young's modulus can be related to the shear modulus as follows:

$$E = 2G(1+\nu) \tag{2.10}$$

Substituting the relation in Equation (2.10) into Equations (2.8) and (2.9) and solving in terms of radial and circumferential stress yields:

$$\sigma_r = G\left(\frac{2\nu}{1-\nu}\right)\epsilon_\theta + 2G\left(\frac{1-\nu}{1-2\nu}\right)\epsilon_r \tag{2.11}$$

$$\sigma_\theta = G\left(\frac{2\nu}{1-\nu}\right)\epsilon_r + 2G\left(\frac{1-\nu}{1-2\nu}\right)\epsilon_\theta \tag{2.12}$$

Combining the kinematic (Equations (2.2) and (2.3)) and constitutive (Equations (2.11) and (2.12)) relations with the equation for equilibrium (Equation (2.1)) yields the differential equation:

$$\frac{d^2u}{dr^2} + \frac{1}{r}\frac{du}{dr} - \frac{u}{r^2} = 0 \tag{2.13}$$

The above equation is a second order differential equation which can be solved by substitution in terms of displacement using the general format below:

$$u = Ar + \frac{B}{r} \tag{2.14}$$

where A and B are constants which can be solved by applying boundary conditions. The boundary conditions are:

$$u \to 0 \text{ as } r \to \infty$$
$$u = a - a_o \text{ when } r = a$$

Applying these boundary conditions the following solutions for constants A and B can be determined:

$$A = 0 \tag{2.15}$$
$$B = (a - a_o)a \tag{2.16}$$

This results in the following equation for displacement at the cavity wall:

$$u = \epsilon_c \frac{a_o a}{r} \tag{2.17}$$

Combining the above relation and the constitutive relations for an incremental change in stress $(\sigma_r - \sigma_{ho})$ allows the stresses to be computed as follows:

$$\sigma_r = p_o + 2G\epsilon_c \frac{a_o a}{r^2} \tag{2.18}$$
$$\sigma_\theta = p_o - 2G\epsilon_c \frac{a_o a}{r^2} \tag{2.19}$$

where p_o is the *in situ* pressure, equivalent to the ambient horizontal stress σ_{ho}.

Recognition that $a - a_o$ is small during elastic expansion, and that $\sigma_r = p$ at the cavity wall, Equation (2.19) can be rewritten as:

$$p - p_o = 2G\epsilon_c \tag{2.20}$$

where p is the internally applied pressure. Rearranging to solve for the shear modulus, G, yields the following equation:

$$G = \frac{0.5(p - p_o)}{\epsilon_c} \tag{2.21}$$

Thus the shear modulus can easily be derived from the slope of the stress-strain curve produced by the pressuremeter during elastic deformation. The above equation is applied to the elastic portion of the curve developed during initial loading and deformation. However, as this section of the curve is often prone to disturbance, or not very well defined, unload-reload cycles are often performed during a test to capture a more realistic representation of the elastic material behavior. Accounting for this, Equation (2.21) can be written in a more general form as:

$$G = 0.5\frac{a}{a_o}\frac{dp}{d\epsilon_c} \tag{2.22}$$

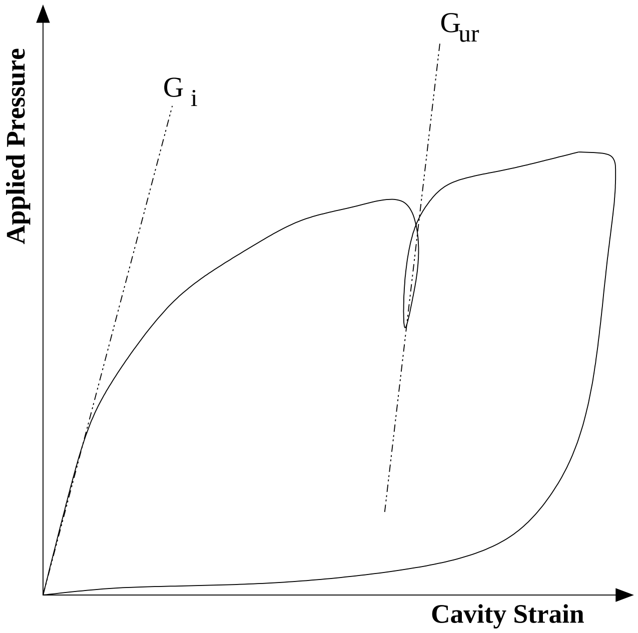

Figure 2.2: Typical Pressuremeter Curve with Initial Modulus: G_i and Unload-Reload Modulus: G_{ur}. This is for illustrative purposes, as the actual slopes of these lines measured as shown would equal $2G$, i.e. $2G_i$.

Figure 2.2 represents the typical curve obtained during a pressuremeter test. The unload-reload loop performed during the loading phase of the test is used to determine the shear modulus, G_{ur}, while the initial elastic phase is used to determine the shear modulus G_i. The unload-reload loop is less prone to error and is often repeatable (usually more than one is performed during a test) and thus is usually accepted as the true shear modulus of the material.

2.1.2 Solution using Stress Boundary Conditions

The solutions for stress and displacement determined in the previous section can also be achieved by utilizing boundary conditions related to stress. If it is initially assumed that the material tested has a finite boundary at radius b (i.e. for a thick walled cylinder) beyond which the influence of the expanding cavity is negligible, then the boundary conditions are as follows:

$$\sigma_{r(r=a)} = p$$
$$\sigma_{r(r=b)} = p_o$$

By combining the equations for equilibrium and kinematics (Equations (2.1) through (2.3)), along with the constitutive stress-strain relations (Equations (2.8) and (2.9)) a differential equation for the radial stress with a general solution as written below will be produced.

$$\sigma_r = C + \frac{D}{r^2} \tag{2.23}$$

where C and D are constants. Applying the boundary conditions and solving for C and D results in:

$$C = \frac{p_o b^2 - p a^2}{b^2 - a^2} \tag{2.24}$$
$$D = \frac{a^2 b^2 (p - p_o)}{b^2 - a^2} \tag{2.25}$$

These values for the constants C and D are true for the case of a thick walled cylinder, but in order to properly mimic the conditions of a pressuremeter test, an infinite medium must be considered and hence $b \to \infty$ must be substituted. Solving for the stress and displacement and making this substitution results in the following relations:

$$\sigma_r = p_o + (p - p_o)\left(\frac{a}{r}\right)^2 \tag{2.26}$$
$$\sigma_\theta = p_o - (p - p_o)\left(\frac{a}{r}\right)^2 \tag{2.27}$$
$$u = \frac{p - p_o}{2G}\frac{a^2}{r} \tag{2.28}$$

It should be noted that these solutions are identical to those obtained in the previous section, but are defined by different parameters.

2.2 Plasticity Models - Undrained Analysis [7][17]

During the elastic phase of loading, the radial stress, σ_r, increases as the circumferential stress, σ_θ, decreases at the same rate (refer to points 1 through 3 in Figure 2.3 and Equations (2.26) and (2.27)). Due to plain strain conditions, the vertical strain is zero ($\epsilon_z = 0$) meaning vertical stress $\sigma_z = \nu(\sigma_\theta + \sigma_r)$ (Equation (2.7)) and therefore the change in vertical stress is also zero in the elastic range. Hence, as there is no change in the mean stress, there is no build up of excess pore water pressure and thus the behavior during elastic deformation is independent of the drainage conditions. However, at the onset of yield (point 3 in Figure 2.3), the conditions in the soil or rock change and either a drained, partially drained or undrained analysis must be adopted. For cohesive materials (i.e. clay) it is assumed that fully undrained conditions are applicable and subsequently no volume change occurs as the surrounding material deforms plastically (points 3 to 4 in Figure 2.3). Due to the resulting fluctuations in pore pressure, a total stress analysis is usually adopted. Generally the models for undrained analysis use a Tresca failure criterion and assume elastic-perfectly plastic behavior. The Tresca yield criterion can be written as:

$$p_f = p_o + S_u \tag{2.29}$$

where p_f is the pressure at which yield or initiation of plastic failure occurs, p_o is the initial or *in situ* pressure and S_u is the undrained shear strength of the material.

If the material deforms in a perfectly plastic manner, then the shear stress at failure, τ_f will remain constant and be equal to the undrained shear strength, S_u once the yield criterion has been satisfied, i.e. when the applied pressure is equal to p_f. In analyzing the shear stresses developed during a pressuremeter test, Palmer (1972), Baguelin (1972) and Ladanyi (1972) all independently arrived at the same solution for the shear stress at any given strain.

$$\tau = 0.5\epsilon_c(1+\epsilon_c)(2+\epsilon_c)\frac{dp}{d\epsilon_c} \tag{2.30}$$

For small strains Equation (2.30) reduces to:

$$\tau = \epsilon_c\frac{dp}{d\epsilon_c} \tag{2.31}$$

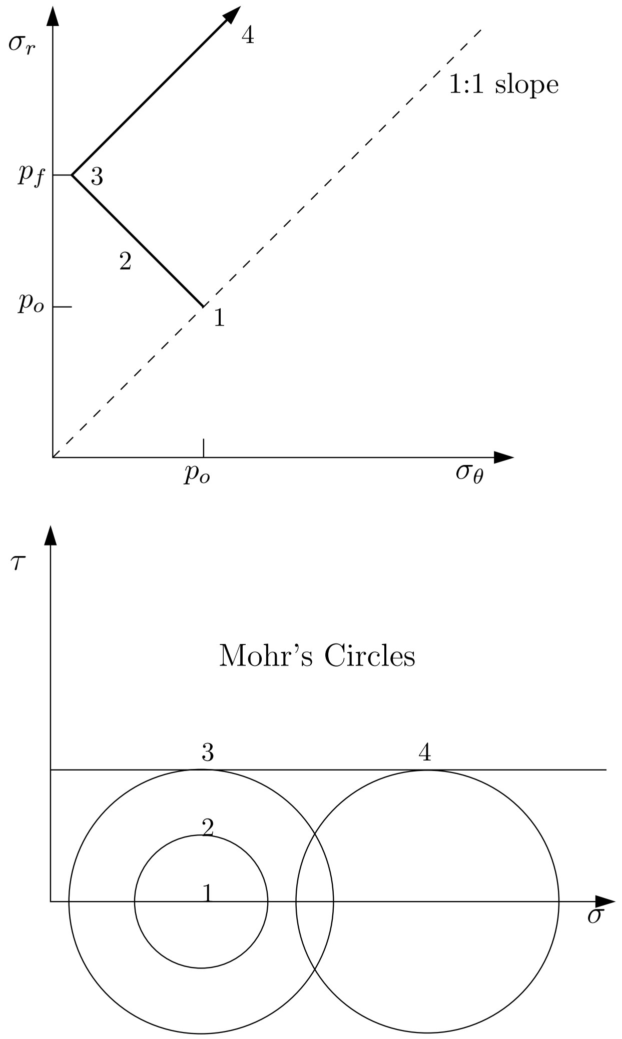

Figure 2.3: Stress Path and Mohr's Circle for Undrained Analysis

Equation (2.31) can also be written in terms of volumetric strains (measured when using a Mẽnard style pressuremeter) as follows:

$$\tau = \frac{dp}{d\left[ln\left(\frac{\Delta V}{V}\right)\right]} \tag{2.32}$$

From inspection of the equations above, it is clear that the shear stress can be determined by multiplying cavity strain by the slope of pressure versus cavity strain or by measuring the slope of a plot of pressure versus the natural log of volumetric strain. Thus, after the initiation of plasticity the shear strength, S_u can be determined in this manner. Utilizing this knowledge, the volumetric strain at the initiation of plastic yield can be written as follows:

$$\frac{\Delta V}{V} = \frac{S_u}{G} \tag{2.33}$$

Gibson and Anderson (1961) used these relations to determine a governing equation for the behavior of a cohesive, undrained, elastic-perfectly plastic material during cavity expansion. By integrating Equation (2.32) with respect to $ln(\Delta V/V)$ the following relation was obtained:

$$p - p_o = S_u\left[1 + ln\left(\frac{G}{S_u}\right) + ln\left(\frac{\Delta V}{V}\right)\right] \tag{2.34}$$

This equation is the most commonly used when analyzing pressuremeter data in a cohesive material and is directly applicable to a Mẽnard pressuremeter which takes measurements in terms of volumetric strains. A more accessible form of the equation for pressuremeters that measure strain in terms of cavity strain (such as the type used in this research) can be written in terms of displacement as follows:

$$p - p_o = S_u\left\{1 + ln\left[\left(\frac{G}{S_u}\right)\left(1 - \frac{a_o}{a}\right)^2\right]\right\} \tag{2.35}$$

A similar equation to that proposed by Gibson and Anderson was developed previously by Mẽnard (1957). Upon the initiation of plasticity, an annulus of soil undergoing plastic deformation is formed around the expanding pressuremeter cavity. As the pressuremeter expands further the radius of the plastic annulus increases. Thus the boundary, beyond which soil is behaving elastically, (known at the elastic-plastic boundary) is moved further away from the expanding cavity, resulting in a stiffness reduction of the pressuremeter

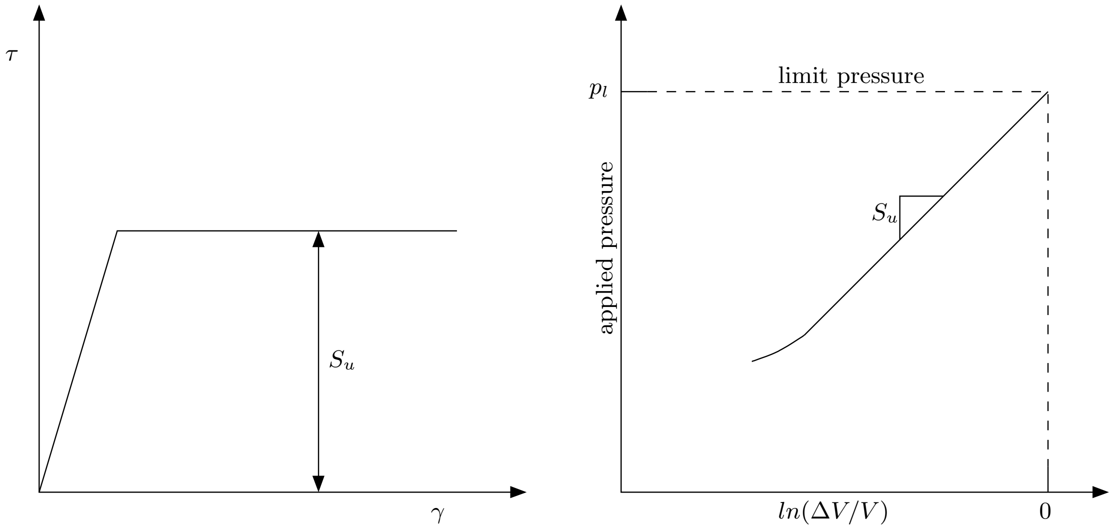

Figure 2.4: Shear Strength for Elastic-Perfectly Plastic Model

response [17]. Eventually a point is reached where the pressuremeter response is entirely dominated by the plastic soil behavior and thus a limiting pressure is achieved. Mẽnard recognized that this occurred when the volumetric strain, $\Delta V/V = 1$, that is the strain at which the change in volume is equivalent to the initial volume or in other words, the volume of the pressuremeter has doubled in size. He deemed the pressure at which this phenomena occurs the 'limit pressure' of the material and developed the following equation to describe it:

$$p_l - p_o = S_u \left[1 + ln\left(\frac{G}{S_u}\right)\right] \tag{2.36}$$

where p_l is the limit pressure and the other parameters are as previously defined. For the Cambridge system, which measures cavity strain, the limiting pressure occurs when the cavity strain has reached 41%. Equation (2.36) led to the development of the following equation describing the pressuremeter response after the initiation of plasticity:

$$p = p_l + S_u ln\left(\frac{\Delta V}{V}\right) \tag{2.37}$$

Using Equation (2.37) the undrained shear strength S_u can be determined by plotting the applied pressure versus the natural log of volumetric strain as displayed in Figure 2.4.

With the equations developed in this section and section 2.1, it is possible to model the entire behavior of an elastic-perfectly plastic, undrained material under an applied radial load. However, the data collected during a pressuremeter test also captures the stress-strain relations as the material is unloaded and the stresses are reversed. The advantage to modeling the unloading portion of the curve is that the effects of disturbance from drilling and probe installation have been overcome and thus the unloading curve could be more representative of the material. The reverse argument is that the deformation caused by the pressuremeter has remolded the surrounding material and hence the material properties have been changed. Jefferies (1988) developed a model for the case of a undrained, elastic-perfectly plastic material during the unloading phase of the pressuremeter test.

As in loading, the material surrounding the expanded pressuremeter cavity initially behaves elastically and is governed by the equation:

$$p - p_{max} = 2G\left[\frac{a - a_{max}}{a_{max}}\right] \tag{2.38}$$

where p_{max} is the maximum pressure reached during the test and a_{max} is the maximum displacement reached. The yield criterion used for unloading is:

$$p - p_{max} = (1 + \beta)S_u \tag{2.39}$$

where $\beta = S_{u(unloading)}/S_{u(loading)}$. Using this criterion for failure yields the following equation for plastic material behavior in extension:

$$p - p_{max} = -S_u \left[\begin{array}{c} (1+\beta) - ln\left\{\left[1 - \left(\frac{a}{a_{max}}\right)^2\right]\left[\frac{G}{(1+\beta)S_u}\right]\right\} \\ -\beta ln\left\{\left[\left(\frac{a}{a_{max}}\right)^2 - 1\right]\left[\frac{G}{(1+\beta)S_u}\right]\right\} \end{array}\right] \tag{2.40}$$

If it is assumed that the shear strength derived from loading is equal to that determined during the unloading phase, i.e. when $\beta = 1$, then the Equation (2.40) reduces to:

$$p - p_{max} = -2S_u\left\{1 + ln\left[\frac{G}{S_u}\left(\frac{a_{max}}{a} - \frac{a}{a_{max}}\right)\right]\right\} \tag{2.41}$$

Other models for cohesive materials have been developed that consider non-linearity resulting from either strain-hardening or strain-softening effects. These models often use a hyperbolic function that is related to different desired parameters or constants determined through lab testing. However, they will not be included in this discussion.

2.3 Plasticity Models - Drained Analysis [7][10][11][12][16][17][22]

The models discussed in the previous section can be used to determine shear strength and stress-strain behavior for a undrained cohesive material. As mentioned previously, elastic behavior is similar regardless of material type due to the coincidence of an increase in radial stress with a decrease in circumferential stress (points 1 through 3 in Figure 2.5). However, to properly analyze sand and rock a drained analysis which considers volume change must be applied. As the material is considered to be completely drained an effective stress analysis is adopted. Most of the developed models use a Mohr-Coulomb yield criterion and express volume change in terms of a dilation angle, ψ. The general Mohr-Coulomb yield criterion expressed in terms related to the cavity expansion of the pressuremeter is:

$$p_f = c' cos\phi' + p_o(sin\phi' + 1) \tag{2.42}$$

where p_f is the applied pressure at the onset of yield (point 3 in Figure 2.5), p_o is the *in situ* pressure (or initial horizontal stress σ_{ho}), c' is the effective cohesion and ϕ' is the internal angle of friction. For a material with no cohesion, such as sand, Equation (2.42) reduces to:

$$p_f = p_o(sin\phi' + 1) \tag{2.43}$$

2.3.1 Solutions for Sand

Two models that are frequently used to determine engineering parameters and stress-strain behavior in sand are those developed by Hughes (1977) and Manassero (1989). Both models use a Mohr-Coulomb yield criterion and adopt a plastic flow rule based on Rowe's stress dilatancy theory. Elastic strain developed after yield are neglected as they are considered negligible in comparison to the plastic strain. Rowe's dilatancy theory relates the principal stress ratio to changes in volume through the following equation:

$$\frac{1 + sin\phi'}{1 - sin\phi'} = \left(\frac{1 + sin\psi}{1 - sin\psi}\right)\left(\frac{1 + sin\phi'_{cv}}{1 - sin\phi'_{cv}}\right) \tag{2.44}$$

where ϕ' is the effective internal angle of friction, ψ is the angle of dilation and ϕ'_{cv} is the angle of shearing resistance at constant volume, also known as the critical friction angle.

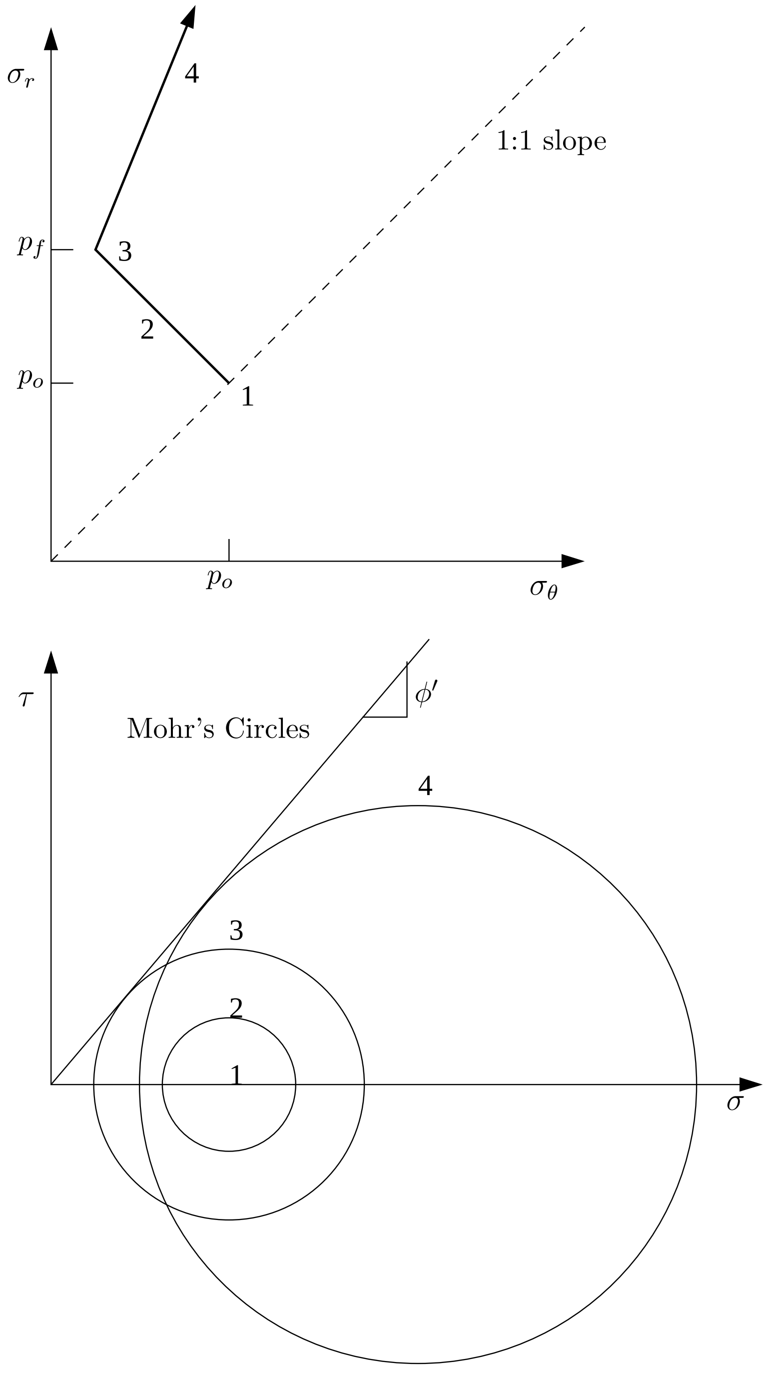

Figure 2.5: Stress Path and Mohr's Circle for Drained Analysis

Volume changes that occur during loading will be dependent upon the initial state of the sand tested. The state of the sand can be described by the void ratio and the effective stresses present prior to loading. If the sand is in a loose state, with a high void ratio, it will contract upon loading, whereas a dense sand, with a low void ratio, will tend to expand, or dilate. The rate of dilation, expressed in terms of the dilation angle, will vary with the changes in volume and shear strain and can be expressed as follows:

$$sin\psi = -\frac{d\epsilon_v}{d\gamma} \tag{2.45}$$

where ϵ_v is the volumetric strain and γ is the shear strain. The effective stress ratio, K, will vary as the applied load and resulting shear strains increase until the sand has been mobilized to a critical state. Once a critical state is achieved changes in volume will cease and the mobilized friction angle and effective stress ratio will become constant. The effective stress ratio can be defined as:

$$K = \frac{\sigma_1'}{\sigma_3'} = \frac{\sigma_r'}{\sigma_\theta'} = \frac{1 + sin\phi'}{1 - sin\phi'} \tag{2.46}$$

For a the critical state condition, the stress ratio, K_{pcv}, can be expressed in a similar way by replacing ϕ' with the critical friction angle, ϕ_{cv}', in Equation (2.46). Using the relationships developed in Equations (2.45) and (2.46), Rowe's dilatancy theory can be expressed as:

$$K = K_{pcv}\left(\frac{1 - \frac{d\epsilon_v}{d\gamma}}{1 + \frac{d\epsilon_v}{d\gamma}}\right) \tag{2.47}$$

The above equation cannot be solved in a closed form solution unless assumptions are made. Hughes (1977) developed a solution by assuming a constant stress ratio, K, and a constant dilation angle, i.e. an elastic-perfectly plastic model. This assumption results in a linear relationship between the volumetric strain and shear strain. The relationship can be written as:

$$\epsilon_v = c - \gamma sin\psi \tag{2.48}$$

where c is a constant defined as illustrated in the Figure 2.6. Equation (2.48) can be rewritten in terms of radial and circumferential strain as follows:

$$-sin\psi = \frac{\epsilon_\theta + \epsilon_r}{\epsilon_r - \epsilon_\theta} \tag{2.49}$$

Using the above relationship along with Rowe's stress dilatancy theory, Hughes developed the following relationship between cavity strain and applied pressure during a pressuremeter test.

$$\epsilon_c + \frac{c}{2} = \left(\epsilon_R + \frac{c}{2}\right)\left[\frac{p}{p_f}\right]^{[(n+1)/(1-N)]} \tag{2.50}$$

where ϵ_R is the strain at the onset of yield, when the pressure p_f is reached, and

$$N = \tfrac{1-sin\phi'}{1+sin\phi'}$$
$$n = \tfrac{1-sin\psi}{1+sin\psi}$$

The constant c is considered to be negligible and is generally ignored. While this is certainly true of dense sands, it may be not, however, be correct for sands in looser states. By plotting Equation (2.50) on a log-log plot (using natural logs), a straight line function is obtained (refer to Figure 2.6). Hughes used the gradient of this line, $s = [(1-N)/(n+1)]$, along with Rowe's relationship to calculate values for ϕ' and ψ. The resulting equations are as follows:

$$sin\phi' = \frac{s}{1+(s-1)sin\phi'_{cv}} \tag{2.51}$$
$$sin\psi = s + (s-1)sin\phi'_{cv} \tag{2.52}$$

Manassero (1989) approached the problem of modeling the drained behavior of an expanding cavity using a finite difference technique. Using the relation for Rowe's dilatancy theory derived earlier in Equation (2.47), Manassero developed the following governing equation in terms of radial and circumferential stresses and strains valid at any strain:

$$\frac{d\sigma_r}{d\epsilon_\theta} = -\sigma'_r\left(\frac{1+K_{acv}(d\epsilon_r/d\epsilon_\theta)}{\epsilon_r - \epsilon_\theta}\right) \tag{2.53}$$

where $K_{acv} = 1/K_{pcv}$. At the cavity wall, $\sigma_r = p$ and $\epsilon_\theta = \epsilon_c$, and can be determined directly from the data collected. Thus the above equation must be solved in terms of radial strain, ϵ_r. Using a finite difference technique, the slope at any point i on the curve obtained during a pressuremeter test is:

$$\frac{dp}{d\epsilon_c} = \frac{p_{(i)} - p_{(i-1)}}{\epsilon_{c(i)} - \epsilon_{c(i-1)}} \tag{2.54}$$

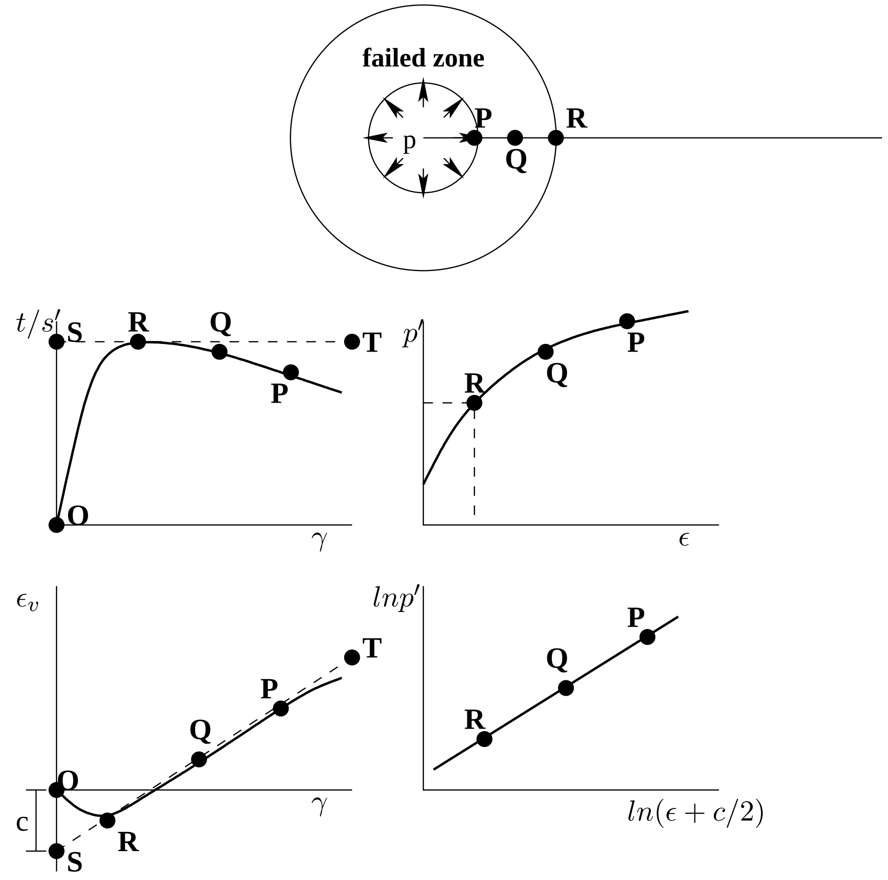

Figure 2.6: Stress-Strain Relations for an Expanding Cavity in Sand (after Hughes et al., 1977)

A similar relationship can be used to describe the change in radial strain with cavity strain:

$$\frac{d\epsilon_r}{d\epsilon_c} = \frac{\epsilon_{r(i)} - \epsilon_{r(i-1)}}{\epsilon_{c(i)} - \epsilon_{c(i-1)}} \tag{2.55}$$

Plugging Equations (2.54) and (2.55) into (2.53) and solving in terms of radial strain yields:

$$\begin{gathered}\epsilon_r = \frac{p_{(i)}\left[\epsilon_{c(i-1)}+K_{acv}\epsilon_{r(i-1)}\right]}{2\left[p_{(i)}(1+K_{acv})-p_{(i-1)}\right]} - \frac{p_{(i-1)}\epsilon_{c(i)}}{2\left[p_{(i)}(1+K_{acv})-p_{(i-1)}\right]} \\ +\frac{p_{(i)}\left[\epsilon_{c(i-1)}-\epsilon_{r(i-1)}\right]}{2K_{acv}p_{(i-1)}} + \frac{p_{(i-1)}\left[\epsilon_{r(i-1)}(1+K_{acv})-\epsilon_{c(i)}\right]}{2K_{acv}p_{(i-1)}}\end{gathered} \tag{2.56}$$

The rest of stress strain curve can then be constructed by determining shear and volumetric strains from Equation (2.53) and the finite difference technique.

2.3.2 Solutions for Rock

The stress path displayed on the left in Figure 2.7 (on the next page) is typical of an expanding cavity in a continuous, homogeneous medium. While the material is behaving elastically, the change in the radial stress is equal and opposite to the circumferential stress until the onset of yield. Once the yield pressure is reached, the radial and circumferential stress increase simultaneously and the material deforms plastically. This is the assumed behavior when modeling soil. When modeling weak rock, however, it is likely that the circumferential stress exceeds the tensile strength, σ_t, of the rock prior to reaching the yield stress, σ_y, resulting in brittle tensile failure leading to fractures and crack propagation (refer to the image on the right in Figure 2.7). Thus the material will no longer behave as a continuum and inclusion of the effects of crack propagation and the tensile strength of the rock will need to be considered.

In performing a pressuremeter test, the applied pressure must equal the horizontal *in situ* stress, defined as p_o in Figure 2.7, before any soil or rock deformation occurs. Once the applied pressure is increased to a value twice that of the initial horizontal stress, the circumferential stress will equal zero provided that the yield pressure p_f is greater than $2p_o$. A further increase in pressure will result in a increase in tensile stress (as the circumferential stress becomes negative) until either the yield pressure or tensile strength of the material is reached. Hence, if the yield stress is reached first, the apparent yield can be defined as:

$$p_f = 2p_o + |\sigma_y| \tag{2.57}$$

and the pressure at which the onset of tensile fracture and crack initiation will occur is:

$$p_c = 2p_o + |\sigma_t| \tag{2.58}$$

From these equations, it is apparent that the potential for fracture and development of cracks in the rock formation is dependent upon the horizontal *in situ* stress and the yield criterion of the material tested. Thus, at greater depths, when a larger horizontal stress is present, crack initiation will be suppressed and the rock will most likely yield as a continuum that can be modeled in a way similar to that of soil, provided a proper yield criterion and flow rule are selected.

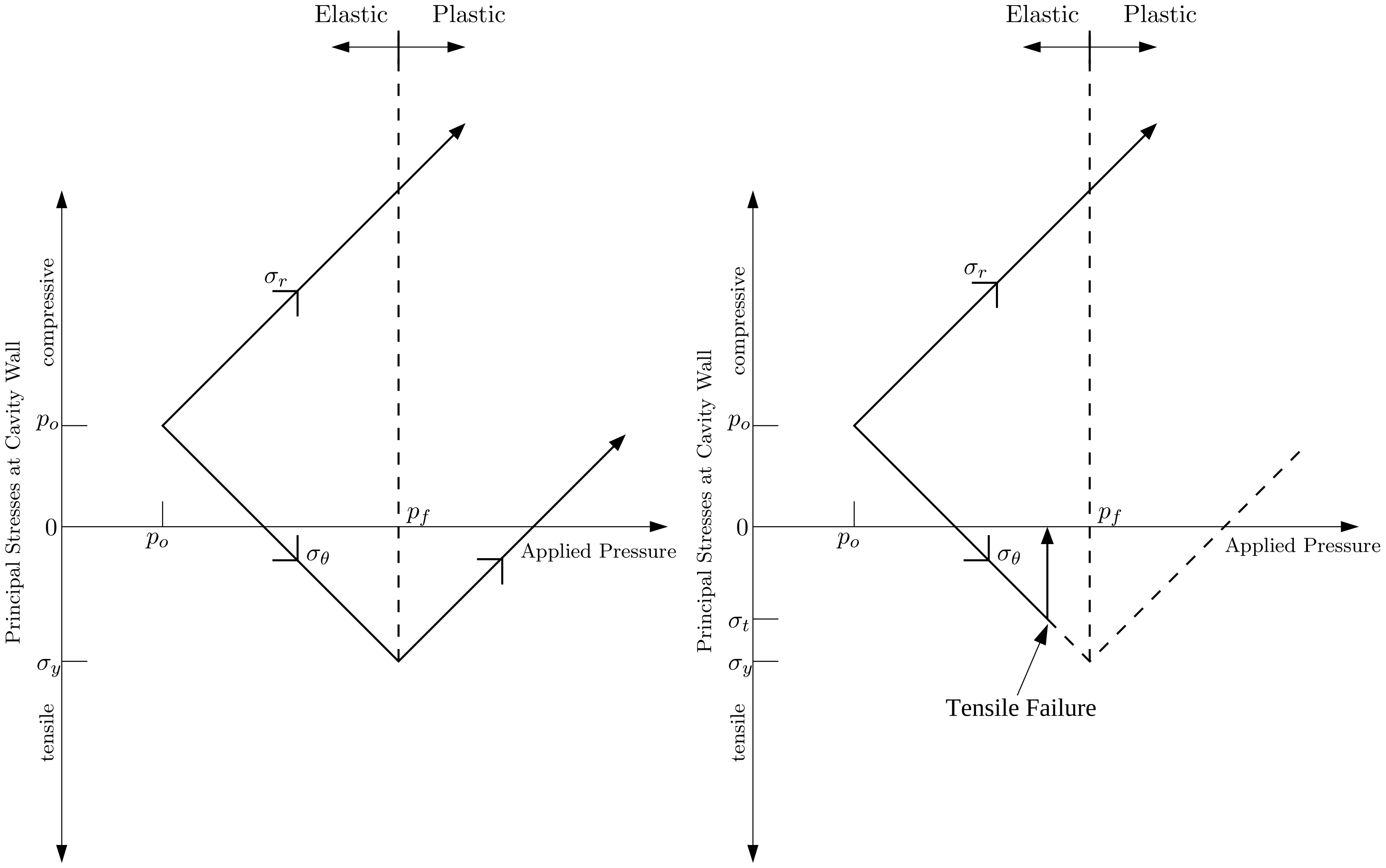

Figure 2.7: Stress Paths for Cavity Expansion in Soil (left) and Rock (right), after Haberfield (1987)

The problem of modeling the reaction of weak rock to an expanding cavity for pressuremeter analysis has been attempted previously by a handful of researchers, most notably, Rocha *et al.* (1966), Ladayni (1976) and Haberfield (1987,1990,1997). The models developed by Rocha and Ladayni are analytical solutions and thus require simplifying assumptions that may not represent the true nature of weak rock. Haberfield produced a more extensive model that utilizes numerical techniques via the finite element method. Using his finite element model, he also developed an alternative empirically based analytical solution for mudstone in Australia. The remainder of this section will be a presentation and discussion of these models.

Model after Rocha (1966)

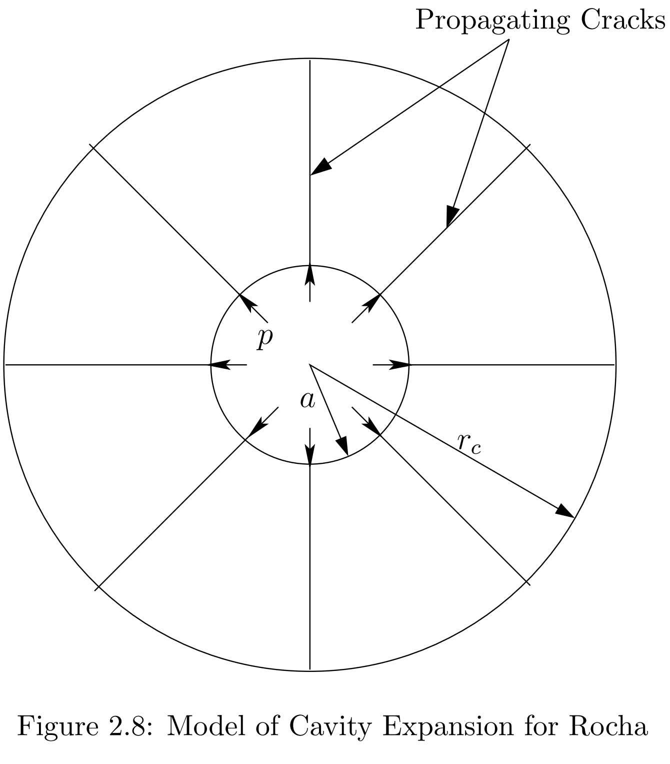

Figure 2.8: Model of Cavity Expansion for Rocha

The model developed by Rocha *et al.* assumed that once the tensile strength of the rock was exceeded, radial cracks would form around the cavity creating a series of wedges as shown in Figure 2.8. He recognized that propagating cracks will not extend infinitely, and thus some method for determining the finite crack length must be imposed. Rocha used the following relationship to determine radial crack growth:

$$r_c = a\sqrt{\frac{p}{|\sigma_t|}} \tag{2.59}$$

where r_c is the radius of crack propagation, a is the initial cavity radius, p is the applied pressure and σ_t is the tensile strength of the rock (refer to Figure 2.8). Using this criteria for crack growth, Rocha used two equations to describe the behavior of the surrounding rock. The first equation describes the elastic deformation of the cavity wall prior to tensile failure. For this initial phase, Rocha adopted the original cavity expansion equation developed by Lamẽ for an elastic medium, written as follows:

$$u = a\frac{p}{E}(1+\nu) \tag{2.60}$$

where u is the cavity displacement, E is Young's modulus, ν is Poisson's ratio and the other parameters are defined as above. The second equation Rocha developed by integrating the radial strains and using the relation in Equation (2.59). This equation applies to a material with natural discontinuities, as found in weak rock, and is independent of the number of cracks present. The wedges of material between the developing cracks is assumed to still behave elastically during this phase. The equation for displacement after crack propagation is:

$$u = a\frac{p}{E}\left(1+\nu+ln\left[\frac{r_c}{a}\right]\right) \tag{2.61}$$

Model after Ladayni (1976)

Ladanyi (1976) developed a model that divided the behavior of rock into five phases. Aside from the usual assumptions of homogeneity, isotropy and axisymmetry, Ladanyi also incorporated the following conditions:

- Behavior is linear elastic prior to failure.
- The rocks yields according to a Mohr Coulomb failure criterion incorporating either a linear progression with a tensile cut-off or yields according to a parabolic function that follows a Fairhurst criterion.

- Dilation is governed by the associative flow rule of the theory of plasticity.
- The rock fails in tension resulting in the propagation of cracks at lower *in situ* stresses and fails in compression at greater *in situ* stresses.

As two different potential failure criterion are considered in Ladanyi's model, there are two ways in which to determine the potential for the occurrence of radial cracks. Based on the criteria chosen, the following inequalities must be satisfied for cracks to develop. For the Fairhurst criterion, cracks will develop if:

$$\frac{p_o}{|\sigma_t|} < 0.5\left[l(l-2)-1\right] \tag{2.62}$$

For the Mohr-Coulomb criterion, cracks will develop if:

$$\frac{p_o}{|\sigma_t|} < \frac{k-2}{4} \tag{2.63}$$

where

$$l = \sqrt{(k+1)}$$

and

$$k = \sigma_c/|\sigma_t|$$

where p_o and σ_t defined as previously, and σ_c is the compressive strength of the rock. Ladanyi argues that if either of the criteria in Equations (2.62) or (2.63) for the initiation of crack propagation is satisfied, then the solution for the rock deformation doesn't depend on the shape of the failure envelope for the rock, but rather the elastic properties, uniaxial tensile strength and uniaxial compressive strength of the intact rock. If the occurrence of cracks is possible, the pressure at which crack initiation will occur is governed by Equation (2.58) developed earlier in this section (i.e. once the apparent tensile strength is reached). The length of the cracks developed once the apparent tensile strength is exceeded is governed by:

$$\frac{r_c}{a} = \frac{p}{2p_o + |\sigma_t|} \tag{2.64}$$

where r_c is the radial crack length, a is the cavity radius and p is the applied pressure.

As the applied pressure is increased, it will eventually become equivalent to the compressive strength of the rock. A further increase in pressure results in the compressive failure of the rock between the propagating cracks and subsequently a crushed zone is produced adjacent to the expanding cavity. Ladanyi argued that crack growth would cease at this stage and thus the final length of the developing cracks could be determined by:

$$\frac{r_f}{a} = \left[\frac{p + S_c}{\sigma_c + S_c}\right]^{\frac{1}{(1-1/m)}} \tag{2.65}$$

where r_f is the final crack length,

$$S_c = c cot\phi$$

and

$$m = \frac{1+sin\phi}{1-sin\phi}$$

with c being the cohesion and ϕ the angle of internal friction.

As mentioned previously, Ladanyi developed his model by dividing the behavior of the rock into phases. By combining information from all phases, a full load-deformation response of the rock is obtained. Assuming that one of the previous yield criterions above is met for the case of tensile failure (i.e. with crack propagation), the governing equations for each phase of Ladanyi's model are as follows:

Phases I and II - $0 < p < p_o$ and $p_o < p < 2p_o + |\sigma_t|$ (Sections $0 - 2$ in Figure 2.9). Linear elastic response of the rock prior to crack initiation. The first phase involves the reestablishment of the original state of the rock as the applied pressure reaches p_o. The radial displacement during these phases is given by:

$$\frac{u}{a} = \frac{p - p_o}{2G} \tag{2.66}$$

Phase III - $2p_o + |\sigma_t| < p < p_f$ (Sections $2 - 3$ in Figure 2.9). Once the apparent tensile strength is exceeded, cracks will propagate radially and increase in length as the pressure is increased. Radial displacement includes the initial displacement given by Equation (2.66) and is given by:

$$\frac{u}{a} = \frac{p}{2G}\left[(1-\nu)ln\left(\frac{p}{2p_o + |\sigma_t|}\right) + \frac{p_o + |\sigma_t|}{2p_o + |\sigma_t|} + \frac{p_o}{p}\right] \tag{2.67}$$

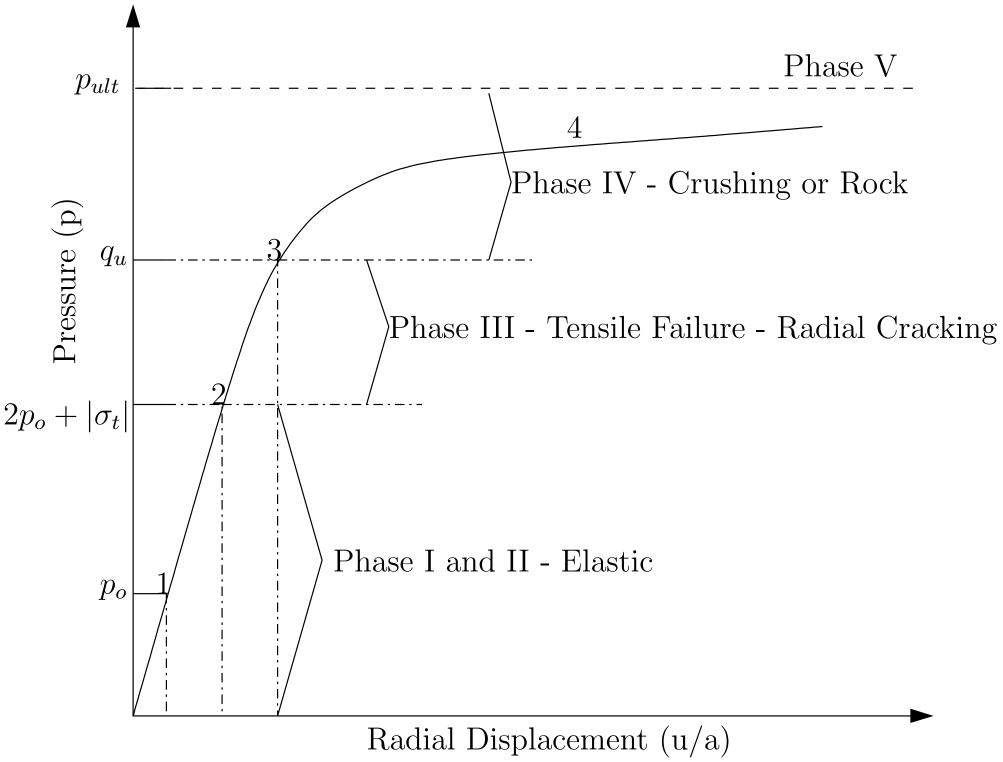

Figure 2.9: Pressure-expansion curve for low $p_o/|\sigma_t|$ ratios showing the relative phases

Phase IV - $\sigma_c < p < p_{ult}$ (Sections $3-4$ in Figure 2.9). In this phase, the compressive strength, σ_t has been exceeded and the material between the propagating cracks begins to crush. The crushed zone will enlarge as the pressure is increased until the ultimate pressure – at which complete failure occurs – is reached. The radial displacement is given by:

$$\frac{u}{a} = \sqrt{\frac{1-\epsilon_{av}}{1-\left(\frac{2u_f}{r_f}+\epsilon_{av}\right)\left(\frac{r_f}{a}\right)}} - 1 + \frac{p_o}{2G} \tag{2.68}$$

where ϵ_{av} is the average volumetric strain as the rock crushes, and u_f is the displacement when $r = r_f$, which can be determined by substituting $p = \sigma_c$ into Equation (2.67).

Phase V - $p = p_{ult}$ (refer to Figure 2.9). The ultimate pressure is associated with the complete failure of the rock. As this pressure, the radial displacement will extend infinitely.

The ultimate pressure is given by:

$$p_{ult} = \frac{\sigma_c + S_c}{\left(\frac{2u_f}{r_f} + \epsilon_{av}\right)^{(m-1)/2m}} - S_c \tag{2.69}$$

Ladanyi also developed equations for the scenario in which radial cracking is suppressed. However, these equations are similar in nature to those developed for sand earlier and thus will not be included here.

Model after Haberfield (1987,1990,1997)

The cavity expansion model for weak rock analysis developed by Haberfield uses a Mohr-Coulomb failure criterion incorporating a $c' - \phi'$ material with a finite element technique to allow for initiation and propagation of radial cracks. As in previous models, different equations govern material behavior during the multiple phases of loading and deformation (i.e. in the Ladanyi model). The different phases as described by Haberfield are illustrated in Figure 2.11 (page 40). During the elastic phase (prior to yield), the governing equation for the material response is the same as previously stated, repeated here for convenience:

$$\epsilon_c = \frac{u}{a} = \frac{p - p_o}{2G} \tag{2.70}$$

where ϵ_c is the cavity strain, u is the cavity displacement, a is the initial cavity radius, p is the applied pressure, p_o is the *in situ* horizontal stress, and G is the shear modulus. It should be noted that as this is a drained analysis, all the material properties are in terms of effective stress.

As the cavity pressure is increased the material will undergo a phase change resulting from either tensile failure and the initiation of radial cracks or as a consequence of satisfying the yield criterion. The potential for crack failure will depend upon the *in situ* stress and tensile strength of the rock tested. If the pressure at which crack initiation occurs, p_c, is less than the material yield pressure, p_f, radial cracks will develop and extend into the surrounding material, where p_c is defined in Equation (2.58) and p_f is defined in Equation (2.42). That is, if:

$$2p_o + |\sigma_t| < c'cos\phi' + p_o(1 - sin\phi') \tag{2.71}$$

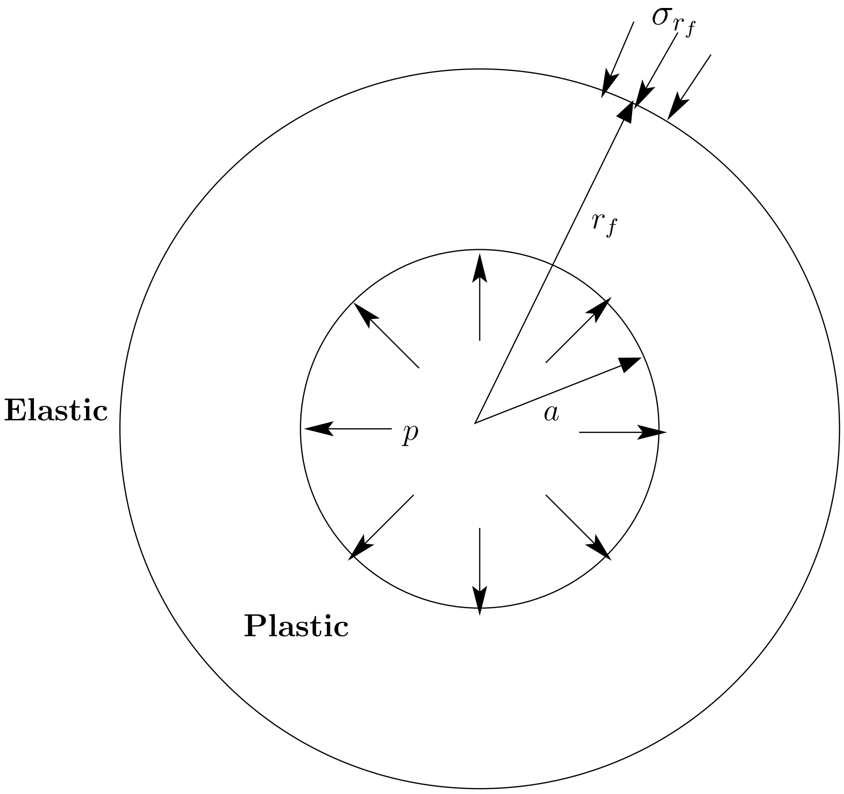

Figure 2.10: Yield zone around and Expanding Cavity

For the case in which the development of radial cracks is suppressed ($p_f < p_c$) the material will yield according to a Mohr-Coulomb failure envelope using a non-associative flow rule to describe the volume change of the material. The adopted flow rule from Davis (1968) is expressed in terms of the dilation angle, ψ as follows:

$$\frac{d\epsilon_r^p}{d\epsilon_\theta^p} = -\frac{1 - sin\psi}{1 + sin\psi} = -\frac{1}{n} \tag{2.72}$$

where $d\epsilon_r^p$ and $d\epsilon_\theta^p$ are the incremental radial and circumferential plastic strains respectively. Manipulating the equations for equilibrium, kinematic relations, and constitutive relations to ensure compatibility, and using the above flow rule allowed the following solution for displacement to be determined:

$$\epsilon_c = \frac{u}{a} = \frac{1}{2G}\left[b_1\left(\frac{r_f}{a}\right)^{\frac{(m-1)}{m}} + b_2\left(\frac{r_f}{a}\right)^{\frac{(n+1)}{n}} + b_3\right] \tag{2.73}$$

where

$$b_1 = \frac{2m}{m-1}\left[(1-\nu)\left(\frac{1+mn}{m+n}\right)-\nu\right](p_f-p_o)$$
$$b_2 = 2n(1-\nu)\left(\frac{m+1}{m+n}\right)(p_f-p_o)$$
$$b_3 = (1-2\nu)\left(\frac{m+1}{m-1}\right)(p_f-p_o)$$
$$\frac{r_f}{a} = \left[\frac{p(m-1)+\hat{\sigma}}{p_f(m-1)+\hat{\sigma}}\right]^{\frac{m}{m-1}}$$
$$\hat{\sigma} = \frac{2c'cos\phi'}{1-sin\phi'}$$
$$m = \frac{1+sin\phi'}{1-sin\phi'}$$
$$n = \frac{1+sin\psi}{1-sin\psi}$$

where c' is effective material cohesion, ϕ' is the effective angle of internal friction and r_f is the radius to the edge of the yield zone (refer to Figure 2.10).

The solution to Equation (2.73) requires knowledge of six parameters. However, to uniquely define a pressuremeter curve only requires three parameters and thus three of the above parameters must be determined by other methods or by relations between the parameters. The shear modulus, G, can be determined by the unload-reload loops performed during the test. Poisson's ratio, ν usually has a known range for a given rock and often lies between 0.15 and 0.35 [11]. Lastly, Rowe's stress dilatancy theory can be applied which allows a relation between the internal angle of friction, ϕ, critical friction angle, ϕ_{cv}, and the dilation angle ψ to be adopted. This still requires knowledge of the critical friction angle, ϕ_{cv}, or for rock, the residual friction angle ϕ_r, which can be considered equivalent to the critical friction angle. Again, for different rock materials, the residual friction angle is often known and more easily determined by laboratory testing. The relationship developed by Haberfield between the residual friction angle, peak friction angle and dilation angle was determined by rearranging that developed by Hughes *et al.* and is given by:

$$sin\psi = \frac{sin\phi - sin\phi_r}{1-(sin\phi)(sin\phi_r)} \tag{2.74}$$

For the case of tensile failure and subsequent radial cracking, Haberfield developed a semi-empirical analytical solution based on his finite element solution to an expanding cavity in weak rock. The analytical solution was obtained by determining an empirical

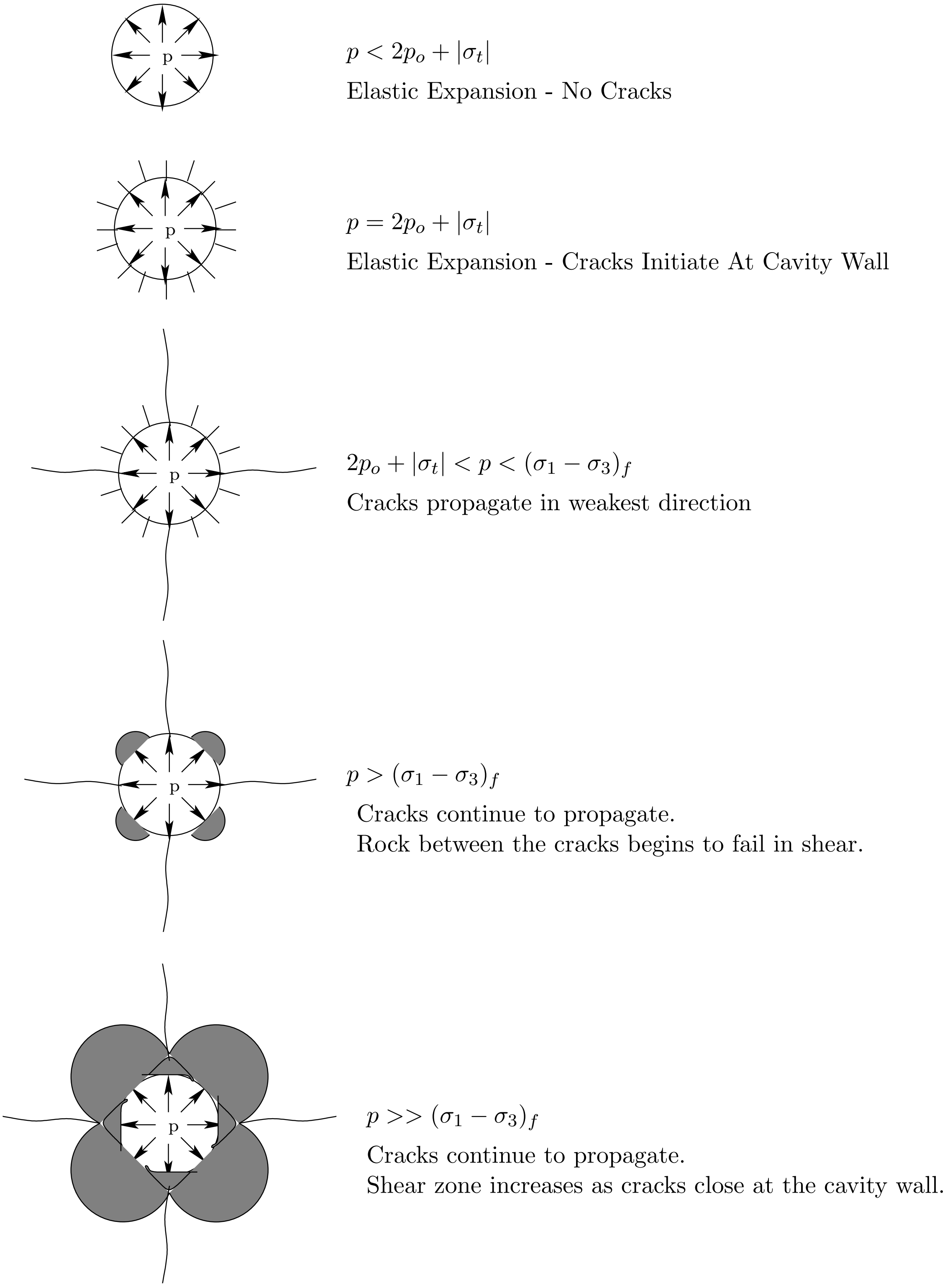

Figure 2.11: Failure process around expanding cavity in soft rock, after Haberfield (1990)

relation for the length of crack growth based on pressuremeter tests performed in siltstone and mudstone. The relation is as follows:

$$\frac{r_c}{a} = 3\left(\frac{p}{p_c} - 1\right) * 10^{-1.88 p_o/p_c} + 1 \tag{2.75}$$

where r_c is the radial length of crack growth and all other parameters are defined as previously stated. Because radial cracking provides relief of the circumferential stress around the pressuremeter, the material between the cracks will only be loaded in compression. Hence, the rock will continue to behave elastically until the compressive strength of the rock, σ_c is reached. The displacement prior to reaching the compressive strength of the rock can be defined as:

$$\epsilon_c = \frac{1}{2G}\left[p(1-\nu)ln\left(\frac{r_c}{a}\right) + p - p_o\frac{r_c}{a}\right] \tag{2.76}$$

This equation is valid as long as the applied pressure is less than the compressive strength of the rock. However, once the compressive strength of the rock is exceeded, the rock will yield and shear zones will develop in the material between the radial cracks. Once the applied pressure has greatly exceeded σ_c cracks at the cavity wall will begin to close creating a shear zone around the entire expanding cavity (refer to Figure 2.11). The cracks, however, will continue to propagate out into the surrounding material. Upon development of this shear zone around the pressuremeter cavity, the displacement is once again governed by Equation (2.73). It should be noted that the semi-empirical equation (Equation (2.75)) was developed for tests in siltstone and mudstone and thus may not apply to other rock types.

The finite element model developed by Haberfield was designed to account for crack propagation taking into account the high stresses (theoretically infinite) that develop at the tip of a propagating crack. Through a series of lab tests, Haberfield determined that generally either two, three or four major cracks developed during tensile failure and the number of cracks was related to the *in situ* pressure applied. Lower *in situ* pressures generally resulted in two diametrically opposite cracks forming, while higher pressures yielded four equally spaced cracks propagating away from the pressuremeter cavity. Generally, using an analysis which included the propagation of four major cracks produced the best results when using the finite element program to determine pressuremeter parameters [10]. As a result of these findings, the finite element program was set up to model crack propagation at predetermined locations. The areas where cracks are allowed to develop have fixed boundaries prior to loading. As the criteria is met to allow for the initiation and propagation of cracks (i.e. when the stress intensity resulting from tensile loading exceeds the fracture toughness of the material at that point), the boundary conditions are released allowing the crack to extend to the next fixed location or node, where the criteria is again checked. Once a location is reached in which the stress intensity is less than the fracture toughness of the material, the crack propagation will cease. This mechanism allows the high stresses developing at the crack tip to be more accurately modeled than previous analytical solutions, which do not consider this additional stress. As mentioned previously, once the applied pressure greatly exceeds the compressive strength of the material, the cracks will begin to close at the cavity wall and a shear zone will develop around the entire cavity. The finite element model is also capable of modeling this phenomena. For more details on the finite element model developed by Haberfield, refer to [10] and [12].

2.4 Discussion of Models

The previous sections have described a number of cavity expansion models accounting for both drained and undrained pressuremeter data analysis. The intention of the previous sections was to provide the reader with a thorough understanding of the models currently available for pressuremeter analysis while also providing the framework necessary for more in depth discussion and details of model development, which is presented in next chapter. The focus of the remaining chapters in this document will be the analysis of weak rock using pressuremeter data. In this light, the forthcoming conversation will be aimed at advantages and disadvantages of the previously discussed models for this purpose. It should be noted that the behavior of the material subjected to pressuremeter loading during the elastic phase is widely agreed upon when assuming linear behavior during this phase. For this reason, this discussion and remainder of this document will focus on constitutive models associated with plastic (or inelastic) behavior.

Inspection of the equation for equilibrium (Equation (2.1)) of which all these models are based, reveals that only the radial (σ_r) and circumferential (σ_θ) stress are considered. The inherent assumption then is that the vertical stress (σ_z) does not influence material behavior during shearing [17]. Therefore, is it assumed at failure that the effective radial stress and effective circumferential stress are the major and minor stress respectively, and that the vertical stress adjusts to prevent strain in vertical direction while remaining the intermediate stress. However, this assumption may not be true in all cases, particularly for formations with a relatively high or low *in situ* lateral stress (σ'_{ho}) in comparison to the *in situ* vertical stress (σ'_{vo}). This principal is illustrated by Figure 2.12 for a Mohr-Coulomb failure criterion for three different hypothetical values of K_o, where K_o is the coefficient of earth pressure at rest and is equal to $\sigma'_{ho}/\sigma'_{vo}$. If this assumption is not true (i.e. σ_z does remain a principal stress at failure), these pressuremeter strength models are invalidated. Fortunately, the range of K_o values for which this assumption is valid increases as the material strength increases. For a friction angle of 40^o, the assumption is valid for K_o values ranging from 0.6 : 2.8 [17]. As the conditions for most weak rock would fall within these bounds, pressuremeter models formulated in under this assumption should remain valid.

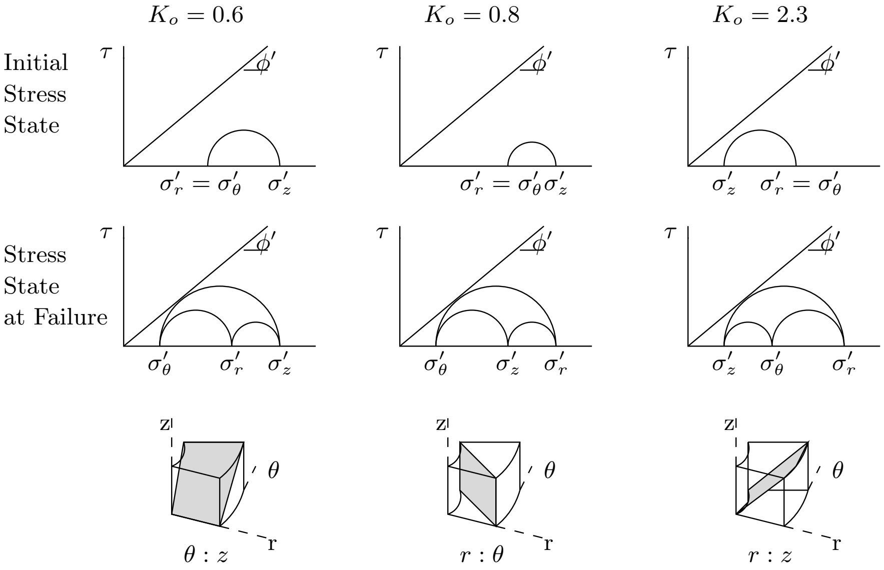

Figure 2.12: Mohr-Coulomb Failure with Different Failure Planes (from Wood and Wroth, 1977) [17]

Considering the models discussed, the models developed by Mẽnard (1957), Gibson and Anderson (1961) and Jefferies (1988) (for unloading) are applicable to cohesive materials with low permeability, and are particularly useful in analyzing pressuremeter tests in clay. However, the assumption that material behavior is undrained is not applicable to fractured material for which drainage will readily occur. Therefore, these models are not appropriate for weak rock analysis. One exception, however, for consideration would be an intact clay shale, under enough overburden pressure to suppress the development of fractures during loading. Thus, these models could be useful for some scenarios, and may at least serve in determining an upper limit for rock shear strength.

Models after Hughes (1977) and Manassero (1989) do consider drained analysis and dilation, which are both important considerations in the analysis of weak rock. However, both models are designed for analysis of a continuum and in no way account for the discontinuous nature of weak rock. These models also assume purely frictional material resistance and thus would not account for the cohesive component, or cementation, of rock. Again, an exception could be made in analyzing an intact weak sandstone with suppressed fracture development for which these models may be applicable.

Rocha (1966), Ladayni (1976) and Haberfield (1987,1990,1997) all designed their models to consider the behavior of weak rock subjected to pressuremeter loading. The most recent of the models is also most likely the best suited for weak rock analysis, however, the models developed by both Rocha and Ladayni also have shortcomings.

The model after Rocha does capture the phenomena described by Haberfield in that cracks develop diametrically opposite each other and new sets of cracks develop as loading is increased and the tensile strength of the rock is exceeded. However, the high stresses that develop at the crack tip are not considered and thus the crack length radius described by Equation (2.59) may be underestimated, making the deformation response inaccurate [10]. Rocha also did not consider the yield or failure of the rock as loading was increased beyond the rock compressive strength.

Ladayni did consider more phases of deformation, including failure of rock due to crushing, but also made inaccurate assumptions. Ladayni assumed that crack propagation would cease once the compressive strength of rock was exceeded (during the crushing phase, Phase

IV - refer to previous section), which is unrealistic because the stress state at the crack tips would remain. Ladayni also applied an associative flow rule to model the plastic material behavior, which is most likely incorrect. While, the overall process described by Ladayni is possible, these inaccuracies greatly affect the deformation behavior making this model undesirable.

The model developed by Haberfield is currently the best method for analyzing pressuremeter data in weak rock to the knowledge of this author. However, this model also has potential shortcomings. The model accounts for both cohesion and frictional resistance, while also accounting for dilation as a result of crack formation and propagation using a non-associative flow rule. The finite element model is designed to account for the formation and propagation of fractures and was used in determining a semi-empirical formula. These features are useful and necessary. However, the model is completely based on a minimal data set in a synthetic rock and a few tests in native mudstone. The synthetic rock was used to perform a qualitative assessment of fracture formation, leading to the determination of the cracking pattern for which the finite element software is limited to. The results of this analysis were then used in developing the semi-empirical formula. Unfortunately, the synthetic rock tested was fully intact, which is often not the case for rock tested in the field. Thus the patterns witnessed by Haberfield may be inaccurate, and it may be more correct to assume that preexisting fractures propagate further during loading and that few, if any new fractures form during a pressuremeter test. Generality of the semi-empirical formula is also lost in that the equation was created based on the synthetic rock (which was modeled after local mudstone in Australia) and thus may not be appropriate for other rock types (noted by [11]). Also of question is the use of a Mohr-Coulomb failure criterion. The addition of a tensile cutoff is important and necessary, but the Mohr-Coulomb criterion was designed to model soil behavior and thus may not be accurate for the interpretation of rock data. Lastly, the Mohr-Coulomb failure criterion does not account for the strength of preexisting fractures, which typically dominate the ability of a rock formation to resist load.

For the reasons listed in the previous paragraphs, the author has further developed a cavity expansion model using a Hoek-Brown failure criterion initiated in [23] for use in pressuremeter analysis. The Hoek-Brown failure criterion, the details of which are in the following chapter, was designed to capture inelastic rock behavior for many different types of rock formations and has been continuously updated and improved (empirically) since it was first created in 1980. The Hoek-Brown failure criterion is non-linear, which is more in line with true rock behavior and allows for consideration of preexisting fractures, something the other rock models introduced lack. Furthermore, equivalent Mohr-Coulomb parameters can be determined from the Hoek-Brown model inputs. Therefore, use of the Hoek-Brown failure criterion for analyzing pressuremeter data in weak rock could prove to be superior to current methods, an idea explored in the remainder of the thesis.

Five pressuremeter data sets were interpreted by the author using the Hoek-Brown model in order to test and calibrate the model and results were compared to Haberfield's Mohr-Coulomb model with a tensile cutoff. The details of these two models and their development as well as a parametric analysis will be presented and discussed in the following chapter. The author will also introduce a third constitutive model, which could be developed into a cavity expansion framework in the future. Further considerations in rock behavior and response to pressuremeter loading are also discussed.

Chapter 3

ROCK MODELS FOR PRESSUREMETER ANALYSIS

A rock mass generally consists of intact rock separated by fractures or joint sets of which the behavior of the fractures often controls the deformation response of the rock mass to an applied load. Therefore, when modeling rock behavior the effect of the fractures must be considered. A number of techniques are used to map fracture networks in rock using outcroppings, borehole core and penetrating radar. In modeling rock behavior this information can be used to directly account for the presence of fractures using statistical variations of the observed fracture patterns and treating the rock mass as a discontinuous medium. However, due to the inherent difficulties in properly defining fracture networks, and often limited data available, rock is also commonly modeled as an equivalent continuous medium. The equivalent continuous medium considers the weakening of the rock mass due to fractures by using reduced stiffness and strength values from those of the intact rock. An example of rock blocks modeled by the two methods mentioned here is illustrated in Figure 3.1.

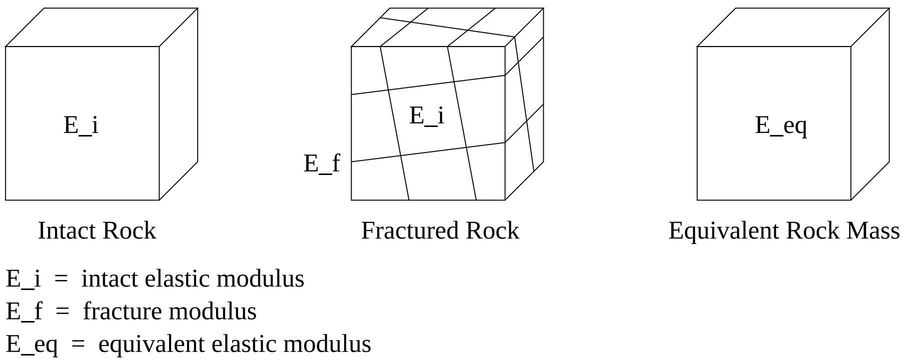

Figure 3.1: Examples of Interpreting Rock Blocks

Using either analysis method (discontinuous or continuous media) a proper constitutive model describing rock behavior is typically required in order to perform analysis for design. The constitutive model selected can be used to capture material behavior for the analysis of rock slopes, tunnels, mine pits, shafts, and rock bolts among other projects. Selection of the proper constitutive model requires knowledge of parameters that can be measured and accurately define the rock response to loading. Common parameters used to define rock include some form of stiffness modulus, such as the elastic (Young's) modulus, shear modulus, bulk modulus and strength parameters, such as the uniaxial compressive strength and shear strength. These values can be determined either through laboratory testing, field *in situ* testing or based on previous knowledge of the rock type. One *in situ* test capable of determining both stiffness and strength parameters in rock is the pressuremeter; hence it is imperative that new models are explored and developed to analyze pressuremeter data.

Pressuremeter data consists of a stress-strain curve where radial stress versus the circumferential or cavity strain (change in radius/initial radius) are directly measured and plotted. The test can be described as an axisymmetric, cylindrical cavity expanding under an applied radial load, under plain strain conditions. The expansion of the cavity is resisted by the surrounding material and thus the recorded data will reflect the material properties of the surrounding rock mass. Before the yield pressure of rock mass is reached, the rock will respond to the applied load in an elastic manner. The behavior of the rock mass beyond yield is then idealized using the constitutive model selected. The actual behavior of the rock mass will depend on many variables including strength of the intact rock, the number of fractures, fracture frequency, fracture length, fracture orientation, aperture of the fractures and roughness of the fracture faces. If allowance of crack formation and propagation is considered, then the yield pressure can be defined by the apparent tensile strength as defined in Chapter 2, Equation (2.58) where $p_c = 2p_o + |\sigma_t|$. As the pressure is increased beyond yield, the radius defining the crack lengths, r_c, increases resulting in a weaker material response. The rock material between the cracks is considered to behave elastically. By comparison, if the rock material is treated as a continuum or it is assumed that cracks are not present, then the yield pressure is determined by the yield criterion selected and the material properties. As the pressure is increased beyond yield, an annulus of plastically deformed (or equivalently plastically deformed) rock forms around the pressuremeter cavity. The material beyond the plastically deformed annulus continues to behave elastically defining a boundary between elastic and plastic zones deemed the elastic-plastic boundary or yield front. As the pressure is further increased, the radius of the elastic-plastic boundary, r_f, increases (Figure 3.2).

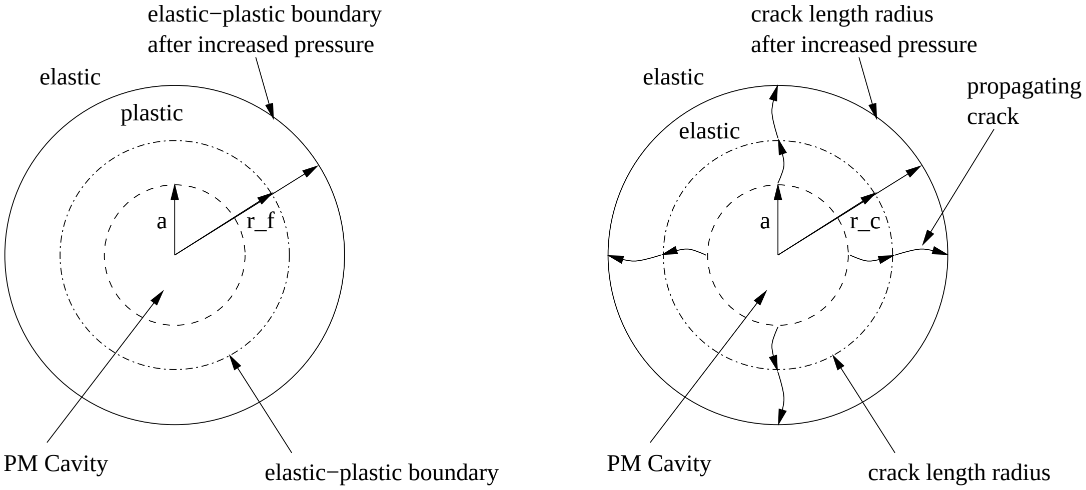

Figure 3.2: Plan View Cross Section of Pressuremeter (PM) Cavity; left - PM modeled assuming an equivalent continuous media; right - PM modeled assuming formation and propagation of radial cracks

It is valid to model pressuremeter data in rock in either of the manners presented above if accurate material parameters useful for design are gained. The remainder of this chapter will be devoted to the exploration of three constitutive models for this purpose. Two of the models were implemented and used to analyze data collected at five different test sites. The structure of the third model will be presented for potential future use in pressuremeter data analysis. The first model presented will be a Mohr-Couloumb model with a tensile cutoff as developed by Haberfield and described in the previous chapter. Further detail of the implementation and a parametric analysis will be presented. A Hoek-Brown cavity expansion model described in [23] and developed further by the author will then be discussed and compared to the model developed by Haberfield. Lastly, a constitutive model developed by Zhu, Kondo and Shao referenced in [8] [14] [15] will be presented.

3.1 Review of Elastic Loading and Governing Equations

Important governing equations, assumptions and material behavior during the elastic phase of loading will be briefly reviewed here. However, it may be useful for the reader to revisit the assumptions listed at the beginning of Chapter 2 as well as the equations presented in Section 2.1 before continuing on.

The stress and strain at any point during loading must be determined in order to properly model data collected by the pressuremeter. For the type of pressuremeter used in this study, the recorded data consists of the applied pressure versus the cavity strain, which is equivalent to the radial stress versus the circumferential strain at the cavity wall. Hence, it is natural to adopt a cylindrical coordinate system in modeling pressuremeter response for which the principal stresses are σ_r, σ_z and σ_θ. It follows the principal strains are defined as ϵ_r, ϵ_z and ϵ_θ as illustrated in Figure 3.3 with reference to the pressuremeter cavity. Under the

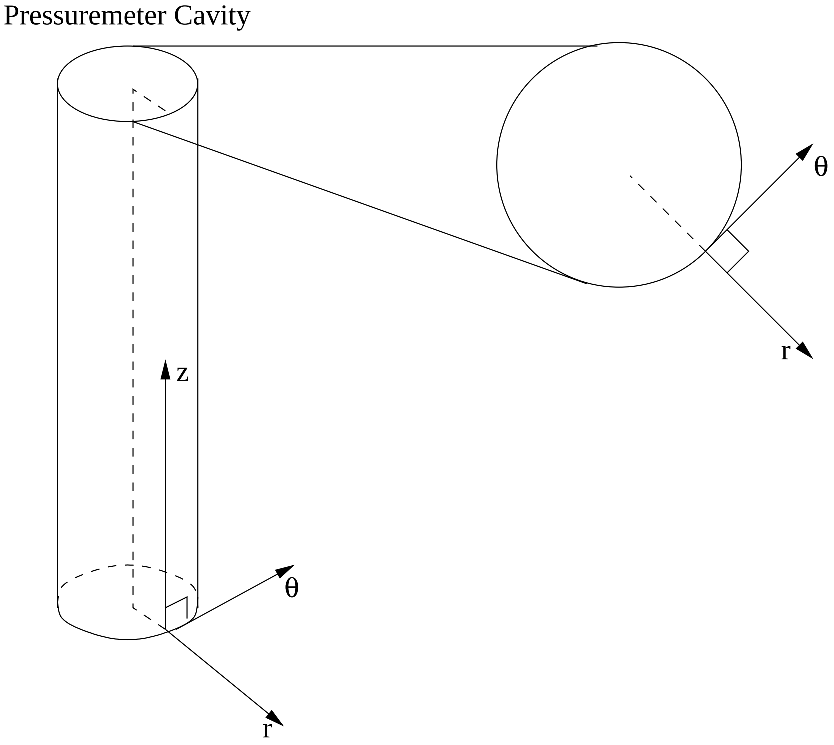

Figure 3.3: Cylindrical Coordinate System for Stress and Strain

assumption of plain strain, (i.e. that the pressuremeter expands as a right cylinder) strain in the vertical or z-direction is equal to zero; that is $\epsilon_z = 0$. The other principal strains can be defined in terms of displacements as

$$\epsilon_\theta = \frac{u}{r} \tag{3.1}$$

and

$$\epsilon_r = \frac{du}{dr} \tag{3.2}$$

where u is displacement relative to radius r. The cavity strain measured during a pressuremeter test is defined by

$$\epsilon_c = \frac{a - a_o}{a_o} \tag{3.3}$$

where a is the inner cavity radius and a_o is the initial cavity radius. Recognizing that at the inner cavity wall, $u = a - a_o$ with reference to $r = a_o$, it can be noted that the cavity strain, ϵ_c, is similar to measuring the circumferential strain, ϵ_θ, at the cavity wall.

Under the assumption of axisymmetric loading, the equation for equilibrium is defined by

$$\frac{d\sigma_r}{dr} + \frac{\sigma_r - \sigma_\theta}{r} = 0 \tag{3.4}$$

which can be used along with boundary conditions to determine the stresses and displacements during the elastic phase of loading. Refer to Section 2.1 for details. The governing equations in the elastic zone are

$$\sigma_r = p_o + (p - p_o)\left(\frac{a}{r}\right)^2 \tag{3.5}$$

$$\sigma_\theta = p_o - (p - p_o)\left(\frac{a}{r}\right)^2 \tag{3.6}$$

$$u = \frac{p - p_o}{2G}\frac{a^2}{r} \tag{3.7}$$

where p is the cavity pressure and p_o is equivalent to the initial ambient pressure or *in situ* horizontal stress σ_{ho}. It should be noted that σ_r is equal and opposite to σ_θ during the elastic phase. Recognition that $a/r = 1$ at the inner wall of the cavity and $a - a_o$ is small during the elastic phase, Equation (3.7) can be rewritten in terms of cavity strain as follows

$$\epsilon_c = \frac{u}{a} = \frac{p - p_o}{2G} \tag{3.8}$$

where G is the shear modulus of the material.

The elastic behavior of the material beyond the elastic-plastic boundary, that is at a radius $r > r_f$, can be determined in a similar manner to that described for the inner cavity wall (refer to Figure 2.10). Applying the boundary condition that at r_f, $p = p_f$ yields the following equations

$$\sigma_r = p_o + (p_f - p_o)\left(\frac{r_f}{r}\right)^2 \tag{3.9}$$

$$\sigma_\theta = p_o - (p_f - p_o)\left(\frac{r_f}{r}\right)^2 \tag{3.10}$$

$$u = \frac{p_f - p_o}{2G}\frac{r_f^2}{r} \tag{3.11}$$

where p_f is the pressure at the initiation of failure.

Using the equations above the material behavior during the elastic phase of loading can be defined. The measured cavity strain and applied radial pressure can be compared to the material response in terms of ϵ_θ and σ_r. The goal then is to determine the point at which elastic behavior ceases, and the resulting stress-strain relation beyond this point as pressure is further increased inside the expanding cavity. This can be accomplished by adopting a yield criterion and flow rule as will be discussed in the following sections for the different constitutive models.

3.2 Mohr-Coulomb Model with Tensile Cutoff

The model developed by Haberfield has been discussed in the previous chapter in Sections 2.3 and 2.4. Although some information is repeated, further development will also be presented here. It should be noted that unless otherwise stated, the ideas presented in the first subsection describing model development are adopted from work by Haberfield as in [10] [11]. As drained analysis is used in the following model, it should be assumed that any parameters listed are in terms of effective values (i.e effective stress, friction angle, cohesion etc.).

3.2.1 Model Development

Employing a Mohr-Coulomb model with a tensile cutoff naturally leads to two yield criterions and thus two different ways of modeling inelastic weak rock behavior. For a given set of parameter inputs, a yield pressure defined by the tensile cutoff and a yield pressure defined by the Mohr-Coulomb failure criterion can both be established. If the yield pressure for the tensile cutoff is less than that of the Mohr-Coulomb failure criterion, then cracks form and propagate. If, however, the yield pressure determined by the standard Mohr-Coulomb failure criterion is reached first, the rock is assumed to behave as a ductile continuum. In terms of principal stresses, the Mohr-Coulomb failure criterion can be written as follows:

$$\sigma_1 = \frac{1 + sin\phi}{1 - sin\phi}\sigma_3 + \frac{2ccos\phi}{1 - sin\phi} \tag{3.12}$$

where ϕ is the internal angle of friction, c is material cohesion and σ_1 and σ_3 are the major and minor principal stresses respectively. Defining

$$m = \frac{1 + sin\phi}{1 - sin\phi} \tag{3.13}$$

and

$$\hat{\sigma} = \frac{2ccos\phi}{1 - sin\phi} \tag{3.14}$$

and taking $\sigma_1 = \sigma_r$ and $\sigma_3 = \sigma_\theta$ Equation (3.12) can be rewritten as

$$\sigma_r = m\sigma_\theta + \hat{\sigma} \tag{3.15}$$

At the initiation of plasticity, once the yield pressure is reached, the radius defining the elastic-plastic boundary, r_f, is equivalent to the radius of the expanding cavity; thus, $r_f/r = r_f/a = 1$, where a is the inner cavity radius. Plugging this into Equations (3.9) and (3.10) and substituting the definitions in these equations into Equation (3.15) the yield pressure, p_f, can be obtained.

$$p_f = \frac{2p_o m + \hat{\sigma}}{m + 1} \tag{3.16}$$

Plugging the definitions of m and $\hat{\sigma}$ from Equations (3.13) and (3.14) into Equation (3.16) and simplifying reduces the expression to the Mohr-Coulomb failure criterion presented in Section 2.3.

$$p_f = ccos\phi + p_o(1 + sin\phi) \tag{3.17}$$

Using the yield criterion defined here and the equation of equilibrium defined previously, the stresses in the plastic failure zone (i.e. $a < r < r_f$) can be determined. Rearranging the relationship for the Mohr-Coulomb criterion defined in Equation (3.15) such that $\sigma_\theta = (\sigma_r - \hat{\sigma})/m$ and substituting this into the equation of equilibrium defined in Equation (3.4) yields the following differential equation

$$\frac{d\sigma_r}{dr} + \frac{\sigma_r(m-1) + \hat{\sigma}}{rm} = 0 \tag{3.18}$$

Equation (3.18) can be rearranged such that

$$\frac{md\sigma_r}{\sigma_r(m-1) + \hat{\sigma}} + \frac{dr}{r} = 0 \tag{3.19}$$

By solving and applying the boundary condition that when $r = r_f$, $\sigma_r = p_f$, the following relationship for radial stress at radius r is obtained

$$\sigma_r = \left[\frac{\hat{\sigma} + p_f(m-1)}{m-1}\right]\left(\frac{r_f}{r}\right)^{\frac{m-1}{m}} - \frac{\hat{\sigma}}{m-1} \tag{3.20}$$

Substituting this definition back into the yield criterion, the circumferential stress is determined.

$$\sigma_\theta = \left[\frac{\hat{\sigma} + p_f(m-1)}{m(m-1)}\right]\left(\frac{r_f}{r}\right)^{\frac{m-1}{m}} - \frac{\hat{\sigma}}{m-1} \tag{3.21}$$

Here the author deviates from the model developed by Haberfield. Haberfield used the boundary condition that at $r = r_o$, $\sigma_r = p$, which is inconsistent with the formulation of strain, which references $r = r_f$ as is presented here. The form of the equation presented here is also more useful for implementation than that presented by Haberfield in [10].

Once yield has occurred, the strains in the plastic zone can be determined incrementally by adding the elastic and plastic components such that

$$d\epsilon_r = d\epsilon_r^e + d\epsilon_r^p \tag{3.22a}$$

$$d\epsilon_\theta = d\epsilon_\theta^e + d\epsilon_\theta^p \tag{3.22b}$$

where ϵ^e denotes the elastic strain component, ϵ^p denotes the plastic strain component and $d\epsilon$ denotes an incremental change. The plastic strain components are determined by a non-associative flow rule written in general form as $\dot{\epsilon}_{ij}^p = \lambda \partial g / \partial \sigma_{ij}$ with g being the plastic potential function and λ a scalar plastic multiplier. The flow rule used here, adopted from Davis (1968), describes dilative volume change via an angle of dilation, ψ, as described in Section 2.3. In terms of incremental strains the flow rule then can be written as

$$d\epsilon_r^p = \lambda \tag{3.23a}$$

$$d\epsilon_\theta^p = -n\lambda \tag{3.23b}$$

where

$$n = \frac{1 + sin\psi}{1 - sin\psi} \tag{3.24}$$

Rearranging Equations (3.23a) and (3.23b) yields

$$d\epsilon_\theta^p + nd\epsilon_r^p = 0 \tag{3.25}$$

Integrating and applying boundary conditions at $r = r_f$ leads to

$$\epsilon_\theta^p + n\epsilon_r^p = 0 \tag{3.26}$$

The strain displacement equations can be rearranged giving

$$\epsilon_r = \epsilon_\theta + r\frac{d\epsilon_\theta}{dr} \tag{3.27}$$

with

$$\epsilon_r = \epsilon_r^p + \epsilon_r^e \tag{3.28a}$$

$$\epsilon_\theta = \epsilon_\theta^p + \epsilon_\theta^e \tag{3.28b}$$

Substituting equations (3.28a) and (3.28b) into Equations (3.26) and (3.27) yields

$$r\frac{d\epsilon_\theta^p}{dr} + \epsilon_\theta^p\left(\frac{n+1}{n}\right) = \epsilon_r^e - \epsilon_\theta^e - r\frac{d\epsilon_\theta^e}{dr} \tag{3.29}$$

From here, the elastic components of Equation (3.29) can be solved using Hooke's law (as stated in Equations (2.5) and (2.6)) and the stress equations previously derived, defined by Equations (3.20) and (3.21). The plastic components, specifically ϵ_θ^p, can then be determined. The resulting equations for the circumferential strains are

$$\epsilon_\theta^e = \frac{1+\nu}{E}\left[(1-\nu-m\nu)\left(\frac{p_f(m-1)+\hat{\sigma}}{m(m-1)}\right)\left(\frac{r_f}{r}\right)^{\frac{m-1}{m}} - (1-2\nu)\left(p_o + \frac{\hat{\sigma}}{m-1}\right)\right] \tag{3.30a}$$

$$\epsilon_\theta^p = D\left(\frac{1+\nu}{E}\right)\left[\left(\frac{r_f}{r}\right)^{\frac{m-1}{m}} - \left(\frac{r_f}{r}\right)^{\frac{n+1}{n}}\right] \tag{3.30b}$$

with

$$D = (1-\nu)\frac{n(m+1)}{m(m+n)}\left[p_f(m-1)+\hat{\sigma}\right] \tag{3.30c}$$

where E is the Young's modulus, ν is Poisson's ratio and everything else is as previously defined. Combining elastic and plastic strains to obtain total circumferential strains gives

$$\epsilon_\theta = \frac{1+\nu}{E}\left(\begin{array}{c}\left[\left(\frac{p_f(m-1)+\hat{\sigma}}{m(m-1)}\right)(1-\nu-m\nu)+D\right]\left(\frac{r_f}{r}\right)^{\frac{m-1}{m}} - D\left(\frac{r_f}{r}\right)^{\frac{n+1}{n}} \\ -(1-2\nu)\left(p_o+\frac{\hat{\sigma}}{m-1}\right)\end{array}\right) \tag{3.31}$$

This can be rewritten as presented in Section 2.3 as

$$\epsilon_\theta = \frac{u}{r} = \frac{1}{2G}\left[b_1\left(\frac{r_f}{r}\right)^{\frac{(m-1)}{m}} + b_2\left(\frac{r_f}{r}\right)^{\frac{(n+1)}{n}} + b_3\right] \tag{3.32}$$

where

$$\begin{aligned} b_1 &= \frac{2m}{m-1}(p_f-p_o)\left[(1-\nu)\left(\frac{1+mn}{m+n}\right)-\nu\right] \\ b_2 &= 2n(1-\nu)\left(\frac{m+1}{m+n}\right)(p_f-p_o) \\ b_3 &= (p_f-p_o)(1-2\nu)\left(\frac{m+1}{m-1}\right) \end{aligned} \tag{3.33}$$

with all parameters as previously defined.

The equations derived thus far follow a Mohr-Coulomb failure criterion and are valid for ductile rock behavior (i.e. plastic deformation occurs). If, however, the apparent tensile strength of the rock is less than the yield pressure associated with the Mohr-Coulomb failure criterion, then the tensile cutoff will be reached a different material model must be considered. The yield pressure related to the apparent tensile strength is

$$p_c = 2p_o + |\sigma_t| \tag{3.34}$$

where p_c is the yield pressure associated with the initiation of tensile cracking and σ_t is the tensile strength of the rock. As discussed in Section 2.3, if this yield pressure, p_c, is less than the previously determined yield pressure, p_f, then it is assumed that brittle fracture occurs, and failure of the rock mass results from the propagation of cracks and not through plastic yield. The material between the propagating cracks is assumed to behave elastically during this process until the compressive strength of the rocks is reached. At this point, the cracks continue to propagate and shear zones appear in the rock between the cracks. This is well illustrated in Figure 2.11. To account for crack propagation, Haberfield developed a finite element model as discussed in Section 2.3. Analyzing pressuremeter data in weak siltstone and mudstone with the finite element model, Haberfield developed empirical equations for cracked rock behavior. In essence, the rock mass is treated as an equivalent continuous medium with altered material properties. The empirical equations developed by Haberfield and used in this study and are as follows

$$\frac{r_c}{r} = 3\left(\frac{p}{p_c} - 1\right) * 10^{-1.88p_o/p_c} + 1 \tag{3.35}$$

where r_c is as illustrated in Figure 3.2, and

$$\epsilon_c = \frac{1}{2G}\left[p(1-\nu)ln\left(\frac{r_c}{r}\right) + p - p_o\frac{r_c}{r}\right] \tag{3.36}$$

where ϵ_c is the cavity strain. All the required equations for implementation of the Mohr-Coulomb model with a tensile cutoff have now been presented. For more information and details on the model developed by Haberfield, the author refers the reader to [10][11][12].

3.2.2 Model Implementation

In order to properly implement the model described above, it is important to first identify the necessary input parameters. As previously mentioned, the aim is to determine the radial stress, σ_r, and circumferential strain, ϵ_θ, for comparison to the recorded applied pressure, p, and cavity strain, ϵ_c, respectively.

During the elastic phase, the response is assumed to be linear elastic, whereby the slope of pressure versus strain is equal to twice the shear modulus (i.e. in Equation (2.22)).

$$\frac{p - p_o}{\epsilon_c} = 2G \tag{3.37}$$

Thus in order to determine the stress-strain response during this phase, knowledge of the *in situ* pressure, p_o, and the shear modulus, G, is required. The end of the elastic response (or beginning of inelastic behavior) is determined by the yield pressure, p_f or p_c. It is clear then that the entire elastic response can be defined by two points, the initial stress-strain, (0,p_o)

and the stress-strain at the initiation of yield, (ϵ_{cf},p_f or p_c), where ϵ_{cf} can be determined by replacing p with p_f or p_c in Equation (3.37). The parameters required to determine the yield pressure can be identified by inspecting Equations (3.17) and (3.34) revealing the tensile strength of the rock σ_t, internal angle of friction ϕ, and material cohesion c, must be determined.

Beyond the yield pressure, the stress-strain response can be determined by Equations (3.20) and (3.32) or by Equations (3.35) and (3.36). It should be noted that Equation (3.35) can be rearranged to solve for pressure, p, as follows

$$p = p_c \left(\frac{\frac{r_c}{r} - 1}{3 * 10^{\frac{-1.88 p_o}{p_c}}} + 1 \right) \tag{3.38}$$

Additional input parameters identified through inspection of the these equations are Poisson's ratio ν, the angle of dilation ψ (this input can be replaced by the critical friction angle ϕ_r by using Rowe's dilatancy relationship (Equation (2.74)) and friction angle, ϕ) and the ratio r_f/r or r_c/r. The radius r in this last parameter can be replaced by the radius of interest defined by the inner cavity wall, a. The radius r_f (or r_c) defines the elastic-plastic (or crack propagation) boundary beyond which elastic behavior is occurring. Upon the initiation of material yield, r_f or r_c is equivalent to the cavity radius a; that is the ratio of r_f/a or r_c/a is equal to one. As the pressure is increased further, the radius r_f or r_c enlarges and extends beyond the radius of the inner cavity wall (Figure 3.2). Thus, the ratio r_f/a or r_c/a, increases as the applied pressure increases. Creating a vector for this ratio from $1 : x$, where x is a number large enough to achieve the required (or desired) strain, therefore allows the elimination of this ratio as an input parameter.

The parameters necessary to define the entire model then are the horizontal *in situ* stress, p_o, shear modulus, G, friction angle, ϕ, cohesion, c, Poisson's ratio, ν, the angle of dilation, ψ, (or if preferred the critical friction angle, ϕ_r) and the tensile strength of the rock σ_t. Details on the determination of these material parameters is reserved for the next chapter where data interpretation is discussed. Using these parameters and the proper equations the model can be effectively implemented for data analysis; best illustrated by a flow diagram (refer to Figure 3.4). The mode of failure for the rock is determined through comparison of the two possible yield pressures, p_c and p_f. If $p_f > p_c$, it is assumed that tensile failure occurs and the rock mass deforms as a result of crack formation and subsequent propagation. However, if the opposite is true (i.e. $p_f < p_c$), it is assumed the rock mass behaves as a continuum and fails according to a Mohr-Coulomb failure criterion with a flow rule utilizing the angle of dilation to account for change in volume.

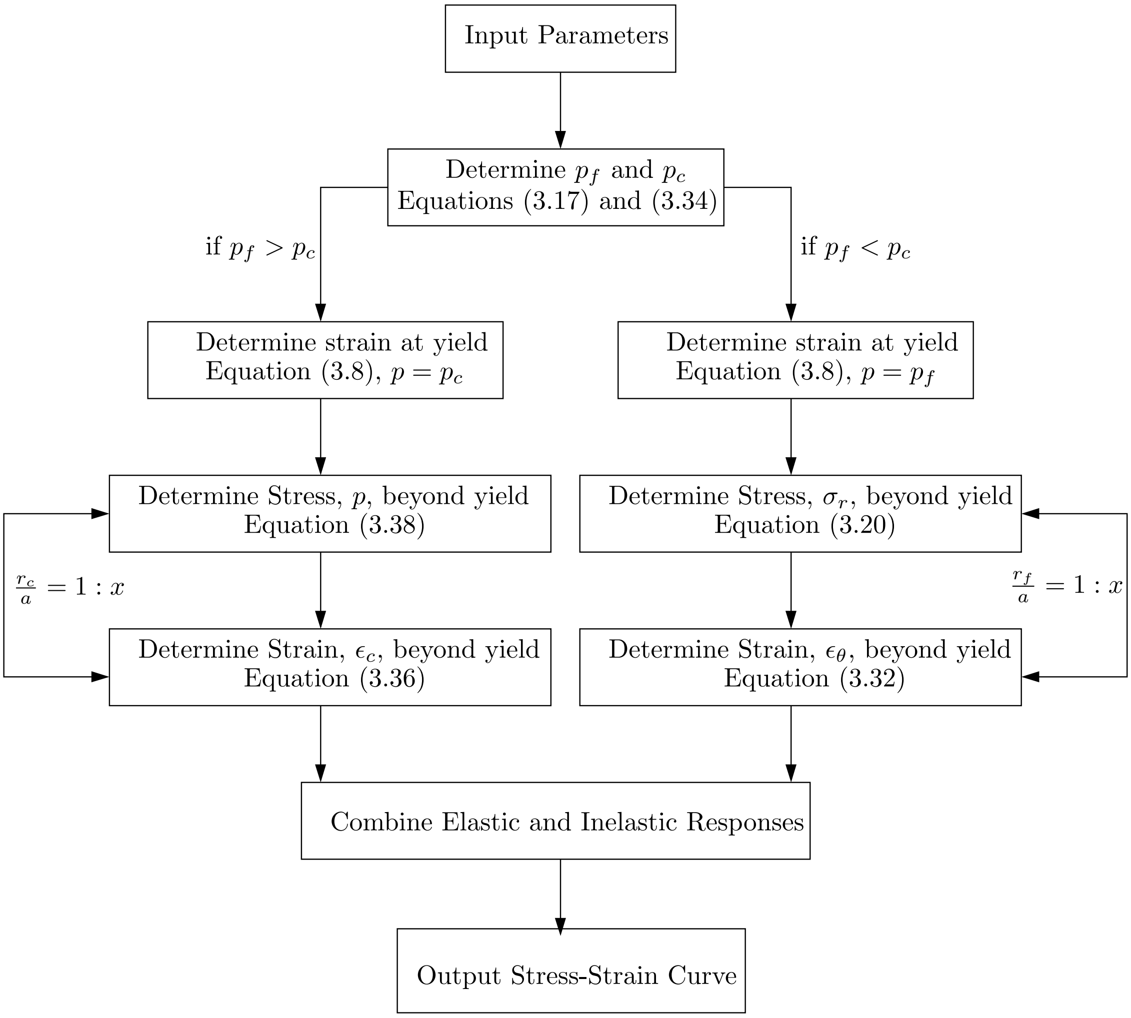

Figure 3.4: Flow Diagram for Implementation of the Mohr-Coulomb model with a Tensile Cutoff

3.2.3 Validation of Model Implementation

The model implementation outlined in Figure 3.4 was coded by the author using MATLAB. In order to analyze data with confidence, however, the code must be validated against a previously known solution. This task was accomplished by comparing plots Haberfield produced as examples in his dissertation [10] against those produced by the author's code. Three different figures, for which the inputs are given in [10] are used for comparison and are displayed in Figures 3.5, 3.6 and 3.7.

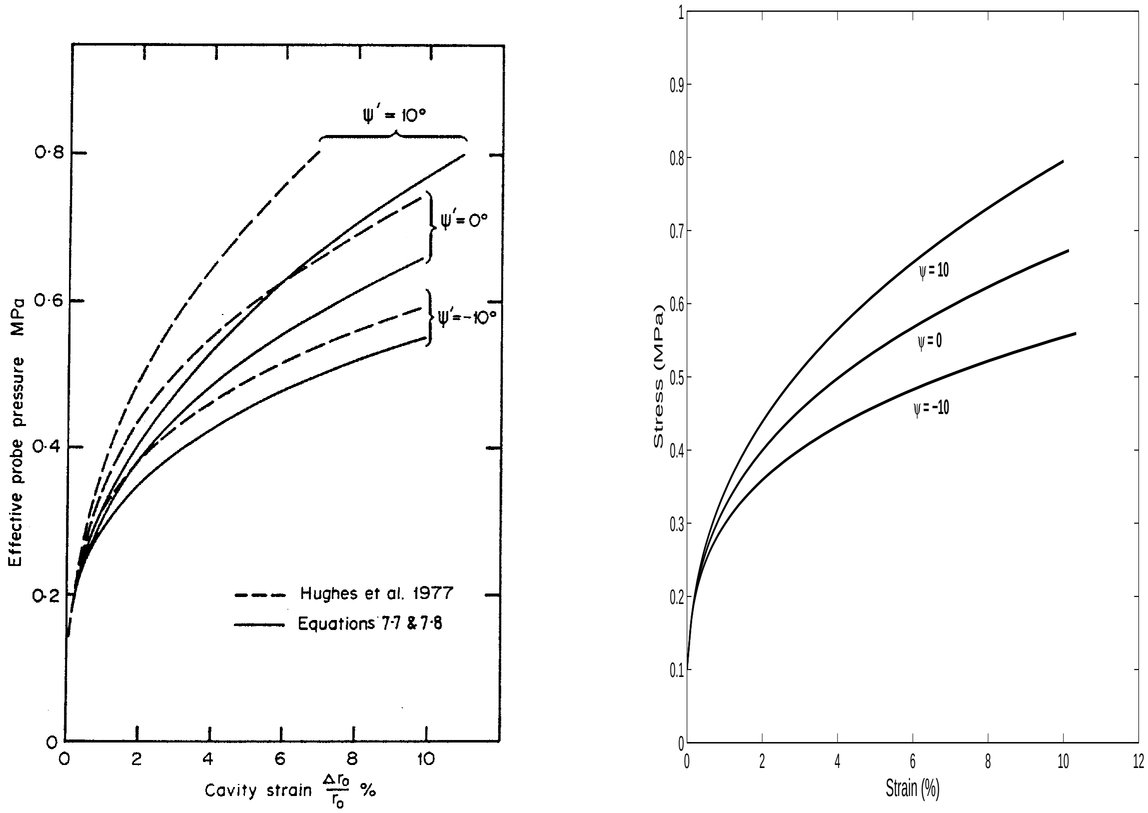

Figure 3.5: Comparison of plots produced by Haberfield [10] (left) and the author (right). Input parameters are G = 30 MPa, p_o = 0.1 MPa, ν = 0.3, c = 0 MPa, ϕ = 30^o and $\psi = -10^o, 0^o, 10^o$. The dashed lines in the Haberfield plot are there for comparison to the Hughes sand model and can be ignored in this comparison.

For the cases in which Young's modulus was given (Figures 3.6 and 3.7), the shear modulus was calculated using Equation (3.39) and used as input into the author's code.

$$G = \frac{E}{2(1+\nu)} \tag{3.39}$$

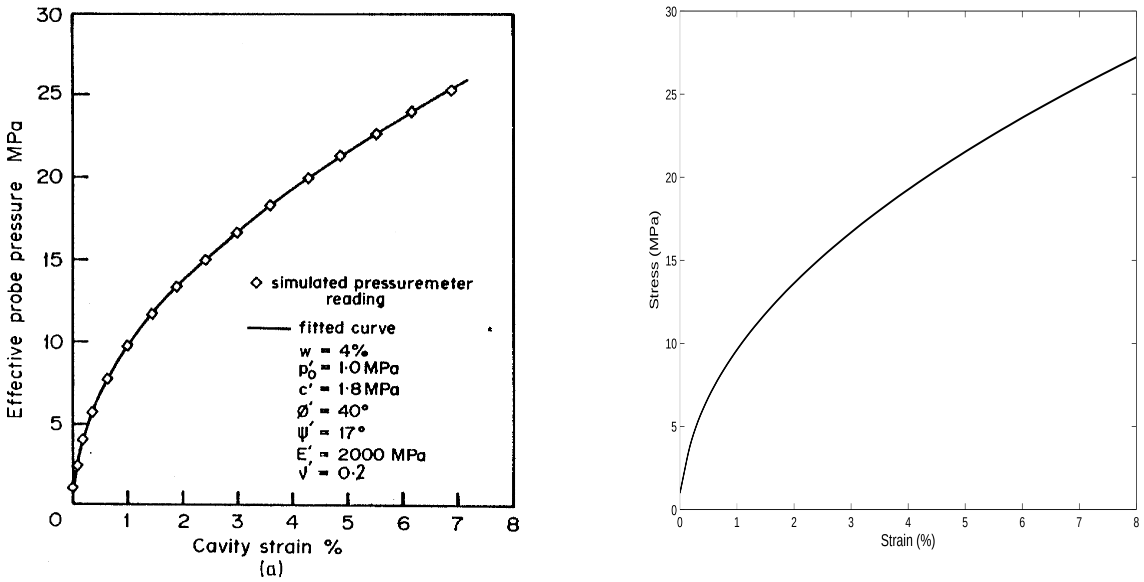

Figure 3.6: Comparison of plots produced by Haberfield [10] (left) and the author (right). Inputs are displayed in the left plot (except water content which is not a model input). Poisson's ratio and Young's modulus were used to determine a shear modulus for the author's plot via Equation (3.39)

.

The three examples presented here represent a variety of conditions for the author's code to be tested against. Weak rock that behaves in a purely frictional manner (i.e no cohesion) with a variance in dilation angle is presented in Figure 3.5. Figures 3.6 and 3.7 represent weak rock with cohesion representative of higher and lower strength respectively. In all cases, the author's code is able to match the stress-strain curve produced by Haberfield in [10]. Confirmation of the match is obtained by systematically comparing different points

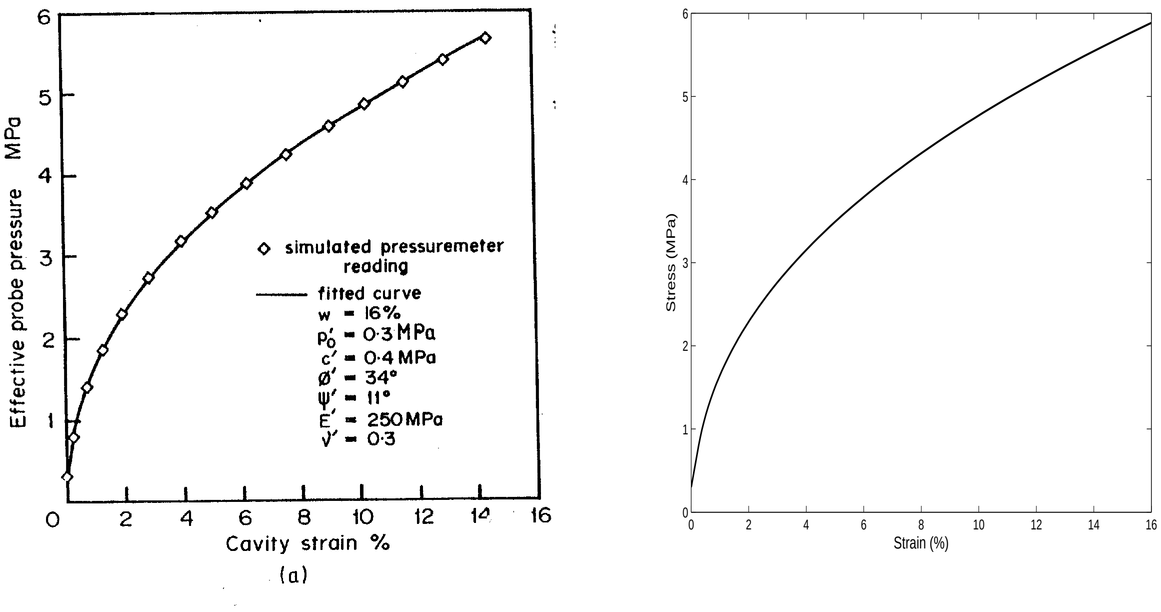

Figure 3.7: Comparison of plots produced by Haberfield [10] (left) and the author (right). Inputs are displayed in the left plot (except water content which is not a model input). Poisson's ratio and Young's modulus were used to determine a shear modulus for the author's plot via Equation (3.39)

.

along the curve. For example, in Figure 3.6 stress values of 10, 14, 17, 19.5, 21, 23.5 and 25 corresponding to 1, 2, 3, 4, 5, 6 and 7% strain can be identified in both plots. This provides validation that the code produced by the author is indeed functioning properly.

3.2.4 Parametric Analysis

Before using a model for data analysis, it is important to first understand the affect of different input parameters on the model output. It is particularly useful to know which parameters qualitatively induce the greatest change in the output of the model. This section is devoted toward illustrating the effects of the input parameters for Haberfield's Mohr-Coulomb model. The easiest way to present this is in graphical form. Thus a series of

Table 3.1: Default Input Values for Parametric Analysis - Mohr-Coulomb

Shear modulus, G	$2,200$ MPa
In Situ stress, p_o	0.4 MPa
Cohesion, c	0.3 MPa
Poisson's ratio, ν,	0.3
Friction angle, ϕ	45^o
Dilation angle, ψ	8.5^o

figures in which the model parameters are altered is presented with discussion to follow.

In the following figures, all parameters are held constant while one parameter is varied. The default values (values assumed by parameters that are not varied in a given graph) of the parameters are presented in Table 3.1. These values are chosen because they are near the average for the data set analyzed and therefore representative of the material of interest. All values are effective values, in that drained analysis is assumed. All the figures have been plotted to the same scale for comparative purposes.

Inspection of Figures 3.8 through 3.12 reveals that the material cohesion, c, shear modulus, G, and the dilation angle, ψ, have the largest effect on the stress-strain output. The choice of *in situ* stress, p_o, can also have a significant impact, while the choice of Poisson's ratio, ν, and surprisingly friction angle, ϕ, have a lesser impact on the stress-strain curve produced. Each of the parameters exhibits a nonlinear response to a constant increment change. That is the change resulting from an incremental increase either grows or decays with an increase in the parameter value. These results warrant a more detailed discussion of the individual parameters.

The selection of shear modulus and *in situ* stress greatly affect the model output, with the impact of shear modulus being greater for the range of interest. In both cases, the influence of the parameter decreases as the parameter increases. For example, an increase in shear modulus from 500 to 2,000 MPa has more impact than a jump from 9,500 to 11,000 MPa. Similarly, an increase in the *in situ* stress from 0.1 to 0.3 MPa has a greater effect than

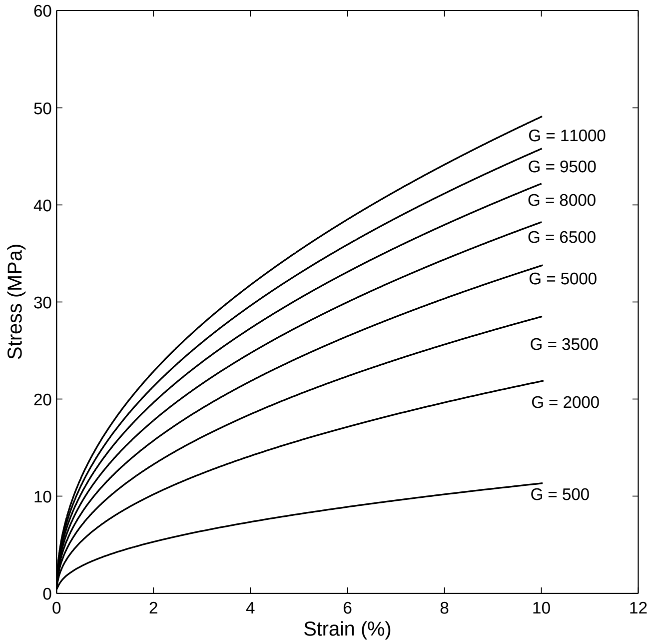

Figure 3.8: Effect of Changing the Shear Modulus, G, for Mohr-Coulomb Model

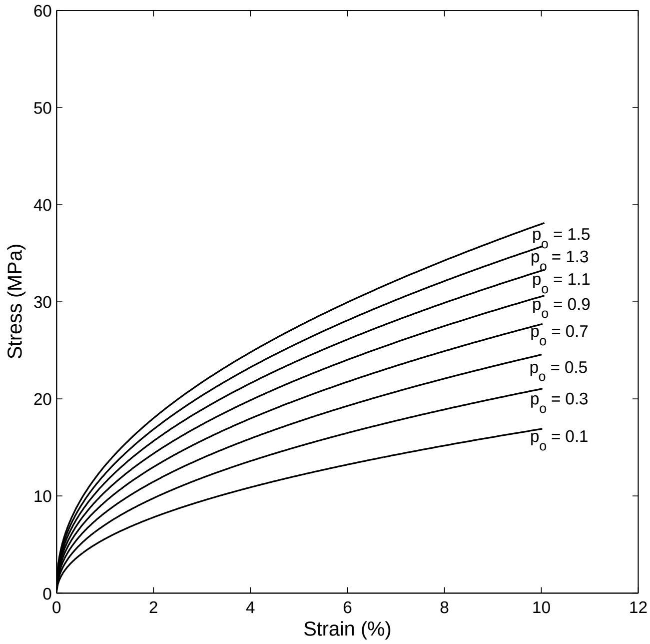

Figure 3.9: Effect of Changing the *In Situ* Stress, p_o, for Mohr-Coulomb Model

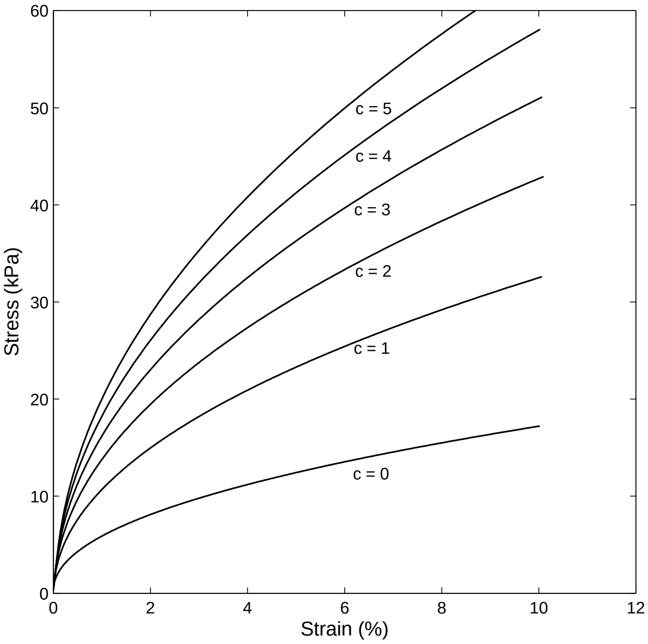

Figure 3.10: Effect of Changing the Material Cohesion, c, for Mohr-Coulomb Model

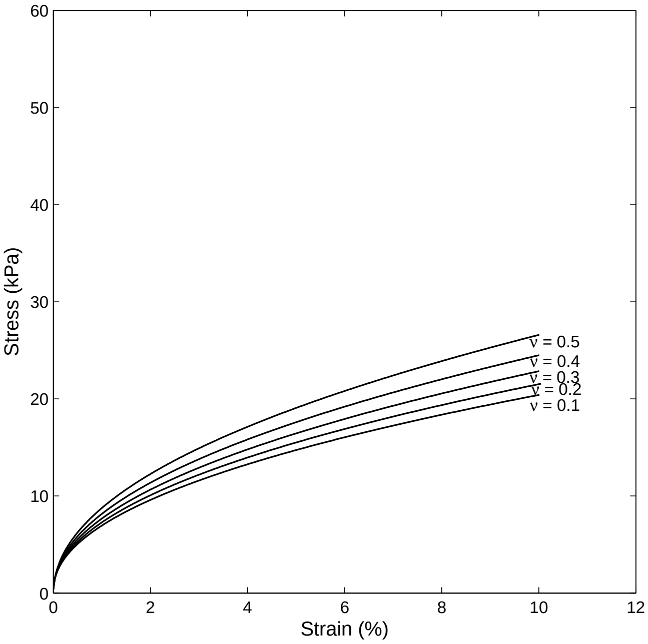

Figure 3.11: Effect of Changing Poisson's Ratio, ν, for Mohr-Coulomb Model

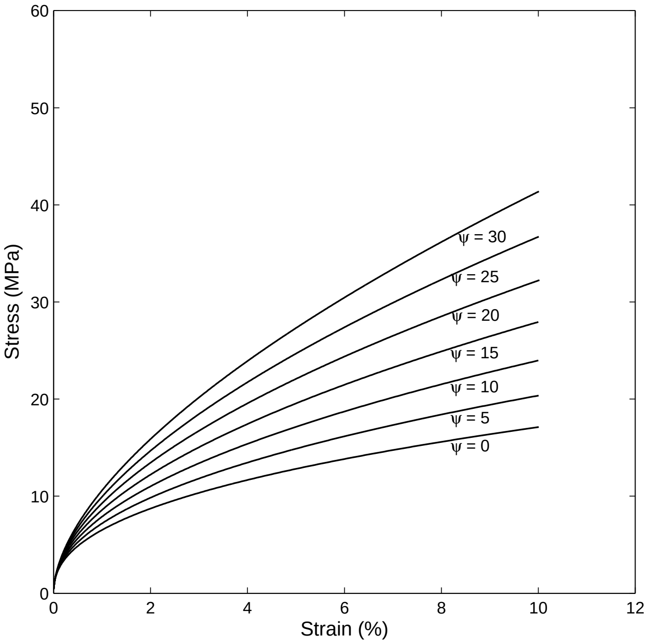

Figure 3.12: Effect of Changing the Dilation Angle, ψ, for Mohr-Coulomb Model

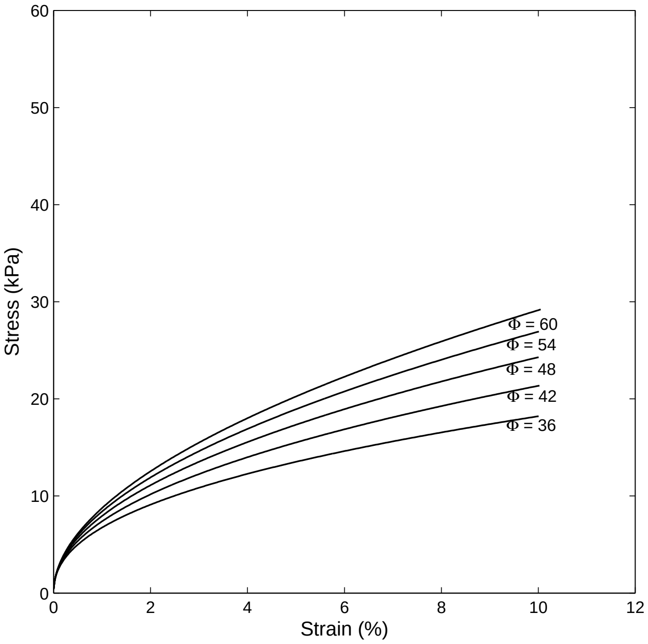

Figure 3.13: Effect of Changing the Friction Angle, ϕ, for Mohr-Coulomb Model

an increase from 1.1 to 1.3 MPa. Thus, the choice of these parameters is most important for a soft material with low confining stress. Fortunately, the shear modulus can be determined from the unload-reload loops performed during a pressuremeter test reducing or eliminating the effect of an improper choice for this parameter on the model output. The lateral *in situ* or ambient stress can be more difficult to determine, but a range can often be defined if the vertical stress in the test region is known. Additionally, the pressuremeter curve can be used to help in the determination of the *in situ* stress - a detail to be discussed in the next chapter.

The choice of Poisson's ratio has the lowest impact on the model output and already has a predefined range between 0 and 0.5. This range is narrowed further in that typically rock will have a Poisson's ratio between 0.15 and 0.35 [11] and ranges of Poisson's ratio for a given rock type are usually available in the literature. Therefore selection of this parameter is not of great concern.

The final three parameters relate to material strength and deformation qualities and can significantly impact the model output. The effect of a change in the material cohesion decreases with an increase in the cohesion value, but the impact at greater values is still significant in comparison to other parameters. The impact of additional cohesion, however, is most prominent in changing a purely frictional response ($c = 0$) into a $c - \phi$ response with both frictional and cohesion strength components (refer to Figure 3.10). The choice of dilation angle has less impact on the model output than choice of material cohesion, but the effect is still important. As the dilation angle increases there is a slight increase in the influence on the model output. This result is logical in that increased dilation should cause a strain-hardening effect and thus an apparent stiffer material response. Inspection of Figure 3.13 leads to the conclusion that the selection of friction angle does not significantly influence the model output. However, in Figure 3.13 the dilation angle is held constant as the friction angle is changed. This is unrealistic as the amount of dilation occurring typically should increase as the friction angle of the material is increased; in other words there is a relationship between the friction angle of the material and the dilation angle. One relationship previously mentioned is Rowe's dilatancy theory, restated here for convenience

$$\frac{1+sin\phi}{1-sin\phi}=\left(\frac{1+sin\psi}{1-sin\psi}\right)\left(\frac{1+sin\phi_{cv}}{1-sin\phi_{cv}}\right) \tag{3.40}$$

where ϕ_{cv} is the critical friction angle. The critical state friction angle should be constant for a given material. Hence a more realistic approach to studying the impact of change in friction angle on model behavior is to hold the critical friction angle constant and allow the dilation angle to change as the friction angle is altered. This approach is used in Figure 3.14 with a critical friction angle of 36^o. The result is that the effect of a change in friction angle is now comparable to the effect of changing the material cohesion, making the choice of the two strength parameters of near equal importance. It should be noted that the two differ in that the effect of change in the friction angle increases with an increase in the value of the friction angle chosen, while the opposite is observed for the material cohesion.

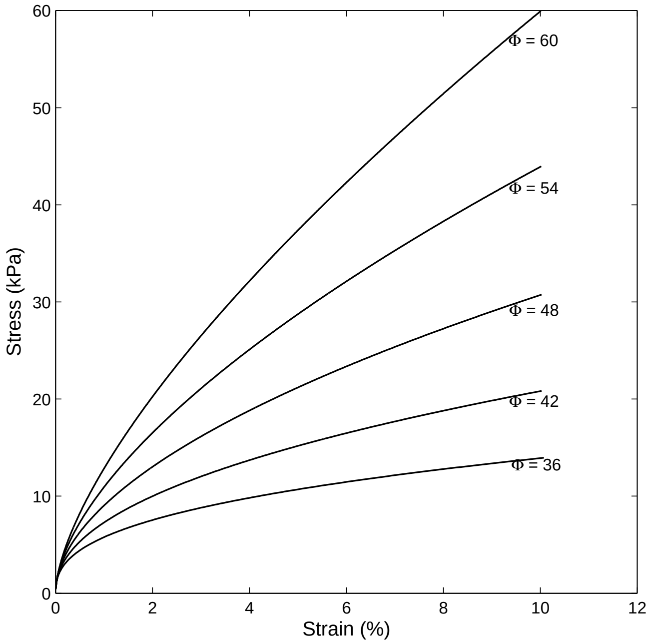

Figure 3.14: Effect of Changing the Friction Angle, ϕ, Holding the Residual Friction Angle Constant While Allowing the Dilation Angle to Change for Mohr-Coulomb Model

One final note should be made regarding the choice of material parameters. The case presented here are centered around the default values in Table 3.1. Lowering or raising the default values may lead to a difference in response to the varied parameters. However, this section does provide a qualitative understanding of which parameters have the greatest influence on the model output if the tensile cutoff is not reached.

For the case of the tensile cutoff, the controlling parameters are those which relate to whether or not the cutoff is reached, namely the shear modulus, rock tensile strength, lateral *in situ* stress and Poisson's ratio. The influence of these parameters is similar in nature to that discussed for the case in which the cutoff is not reached and thus a parametric analysis will not be presented here. Furthermore, it was found that for the weak rock formations studied in this thesis, this empirical model typically did not capture the rock behavior. Therefore, the author has chosen not to emphasize the tensile cutoff model.

3.3 Hoek-Brown Model

The Hoek-Brown failure criterion is widely accepted and extensively used in rock engineering projects to describe rock mass behavior [6]. Originally developed in 1980 to model the behavior of intact and jointed rock masses for underground excavation, the criterion has evolved over time to account for weak and heavily fractured rock masses. The criterion's most recent iteration, released in 2002 in [6] is supplemented by further improvement of classification schemes associated with the model parameters, such as in [18]. The criterion is non-linear and empirical, based on a plethora of rock data and observed behavior over the years. The non-linear nature of the criterion is likely more appropriate for modeling the true behavior of a rock mass.

In terms of principal stresses, the Generalized Hoek-Brown criterion can be written as follows

$$\sigma_1' = \sigma_3' + \sigma_c \left(m_b \frac{\sigma_3'}{\sigma_c} + s \right)^b \tag{3.41}$$

where σ_1' and σ_3' are the effective major and minor principal stresses respectively, σ_c is the uniaxial compressive strength of intact rock, m_b is the reduced value of the Hoek-Brown material constant, m_i given by

$$m_b = m_i exp\left(\frac{GSI - 100}{28 - 14D}\right) \tag{3.42}$$

s and b are constants based on the rock mass characteristics defined as

$$s = exp\left(\frac{GSI - 100}{9 - 3D}\right) \tag{3.43}$$

$$b = \frac{1}{2} + \frac{1}{6}\left(e^{-GSI/15} - e^{-20/3}\right) \tag{3.44}$$

GSI is the Geological Strength Index $(0-100)$ and D is a disturbance parameter $(0-1)$. As in Section 3.2, effective stress (i.e. drained) analysis is applicable here and thus the prime (') is dropped in future equations for convenience.

As the reader may be unfamiliar with some of the parameters mentioned, a brief description is included here. The Hoek-Brown material constant for intact rock, m_i, generally ranges from a value of 2 to 35. Higher numbers indicate greater interlocking and frictional resistance, and thus greater strength. Ideally values for this parameter should be determined through lab or *in situ* testing, however, values can be assigned based on rock type as outlined in the chart image in Figure 3.15, taken from [18]. The Geological Strength Index, GSI, is a system used to rate rock mass strength based on the rock structure and joint roughness. A rock with few discontinuities and sharp asperities on its joint faces will provide more resistance to load than a rock with developed shear planes and smooth joint faces. The system rates a rock mass from $0-100$, with values assigned based on the chart displayed in Figure 3.16, taken from [18]. The use of the GSI system has been extensively covered in the literature; some helpful resources for the interested reader include [20][13][18][19]. The disturbance parameter, D, is a qualitative tool used to assign a value based on observed disturbance resulting from stress relaxation and blasting. The parameter ranges from $0-1$ with 0 representing an undisturbed rock mass and 1 being highly disturbed. General guidelines are given in Figure 3.17, taken from [6]. Lastly, the uniaxial compressive strength of the intact rock, σ_c, represents the maximum resistance to failure under an applied axial load where failure is defined by crushing of the grains or ultimate failure of the rock material. The uniaxial compressive strength should be determined through laboratory testing

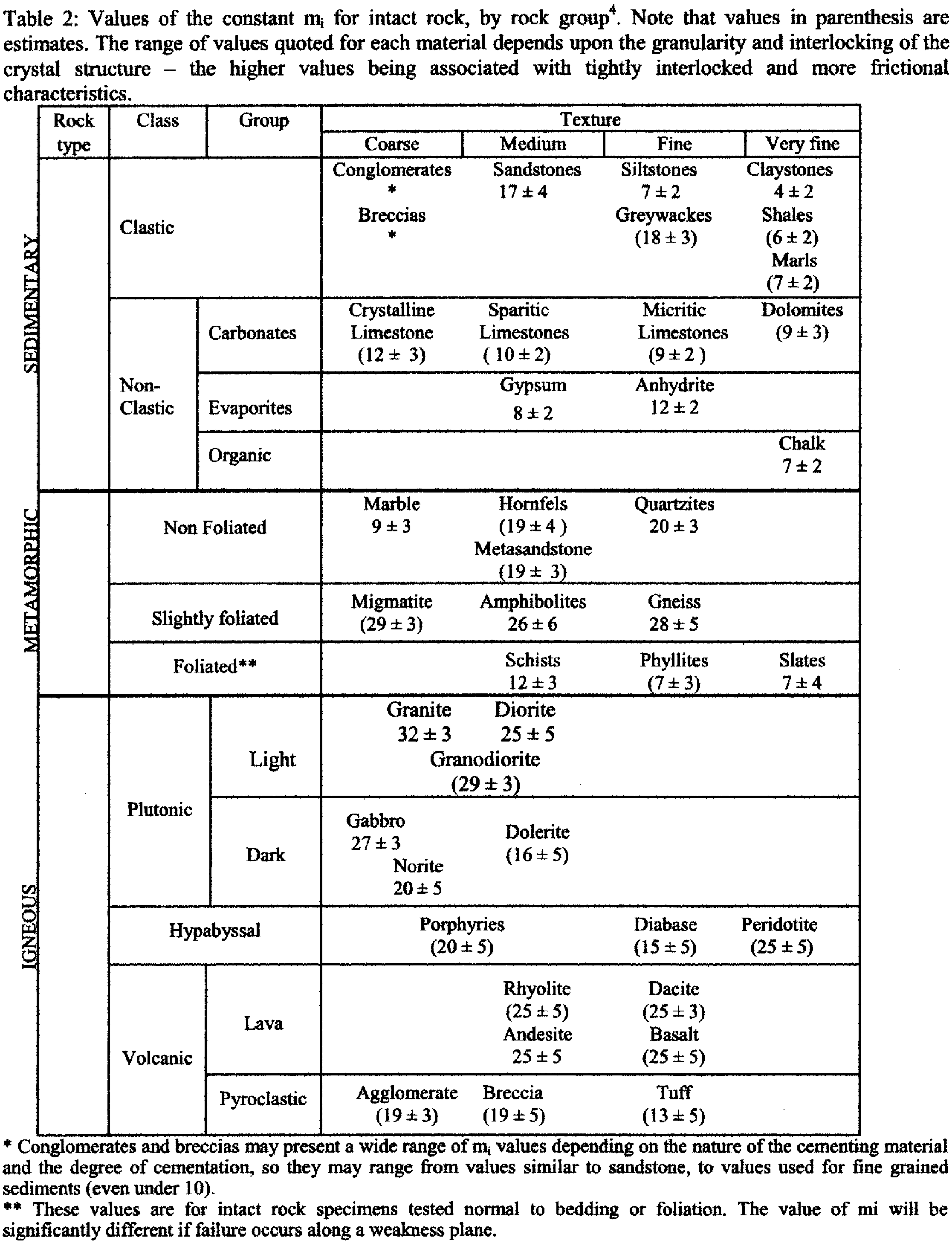

Table 2: Values of the constant m_i for intact rock, by rock group[4]. Note that values in parenthesis are estimates. The range of values quoted for each material depends upon the granularity and interlocking of the crystal structure – the higher values being associated with tightly interlocked and more frictional characteristics.

Rock type	Class	Group	Texture			
			Coarse	Medium	Fine	Very fine
SEDIMENTARY	Clastic		Conglomerates * Breccias *	Sandstones 17 ± 4	Siltstones 7 ± 2 Greywackes (18 ± 3)	Claystones 4 ± 2 Shales (6 ± 2) Marls (7 ± 2)
	Non-Clastic	Carbonates	Crystalline Limestone (12 ± 3)	Sparitic Limestones (10 ± 2)	Micritic Limestones (9 ± 2)	Dolomites (9 ± 3)
		Evaporites		Gypsum 8 ± 2	Anhydrite 12 ± 2	
		Organic				Chalk 7 ± 2
METAMORPHIC	Non Foliated		Marble 9 ± 3	Hornfels (19 ± 4) Metasandstone (19 ± 3)	Quartzites 20 ± 3	
	Slightly foliated		Migmatite (29 ± 3)	Amphibolites 26 ± 6	Gneiss 28 ± 5	
	Foliated**			Schists 12 ± 3	Phyllites (7 ± 3)	Slates 7 ± 4
IGNEOUS	Plutonic	Light	Granite 32 ± 3 Granodiorite (29 ± 3)	Diorite 25 ± 5		
		Dark	Gabbro 27 ± 3 Norite 20 ± 5	Dolerite (16 ± 5)		
	Hypabyssal		Porphyries (20 ± 5)		Diabase (15 ± 5)	Peridotite (25 ± 5)
	Volcanic	Lava		Rhyolite (25 ± 5) Andesite 25 ± 5	Dacite (25 ± 3) Basalt (25 ± 5)	
		Pyroclastic	Agglomerate (19 ± 3)	Breccia (19 ± 5)	Tuff (13 ± 5)	

* Conglomerates and breccias may present a wide range of m_i values depending on the nature of the cementing material and the degree of cementation, so they may range from values similar to sandstone, to values used for fine grained sediments (even under 10).

** These values are for intact rock specimens tested normal to bedding or foliation. The value of mi will be significantly different if failure occurs along a weakness plane.

Figure 3.15: Chart for use in Determining the Hoek-Brown Constant, m_i, for Different Rock Types. Original Image is Table 2 in [18].

Table 3: Geological strength index for jointed rock masses.

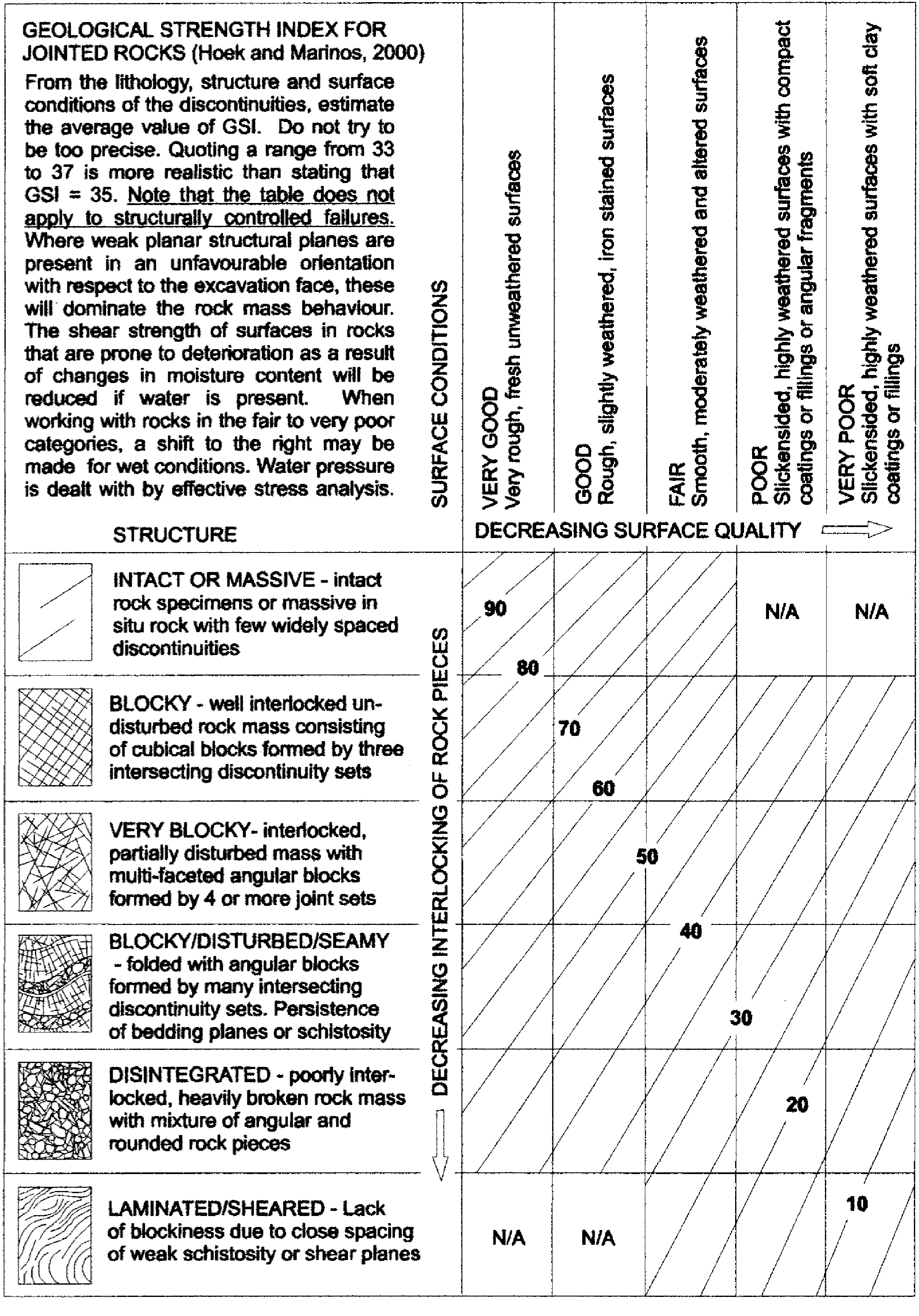

GEOLOGICAL STRENGTH INDEX FOR JOINTED ROCKS (Hoek and Marinos, 2000)

From the lithology, structure and surface conditions of the discontinuities, estimate the average value of GSI. Do not try to be too precise. Quoting a range from 33 to 37 is more realistic than stating that GSI = 35. Note that the table does not apply to structurally controlled failures. Where weak planar structural planes are present in an unfavourable orientation with respect to the excavation face, these will dominate the rock mass behaviour. The shear strength of surfaces in rocks that are prone to deterioration as a result of changes in moisture content will be reduced if water is present. When working with rocks in the fair to very poor categories, a shift to the right may be made for wet conditions. Water pressure is dealt with by effective stress analysis.

Figure 3.16: Chart for use in Determining the Geological Strength Index, *GSI*, for Different Rock Types. Original Image is Table 3 in [18].

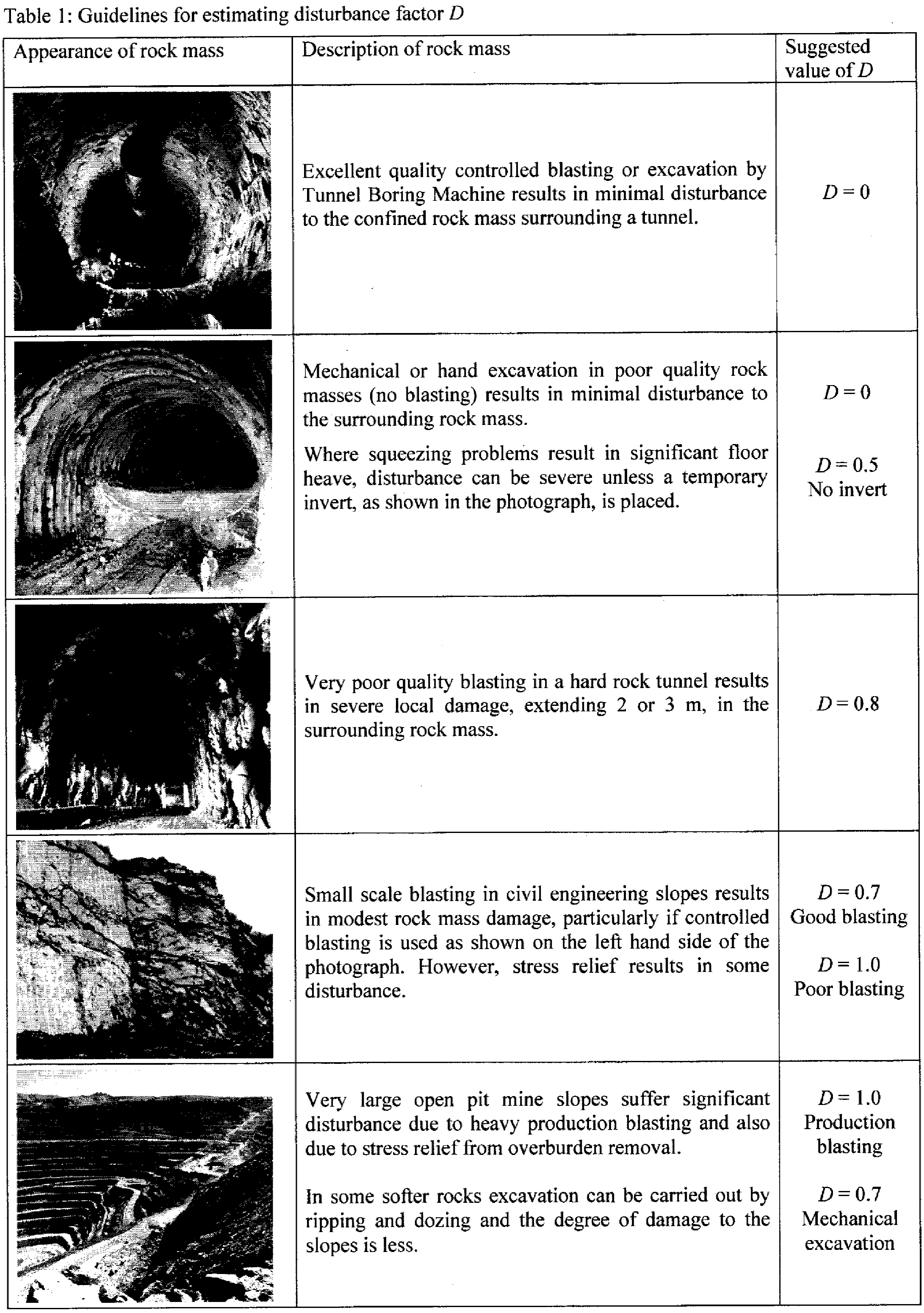

Table 1: Guidelines for estimating disturbance factor *D*

Appearance of rock mass	Description of rock mass	Suggested value of *D*
	Excellent quality controlled blasting or excavation by Tunnel Boring Machine results in minimal disturbance to the confined rock mass surrounding a tunnel.	$D = 0$
	Mechanical or hand excavation in poor quality rock masses (no blasting) results in minimal disturbance to the surrounding rock mass. Where squeezing problems result in significant floor heave, disturbance can be severe unless a temporary invert, as shown in the photograph, is placed.	$D = 0$ $D = 0.5$ No invert
	Very poor quality blasting in a hard rock tunnel results in severe local damage, extending 2 or 3 m, in the surrounding rock mass.	$D = 0.8$
	Small scale blasting in civil engineering slopes results in modest rock mass damage, particularly if controlled blasting is used as shown on the left hand side of the photograph. However, stress relief results in some disturbance.	$D = 0.7$ Good blasting $D = 1.0$ Poor blasting
	Very large open pit mine slopes suffer significant disturbance due to heavy production blasting and also due to stress relief from overburden removal. In some softer rocks excavation can be carried out by ripping and dozing and the degree of damage to the slopes is less.	$D = 1.0$ Production blasting $D = 0.7$ Mechanical excavation

Figure 3.17: Chart for use in Determining the Disturbance due to Stress Relaxation and Blasting, D, for Different Rock Types. Original Image is Table 1 in [6].

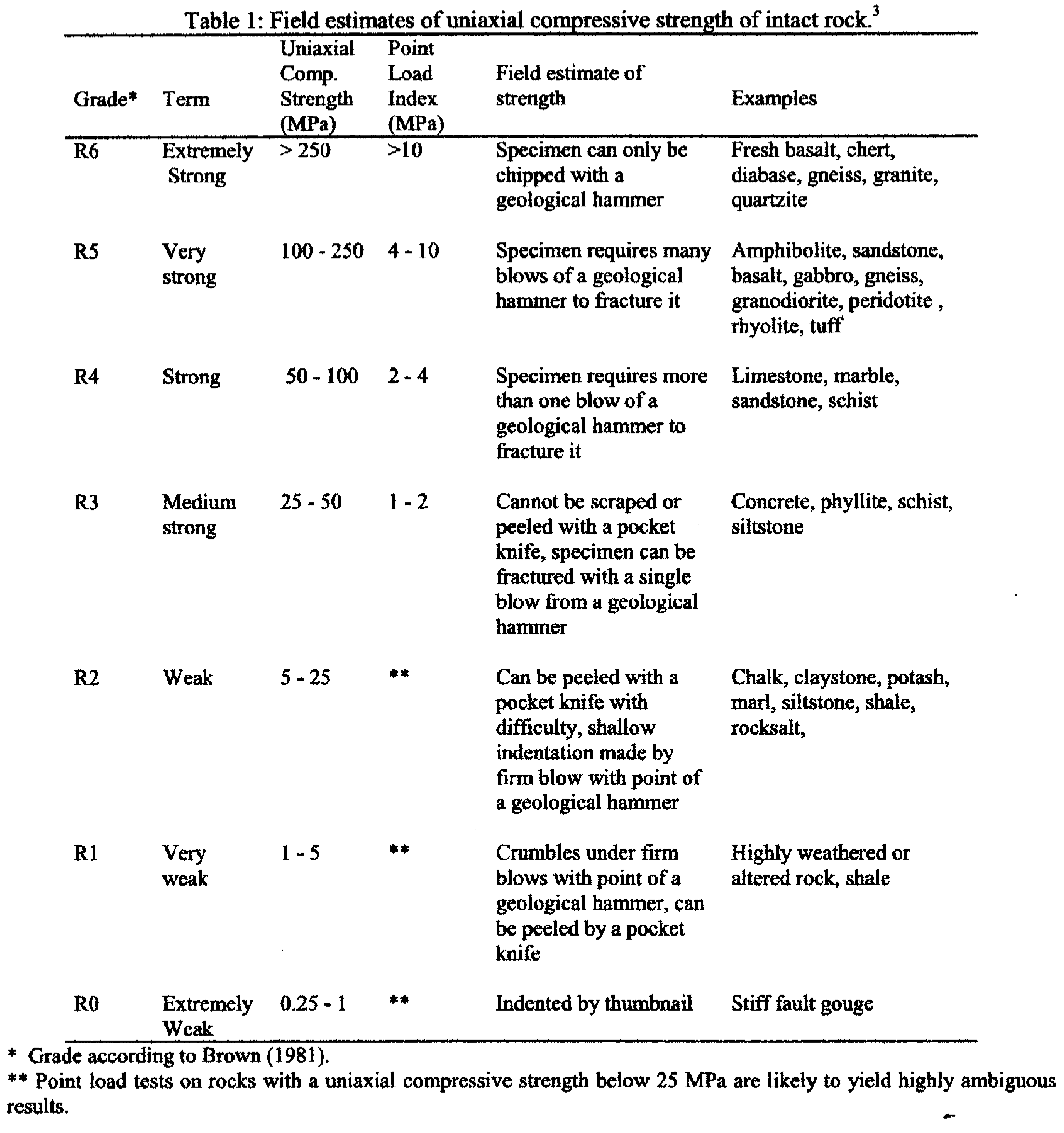

Table 1: Field estimates of uniaxial compressive strength of intact rock.[3]

Grade*	Term	Uniaxial Comp. Strength (MPa)	Point Load Index (MPa)	Field estimate of strength	Examples
R6	Extremely Strong	> 250	>10	Specimen can only be chipped with a geological hammer	Fresh basalt, chert, diabase, gneiss, granite, quartzite
R5	Very strong	100 - 250	4 - 10	Specimen requires many blows of a geological hammer to fracture it	Amphibolite, sandstone, basalt, gabbro, gneiss, granodiorite, peridotite , rhyolite, tuff
R4	Strong	50 - 100	2 - 4	Specimen requires more than one blow of a geological hammer to fracture it	Limestone, marble, sandstone, schist
R3	Medium strong	25 - 50	1 - 2	Cannot be scraped or peeled with a pocket knife, specimen can be fractured with a single blow from a geological hammer	Concrete, phyllite, schist, siltstone
R2	Weak	5 - 25	**	Can be peeled with a pocket knife with difficulty, shallow indentation made by firm blow with point of a geological hammer	Chalk, claystone, potash, marl, siltstone, shale, rocksalt,
R1	Very weak	1 - 5	**	Crumbles under firm blows with point of a geological hammer, can be peeled by a pocket knife	Highly weathered or altered rock, shale
R0	Extremely Weak	0.25 - 1	**	Indented by thumbnail	Stiff fault gouge

* Grade according to Brown (1981).

** Point load tests on rocks with a uniaxial compressive strength below 25 MPa are likely to yield highly ambiguous results.

Figure 3.18: Chart Providing General Guidelines for Determining the Intact Uniaxial Compressive Strength, σ_c, for Different Rock Types. Original Image is Table 1 in [18].

or other testing methods. However, if this information is not available, the chart from [18] reproduced in Figure 3.18 can be used to estimate a value for a given rock type.

More details of the Hoek-Brown failure criterion are presented in the remaining sections of this thesis. The aim of the above section is to provide background information for future discussion.

3.3.1 Model Development

A similar procedure to that used in Section 3.2 for development of a cavity expansion Mohr-Coulomb model can be utilized to define a cavity expansion model using the Hoek-Brown failure criterion. The governing equations for the elastic material response ($p_o < p < p_f$) are the same as previously defined in Section 3.1. Equations governing the behavior of the material beyond yield are presented here. It should be noted that a similar derivation is presented in [23]. However, changes and corrections are made by the author here, particularly in the derivation of the stress equations. The derivation of the deformation equations is the same. Implementation of the model with application towards pressuremeter analysis, however, is original work performed by the author to best of his knowledge.

The Hoek-Brown failure criterion in Equation (3.41) can be written in terms of a cylindrical coordinate system as

$$\sigma_r = \sigma_\theta + \sigma_c \left(m_b \frac{\sigma_\theta}{\sigma_c} + s \right)^b \tag{3.45}$$

where $\sigma_1 = \sigma_r$ and $\sigma_3 = \sigma_\theta$. Recognizing that $r_f/r = 1$ at the initiation of yield, the yield pressure, p_f, can be determined by plugging the definitions in Equations (3.9) and (3.10) for σ_r and σ_θ into Equation (3.45). The resulting equation can be expressed as follows

$$\sigma_{rf} = p_f = \frac{\sigma_c}{2} \left[\frac{m_b}{\sigma_c} (2p_o - p_f) + s \right]^b + p_o \tag{3.46}$$

where an iterative method is required to determine p_f.

To determine the stresses developed beyond yield (i.e. $p > p_f$), the yield criterion defined in Equation (3.45), and the equation of equilibrium defined in Equation (3.4) must both be satisfied. Substituting the yield criterion into the equilibrium equation yields

$$\frac{d\left[\sigma_\theta + \sigma_c \left(m_b \frac{\sigma_\theta}{\sigma_c} + s \right)^b \right]}{dr} + \frac{\sigma_c \left(m_b \frac{\sigma_\theta}{\sigma_c} + s \right)^b}{r} = 0 \tag{3.47}$$

Rearranging gives

$$\frac{d\left[\sigma_\theta + \sigma_c\left(m_b\frac{\sigma_\theta}{\sigma_c} + s\right)^b\right]}{\sigma_c\left(m_b\frac{\sigma_\theta}{\sigma_c} + s\right)^b} + \frac{dr}{r} = 0 \tag{3.48}$$

Through substitution Equation (3.48) can be integrated to form the following solution

$$(b)ln\left(m_b\frac{\sigma_\theta}{\sigma_c} + s\right) - \frac{\left(m_b\frac{\sigma_\theta}{\sigma_c} + s\right)^{(1-b)}}{m_b(b-1)} + ln(r) + C = 0 \tag{3.49}$$

where C is an integration constant. Applying the boundary condition that when $r = r_f$, $\sigma_\theta = \sigma_{\theta f}$ and solving yields

$$(b)ln\left(\frac{A\sigma_{\theta f} + s}{A\sigma_\theta + s}\right) - \frac{1}{m_b(b-1)}\left[(A\sigma_{\theta f} + s)^{(1-b)} - (A\sigma_\theta + s)^{(1-b)}\right] + ln\left(\frac{r_f}{r}\right) = 0 \tag{3.50}$$

for any radius r where $A = m_b/\sigma_c$ and σ_θ is the circumferential stress at radius r. Solving Equation (3.50) for σ_θ requires a numerical method which is discussed in the next subsection, *Model Implementation*. The radial stress, σ_r, is then determined by plugging the solution to σ_θ from Equation (3.50) into the Hoek-Brown failure criterion.

The strains beyond yield can be determined incrementally by applying a flow rule and appropriate boundary conditions. The same non-associative flow rule used in Section 3.2 is utilized here for the Hoek-Brown model. The resultant flow rule in terms of radial and circumferential strain previously written in Equation (3.26) is repeated here for convenience.

$$\epsilon_\theta^p + n\epsilon_r^p = 0 \tag{3.51}$$

where

$$n = \frac{1 + sin\psi}{1 - sin\psi} \tag{3.52}$$

and ψ is the dilation angle as previously stated. The plastic strain components can be written in terms of the total strain and elastic strain components by rearranging the relations in Equations (3.28a) and (3.28b),

$$\epsilon_r^p = \epsilon_r - \epsilon_r^e \tag{3.53a}$$

$$\epsilon_\theta^p = \epsilon_\theta - \epsilon_\theta^e \tag{3.53b}$$

The elastic strain components at the elastic-plastic interface can be determined by setting $r = r_f$ in Equation (3.11), resulting in

$$\epsilon_\theta^e = -\epsilon_r^e = \frac{p_f - p_o}{2G} = B_o \tag{3.54}$$

with the newly defined variable B_o created for convenience. Substituting these values into the flow rule (Equation (3.51)) yields the following differential equation.

$$\frac{u}{r} + n\frac{du}{dr} = B_o(n-1) \tag{3.55}$$

Solving and applying the boundary condition $u_{r=r_f} = r_f B_o$ results in an expression for the displacement in the plastic zone for radius r.

$$u = -rB_o\frac{n-1}{n+1} + r_f B_o\frac{2n}{n+1}\left(\frac{r_f}{r}\right)^{1/n} \tag{3.56}$$

Dividing both sides by r yields the total circumferential strain beyond yield.

$$\epsilon_\theta = -B_o\left[\frac{n-1}{n+1} + \frac{2n}{n+1}\left(\frac{r_f}{r}\right)^{(1/n)+1}\right] \tag{3.57}$$

All the necessary equations to implement the Hoek-Brown cavity expansion model have now been presented. For additional information on this derivation, the author refers the reader to [23].

3.3.2 Model Implementation

The Hoek-Brown model can be implemented in a manner similar to that described for the Mohr-Coulomb model with extra complications due to model non-linearity. However, before discussing the practical details of implementing the model, it is important to establish the input parameters required to define the model.

The material response during the elastic phase of loading is identical to that of the Mohr-Coulomb model and hence governed by the same equations. The two models differ, however, in the determination of the end of elastic behavior defined by the yield pressure, p_f. As before, the elastic zone can be described by two points, $(0, p_o)$ and (ϵ_{cf}, p_f), where p_f is defined in Equation (3.46) and ϵ_{cf} is equal to B_o in Equation (3.54). To satisfy Equation (3.46), knowledge of the reduced Hoek-Brown parameter, m_b, the uniaxial compressive strength, σ_c, constants s and b, and the *in situ* stress p_o is required to determine the yield stress, p_f. Additionally, shear modulus, G, must be known to solve Equation (3.54) for ϵ_{cf}. Further inspection of the parameters reveals that m_b, s and b as defined in Equations (3.42), (3.43) and (3.44) respectively can be determined if the Hoek-Brown parameter, m_i, the Geological Strength Index, GSI, and the damage parameter D are known.

Beyond the yield pressure, radial stress is determined by solving Equation (3.50) for σ_θ and plugging this value into the Hoek-Brown failure criterion of Equation (3.45). Strain is determined by Equation (3.57). In addition to the parameters necessary to define elastic behavior, these equations require knowledge of the dilation angle, ψ, and ratio r_f/r where r is the radius of interest (inner cavity radius, a, in this case) and r_f again defines the radius to the elastic-plastic boundary or yield front. As in the case of the Mohr-Coulomb model, this last parameter can be eliminated by defining a vector for the ratio r_f/a from $1 : x$ where x is a number large enough to achieve the required strain for modeling data.

The necessary parameters to define the entire model then are the *in situ* stress, p_o, shear modulus, G, uniaxial compressive strength of intact rock, σ_c, Geological Strength Index, GSI, the Hoek-Brown parameter, m_i, dilation angle, ψ, and the damage parameter D. Using these parameters as inputs, and the proper equations the model can be set up for data analysis as illustrated in the flow diagram in Figure 3.19. Details of the implementation that warrant further discussion include the process for determining the yield pressure and the incremental determination of the stress-strain values beyond yield.

The yield pressure, p_f, can be found on both sides of Equation (3.46), therefore requiring an iterative procedure to solve for p_f. One method that can be applied is to loop through a number of values (or guesses) for p_f on the right-hand side of the equation and check the solution of the equation against the variable input. The looping of variables ends when an acceptable tolerance (or difference between the guess and output) is reached. This method was employed here with a tolerance of 0.005. As this method lends itself to the possibility of multiple solutions, it is important to apply natural bounds to the input value of the parameter. It is impossible for the yield pressure to be below the *in situ* stress of the material and thus p_o can be used as a lower bound. The upper bound can be found through inspection of Equation (3.46). If the evaluated expression inside the brackets

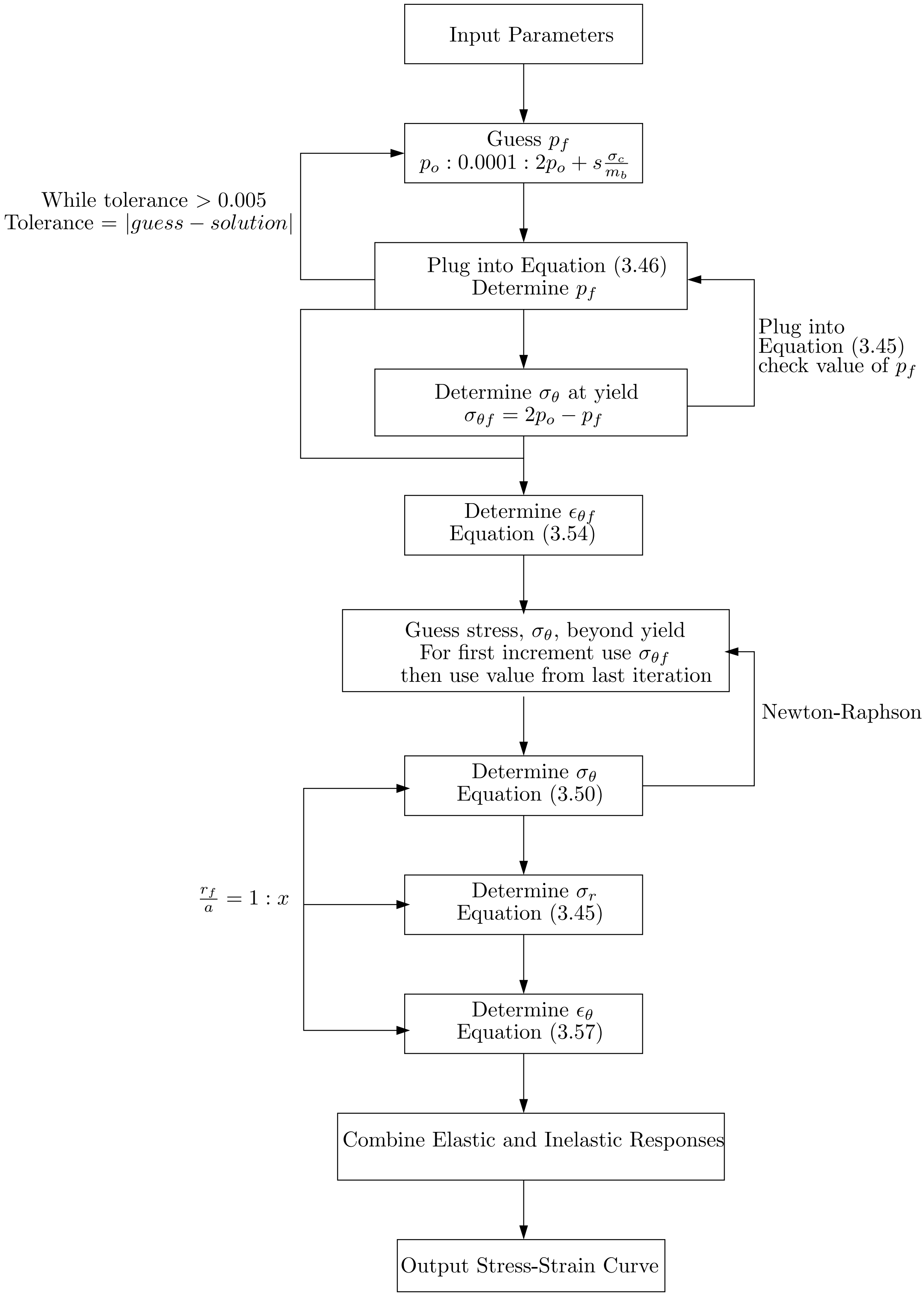

Figure 3.19: Flow Diagram for Implementation of the Hoek-Brown Model

$(m_b/\sigma_c(2p_o - p_f) + s)$ is negative, the solution to the equation will become imaginary. Thus the point at which this expression equals zero can be used as an upper bound for the yield pressure. This occurs when $p_f = 2p_o + s\sigma_c/m_b$. Once an acceptable solution for p_f is determined a further check for accuracy can be applied. Because the yield stress marks the end of elastic behavior, the elastic relations still apply. Therefore the yield criterion and the governing elastic equations must be satisfied at the point of yield. Using the elastic equations, the circumferential stress at failure, $\sigma_{\theta f}$, should be equal to $p_o - (\sigma_{rf} - p_o)$ or $2p_o - p_f$ with $\sigma_{rf} = p_f$. This value for $\sigma_{\theta f}$ can be plugged into the Hoek-Brown failure criterion; the result should be equal to p_f previously determined.

Once the yield stresses σ_{rf} and $\sigma_{\theta f}$ have been reached, inelastic stress and strain values are determined by Equations (3.50) and (3.57) incrementally. To solve Equation (3.50) for each increment an iterative method is required, a result of the non-linearity of the failure criterion. The iterative method adopted here is the well known Newton-Raphson method which can be written in common form as follows

$$\chi_{j+1} = \chi_j - \frac{f(\chi_j)}{f'(\chi_j)} \tag{3.58}$$

where χ_j is the current guess for the value of variable χ, $f(\chi_j)$ is the function evaluated at χ for the current guess, $f'(\chi_j)$ is the derivative (or slope) of the function and χ_{j+1} is the next guess for χ. The Newton Raphson method is designed to find roots of a function for the case when $f(\chi) = 0$. Essentially the method works by applying a tangent line at the point where the function is evaluated (based on the guess) and a new guess is formed by taking the value associated with the $\chi - intercept$ of the tangent line as illustrated in Figure 3.20. The process is then repeated. After a few iterations a local maxima or minima is found as a solution. Because this equation is solved for a number of small increments, the value determined in the previous increment is always used as a first guess for the next increment, knowing this value should be close to the correct answer. Once σ_θ is determined at each increment, σ_r is calculated by plugging σ_θ into the Hoek-Brown failure criterion.

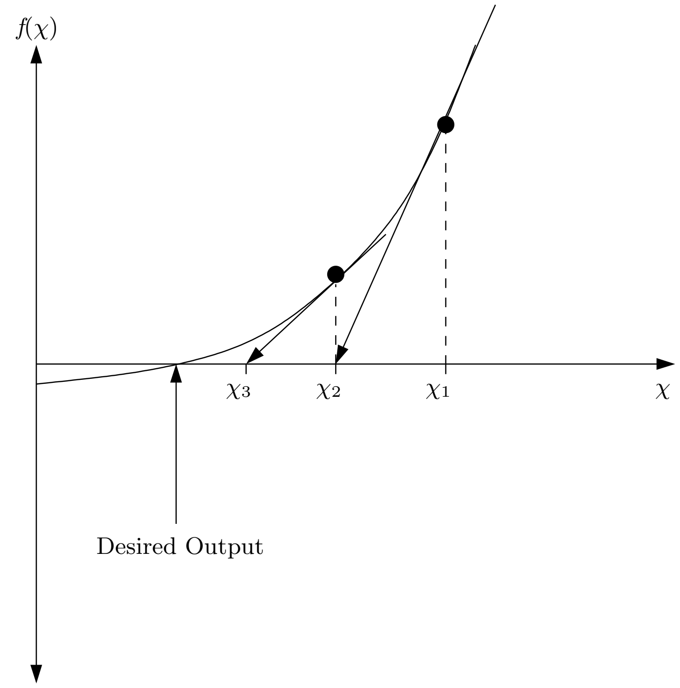

Figure 3.20: Example of Newton-Raphson Method

3.3.3 Validation of Model Implementation

The model implementation outlined in Figure 3.19 was coded by the author using MATLAB. As stated previously, it is important to validate the implementation before analyzing data. However, to the author's knowledge a previous implementation of the model does not exist for comparison. Thus, the validity of the model itself must be proven which will in turn validate the model implementation.

Two methods are adopted here to confirm the model machinery is functioning properly. The first method utilizes external data from one of the five data sets analyzed for this thesis in which the model input parameters had been determined by other methods. If these material parameters can be used as inputs to the pressuremeter model and the resultant stress-strain curves are in good agreement with the pressuremeter data, then it can be said the model is valid. The second method utilizes the Mohr-Coulomb model. For a given set of Hoek-Brown model parameters, an equivalent cohesion and friction angle can be determined

Table 3.2: Hoek-Brown Parameters Determined by External Methods in Tuff

Uniaxial Compressive Strength, σ_c	$70 - 105$ MPa
Geological Strength Index, GSI	$40 - 65$
Hoek-Brown Parameter, m_i	$8 - 18$
Damage Parameter, D,	0

(more details on this are provided in the next chapter). Using the equivalent $c - \phi$ values as inputs into the Mohr-Coulomb model should produce a stress-strain curve similar to the Hoek-Brown stress-strain curve (at least within the same range) further validating the Hoek-Brown pressuremeter model.

The data set used for model validation consists of pressuremeter tests in meta-welded tuff. Hoek-Brown parameters were determined based on logging of core and laboratory testing with results and details reported in [1]. A summary of the parameter ranges determined in [1] is given in Table 3.2. The attentive reader would note that the uniaxial strength range of the meta-welded tuff adheres to the definition of *strong* rock as defined in Figure 1.4. However, because the Hoek-Brown model is valid for both weak and strong rock [6] [18], validating the Hoek-Brown pressuremeter model against strong rock data will inherently validate the model against weak rock as well.

In all, 22 pressuremeter tests were performed in the meta-welded tuff and all were tested against the parameter ranges provided by the lab and field data. The Hoek-Brown pressuremeter model achieved a good fit to all 22 tests using the parameter ranges given. Shear modulus values were obtained from the unload-reload loops of each test. The *in situ* stress was determined based on the overburden stress and previously accepted analysis performed on the data set. The dilation angle was adjusted to provide the best fit to the data; determined to typically range from 9 - 11 degrees with a mean of 9.8 degrees. The small range of values used for the dilation angle indicates consistency in the data and rock formation. It also provides confidence that a good fit was not achieved via radical or erratic changes in the parameter (which would lead to uncertainty in the model validation).

Additionally, good quality rock is listed as having a dilation angle around 11.5 degrees in [13]. As this rock formation was fairly intact and could be considered to be fairly good quality, values around 10 degrees are agreeable. A sample of two tests is provided here to illustrate model fit to the tuff data set.

The two tests chosen for display here are tests I-90-04 and I-90-19 at depths of 25.9 meters and 18.1 meters respectively. Both tests require inputs towards the lower end of the spectrum for the defined parameter range indicating the tests are performed in the weaker zones of the tuff than is typical of the formation. Tests were performed in tuff with strength values towards the higher end of the spectrum as well and were also validated against the model.

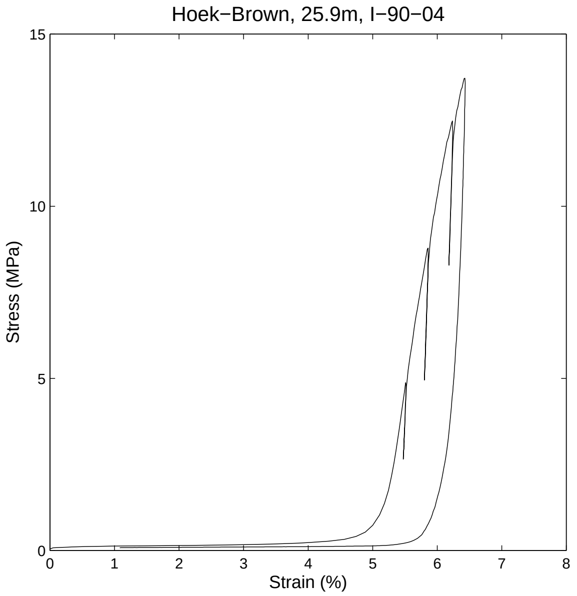

Figure 3.21: Typical Pressuremeter test in Meta-Welded Tuff. Test I-90-04 at 25.9m depth.

Test I-90-04 presented in Figure 3.21 is an example of a typical test performed in the meta-welded tuff. The recorded data requires two shifts be made before analyzing the data. First, the strain must be adjusted to reflect an appropriate point for zero strain. Apparent strain is recorded in which the pressuremeter expands before reaching the borehole wall due to a slightly oversized test pocket. This apparent strain must be removed via a strain shift of the data. Once the pressuremeter membrane has expanded and makes contact with the borehole wall, material response is recorded as a stress-strain curve.

Second, because we are performing an effective stress analysis, the water pressure present must be removed requiring a stress shift in the data. After making these changes, test I-90-04 appears as presented in Figure 3.22. Use of both these shifts are discussed in detail in the next chapter. Using the input parameters displayed in Table 3.2, the Hoek-Brown model fit to the data is presented in Figure 3.23. The discrepancy near the beginning of the curve can be explained by disturbance due to drilling action and stress relaxation which the model does not consider. Beyond that, it is clear that the model performs well and is capable of reproducing an idealized version of the recorded data. The model curve also sheds light on the material behavior had the pressure been increased further during the test allowing for greater strain of the rock mass to be achieved.

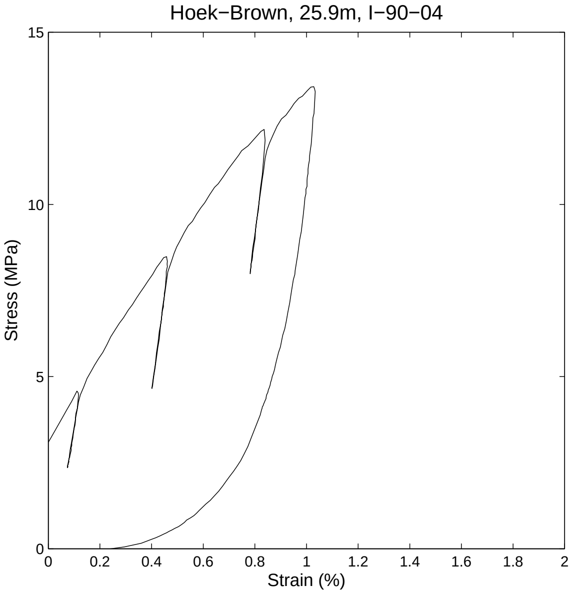

Figure 3.22: Test I-90-04 at 25.9m depth in Meta-Welded Tuff after Stress and Strain Shift Performed.

Analysis of a more atypical test, test I-90-19, in which the tuff is the weakest encountered in the data set is presented in Figure 3.24. Typically on this site, tests are terminated due

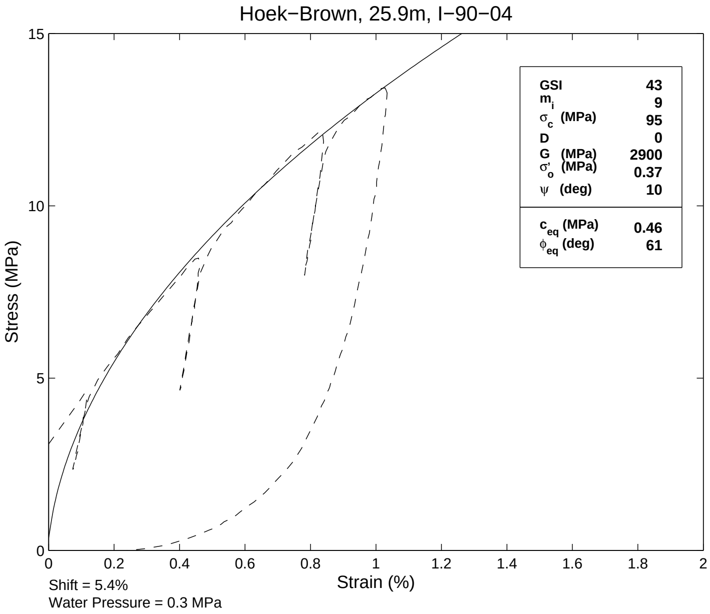

Figure 3.23: Test I-90-04 at 25.9m depth in Meta-Welded Tuff with Model Curve (solid line) Fitted to Data (dashed line).

to pressure limitations of the instrument (to avoid blowing the membrane and causing serious damage), subsequently leading to minimal rock strain (1 - 2%) a reflection of the strong nature of the tuff. However, strain near 3% is achieved in test I-90-04 allowing for comparison of the data to the model at higher strains (for this rock type). Inspection of Figure 3.24 reveal the model, again, performs well using parameters within the range determined by lab and field testing. This further confirms the model validity for analyzing pressuremeter data.

As mentioned previously, another check against the performance of the Hoek-Brown pressuremeter model is to compare the output of the Hoek-Brown model to the Mohr-Coulomb model using the equivalent $c - \phi$ values determined by the Hoek-Brown model. Of course there are inherent differences between the two models, notably that the Mohr-Coulomb model has a linear yield criterion while the Hoek-Brown failure criterion is non-linear. Thus even using equivalent Mohr-Coulomb parameters, the Hoek-Brown model will naturally give a different result. Also, there are multiple approaches to determining the

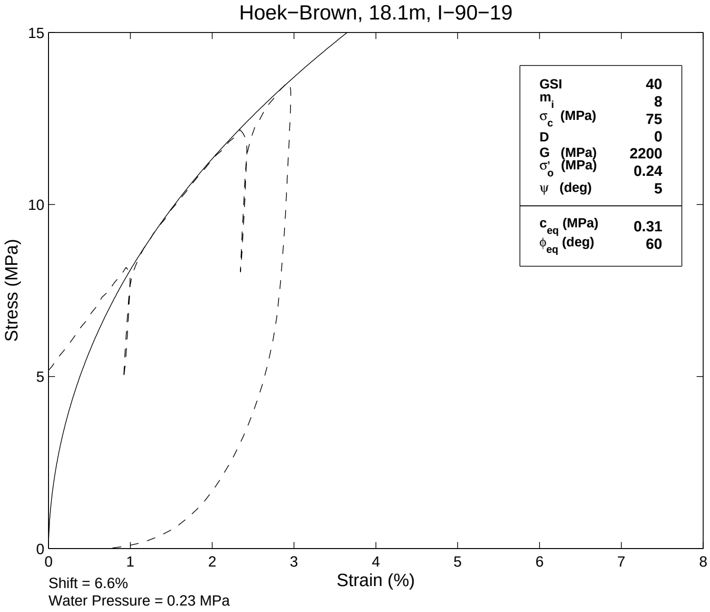

Figure 3.24: Test I-90-19 at 18.1m depth in Meta-Welded Tuff with Model Curve (solid line) Fitted to Data (dashed line).

equivalent Mohr-Coulomb parameters using the Hoek-Brown model, which can also lead to different results (more on this in the next chapter). However, regardless of these differences, it should be possible to create two similar curves using the Hoek-Brown model and the equivalent $c-\phi$ values as inputs into the Mohr-Coulomb model. An example comparing the two models for three different strength levels is displayed in Figure 3.25. The dashed lines represent the Hoek-Brown curve and the solid lines represent the equivalent Mohr-Coulomb curve. The input numbers themselves are insignificant, but it should be noted that common parameters between the two models are maintained for each comparison (i.e. the same shear modulus, *in situ* stress etc., is used in a given comparison). As expected the curves lie in the same range, but the overall shape differs. In particular, the Hoek-Brown model tends towards a strength limit more quickly at higher strains, a result due to the differences in the yield criterions. Further comparison of these models is reserved for later, however, the fact that the two models produce similar results further validates that the Hoek-Brown model is properly implemented and may be suitable for pressuremeter analysis.

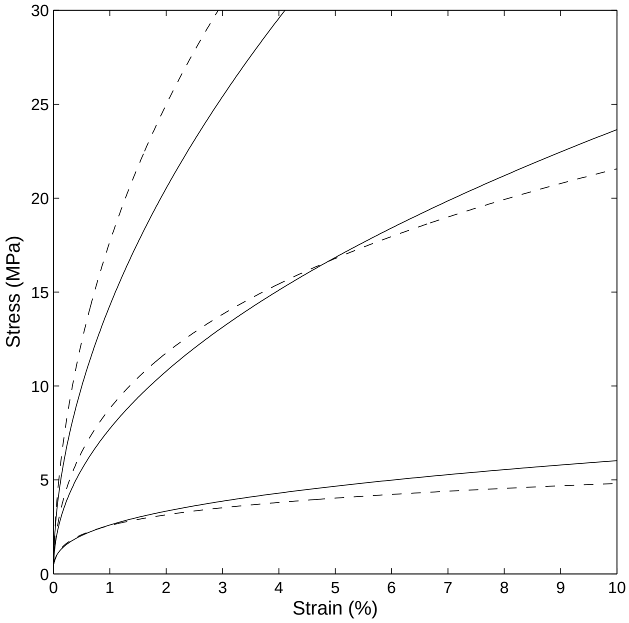

Figure 3.25: Comparison of Mohr-Coulomb Model (Solid Line) to Hoek-Brown model (Dashed Line) Using Equivalent Effective Cohesion and Effective Friction Angle as Determined by the Hoek-Brown Parameters.

3.3.4 Parametric Analysis

As previously emphasized, it is important to understand the affect of the model input parameters on the resulting stress-strain curve before using the model for data analysis. By performing a parametric analysis the inputs that most heavily impact the model response can be identified. The results of such an analysis are presented in Figures 3.26 through 3.32. Each figure is produced by changing one input parameter while all other inputs remain constant. The default parameters (i.e. those held constant as others are changed) are listed in Table 3.3 and represent near average values for the data set analyzed. Drained analysis is assumed and the figures are all plotted to the same scale for comparative purposes. The remainder of this section is dedicated towards discussion of the parametric effects on model output.

From inspection of Figures 3.26 through 3.32, it can be established that the Geological

Table 3.3: Default Input Values for Parametric Analysis - Hoek-Brown

Shear modulus, G	$2,200$ MPa
In Situ stress, p_o	0.4 MPa
Geological Strength Index, GSI	33
Uniaxial Compressive Strength, σ_c	14 MPa
Hoek-Brown Parameter, m_i,	10
Dilation angle, ψ	8.5^o
Damage Parameter, D	0

Strength Index, GSI, and the uniaxial compressive strength of intact rock, σ_c, have the greatest impact on the stress-strain curve produced by the Hoek-Brown model. The choice of GSI is based on a rating (from $0 - 100$) of the rock condition in terms of the amount of fracturing (or joints) and conditions of the joint interfaces. As joint strength will largely dictate the material response to loading, it is logical that this parameter would dominate the model response. The effect of GSI increases as the parameter value is increased towards a value of 100, representing intact rock. A similar trend is found in observing the effect of σ_c with a less significant overall impact. However, using uniaxial compressive strength values for very strong rock ($\sigma_c > 250$ MPa) may result in a stress-strain curve similar to that produced for $GSI = 100$. Thus the importance of selection of these two parameters is high and must be considered carefully.

The choice of dilation angle, ψ, and the Hoek-Brown constant, m_i, can also have a significant influence on the model output. The Hoek-Brown constant represents a measure of joint interlocking and frictional resistance with the typical range of values illustrated in Figure 3.30. The effect of a change in input on the model response diminishes quickly as higher values of m_i are reached, essentially capping the resistance to load gained from the joint interlocking. At lower values of m_i, a small increase in interlocking can have a more significant impact. The choice of dilation angle directly impacts the deformation response of the model. The effect of the parameter choice increases slightly as the parameter value

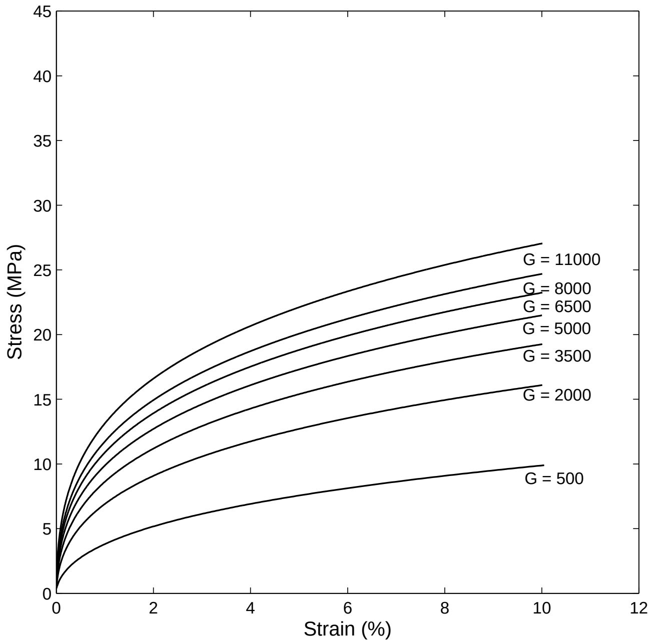

Figure 3.26: Effect of Changing the Shear Modulus, G, for Hoek-Brown Model

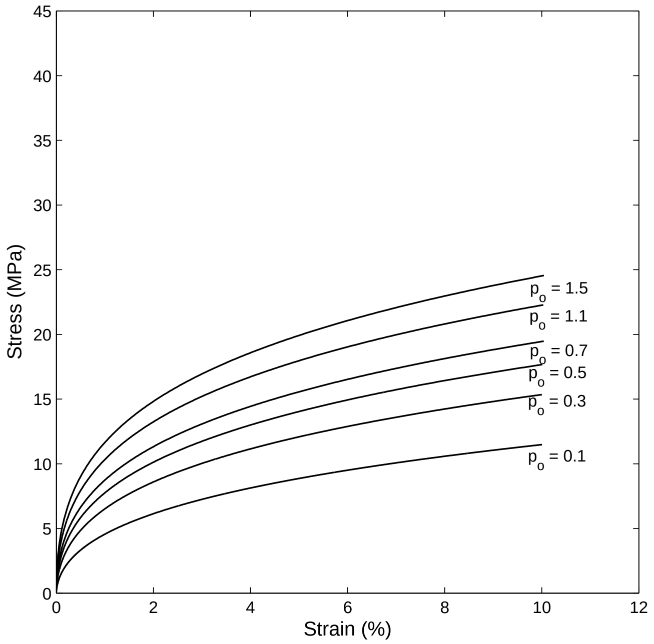

Figure 3.27: Effect of Changing the *In Situ* Stress, p_o, for Hoek-Brown Model

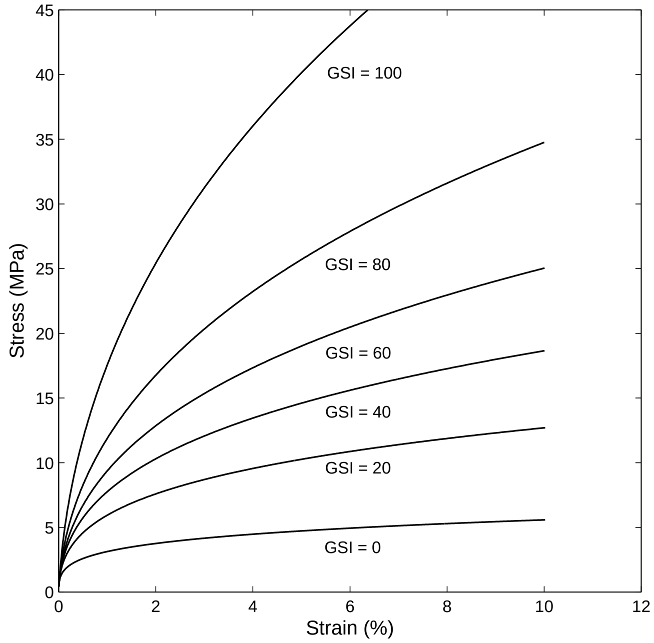

Figure 3.28: Effect of Changing the Geological Strength Index, GSI, for Hoek-Brown Model

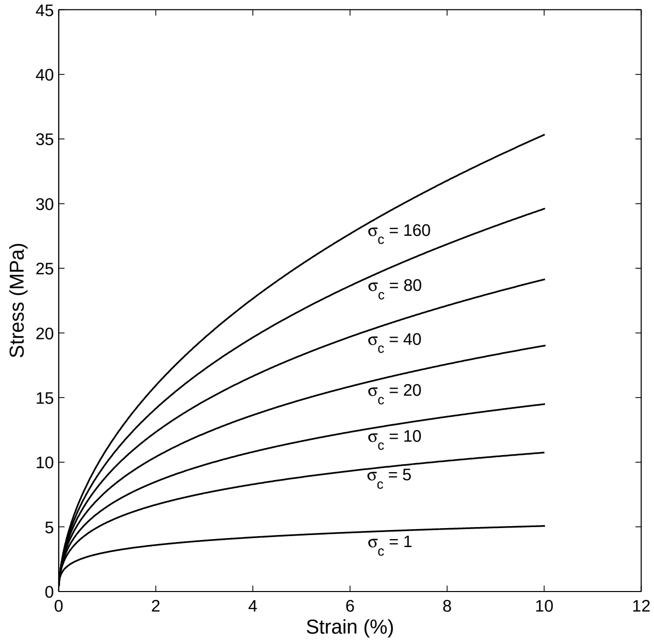

Figure 3.29: Effect of Changing the Uniaxial Compressive Strength, σ_c, for Hoek-Brown Model

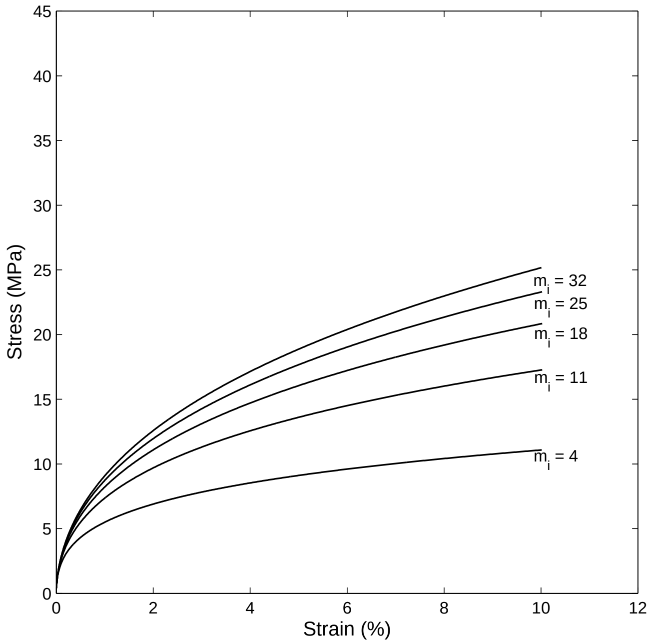

Figure 3.30: Effect of Changing the Hoek-Brown Parameter, m_i, for Hoek-Brown Model

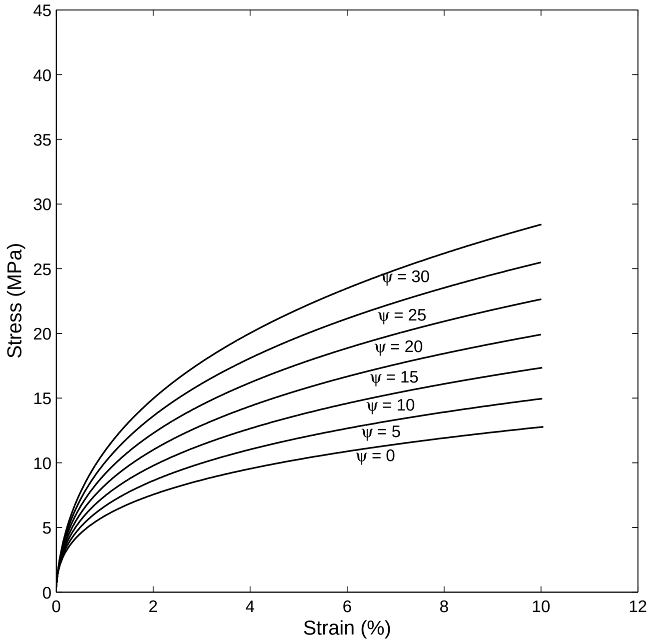

Figure 3.31: Effect of Changing the Dilation Angle, ψ, for Hoek-Brown Model

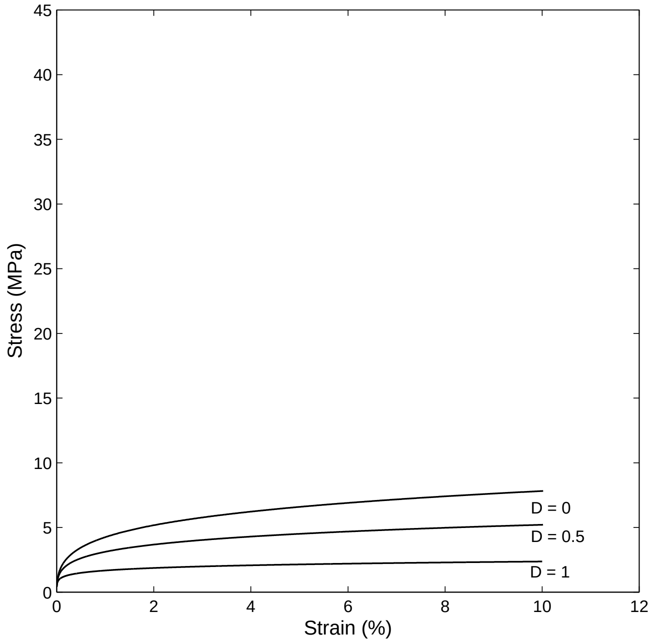

Figure 3.32: Effect of Changing the Damage Parameter, D, for Hoek Brown Model

increases, indicating a strain-hardening effect. Although the overall impact of the choice of dilation angle is similar to that of the Hoek-Brown constant, it can be stated that at lower ranges, the choice of m_i is more important while the opposite is true at higher values.

Two parameters that also represent a relatively large effect on model response are the shear modulus, G, and *in situ* stress, p_o. The trends and effects of both these parameters is similar. The influence of both parameters decays as the parameter value is increased. As is stated previously, although the impact of these parameters is important, the shear modulus can be determined using the pressuremeter test data and a range for the *in situ* stress is generally known or can be established based on the pressuremeter data and other sources. A large error in either choice, however, could lead to erroneous results.

The choice of the damage parameter, D, has the smallest impact by a large margin. As is expected, a choice which represents no damage (0) is reflected in the model output as a larger resistance to loading. As this parameter is largely aimed toward tunnel blasting and not drilling disturbance for a pressuremeter test, it's importance to this model is less significant. However, it should not be ignored in cases where obvious drilling disturbance is present.

It should be noted that these trends discussed are based on the default parameters chosen and use of a different set of default parameters could affect the results. However, these values are representative of this study and qualitatively represent the overall model response relating to changes in the input parameters. Most importantly, the input parameters that impact the model output the greatest are established; a significant consideration in analyzing pressuremeter data.

3.4 Multiscale Damage Model

The two models established thus far in this chapter are developed directly for pressuremeter analysis and are utilized in analyzing pressuremeter data in rock (presented in Chapter 4). While the two models, Mohr-Coulomb and Hoek-Brown, are the main focus of this thesis, other constitutive rock models were explored for development into a pressuremeter analysis framework. One of particular interest and perhaps greater complexity is that established by Kondo, Zhu, Shao and Pensee in [8] (Additionally [9], [15], and [14]).

The Hoek-Brown and Mohr-Coulomb models as presented in this thesis are aimed at capturing rock mass behavior as a continuum accounting for fracture, crack formation and propagation through empirical equations and induced dilation. Both models could, however, be adopted into a finite element mesh allowing for crack propagation at predetermined locations at a macroscopic scale (see Haberfield [10]). The model developed by Kondo *et al* (which from here on will be referred to as the Kondo model for convenience) considers another approach by relating damage induced by microcrack development to the response of the macroscopic rock mass; hence the model is multiscale.

The multiscale damage model attempts to account for the many effects microcracks can have on the rock mass structure including: non-linear stress-strain relations, deterioration of elastic properties, induced anisotropy, irreversible deformation, volumetric dilatancy, hysteresis, and the effect of microcrack closure [8]. These effects are accounted for by considering microcrack density (number of microcracks per unit volume), while individually determining the size of open cracks and frictional resistance to sliding along closed crack faces. This is achieved using an Eshelby based solution in a standard thermodynamics framework. Knowledge of micromechanics, damage modeling, Eshelby homogenization schemes, energy-based material modeling and tensor mathematics is required to fully appreciate the intricacies of the development of the Kondo model. However, descriptions of these topics is beyond the scope of this thesis and although many sources are available, information relevant to the Kondo model can be found in [3], [21], [8], [9], [15], and [14]. Highlights of the model framework developed in these sources will be presented here.

Four major components necessary to establishing a thermodynamics material model are a free energy function, state equations, a yield condition and evolution laws for internal variables. The Kondo model was developed within this framework. The development of each of these components will be discussed in successive order.

3.4.1 Free Energy

An expression describing the free energy (in this case the macroscopic free energy) is accomplished for the Kondo model by considering a composite material where zones are weakened by microcrack inclusions for which the Eshelby solution for penny-shaped cracks is assumed. Dimension and orientation of the penny-shaped cracks is described by radius, a, half opening, c, and unit normal vector $\underline{n}$ as illustrated in Figure 3.33. Considering a representative

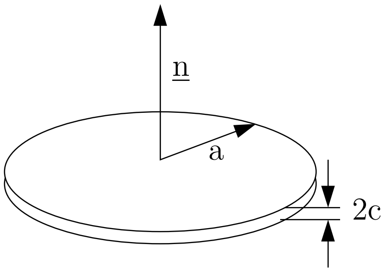

Figure 3.33: Penny-Shaped Crack Schematic

elementary volume of the composite material with uniform macroscopic stress ($\mathbf{\Sigma}$) applied to the boundary, the macroscopic strain can be written as

$$\mathbf{E} = \mathbf{E}^s + \mathbf{E}^c \tag{3.59}$$

where $\mathbf{E}^s$ and $\mathbf{E}^c$ are both second order tensors representing strain contributions from the solid (uncracked) matrix and microcracks respectively. The microcrack contribution can be defined in terms of kinematic parameters as follows

$$\mathbf{E}^c = \beta(\underline{n} \otimes \underline{n}) + \underline{\gamma} \otimes^s \underline{n} \tag{3.60}$$

where β tracks the open/closure state of a crack and $\underline{\gamma}$ characterizes sliding along the crack interface. This expression can be related to the local stress at the crack interface, $\boldsymbol{\sigma}^c$, ($\boldsymbol{\sigma}^c = 0$ for the case of open cracks) by again decomposing the problem into two parts with defined macroscopic strains at the boundary of which the details can be found in [8]. The resulting solution is

$$\beta(\underline{n} \otimes \underline{n}) + \underline{\gamma} \otimes \underline{n} = \phi^c \mathbb{A}^c : (\mathbf{E} - \mathbb{S}^s : \boldsymbol{\sigma}^c) = \mathbf{E}^{pl} \tag{3.61}$$

where ϕ^c is the volume fraction of cracks, $\mathbb{A}^c$ is the fourth order concentration tensor associated with a family of microcracks (this can be defined in terms of the Eshelby tensor for penny-shaped cracks), and $\mathbb{S}^s = (\mathbb{C}^s)^{-1}$ with $\mathbb{C}^s$ defined as the fourth order elasticity tensor for the solid matrix (as typically defined for a linear elastic isotropic continuum). Adding the contribution of the solid matrix, the following stress-strain relationship can be established

$$\boldsymbol{\sigma}^c = \boldsymbol{\Sigma} - \mathbb{C}^{pl} : \mathbf{E}^{pl} \tag{3.62}$$

with

$$\mathbb{C}^{pl} = \left[\phi^c \mathbb{A}^c : (\mathbb{I} - \phi^c \mathbb{A}^c)^{-1} : \mathbb{S}^s\right]^{-1} \tag{3.63}$$

where $\mathbb{I}$ is the fourth order identity tensor. Finally, using Equation (3.62) and Equation (3.60) the free energy relationship can be established for a cracked material.

$$W = \frac{1}{2}(\mathbf{E} - \mathbf{E}^{pl}) : \mathbb{C}^s : (\mathbf{E} - \mathbf{E}^{pl}) + \frac{1}{2}\mathbf{E}^{pl} : \mathbb{C}^{pl} : \mathbf{E}^{pl} \tag{3.64}$$

Utilizing the free energy equation above, thermodynamic forces associated with internal variables $\mathbf{E}^{pl}$, β, and $\underline{\gamma}$ can be established as follows

$$\mathbf{F}^{pl} = -\frac{\partial W}{\partial \mathbf{E}^{pl}} = \boldsymbol{\Sigma} - \mathbb{C}^{pl} : \mathbf{E}^{pl} = \boldsymbol{\sigma}^c \tag{3.65}$$

$$F^{\beta} = -\frac{\partial W}{\partial \beta} = \boldsymbol{\sigma}^c : (\underline{n} \otimes \underline{n}) \tag{3.66}$$

$$\underline{F}^{\gamma} = -\frac{\partial W}{\partial \underline{\gamma}} = \boldsymbol{\sigma}^c \cdot \underline{n} \cdot (\mathbf{1} - \underline{n} \otimes \underline{n}) \tag{3.67}$$

where $\mathbf{1}$ is the second order identity tensor. Considering a family of microcracks and using the thermodynamic forces defined above, Kondo *et al* developed the following expression for the Gibb's free energy

$$\begin{aligned}\Psi = \tfrac{1}{2}\boldsymbol{\Sigma} : \mathbb{S}^s : \boldsymbol{\Sigma} + \tfrac{1}{2}\boldsymbol{\Sigma} : \sum_{r=1}^{N_o} w^r d^r \left(\frac{1}{H_0}\mathbb{E}^{2,r} + \frac{1}{2H_1}\mathbb{E}^{4,r}\right) : \boldsymbol{\Sigma} \\ + \boldsymbol{\Sigma} : \sum_{r=1}^{N_c} w^r \left[\beta^r (\underline{n}^r \otimes \underline{n}^r) + \underline{\gamma}^r \otimes^s \underline{n}^r\right] - \frac{1}{2}\sum_{r=1}^{N_c} \frac{w^r}{d^r}\left[H_0(\beta^r)^2 + H_1 \underline{\gamma}^r \cdot \underline{\gamma}^r\right]\end{aligned} \tag{3.68}$$

where superscript r represents the r^{th} microcrack family, d is an internal damage variable, w is a weighting factor for each microcrack family, N_o represents the number of open microcracks, and N_c is the number of closed microcracks. Additionally

$$\mathbb{E}^{2,r} = \underline{n}^r \otimes \underline{n}^r \otimes \underline{n}^r \otimes \underline{n}^r \tag{3.69a}$$

$$\mathbb{E}^{4,r} = \frac{1}{2}\left[\underline{n}^r \otimes \underline{n}^r \overline{\otimes} (\mathbf{1} - \underline{n}^r \otimes \underline{n}^r) + (\mathbf{1} - \underline{n}^r \otimes \underline{n}^r) \overline{\otimes} \underline{n}^r \otimes \underline{n}^r\right] \tag{3.69b}$$

and

$$H_0 = \frac{3E^s}{16\left[1 - (\nu^s)^2\right]} \tag{3.70a}$$

$$H_1 = H_0\left(1 - \frac{\nu^s}{2}\right) \tag{3.70b}$$

where E^s is the Young's Modulus and ν^s is Poisson's ratio of the solid material matrix.

3.4.2 State Parameters

With the energy functions fully defined, the state parameters can be determined in the same manner as the thermodynamic forces in Equations (3.65) through (3.67). The two state laws needed for the Kondo model include a macroscopic stress-strain relationship (which is always necessary) as well as a thermodynamic force related to the internal damage parameter d, defined by $\mathbf{E} = \partial\Psi/\partial\boldsymbol{\Sigma}$ and $F^{d^r} = \partial\Psi/\partial d^r$ respectively. The resulting equations can be written as follows

$$\mathbf{E} = \mathbb{S}^s : \boldsymbol{\Sigma} + \sum_{r=1}^{N_o} w^r d^r \left(\frac{1}{H_0}\mathbb{E}^{2,r} + \frac{1}{2H_1}\mathbb{E}^{4,r}\right) : \boldsymbol{\Sigma} + \sum_{r=1}^{N_c} w^r \left[\beta^r(\underline{n}^r \otimes \underline{n}^r) + \underline{\gamma}^r \otimes^s \underline{n}^r\right] \tag{3.71}$$

where for open microcracks

$$F^{d^r} = \frac{1}{2}\mathbf{\Sigma} : \left(\frac{1}{H_0}\mathbb{E}^{2,r} + \frac{1}{2H_1}\mathbb{E}^{4,r} \right) : \mathbf{\Sigma} \tag{3.72}$$

and

$$F^{d^r} = \frac{1}{2(d^r)^2}\left[H_0(\beta^r)^2 + H_1\underline{\gamma}^r \cdot \underline{\gamma}^r \right] \tag{3.73}$$

for closed microcracks.

3.4.3 Yield Criterion

In order to account for both damage and friction (and the coupling between them) encountered on the closed microcrack faces, two yield criterion are developed for the Kondo model. The yield criterion concerning frictional resistance adopts a Coulomb criterion which can be expressed in terms of the thermodynamic force associated with internal variables β and $\underline{\gamma}$

$$g(\boldsymbol{\sigma}^c) = |\underline{F}^{\gamma}| + \mu_c F^{\beta} = 0 \tag{3.74}$$

where μ_c is the coefficient of friction for a microcrack face. The yield criterion concerning damage resulting from microcrack growth is based on a generic energy release rate and is defined as follows

$$f(F^d, d) = F^d - R(d) = 0 \tag{3.75}$$

where

$$R(d) = c_o + c_1 d \tag{3.76}$$

and c_o and c_1 are energy coefficients that represent a damage threshold and the kinetics of damage evolution respectively.

3.4.4 Evolution Laws

The evolution laws define the rate of change for the internal variables through an associative or non-associative flow rule. The internal variables identified for the Kondo model are plastic strain, $\mathbf{E}^{pl}$, the damage variable, d, the opening/closing mechanism for microcracks, β, and the frictional sliding parameter, $\underline{\gamma}$. Adopting a normality rule, Kondo *et al* defined the following evolution laws

$$\dot{d} = \dot{\lambda}^d \frac{\partial f(F^d, d)}{\partial F^d} = \dot{\lambda}^d \tag{3.77}$$

$$\dot{\underline{\gamma}} = \dot{\lambda}^\gamma \frac{\partial g}{\partial F^\gamma} = \dot{\lambda}^\gamma \underline{v} \tag{3.78}$$

$$\dot{\beta} = \mu_c \dot{\lambda}^\gamma \tag{3.79}$$

$$\dot{\mathbf{E}^{pl}} = \dot{\beta}(\underline{n} \otimes \underline{n}) + \dot{\underline{\gamma}} \otimes^s \underline{n} = \dot{\lambda}^\gamma \left(\underline{v} \otimes^s \underline{n} + \mu_c \underline{n} \otimes \underline{n} \right) \tag{3.80}$$

where $\dot{\lambda}^d$ and $\dot{\lambda}^\gamma$ are multipliers that can be determined by simultaneously satisfying the condition where $\dot{f} = 0$ and $\dot{g} = 0$. The vector $\underline{v}$ represents a unit vector in the direction of sliding defined by $\underline{v} = \underline{F}^\gamma / |\underline{F}^\gamma|$.

3.4.5 Discussion

All the information presented thus far in Section 3.4 can be found in greater detail in the sources previously mentioned, however, further discussion of the model in the framework of this thesis is warranted. Implementation of the Kondo model in general requires the determination of the tangent operator, which relates the rate form of macroscopic stress to the rate form of macroscopic strain. A numerical scheme (such as the Newton-Raphson) is also required for implementation due to the model non-linearity. Both these pieces of information are described in [8]. In order to use this model for pressuremeter analysis, however, further modifications would be necessary.

Although tensors can be considered dimensionless, they typically need to be interpreted in matrix or vector form in order to implement them into a computer code, which requires choice of a coordinate system. Often a Cartesian coordinate system is adopted and indeed this is the system utilized by Kondo *et al* in testing their model against data collected. Thus it is best to first test the implementation of the model in this system against a solution produced by Kondo *et al*, as is illustrated in Figure 3.34. Figure 3.34 represents a material subjected to a simple shear monotonic loading path with one crack family in the $\underline{e}_3$ direction (i.e. $\underline{n} = \{0, 0, 1\}$). An initial compressive stress $\mathbf{\Sigma}_{33} = 10$ MPa is applied to ensure that cracks remain closed during the loading process. The model input parameters for Figure

Table 3.4: Input Parameters for Figure 3.34

Young's Modulus, E^s	$33,330$ MPa
Poisson's Ratio, ν^s	0.23
Energy Coefficient, c_o	$2.5X10^{-3}\ Jm^2$
Energy Coefficient, c_1	$0.08\ Jm^2$
Coefficient of Friction, μ_c	0.4
Initial Damage Parameter, d_o	0.1

3.34 are summarized in Table 3.4. The dashed lines in Figure 3.34 are reference points for comparison between the two graphs. It should be noted that while the two stress-strain curves are in good agreement, the volumetric strain curve produced by the author is slightly different than that published by Kondo *et al.* This must be looked into further.

Once it can be confirmed that the implemented model is functioning properly, additional steps must be taken to adapt the Kondo model to analyzing pressuremeter data. A cylindrical coordinate system should be adopted and thus transformation from the cartesian system would be required. Restrictions would also need to be put in place to account for plain strain conditions. The horizontal *in situ* stress would be added as another input parameter. The addition of this parameter, however, could be accomplished in a similar manner to the loading scenario above where an initial load $\mathbf{\Sigma}_{33}$ was applied. Lastly, a choice must be made on the number and direction of microcrack families that should be considered when analyzing pressuremeter data, a potentially difficult, but crucial decision.

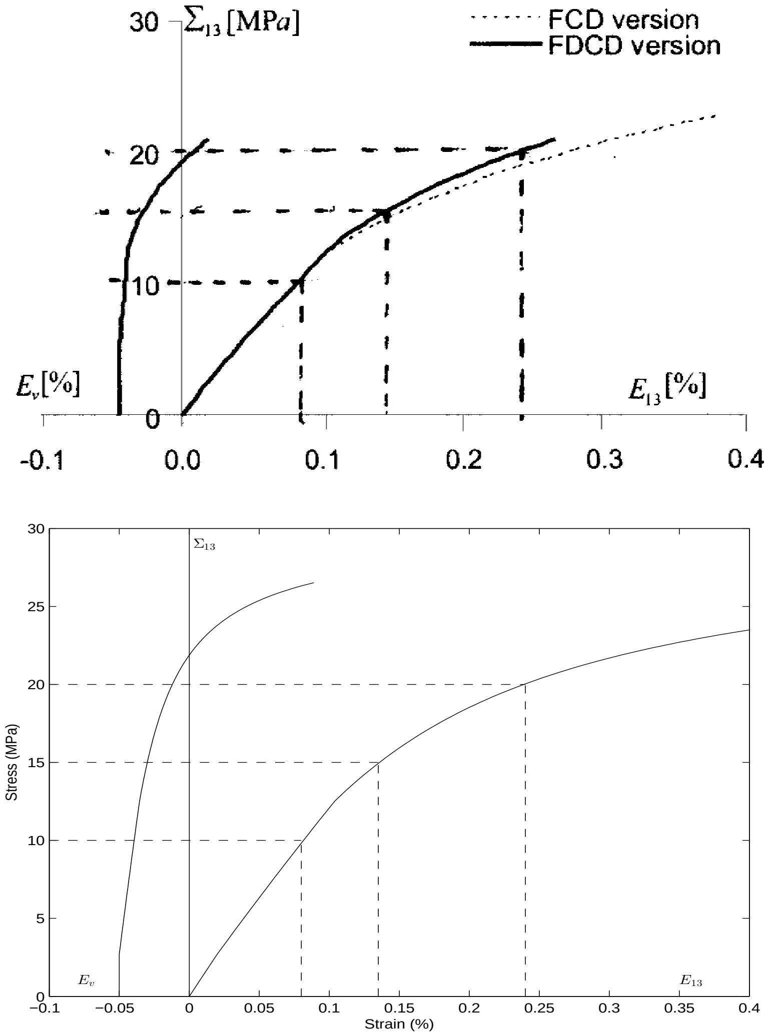

Figure 3.34: Comparison of Model Response. Top is produced by Kondo *et al* in [8]. Bottom is produced by author using MATLAB.

.

Chapter 4

DATA INTERPRETATION AND RESULTS

A number of pressuremeter models along with a framework for model development have been introduced. The focus of this chapter is on the application of these models to analyzing pressuremeter data. Corrections to the raw data and determination of common parameters (such as the shear modulus) are discussed. Analysis of pressuremeter tests in soil is briefly touched upon, but attention is mainly aimed at the analysis of weak rock. Specifically, use of the Mohr-Coulomb and Hoek-Brown models for interpreting pressuremeter data collected in weak rock is discussed. As many techniques for analysis of pressuremeter data are available, the methods discussed here should be considered in no way exhaustive.

4.1 Rock Data

Pre-bored pressuremeter data was collected at five different sites as part of geotechnical investigation for infrastructure projects. The locations of these sites and project specific information not publicly distributed will not be disclosed here. Pertinent information required for data analysis, such as rock type, depth of test location and static ground water table are most easily presented in a boring–log–type format as exhibited in Figures 4.2 through 4.9. A key for these figures is provided in Figure 4.1. For convenience Table 4.1 can be used as a quick reference, listing all rock types encountered, depth range and number of tests performed on each site. Appendix A at the end of this document provides stress-strain plots of all the data modeled using the Hoek-Brown method. Each pressuremeter test is given a reference name with a letter designation followed by a number (i.e. kaz01 for the first test performed on site 3). This designation is useful for reviewing the plots given in the Appendix. The designation for each site is given in Table 4.1. Additionally, a more specific version of this information with test name, depth, and rock type for each test is presented in Appendix A for each site.

Table 4.1: Rock Data Information by Site

Site	Depth Range (m)	# Tests	Designation	Rock Types
1	40 - 75	4	CRCXX	Cemented Cobble & Gravel Matrix
2	15 - 25	22	I–90–XX	Meta Welded Tuff
3	1 - 17	40	kazXX	Gruss, Loam, Mudstone, Siltstone
4	29 - 122	31	sr710-XX	Diorite, Sandstone, Siltstone, Conglomerate
5	10 - 27	18	WallerXX	Limestone, Shale

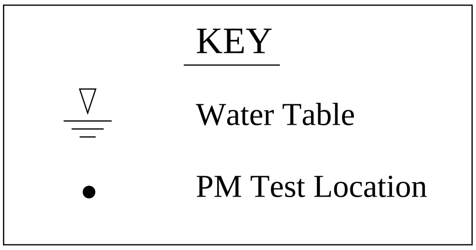

Figure 4.1: Key For Figures 4.2 through 4.9

The data was collected using a Cambridge type pre-bored pressuremeter where applied pressure versus average cavity strain (change in radius/initial radius) is measured by a pressure sensor and three feeler arms equipped with strain gauges spaced equidistantly around the cylindrical instrument, respectively. Test pockets for the instrument on all sites were formed using either mud-rotary drilling methods or coring methods. If mud-rotary was employed a 2–15/16" tricone bit was typically used to form the test pocket, while an NQ core barrel was used if the rock was cored. Further detail of the equipment used and data collection techniques was provided in Chapter 1, Section 1.1. The remainder of this chapter will focus on interpretation of the data collected.

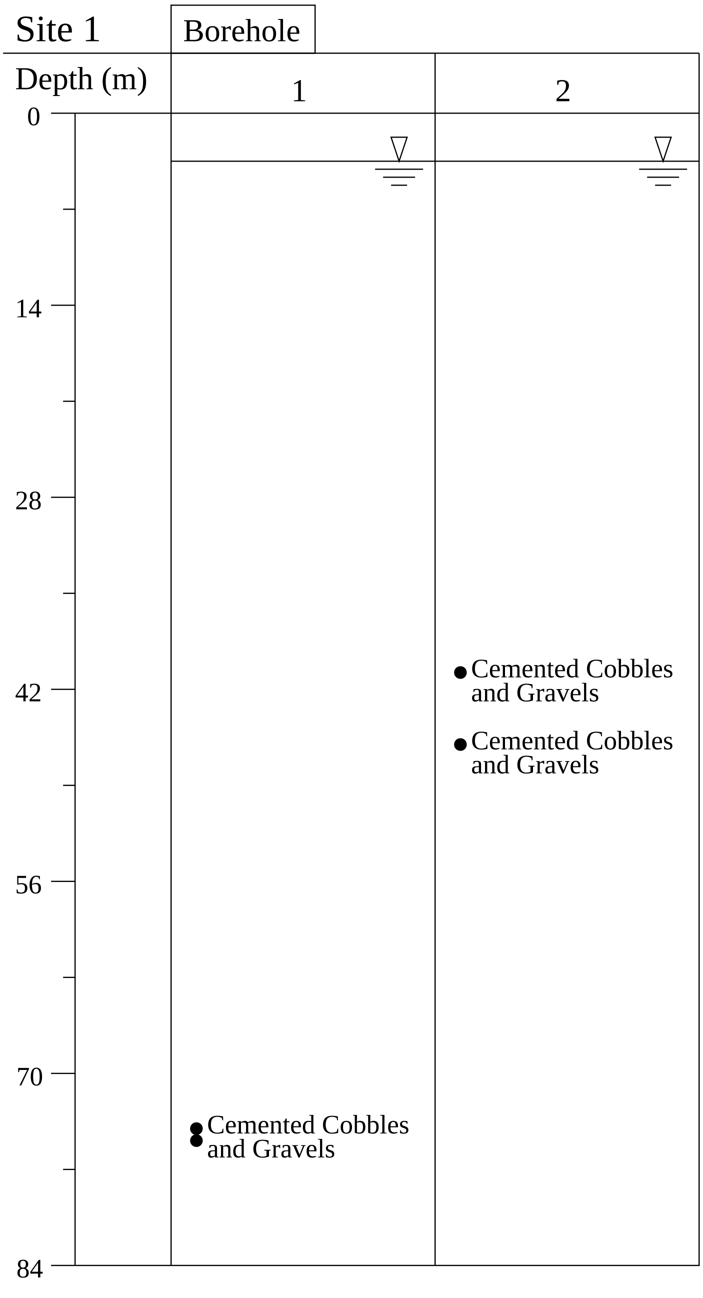

Figure 4.2: Two Boreholes for Site 1 With Pressuremeter Test Locations Marked

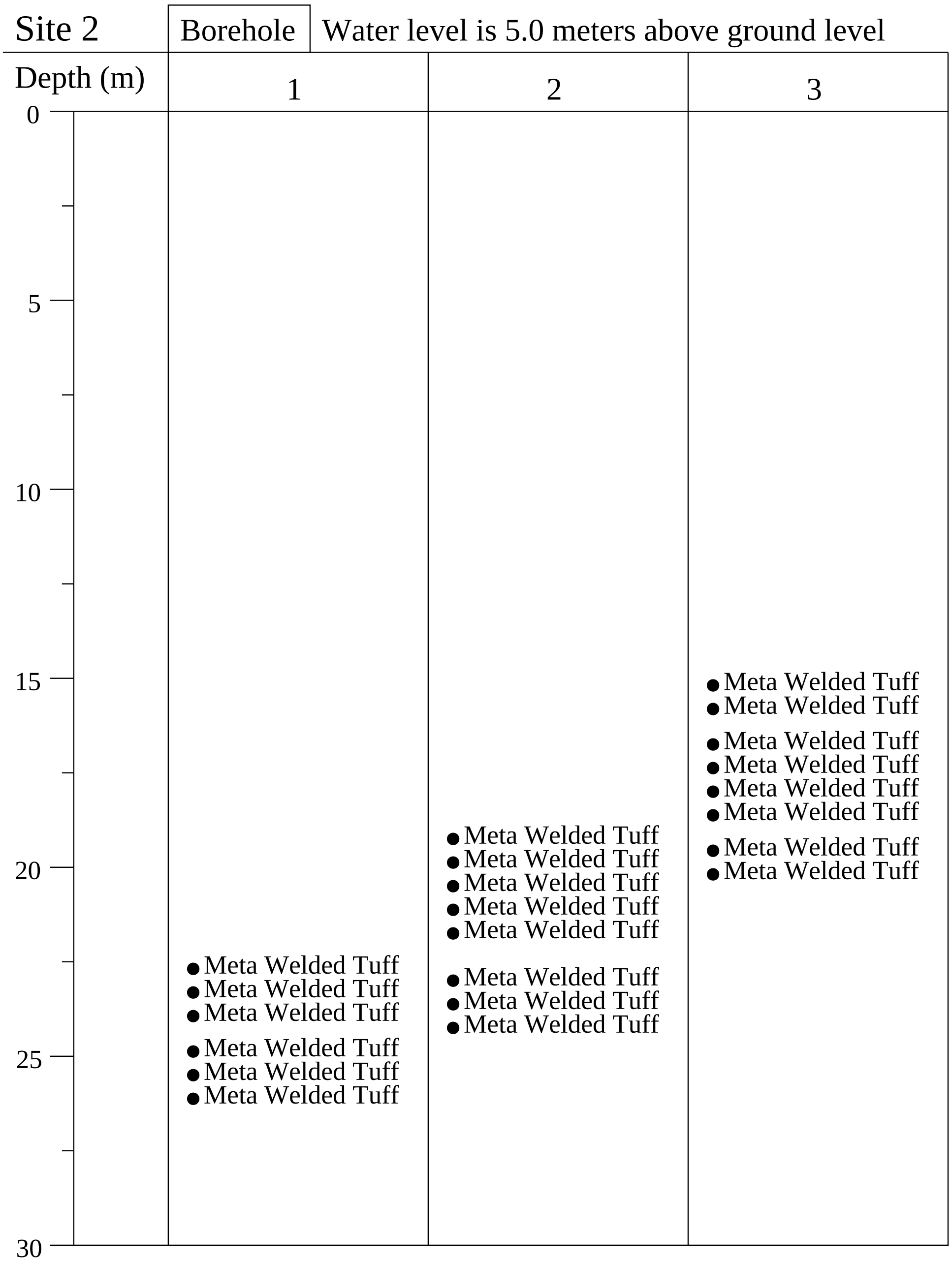

Figure 4.3: Three Boreholes for Site 2 With Pressuremeter Test Locations Marked

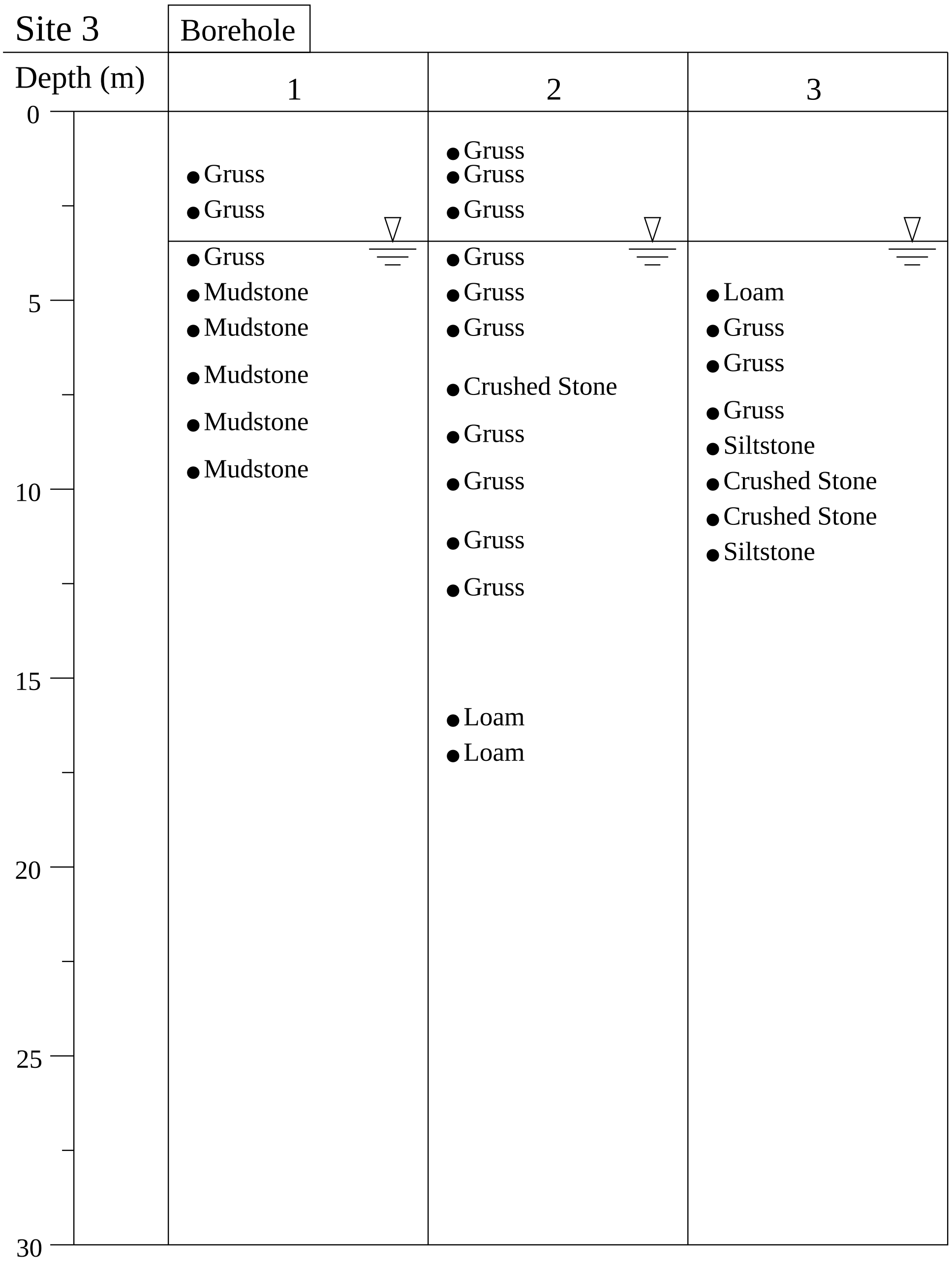

Figure 4.4: First Three Boreholes for Site 3 With Pressuremeter Test Locations Marked

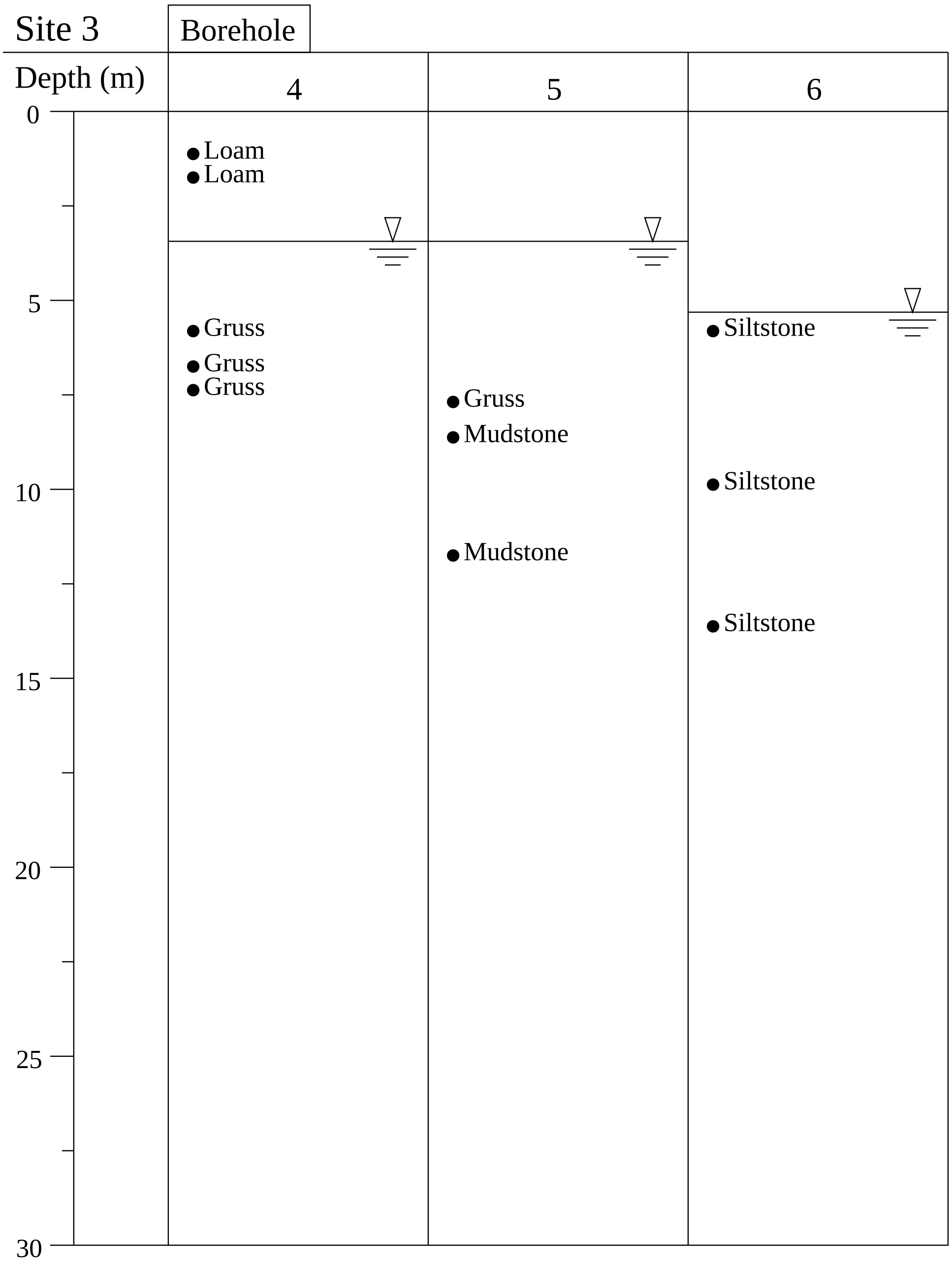

Figure 4.5: Last Three Boreholes for Site 3 With Pressuremeter Test Locations Marked

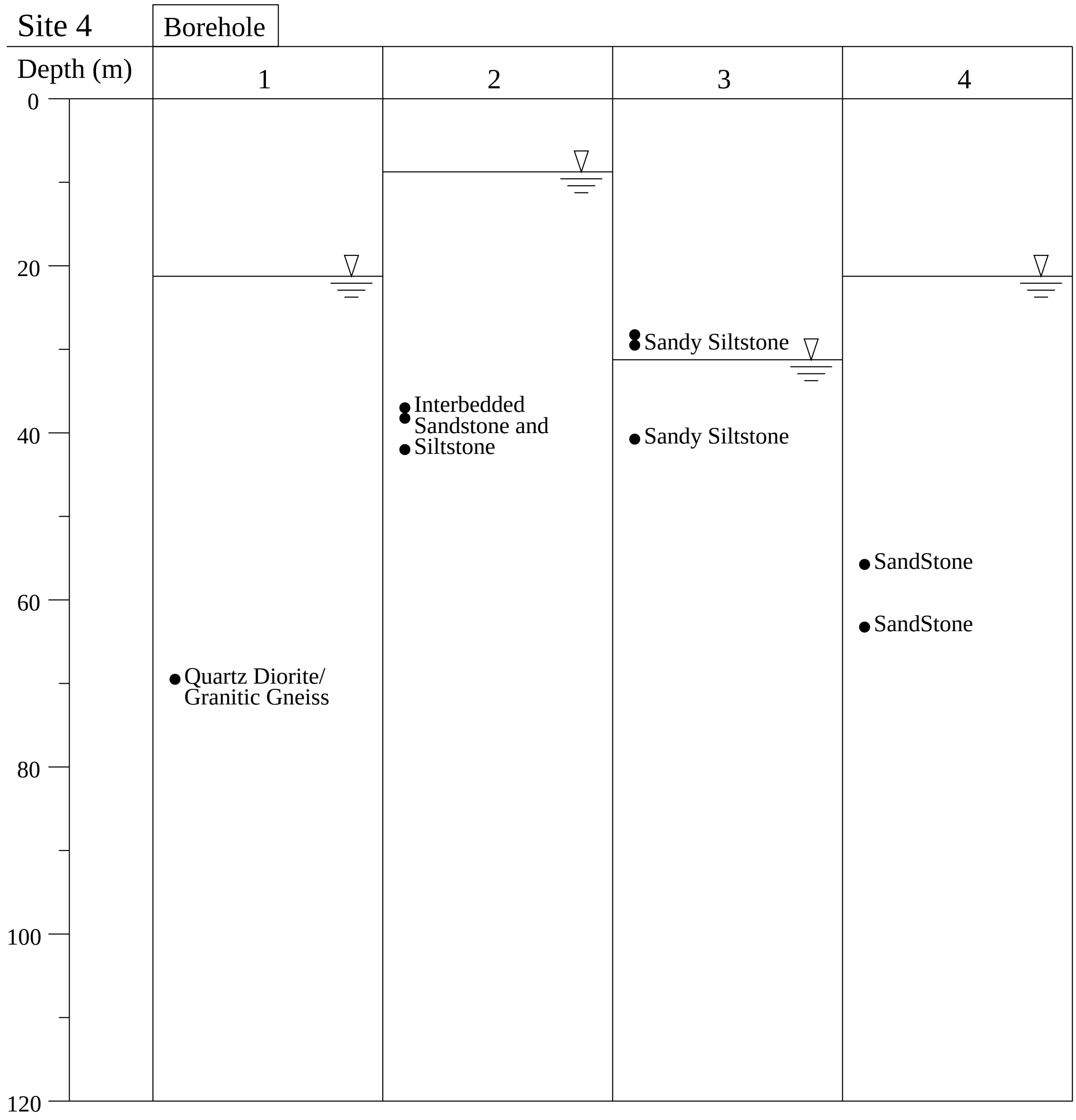

Figure 4.6: First Four Boreholes for Site 4 With Pressuremeter Test Locations Marked

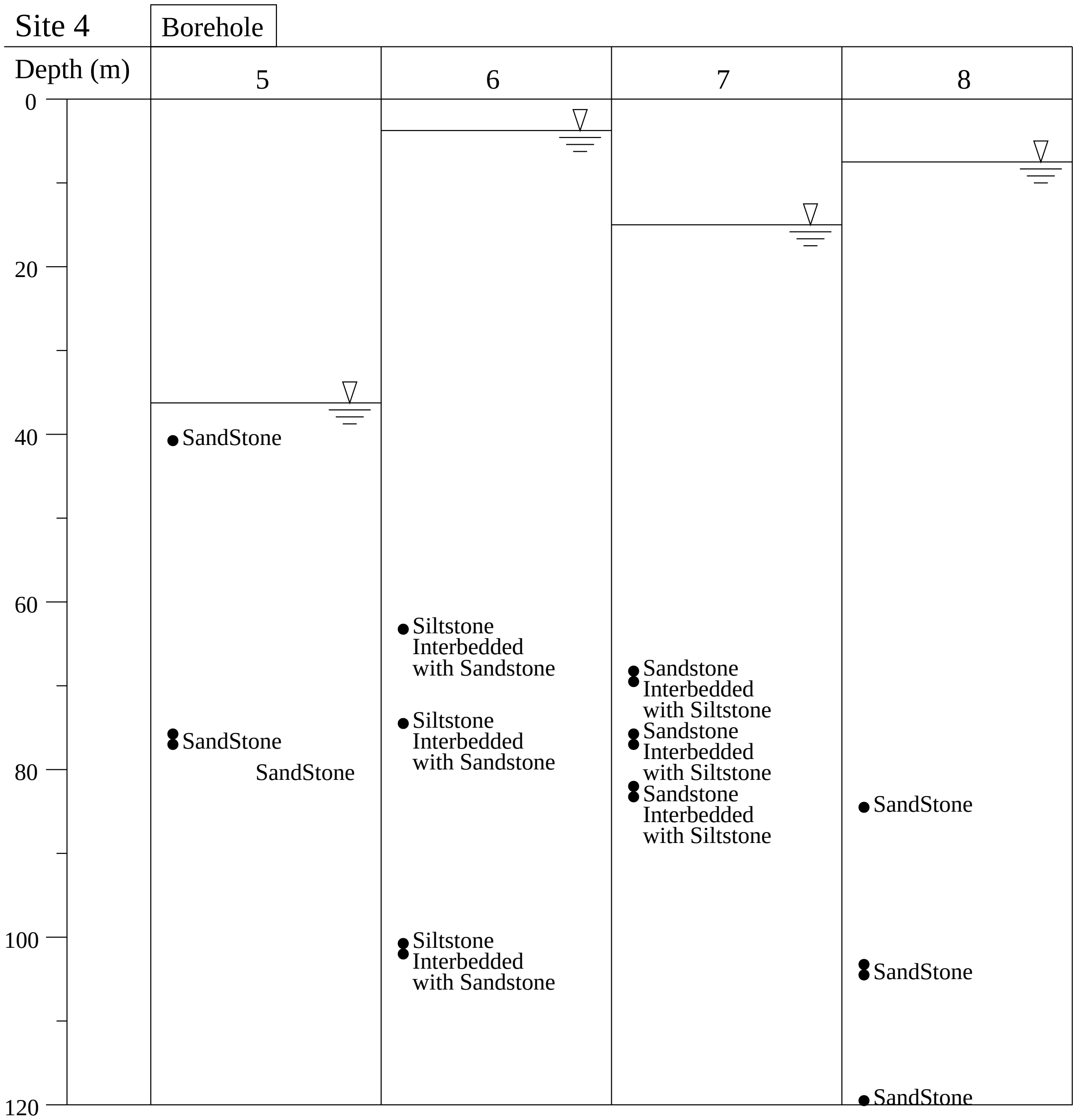

Figure 4.7: Next Four Boreholes for Site 4 With Pressuremeter Test Locations Marked

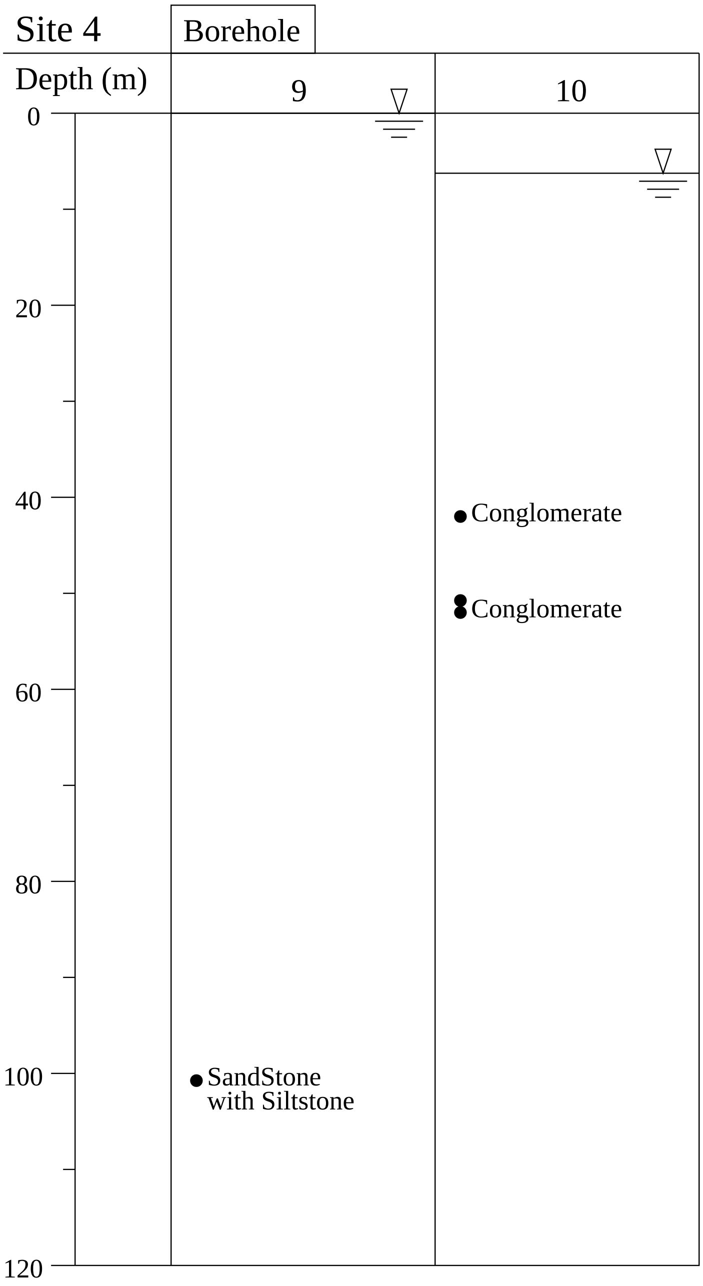

Figure 4.8: Last Two Boreholes for Site 4 With Pressuremeter Test Locations Marked

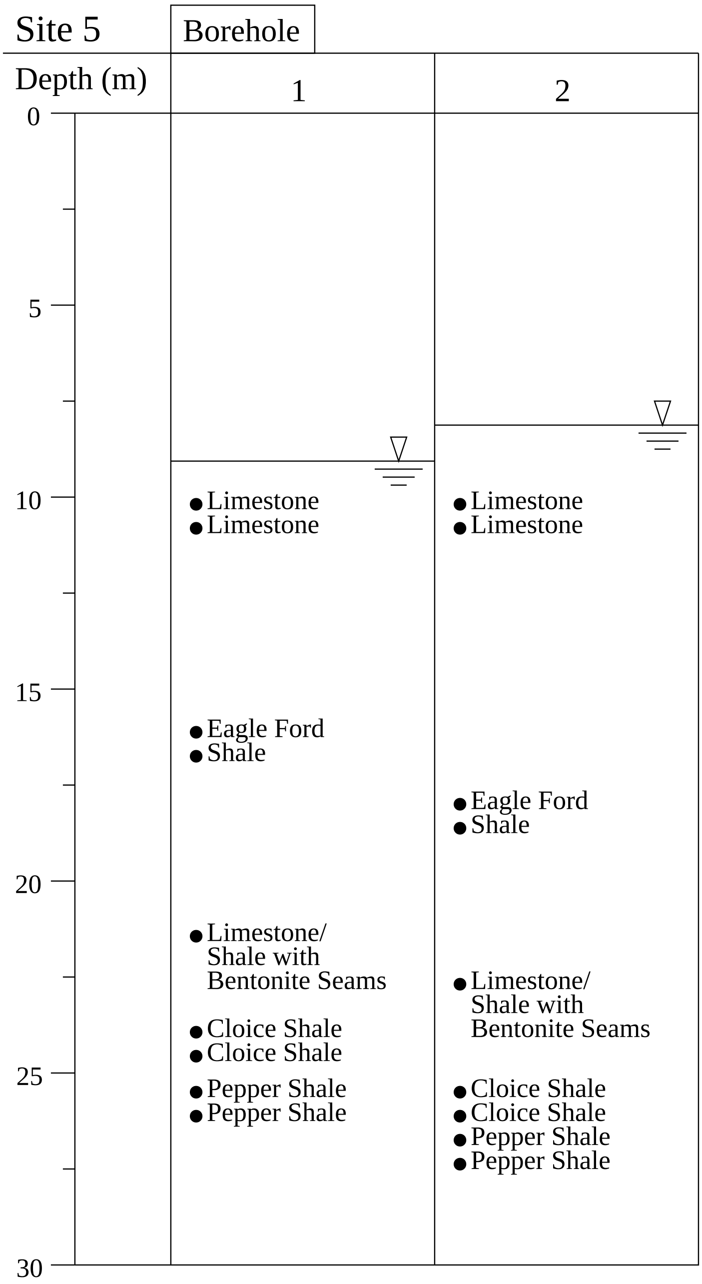

Figure 4.9: Two Boreholes for Site 5 With Pressuremeter Test Locations Marked

4.2 Data Interpretation

Many methods of data interpretation, typically graphical in nature, are available and different methods can be employed on a site by site, and even test by test basis. The interpretation techniques described here should not be considered applicable to all pressuremeter tests. However, some of the methods introduced can be generally applied for pressuremeter analysis. Other methods discussed are more specific to this data set and the models introduced, something the author attempts to note throughout. It would be overwhelming to present analysis details for each of the 115 pressuremeter tests utilized in this study. Thus, interpretation of a few representative tests is presented here and general trends from the entire data set are discussed. Plots of all the tests analyzed by the Hoek-Brown model are given in Appendix A at the end of this document.

4.2.1 Corrections of Raw Data

Before any analysis is performed, corrections must be made to the raw pressuremeter data collected in the field. Factors that can affect the data include end effects, disturbance due to stress relief, drilling action and probe installation, electronic drift, membrane thinning, membrane compression and membrane strength. End effects result from the coupling of the membrane at each end of the pressuremeter causing an irregular shape during membrane expansion (i.e. the ends of the membrane do not expand as a right cylinder). Typical expansion is on the order of twelve millimeters diametrically for the system used in this study and the length of the expanded zone is 6 times the probe diameter (i.e. $L/D = 6$). Studies have shown that end effects for probes with a length to diameter ratio of 6 can be significant for soft clays [24], [7], however, for overconsolidated materials, end effects have been found to be negligible [24]. The type of pressuremeter probes considered in these studies of end effects is not specified, but could have significant impact. The amount of expansion for a Menard type pressuremeter is typically significantly greater than the system used for this study, which would lead to an increased influence in end effects. The influence of end effects is typically ignored for the type of pressuremeter used in this study and thus the effects were not considered in interpreting the data presented here. The other factors listed affecting the data can be accounted for through membrane corrections and zeroing of the data.

Membrane Corrections

During a pressuremeter test, as the rubber membrane expands under pressure, the strength of the membrane provides resistance to expansion. Thus a certain amount of pressure is required to overcome the membrane strength, which must be removed from the data. By expanding the membrane in air (with no additional resistance) a measure of the resistance from the membrane is achieved. An example of a air membrane correction is given in Figure 4.10. The membrane is loaded and unloaded several times to determine the overall trend in the membrane behavior. The slope and y-intercept of the line fitted to the air membrane correction can be used to adjust the pressuremeter data. The result of this membrane calibration is more pronounced, and hence more important, for tests in which a lower overall applied pressure is achieved.

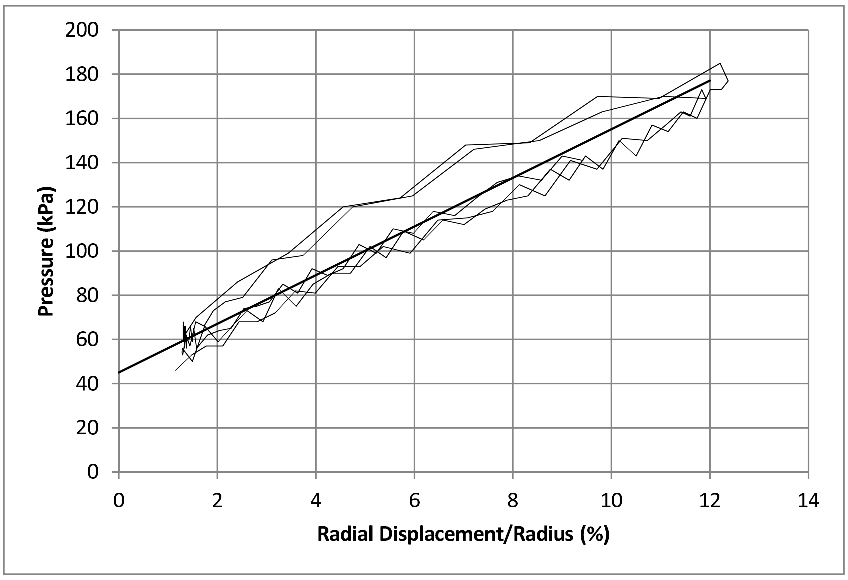

Figure 4.10: Air Membrane Calibration Test With Fitted Slope for Data Correction

The membrane stiffness and compressibility will also affect the recorded pressuremeter data. At high pressures, compression of the membrane against the borehole wall and membrane thinning will occur. Electronic drift can also result from high amounts of applied pressure on the signal receiving computer board in the instrument. The combination of these effects can be captured by expanding the membrane against a rigid steel tube. An example of a tube membrane correction is given in Figure 4.11. Again the membrane is loaded and unloaded multiple times. As the pressure is increased, it can be noted that a fairly constant slope is achieved. A line fitted to the slope of the tube membrane calibration can be applied to the pressuremeter data leading to a slight shift in the measured stiffness. This membrane correction is more applicable for tests in which pressures greater than 1 MPa are reached. It should be noted that the initial loading and final unloading portion of the membrane calibration tests in both Figure 4.10 and 4.11 has been removed as this information is not needed and introduces clutter to the plots. Note that the strain in Figure 4.11 begins at 9%, the required strain for the membrane to reach the walls of the steel tube for this particular membrane.

The influence of applying the membrane corrections in Figures 4.10 and 4.11 to raw pressuremeter data is illustrated in Figure 4.12. It can be seen that shifts in both stress and strain values occur, influencing the apparent stiffness and strength of the material. The result is that the true material strength is less than that of the membrane and material combined, while the material stiffness is greater for this case.

Origin Shift and Water Pressure

The origin shift and shift accounting for water pressure should not necessarily be considered corrections, but rather adjustments to the data to aid in analysis. While the membrane corrections discussed above can and should be applied to all data, the origin and water pressure adjustments are introduced on a test by test basis and are sometimes not required. These two shifts were touched upon earlier in Section 3.3 in the *Validation of Model* subsection, however, more insight is provided here.

Adjusting the data to account for water pressure is only necessary when considering

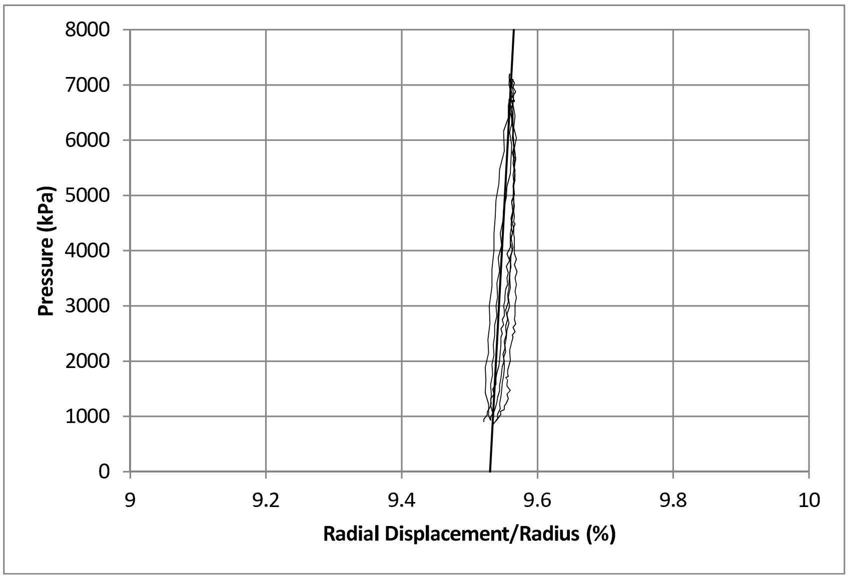

Figure 4.11: Tube Membrane Calibration Test With Fitted Slope for Data Correction

drained analysis. For undrained analysis, total stress analysis is often utilized and thus accounting for the water pressure through a data shift is not required.

For drained analysis, the static water pressure present must be subtracted from the measured pressure to ensure effective stress analysis is established. If the water table is known, the water pressure at a given depth can be calculated as follows

$$p_w = \gamma_w D_w \tag{4.1}$$

where γ_w is the unit weight of water ($9.81kN/m^3$) and D_w is the depth of water (the difference between the depth of the water table and the point of interest). If the water table is unknown, the water pressure can be estimated by the pressuremeter curve. In a free draining material (such as sand, gravels and fractured rocks), there is a point during the final unloading that can be identified where the water pressure outside the membrane has overcome the applied pressure inside the membrane causing the membrane to rapidly collapse. The pressure at which this collapse occurs can be used as an estimate for the

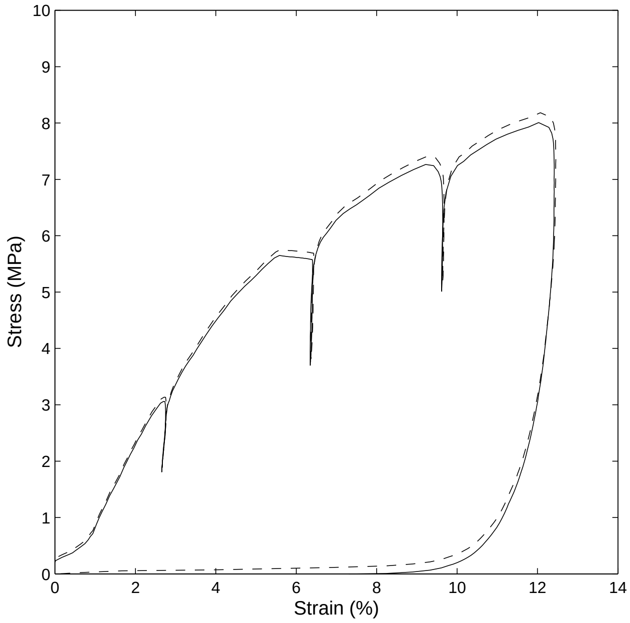

Figure 4.12: Change in raw data after applying membrane corrections for test kaz28 at 7.9 meters depth. The solid line represents the data after the membrane corrections have been applied. The dashed line represents the raw data.

ambient water pressure for the formation tested. For test kaz28 in Figure 4.12, it was determined the water table is at a depth of 4 meters. The test was performed at 7.9 meters and thus the water pressure at the test location is 0.04 MPa. Had the water table been unknown, it could have been concluded that a small amount of water pressure was present for test kaz28. This is apparent through inspection of Figure 4.12. A well defined membrane collapse resulting from water pressure exists, but after applying membrane corrections, this collapse appears to occur near a pressure value of zero. The result of removing the water pressure from the total applied pressure for test kaz28 is given in Figure 4.13.

Use of a pre-bored pressuremeter often results in the necessity of a shift in origin or zeroing of the data (typically this is not necessary for a self-boring pressuremeter test). Depending upon the formation drilled and drilling techniques used, a test pocket can either have a diameter too large or too small for the pressuremeter or can be prone to drilling disturbance. Disturbance can also occur from instrument installation and stress relaxation

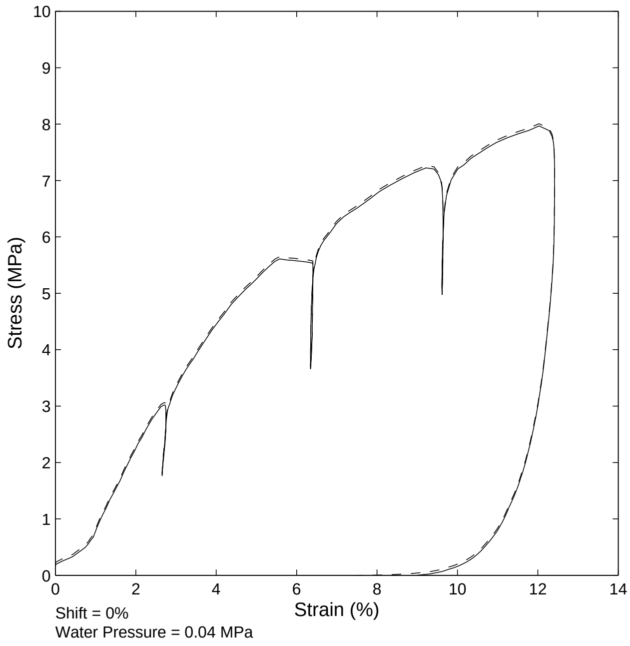

Figure 4.13: Change in data after applying water pressure shift for test kaz28 at 7.9 meters depth. The solid line represents the data after the shift has been applied. The dashed line represents the data before the shift.

at the borehole wall. If the test pocket diameter is slightly too small, and the pressuremeter is forced in (as is possible in a clay), then some strain has already been applied to the formation and the resulting origin will be less than the measured 0% strain by the pressuremeter. If, however, the test pocket diameter is slightly large, or drilling disturbance is present, then the measured strain will be greater than the actual strain applied to the undisturbed formation. Therefore, the origin must be adjusted to account for these effects.

Ideally the origin should define a point on the pressuremeter curve in which the *in situ* horizontal stress (in this case effective stress) coincides with 0% strain. In an ideal test, once the applied pressure is greater than the combination of *in situ* stress, water pressure and membrane strength (of which the membrane effects and water pressure have been removed for analysis), then the pressuremeter would begin to expand against the surrounding undisturbed formation. However, tests are typically not ideal and thus for the same reasons a shift in the data is necessary in a non-ideal case, the point in which the applied pressure equals the *in situ* stress may not coincide with the point that should be considered as the strain origin. This can be illustrated through inspection of test kaz28 in Figure 4.14.

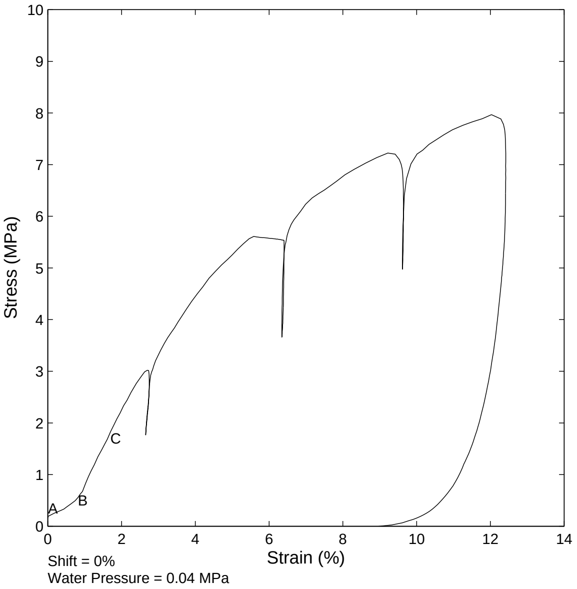

Figure 4.14: Test kaz28 in gruss - an example of a pressuremeter test in weak rock.

At point A in Figure 4.14, deemed the lift-off point, the pressuremeter begins to expand against the rock formation. Point B marks a significant change in the slope of the pressuremeter curve, revealing the presence of disturbance and possible failure in extension from stress relief at the borehole wall between points A and B. Between points B and C, it appears that the measured stress and strain are representative of the undisturbed rock formation. However, at point C, a small inflection can be identified, suggesting the presence of an annulus of softened material around the expanding pressuremeter. Thus, it is after point C that the data captured is truly representative of the undisturbed rock formation. Given the depth of this test (7.9 meters) and considering the weathered nature of the formation, it is highly unlikely that the horizontal *in situ* stress is as high as the value recorded at point C. However, point C can be considered the strain origin for the undisturbed rock formation.

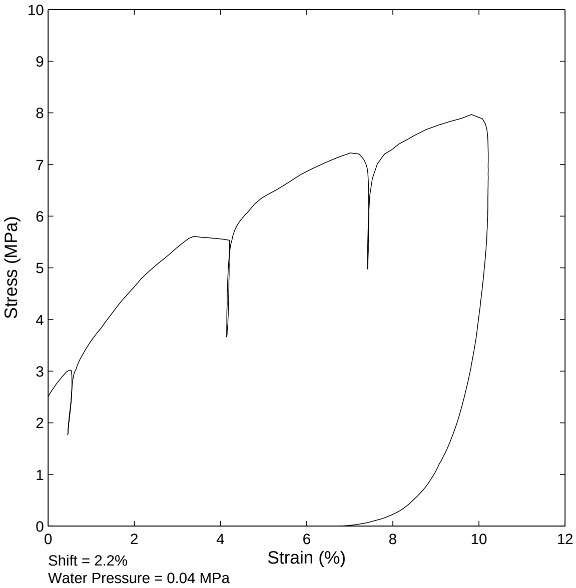

Figure 4.15: Test kaz28 After Origin Shift Applied

It should be understood from this example that the choice of a natural origin can be difficult and requires judgement. The goal is to identify a point in which disturbance to the rock formation at the borehole wall is overcome and zero the strain readings at this point, as is displayed for test kaz28 in Figure 4.15. This allows the pressuremeter data to be modeled with an ideal pressuremeter curve. Due to the inherent difficulties in selecting the proper origin, this choice is often iterative, with adjustments made during the modeling or curve fitting process as is discussed in more detail in the following sections.

4.2.2 Determination of Common Parameters: Horizontal In Situ Stress and Shear Modulus

Two parameters that are typically determined from pressuremeter data and often required as inputs to pressuremeter analysis models are the horizontal *in situ* stress and shear modulus. This section is dedicated towards commonly used methods and thoughts on determining these values.

Shear Modulus

The shear modulus is an elastic parameter and therefore is determined by the elastic portion of the pressuremeter curve. The two areas of the pressuremeter curve in which elastic behavior occurs are the initial loading (and unloading) curve and the unload-reload loops. As was defined in previous sections, the shear modulus can be determined as follows

$$G = 0.5 \frac{a}{a_o} \frac{dp}{d\epsilon_c} \tag{4.2}$$

where a is the probe radius, a_o is the initial probe radius, dp is the change in pressure and $d\epsilon_c$ is the change in cavity strain. For the initial loading curve a/a_o will be close to unity and thus the initial shear modulus can be defined as

$$G_i = 0.5 \frac{p - p_o}{\epsilon_c} \tag{4.3}$$

because $d\epsilon_c = \epsilon_c - 0$. The unload-reload modulus is the average of the unloading and reloading secant shear modulus and can be defined over small strain ranges as

$$G_{ur} = 0.5 \frac{\Delta p}{\Delta \epsilon_c} \tag{4.4}$$

Therefore, the initial shear modulus can be determined by half the slope of the initial loading portion of the pressuremeter curve and the unload-reload shear modulus can be determined by taking half the slope of a best fit line to an unload-reload loop.

Typically the initial loading portion of the pressuremeter curve is prone to disturbance resulting in unreliable shear modulus values. For this reason, the unload-reload loops are often utilized for determining the shear modulus that is more representative of the surrounding formation.

Figure 4.16 is a close-up view of an unload-reload loop performed for test kaz28 (the middle or second unload-reload loop in the test). Unloading occurs between points A and B, while reloading occurs between points B and C. The unload-reload shear modulus, G_{ur}, is marked by the dashed line (this slope is actually twice the shear modulus).

A number of factors should be considered in performing and analyzing unload-reload loops. During unloading, the surrounding material initially behaves elastically, but eventually will fail in extension if the pressure is reduced too far. Therefore, it is crucial that

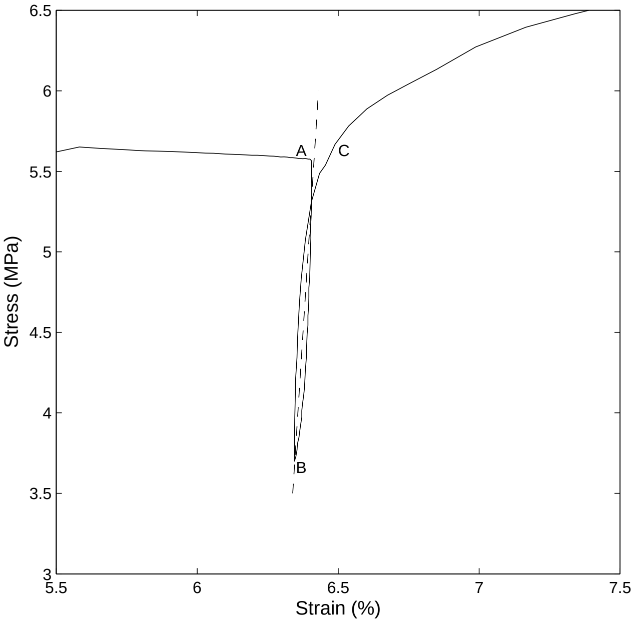

Figure 4.16: Close-up view of unload-reload loop. The dashed line represents the unload-reload shear modulus.

reloading be initiated (point B in Figure 4.16) prior to reaching this threshold for failure. The point at which extensional yield occurs will vary due to loading conditions (drained or undrained) and material properties, however, a typical recommendation is to avoid exceeding 36% of the pressure at the initiation of loading (point A in Figure 4.16) for drained frictional materials or twice the shear strength for undrained clay [7]. Typically, this point can also be identified during the testing process by a sudden change in the slope of the unloading curve. This gives the field operator an indication to initiate reloading. In Figure 4.16 point B is at a pressure 70% of that at point A, indicating the response should be elastic in nature.

Material creep (movement under a constant load) can affect the unloading portion of an unload-reload loop. The tendency to creep outward can offset the tendency towards inward movement during unloading. This effect can be reduced or eliminated by allowing the material to creep prior to unloading, represented by the flat portion of the curve prior to point A in Figure 4.16. It is not always possible to perform a creep test during a pressuremeter test, but at least one should be performed when conditions allow.

Another factor to consider is the hysteresis of the unload-reload loop. Typically linear-elastic behavior is assumed and a constant unload-reload modulus is chosen based on the average of the unloading and reloading portions of the loop (as in Figure 4.16). However, in reality non-linear elastic behavior is often observed, especially in soft clays. While this is not considered in this study, it is worth noting, with further information available in [7] and [4].

Finally, the location (or strain at the initiation of unloading) of the unload-reload loop should be considered. For the shear modulus to be representative of the material, any disturbance present should be sufficiently overcome before unload-reload loops are performed. The first unload-reload loop in test kaz28 in Figure 4.17 is an example of a unload-reload loop subject to disturbance. The shear modulus represented by this loop is greater than the initial modulus measured but noticeably much less than those obtained later in the test from the other unload-reload loops. It is recommended that this modulus value not be considered for analysis. For a material that is neither strain-softening nor strain-hardening, the unload-reload loops should be parallel as the shear modulus should be constant and not dependent upon material strain. However, some rocks and denser sands under drained loading conditions will exhibit strain-hardening behavior and thus the shear modulus obtained from unload-reload loops should increase as the load is increased. An example illustrating this point is given in Figure 4.17 where an increase in modulus from 1,400 MPa to 2,000 MPa is observed. The opposite would occur for a material exhibiting strain softening behavior in that a noted decrease in the shear modulus values would be observed with increased strain.

All shear modulus values obtained that are not considered heavily affected by disturbance should be reported as the value used for design may vary depending upon strain levels considered for the given problem. The initial shear modulus should be considered as a lower bound for the material, but should not typically be considered in design unless disturbance is expected. If a shear modulus value is required for modeling the pressuremeter curve, a range of values can be used to check for the best fit to the data. Knowledge of other input parameters, judgement of the best fit and trends in the data for a given formation can all

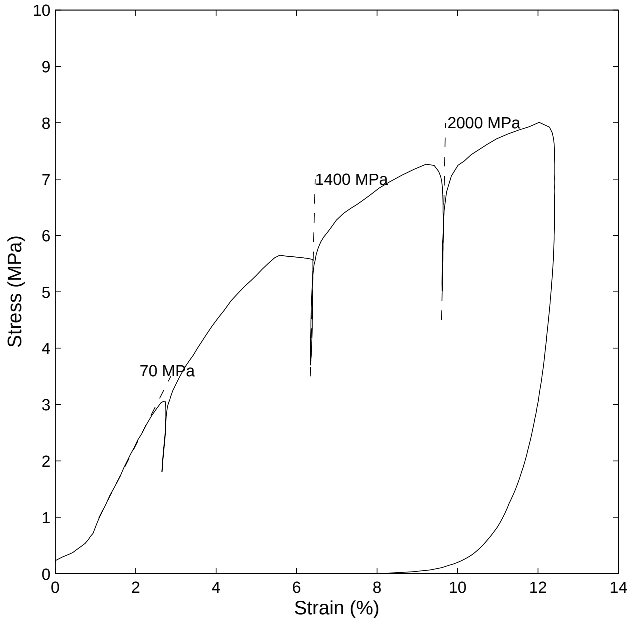

Figure 4.17: Shear Modulus Values for Test kaz28

provide guidance.

Shear modulus values were determined using software developed by *In Situ Engineering* for the data set used in this theses. These values were used as inputs into the MATLAB codes developed by the author for modeling the rock data. The shear modulus values reported on the plots in Appendix A represent the modulus values determined by the unload-reload loops. The plots in which the modulus values are determined are not included, but follow the method described here and displayed in Figure 4.17.

Lateral In Situ Stress

The horizontal *in situ* stress, σ_{ho}, can often be difficult to define for pre-bored pressuremeter tests, especially in the presence of disturbance. A number of methods have been developed to aid in the determination of *in situ* stress, however, these typically apply to soils and still require a high quality (little disturbance present) test. This section will touch upon some of these methods and discuss typical approaches to determining *in situ* stress.

The most basic approach to determining *in situ* stress is the lift-off method. The *in situ* stress is considered equal to the pressure at which the pressuremeter expansion begins. This can be applied to self-boring pressuremeter tests and tests in which minimal disturbance is present. Difficulties, however, arise in using this method in oversized and undersized test pockets or tests in which large amounts of disturbance exists. This can be illustrated by our earlier example in Figure 4.14 for which point A would be considered the lift-off pressure around 0.1 MPa. While this may be the correct choice, it could also be argued that the inflection marked at point B around 0.3 MPa is more appropriate as it appears any stress relaxation caused has been recovered. Therefore, this method is not applicable to all cases and should be used with caution. An incorrect choice in *in situ* stress can lead to incorrect estimates in the peak shear strength of the material. An example of a test where the lift-off method may be more appropriate is given in Figure 4.18 for test sr710-12, for which an origin shift is not required.

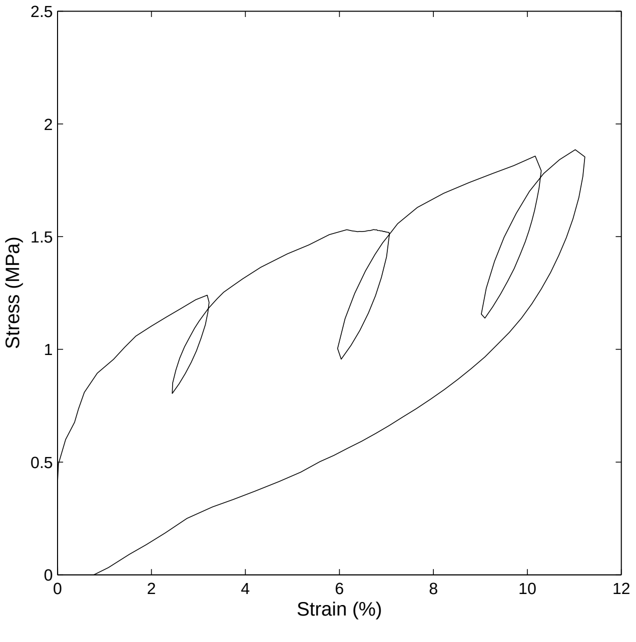

Figure 4.18: Test sr710-12 in interbedded siltstone and sandstone. No origin shift is required thereby allowing the lift-off *in situ* stress method to be applied.

Iterative procedures involving the yield point and estimates of the material shear strength have also been developed. However, these methods are typically only applicable to clay or sand, in which the yield criterion can be defined in terms of only two parameters, such as *in situ* stress and either cohesion or the peak angle of shearing resistance (friction angle) for clay and sand respectively. Elastic-perfectly plastic behavior is often assumed and typically the methods require that the pressuremeter data has an identifiable point of yield. One such method worth noting is the Marsland and Randolph method, which has been successively applied for clays. Details of this method and others of this nature can be found in [7] and [17]. Unfortunately, it would be difficult to apply these methods to most tests in rock. Typically a well defined yield point does not exist for tests in rock due to the non-linear nature of failure. Further complications also arise from the increased number of parameters necessary to define the rock mass strength and yield criterion.

Other methods to be considered include curve-fitting methods using mathematical functions and empirical correlations to external data. Currently a testing method deemed the balance pressure test is under development, in which the pressure is held constant at different increments during unloading and the amount of creep is recorded and compared. This method proves to be a promising alternative method for future use.

Another approach is to estimate the horizontal *in situ* stress based on knowledge of the local geology, material type and vertical *in situ* stress, which is often known or can be easily determined. This estimate can then be used in modeling the entire pressuremeter curve and the original value adjusted along with other inputs until a best fit is achieved. If other material parameters are known or determined externally, this method can be especially powerful.

In essence, the last approach requires knowledge or an estimate of k_o, or the coefficient of earth pressure at rest for the soil or rock tested. While this can be a more straightforward approach in normally consolidated soils, difficulty does arise in considering overconsolidated soils and rock. Stress present in rock formations is complicated by fractures, locked in stress resulting from the formation of the rock or regional movement and anisotropy. In fact, the major principal stress axes in a rock formation may not be vertical and horizontal, as is typically assumed in soil, further invalidating the assumption of k_o. However, at shallower depths, where regional stress impacts may be less or in more intact rock formations, an estimate of stress using k_o may be useful. Considering smaller regions (such as adjacent tests within a borehole), it may be possible to use k_o as a measure of consistency between boreholes. Typically a number of pressuremeter tests are conducted in a given formation over a finite range of depths. For certain tests the horizontal *in situ* stress is more easily determined, such as in Figure 4.18. Using this test then as a reference, a k_o value can be identified and applied to similar tests conducted under similar stress conditions in the same formation. Thus, using trends in the data set as a whole, the *in situ* stress can be more easily identified. While this method may be applicable in some cases, it should be used with caution, particularly for tests in rock. However, the method should at the very least provide a range of stress values, that coupled with the information pulled from the pressuremeter data can narrow the choice of the horizontal *in situ* stress. Keep in mind that it is not unusual in rock for k_o values to be greater than 1.

In absence of other data, or in addition to the data collected, regional stresses can also typically be identified on the World Stress Map online. This map can give an indication of the regional stresses in many areas throughout the world and should be viewed when performing stress analysis in rock.

What should be gained from the discussion above is that determination of the *in situ* stress for pre-bored pressuremeter tests with imperfect test pockets can be difficult. Furthermore, one method cannot always be relied upon and thus it may be practical to try multiple methods. Furthermore the process is subjective and requires good judgment.

The *in situ* stress was determined using the k_o approach for the data analyzed for this thesis. To start a k_o value of 1 was assumed. Adjustments were then made while modeling the entire pressuremeter curve. This data set had also been previously analyzed by other methods and thus the previously determined *in situ* stress values were considered. As the aim of this study was to test the feasibility of using the Mohr-Coulomb and Hoek-Brown models to analyze rock data, determining the exact value for the *in situ* stress was not of concern. It was more important that given a realistic range of values for the input parameters, a good fit to the data could be achieved thereby testing the applicability of the two models.

4.2.3 Determination of Shear Strength of Soils

While the elastic portion of the pressuremeter curve can be defined by the *in situ* stress and shear modulus, the inelastic portion of the curve is a function of the material shear strength. Shear strength is defined by different parameters depending upon the constitutive model chosen to represent inelastic behavior. Modeling of soil behavior subjected to pressuremeter loading is typically less complicated than modeling of rock behavior. This section will be dedicated toward determining the shear strength of soils, providing a bridge to the discussion of modeling for the determination of rock strength thereby allowing the additional complications associated with rock modeling to be fully realized.

For soils, it is typical to assume a Mohr-Coulomb failure criterion, whereby soil shear strength is defined by cohesive strength and/or frictional resistance through parameters cohesion, c, and angle of shearing resistance (friction angle), ϕ, respectively. In considering measures of cohesion and friction angle of soil, further considerations, such as drainage conditions and soil state must be included. For the case of free drainage, volume changes must be considered and effective stress analysis employed, making cohesion and friction angle effective parameters, typically denoted by a ($'$) symbol, such as ϕ'. For undrained conditions, soil volume remains constant, but pore pressure values will change and either total stress analysis or effective stress analysis may be considered. In the case of clays, if undrained conditions are expected, shear strength is often defined as the undrained shear strength, denoted c_u or S_u. The state of the soil (loose or dense relative to the confining pressure applied to the soil) will also determine soil behavior when subjected to loading. However, regardless of the initial state the loading stress path for all soils eventually will culminate at the critical state condition as illustrated in Figure 4.19. Once the critical state is achieved, shearing occurs at constant volume and material strength in this state may differ from the initial peak strength values. Thus, in considering sands it is important to note whether the peak friction angle, ϕ', or critical friction angle (also deemed the friction angle at constant volume), ϕ_{cv} is relevant.

In analyzing pressuremeter data in soil, it is typical to consider idealized material behavior such as that of undrained clay defined by the undrained shear strength, S_u, or drained

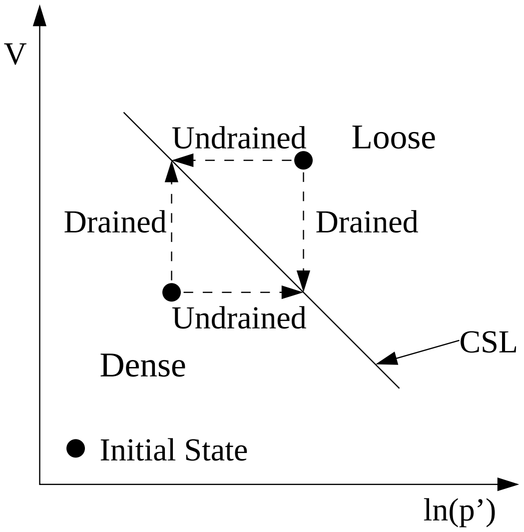

Figure 4.19: Critical State Soil Diagram: CSL = Critical State Line; V = Volume; p = Average Stress State

sand defined by the peak friction angle, ϕ'. A number of methods and models have been developed to analyze pressuremeter data in this idealized manner and some have been discussed in detail in Sections 2.2 and 2.3 for clay and sand respectively. One method described in Sections 2.2 and 2.3 is to graphically fit an idealized pressuremeter curve to recorded pressuremeter data in order to determine material shear strength parameters. While this is not the only method available, it is a robust method and allows consideration of the entire pressuremeter curve, including the interaction of other controlling parameters, such as shear modulus and *in situ* horizontal stress. The remainder of this section will focus on modeling pressuremeter data using these types of models.

A model typically used for analyzing pressuremeter data in clay is the Gibson & Anderson model. The Gibson & Anderson model assumes undrained conditions, and a purely cohesive material that fails at a constant volume with a constant shear strength. Under these assumptions, an idealized pressuremeter curve can be defined by three material parameters: shear modulus, total *in situ* lateral stress and undrained shear strength. These three values can be adjusted until an appropriate fit is achieved between the idealized curve and the recorded data. Because total stress is used, the static water pressure should not be removed from the data prior to analysis. If the shear modulus and lateral stress are known or can be confidently determined by the methods listed in the previous sections, then the undrained shear strength can be found with little adjustment. However, if, for instance the shear modulus is determined by the unload-reload loops, but the lateral *in situ* stress is not known or difficult to determine, then adjustments can be made to the lateral stress and shear strength input parameters in an iterative fashion until a good fit to the data is achieved.

The Gibson & Anderson model considers the loading portion of the pressuremeter curve, however, the unloading [1] portion of pressuremeter data can also be modeled through a method developed by Jefferies. Following the same assumptions as the Gibson model, the origin of the modeling curve can be shifted to coincide with the beginning of the final unloading (i.e. point B in Figure 4.20) and the shear strength can be determined. In unloading, due to the reversal of stress, the apparent shear strength should be twice that of the shear strength determined by the initial loading, as is illustrated in Figure 4.20. While a new origin must be chosen, modeling the unloading curve essentially eliminates the input of *in situ* stress, thereby narrowing the judgment required for determining the shear strength. Furthermore, modeling the unloading curve provides further confirmation of the modeling performed on the loading portion of the curve. Typically both the loading and unloading portions of the pressuremeter curve will be modeled simultaneously providing a measure of consistency in the shear strength values determined by the two methods.

A model typically used to analyze pressuremeter data collected in sand is that developed by Hughes *et al.* The Hughes model assumes drained, purely frictional, elastic-perfectly plastic behavior. Volume change is considered via a dilation angle, which, using Rowe's dilatancy theory is correlated to the critical friction angle. With these assumptions, an idealized pressuremeter curve can be formed using the shear modulus, effective *in situ* lateral stress, critical friction angle and peak friction angle. Already, the introduction of

---

[1] Modeling the unloading portion of a pressuremeter curve is less straightforward in drained materials. Therefore it is typical to only model the loading curve in such materials. The rest of the thesis will focus on modeling of only the loading portion of the pressuremeter curve.

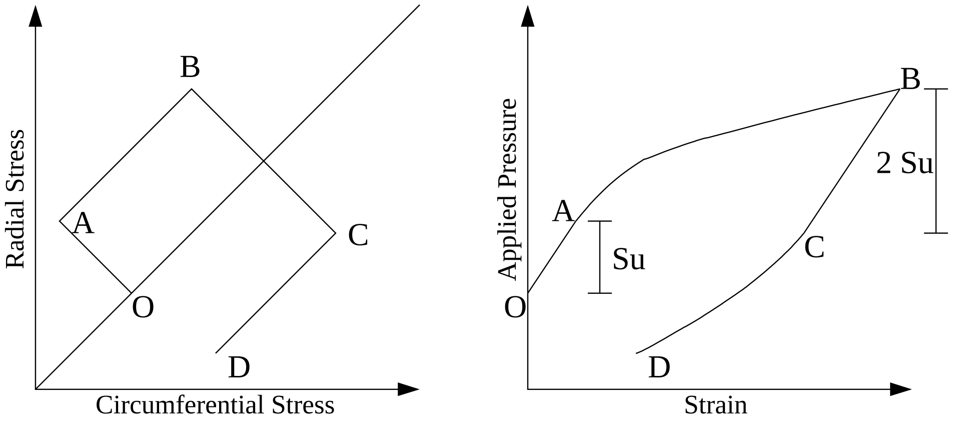

Figure 4.20: Stress Path (left) and Ideal Pressuremeter Curve (right) for an undrained test in clay in which shearing occurs at constant volume during loading and unloading.

drained conditions and therefore volume change, (as is assumed in modeling rock behavior) has further complicated the modeling process by introducing a fourth input parameter. Fortunately, the critical friction angle for a number of different sand types if often known or can be more easily determined by other testing methods. The critical friction angle should not vary significantly for a given sand and therefore, when a number of tests are performed in a particular sand formation, the critical friction angle can be held constant throughout the analysis of all such tests. Again, an iterative procedure is used to determine a best fit of the idealized pressuremeter curve to pressuremeter data.

It is important and typical to have more than one test in a particular sand or clay formation. As was discussed in detail in the subsection for *in situ* stress, in analyzing a number of tests, overall trends in the data can be found. If strength parameters determined are fairly consistent with depth or around a particular testing location, confidence in the strength determined is gained. With many tests in a borehole, outliers can be discovered in a fairly homogenous formation, or in layered formations, relatively weak and strong layers can be identified.

When pressuremeter data is collected, typically other forms of testing, such as standard penetration tests, are also being performed in the same borehole, which helps identify the type of soil or rock in which a pressuremeter test is performed. However, even if other information about the formation tested is unavailable, noted differences in the pressuremeter data can be used as indicators of the material characteristics. Figure 4.21 highlights the differences typically found between a pressuremeter test performed in sand and a test performed in clay. Once the yield strength is reached in clay, the pressuremeter curve tends to curl over quickly and then flatten out as additional pressure and cavity strain are induced. The unloading curve will ideally follow a similar path to the loading curve as the stresses are reversed and the applied pressure may approach zero before the membrane has completely collapsed. In sand, beyond the yield point, the pressuremeter curve will often continue on a relatively steeper slope than clay. Resistance continues to build as applied pressure and cavity strain are induced. During unloading, there is less rebound from the sand and often the unloading path will follow a steep gradient until the static water pressure is reached. At the static water pressure the pressuremeter membrane is forced to collapse, a result not seen in clay due to differences in porosity. Finally, in clay, unload-reload loops typically exhibit higher levels of hysteresis than tests performed in sand, a difference illustrated in Figure 4.22. These indicators listed can help identify which model should be used in analyzing the data collected.

What happens if a pressuremeter test can't be modeled effectively by a clay or sand model? Some overconsolidated or cemented soils may have components of both cohesion and friction that should be considered in strength analysis. Rock strength will be a function of both cohesive and frictional strength components and is even further complicated by the introduction of fractures, both preexisting and those created due to applied loading. The tests presented in Figure 4.22 represent a more sand-like or clay-like response, but in fact test kaz13 was performed in gruss - a weathered siltstone - and test sr710-12 was performed in interbedded siltstone and sandstone. Even though similar materials are tested, the response is completely different for the two tests and in reality both have components of cementation or cohesion and frictional resistance. For this reason, different strength parameters must be considered in modeling rock and hence different pressuremeter models used in analysis.

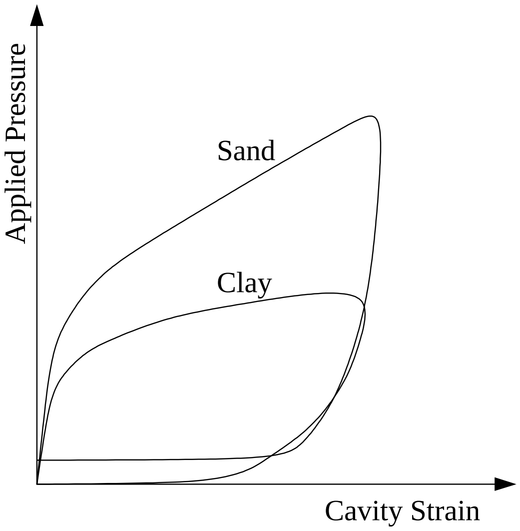

Figure 4.21: Typical Idealized Pressuremeter Curves for Clay and Sand.

4.2.4 Determination of Rock Strength

The focus of this section is on the models considered for pressuremeter analysis by the author in this thesis, Haberfield's Mohr-Coulomb model with a tensile cutoff, and the Hoek-Brown model. The author is in no way claiming that these models are the only means of analyzing pressuremeter rock data or that the strength values determined through this analysis are exact or should be considered for design. The aim was to calibrate the Hoek-Brown model against a data set while using realistic input values. A comparison was then made to the Mohr-Coulomb model using equivalent inputs. The methodology for comparing the two models along with sample results is presented. Discussion of model performance is reserved for the next chapter.

Methodology

The introduction of additional required input parameters for the two rock models provides additional complexity in the modeling of pressuremeter rock data. As discussed above, modeling sand required four input parameters. Both the Mohr-Coulomb model and Hoek-Brown model require three additional input parameters to be defined. The result is the loss

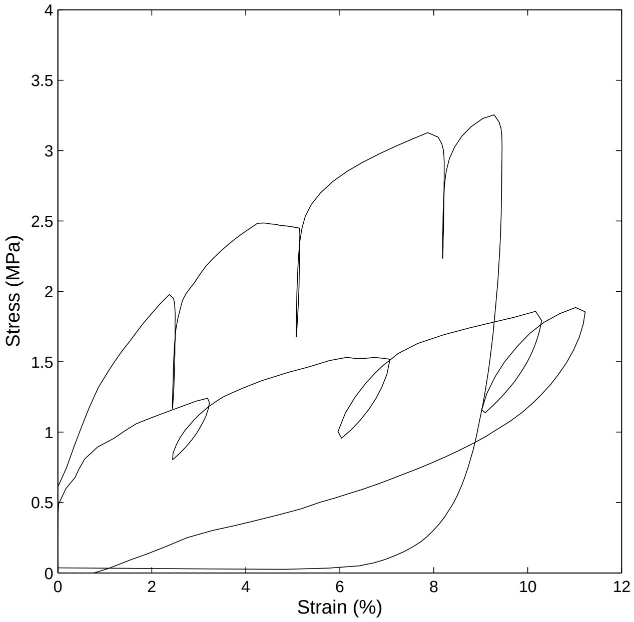

Figure 4.22: Test kaz13 (test that achieves a higher overall pressure with tight unload-reload loops) represents a frictional or more sand-like response. Test sr710-12 (test that achieves a lower overall pressure and unload-reload loops with large amounts of hysteresis) represents a more clay-like response.

of uniqueness. A pressuremeter curve can be uniquely defined by as few as three parameters. Thus in using the rock models some of the parameters must be determined externally, while the modeling of the pressuremeter curve provides confirmation or can help determine those parameters not defined by other methods. Drained analysis is used so effective stress analysis is assumed throughout the section.

For this study, there was no prior knowledge of the values of the material parameters with the exception of Site 2. For Site 2, the Hoek-Brown strength parameters for the meta-welded tuff tested were learned from [1]. The data from this site was used to validate the Hoek-Brown model and ensure that it was functioning correctly (refer to Section 3.3). For the other test sites, however, a range of parameters could be determined for the Hoek-Brown inputs based on the charts and information provided in [6], [18] and [13] as well as figures 3.15 through 3.18. Particularly [18] focuses on defining parameter ranges for weak rock

Table 4.2: Established Hoek-Brown Parameter Ranges for Rocks Types Analyzed

Rock Type	$\sigma_c(MPa)$	GSI	m_i
Diorite	> 250	50–90	20 ± 3
Siltstone	$25 - 50$, $5 - 25$	20–45, 5–25 brecciated	7 ± 2
Mudstone	$25 - 50$, $5 - 25$	20–45, 5–25 brecciated	4 ± 2
Sandstone	$50 - 100$	45–90, 30–45 brecciated	17 ± 2
Shale	$5 - 25$	20–45, 5–25 brecciated	6 ± 2
Limestone	$50 - 100$	45–90, 30–45 brecciated	10 ± 4

and even interbedded formations. Using this information ranges were established for the Hoek-Brown parameters and are provided in Table 4.2 (Tuff is excluded as those ranges were not determined in this manner and are given in Section 3.3). Some of the rock types analyzed, such as the cemented cobble & gravel matrix, could not be defined as easily. For those tests more broad guidelines were followed. In [13] examples for good quality, average quality and poor quality rocks is given. The values chosen for those examples were used as a broader guideline and are presented in Table 4.3. Included in this table is a measure of the dilation angle, not provided for individual rock types listed in Table 4.2.

The variable ranges listed in Tables 4.2 and 4.3 could be adjusted for the different rock types if the level of fracture was considered extreme or the test appeared weaker than average for the given rock type. These judgments were made based upon the recorded pressuremeter data on a case by case basis. The Rock Quality Designation (RQD) was also used as a measure of fracture level and rock quality for each of the tests in which this information was available.

The required input parameters to create an idealized pressuremeter curve using the Hoek-Brown model are shear modulus, G, lateral *in situ* stress, p_o, Geologic Strength Index, GSI, Hoek-Brown parameter, m_i, uniaxial compressive strength, σ_c, dilation angle, ψ, and damage parameter, D. The shear modulus was determined by the unload-reload loops for each test, and the *in situ* stress was determined in the manner described at the end

Table 4.3: Broad General Guidelines

Rock Quality	$\sigma_c(MPa)$	GSI	m_i	ψ
Good Quality	150	75	25	11.5^o
Average Quality	80	50	12	4^o
Poor Quality	20	30	8	0^o

of the *Lateral In Situ Stress* section. GSI, the Hoek-Brown parameter and uniaxial compression strength were determined as just discussed, leaving the dilation angle and damage parameter. The damage parameter was created by Hoek to consider blasting damage and stress relaxation. Because the strain origin is shifted to compensate for disturbance present and the influence of the damage parameter is small compared to other inputs, it was decided that the damage parameter would be set to 0 for analysis (i.e. no damage). This allowed the one free variable, dilation angle, to be determined by fit to the pressuremeter data given all the other parameters and adhering to the general guidelines in Table 4.3. It should be noted that dilation (or increase in volume), for the case of rock analysis is physically associated with the movement along fractures or joints as illustrated in Figure 4.23.

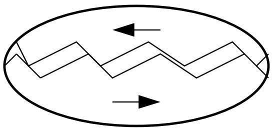

Figure 4.23: Dilation Caused by Shearing Along a Fracture.

After defining input parameters for the Hoek-Brown model, comparable parameters had to be established for the Mohr-Coulomb model. In initially establishing the Hoek-Brown failure criterion, Hoek recognized that many engineering programs were set up for analysis using the Mohr-Coulomb failure criterion. For this reason, Hoek established a method to determine an equivalent cohesion and friction angle based on the inputs for the Hoek-Brown criterion. An average linear relationship is fit to the Hoek-Brown failure envelope by balancing areas above and below the Mohr-Coulomb failure criterion for a minor principal stress range of $\sigma_t < \sigma_3 < \sigma_{3max}$. This is graphically illustrated in Figure 4.24. The equivalent Mohr-Coulomb parameters are calculated as follows

$$\phi = sin^{-1}\left[\frac{6bm_b\left(s+m_b\sigma_{3n}\right)^{b-1}}{2(1+b)(2+b)+6bm_b\left(s+m_b\sigma_{3n}\right)^{b-1}}\right] \tag{4.5}$$

$$c = \frac{\sigma_c\left[(1+2b)s+(1-b)m_b\sigma_{3n}\right]\left(s+m_b\sigma_{3n}\right)^{b-1}}{(1+b)(2+b)\sqrt{\left(6bm_b\left(s+m_b\sigma_{3n}\right)^{b-1}\right)/\left((1+b)(2+b)\right)}} \tag{4.6}$$

where m_b, s, and b are as defined in Equations (3.42), (3.43) and (3.44) respectively and $\sigma_{3n} = \sigma_{3max}/\sigma_c$.

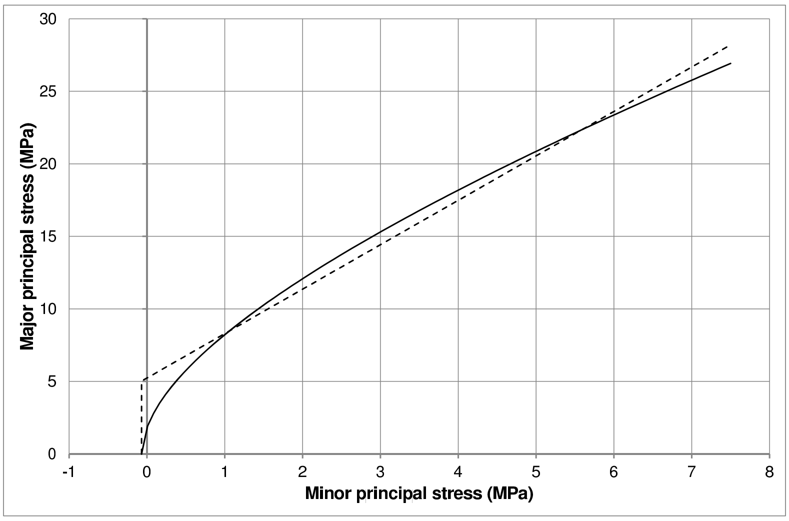

Figure 4.24: Principal Stress Plot of Hoek-Brown (curved solid line) and Equivalent Mohr-Coulomb (straight dashed line) failure envelopes for the case of $\sigma_{3max} = 8$

The importance of establishing an appropriate σ_{3max} is significant as it greatly impacts the equivalent $c - \phi$ calculated. Through inspection of Figure 4.24, where $\sigma_{3max} = 8$, it can be identified that a lower σ_{3max} value would result in a higher friction angle and lower cohesion due to the relative steepness of the Hoek-Brown failure envelope at lower stresses. The value chosen for σ_{3max} depends upon the application to which it is being applied. In

[6], Hoek establishes a definition of σ_{3max} for the case of tunnels and slopes. Given the nature of loading applied here, it was determined that the equation for tunneling was more appropriate as it more closely mimics loading during a pressuremeter test. It can be written as

$$\frac{\sigma_{3max}}{\sigma_{cm}} = 0.47 \left(\frac{\sigma_{cm}}{\gamma H} \right)^{-0.94} \tag{4.7}$$

where σ_{cm} is defined as the global rock mass strength and can be equated as follows

$$\sigma_{cm} = \sigma_c \frac{(m_b + 4s - b(m_b - 8s)) \left(m_b/4 + s\right)^{b-1}}{2(1+b)(2+b)} \tag{4.8}$$

Due to orientation of loading for the pressuremeter, and the fact that most often a $k_o = 1$ is assumed for the analysis, γH in Equation (4.7) was replaced with p_o. It should be noted that σ_{3max} can be determined more generally and it is recommended that a range of values be used in determining equivalent $c - \phi$ values.

The required input parameters to establish an idealized pressuremeter curve using the Mohr-Coulomb model with a tensile cutoff are shear modulus, G, lateral *in situ* stress, p_o, cohesion, c, friction angle, ϕ, tensile strength, σ_t, dilation angle, ψ, and Poisson's ratio, ν. The same shear modulus, *in situ* stress and dilation angle used to analyze the data with the Hoek-Brown model were used as inputs to the Mohr-Coulomb model. Cohesion and friction angle were determined as just described. As with cohesion and friction angle, the tensile strength can also be calculated using the Hoek-Brown failure envelope as follows

$$\sigma_t = \frac{s\sigma_c}{m_b} \tag{4.9}$$

leaving only Poisson's ratio to be determined. Typically, Poisson's ratio is somewhere between 0.15 and 0.35 for rock [11]. Using this range along with the other established parameters a fit to the data was achieved for each test. By using equivalent parameters or the same identical inputs when possible, an ample comparison between the Hoek-Brown and Mohr-Coulomb models could be established.

Sample Results

Using the methodology outlined above, the following steps were used to analyze the data and compare the two models.

1. Using the range of inputs established in Table 4.2 and Table 4.3 the data was fit using the Hoek-Brown model and an equivalent cohesion and friction angle were determined.

2. Due to the difference in nature of the two models, the shift required to locate a proper strain origin (see subsection 4.2.1) was usually slightly different for the two modeling approaches. For this step the origin shift used for the Hoek-Brown model was maintained. Then using the equivalent $c - \phi$ values, Poisson's ratio was adjusted until a good fit to the *beginning* of the pressuremeter curve was established. This often resulted in a poor fit to the latter portion of the pressuremeter data.

3. In the above step, the tensile cutoff may have been reached as a result of the given inputs of *in situ* stress, p_o, and tensile strength, σ_t, and the yield value determined (as defined by Equation (4.9)). If the cutoff was reached, a cracked response defined by Haberfield's empirical equation was compared to the data. The tensile strength was then shifted to a higher value forcing a non-cracked response in order to continue the analysis using the Mohr-Coulomb model.

4. Next a shift in the strain origin was made as appropriate. The input value for Poisson's ratio was also changed to a more realistic value if an unrealistic input was required in Step 2. The data was then modeled by setting $c = 0$, thus modeling the data as if the material response was purely frictional. This provided a maximum limit to the material friction angle.

5. The input for cohesion was then set to be equal to the equivalent cohesion value determined in Step 1 and the friction angle was lowered until a good fit to the data was achieved.

6. The fit from Step 5 was then further adjusted by tweaking the friction angle and cohesion values. Typically, the friction angle was set somewhere between the maximum limit and the Hoek-Brown equivalent and cohesion between zero and the Hoek-Brown equivalent. If a good fit to the data could not be achieved in this way, the values

would either be increased or decreased as was appropriate. Typically these changes in the input values were not extreme.

7. Finally, if it seemed an appropriate fit was still not achieved, the equivalent cohesion and friction angle determined in Step 1 were used as inputs and Poisson's ratio was adjusted (within reason) until a good fit to the data was achieved. The strain origin was also shifted during this step when necessary.

By following the steps outlined above, the Mohr-Coulomb model could be tested against the Hoek-Brown model without bias. Essentially a range of values for friction angle and cohesion was established using extremes and the equivalent cohesion and friction angle determined through the Hoek-Brown modeling. The overall fit accomplished by the two models could be observed during this process. Equally important it could be established whether or not a good fit to the data could be achieved using the equivalent $c-\phi$ determined by the Hoek-Brown model (or at least values near those) thereby further calibrating and validating the use of the Hoek-Brown model.

Using the system outlined in Steps $1-7$, the average equivalent friction angle and cohesion determined by the Hoek-Brown model were 50.6^o and 0.38 MPa respectively. After final adjustments were made in analyzing data with the Mohr-Coulomb model, the average friction angle and cohesion determined were 48.6^o and 0.6 MPa respectively. Two of the sites tested (Site 2 & Site 5) consisted of data in rock formations that pushed the bounds of what could be considered weak rock (in that the rocks tested were towards a higher strength range). Not including data from these two sites, the average equivalent friction angle and cohesion determined by the Hoek-Brown model were 46.9^o and 0.12 MPa respectively. After final adjustments the average friction angle and cohesion determined were 44.8^o and 0.17 MPa respectively by the Mohr-Coulomb model. It is clear then that little adjustment of the equivalent friction angle and cohesion established by the Hoek-Brown model was required to achieve a good fit for the Mohr-Coulomb model, thus providing confidence in the Hoek-Brown modeling process. It should be noted here again, that the author is not claiming, however, that the values determined are exact or should be used in design, but given realistic values a good fit was achieved. The determination of the equivalent $c-\phi$ values is sensitive to the determination of σ_{3max}; using a higher σ_{3max} would result in lower friction angles and higher cohesion values, which may be more representative of the material than the values reported here.

Walking through the steps, Figure 4.25 is an example of Step 1 in the modeling process. Good fits to both tests, I–90–19 and kaz28 are achieved using the Hoek-Brown model. Both required origin shifts due to enlarged test pockets and disturbance (likely due to stress relaxation) of the borehole wall. Pressure due to the static water level has also been removed. Both these values are recorded below the plot box to the left. The parameter inputs are given in a box in the upper right hand corner of the plot. The equivalent cohesion and friction angle are also reported here.

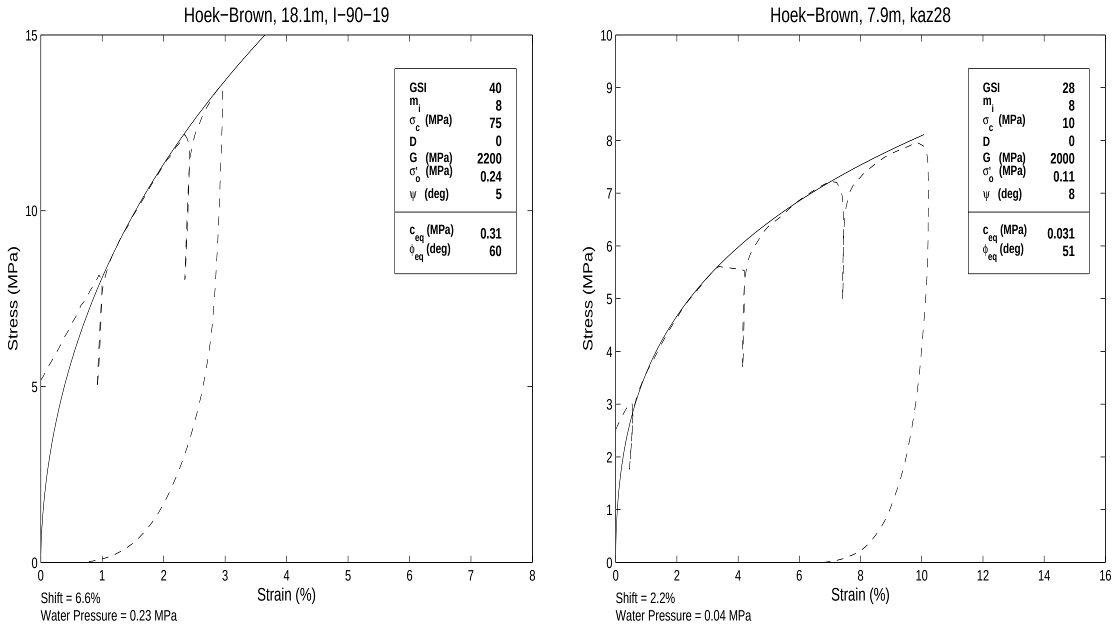

Figure 4.25: Step 1: Two pressuremeter tests with data (dashed line) fitted with the Hoek-Brown model (solid line). Left: I–90–19 in meta-welded tuff; Right: kaz28 in gruss.

Figure 4.26 represents Steps 2 and 3 for test kaz28 and I–90–19 respectively. Using the tensile strength determined by the Hoek-Brown inputs, the tensile cutoff was not reached for test kaz28 resulting in a ductile response modeled by the Mohr-Coulomb failure criterion. Poisson's ratio was increased forcing the fit of the idealized model curve to follow the same

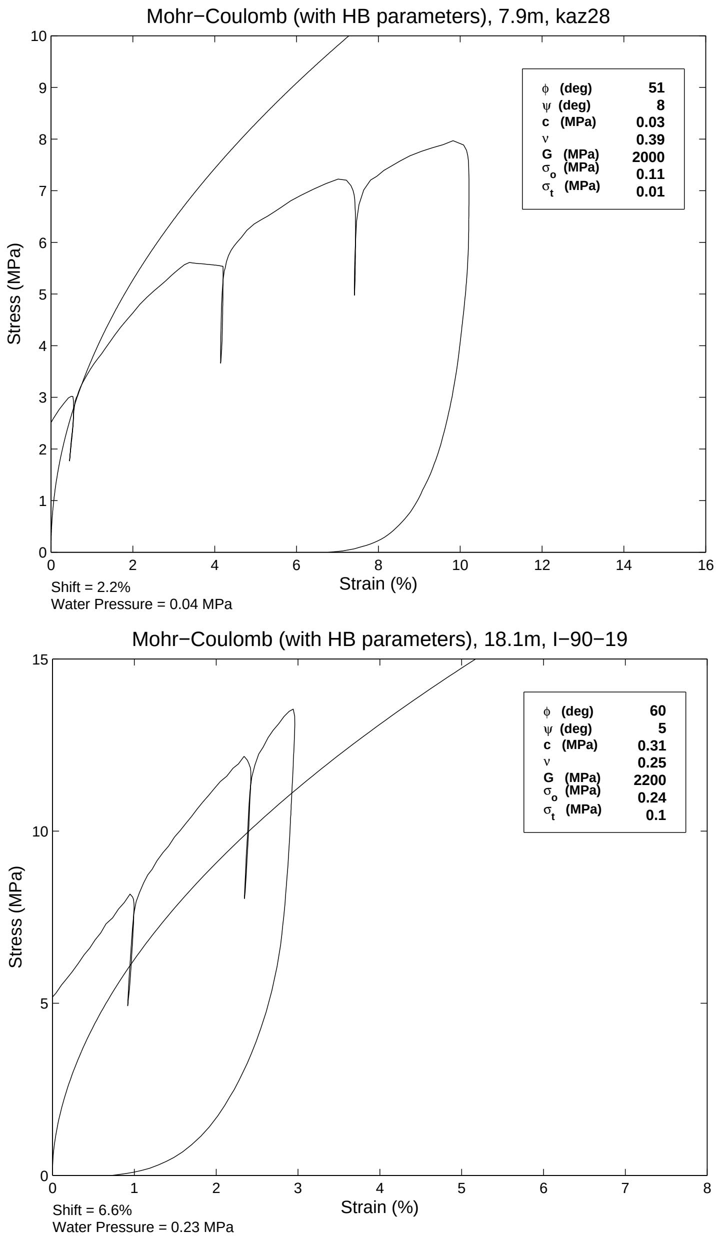

Figure 4.26: Steps 2 & 3: Top: the tensile cutoff has not been reached for test kaz28. Bottom: the tensile cutoff has been reached for test I-90-19 triggering use of the empirical model for cracked response.

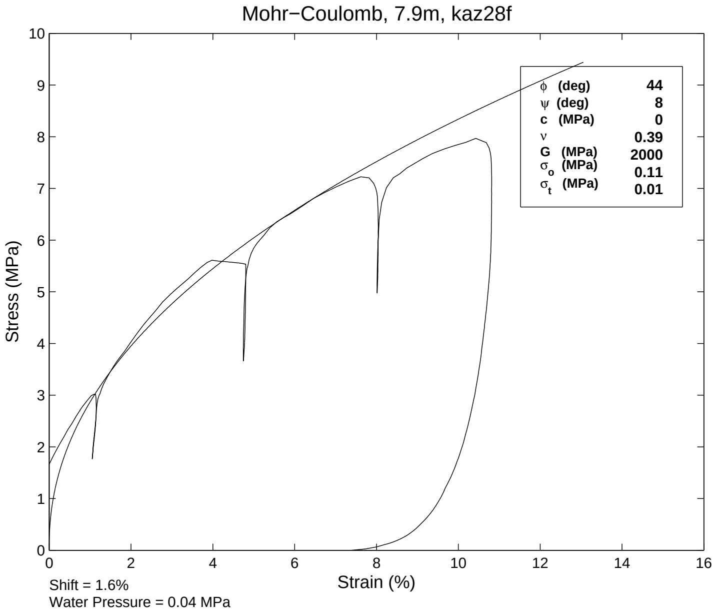

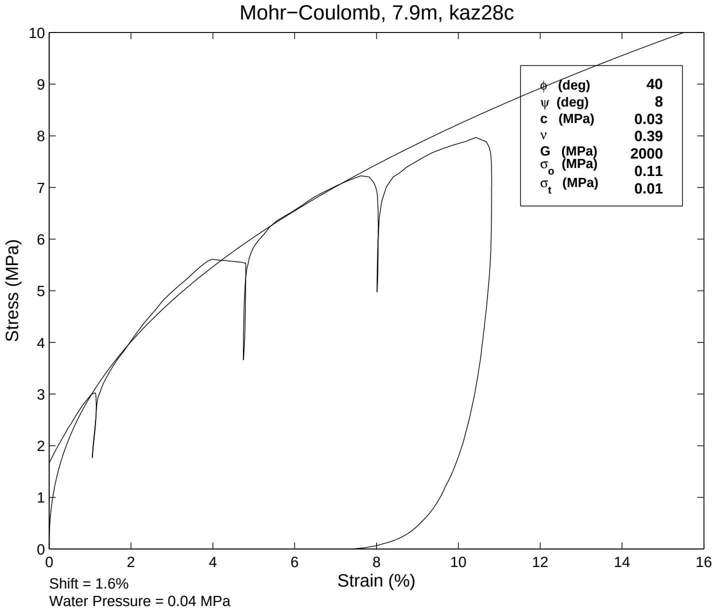

Figure 4.27: Steps 4 & 5: Top: test kaz28 modeled with a frictional component only. Bottom: test kaz28 modeled with frictional and cohesive components.

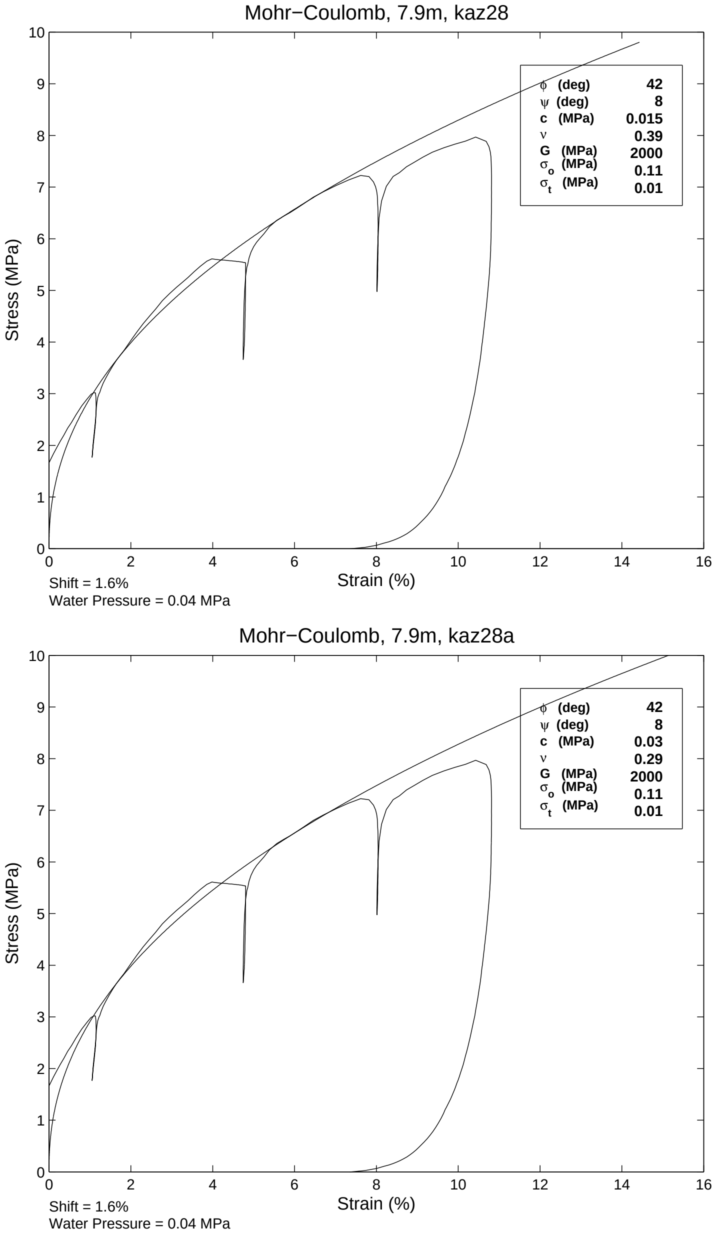

Figure 4.28: Steps 6 & 7: Test kaz28 modeled with adjusted frictional and cohesive components.

path as the beginning of the Hoek-Brown idealized model curve produced in Step 1. The result is a poor overall fit. For test I–90–19 the tensile cutoff was reached prior to the Mohr-Coulomb yield, triggering the use of the empirical equation designed to capture the material response resulting from crack formation and propagation. It can be seen that although the overall shape of the idealized model curve is appropriate, the magnitude is incorrect. This result was typical of most tests in which the cracked model response was triggered. Of the 115 tests analyzed, 44 induced a cracked model response, of which only 5 resulted in a good fit to the data. The formulation of the cracked response model was based on pressuremeter data in mudstone in idealized conditions and thus is likely not suitable for many other rock types. Therefore adjustments must be made before future use of this method is applied.

The top plot in Figure 4.27 represents Step 4 for kaz28 in which the cohesion is set to zero and the test is modeled using friction angle as the only measure of strength. The strain origin was shifted from Step 2. Poisson's ratio was maintained because, although high for weak rock, the value is not unrealistic. The overall fit to the data is fairly poor, an expected result because most rocks will have some component of cohesive strength. However, modeling in this way provides an upper bound for the friction angle of the material. It should be noted that the upper bound determined for test kaz28 is 44^o, while the equivalent friction determined via the Hoek-Brown method is 51^o. This is a case in which the choice of σ_{3max} is likely too conservative resulting in a higher than realistic equivalent friction angle.

The bottom plot in Figure 4.27 represents Step 5 for kaz28 in which the equivalent Hoek-Brown cohesion has been introduced as an input and the friction angle has been lowered until a best fit with the data is achieved, occurring when $\phi = 40^o$. The overall fit is better than in Step 5, but not great in comparison to the Hoek-Brown fit from Step 1.

Steps 6 & 7 are represented in Figure 4.28 for test kaz28 in which final adjustments are made to the input values for cohesion and friction angle. Little further improvement of the model fit to the data from Step 5 was achieved in this case.

Test kaz28 is a clear example in which a better overall fit was achieved by the Hoek-Brown model over the Mohr-Coulomb model. However, the equivalent friction angle determined by the Hoek-Brown method was significantly higher than that determined by the Mohr-Coulomb model, an important insight that could have resulted from a poor determination of *in situ* stress or incorrect formulation for determining σ_{3max}. Therefore valuable insight can be gained by modeling the test with both methods.

The results of analyzing test sr710-12 in interbedded siltstone and sandstone is presented in Figure 4.29. Despite the additional complications arising from dealing with two different types of rock behavior, both the Hoek-Brown model and Mohr-Coulomb model adequately fit the pressuremeter data curve. This is a case of fairly weak sedimentary rock which may have characteristics similar to soil, aiding in the nice fit accomplished by the Mohr-Coulomb model. No shift in strain origin was required for this test indicating low levels of disturbance from drilling action and stress relief. Without disturbance, it is easier to determine the *in situ* lateral stress, which leads to easier determination of other input parameters. Perhaps not coincidentally then, the equivalent Hoek-Brown friction angle matches that used in the Mohr-Coulomb model. However, the equivalent cohesion did require a small adjustment from an initial value of 0.018 MPa to 0.05 MPa.

Disturbance can heavily influence the initial part of the pressuremeter data curve, which in turn affects the ease in which that data can be analyzed. Greater judgment is required for a disturbed test, which can affect the input parameters required to achieve a good fit and thus alter strength parameters determined. Typically the initial disturbance is overcome as loading is increased during a test and a new strain origin can be established for analysis, but this requires experience, judgment and some imagination. Highly disturbed tests should not be analyzed for strength properties. Test sr710-12 is ideal for pressuremeter analysis in that it represents very high quality data. That is not to say, however, tests that require a shift in origin or have small levels of disturbance are not representative of high quality data.

An example of a high quality test with minor disturbance is given in Figure 4.30 for test crc06 in cemented cobbles & gravels. Test crc06 represents a much stiffer and stronger formation than test sr710-12, but yields similar results. The fit achieved by both models is reasonably good, with a slightly better fit achieved by the Hoek-Brown model (likely a result of the non-linear yield criterion). In this case, the data was ably modeled by the Mohr-Coulomb model using the exact equivalent $c-\phi$ values determined by the Hoek-Brown analysis.

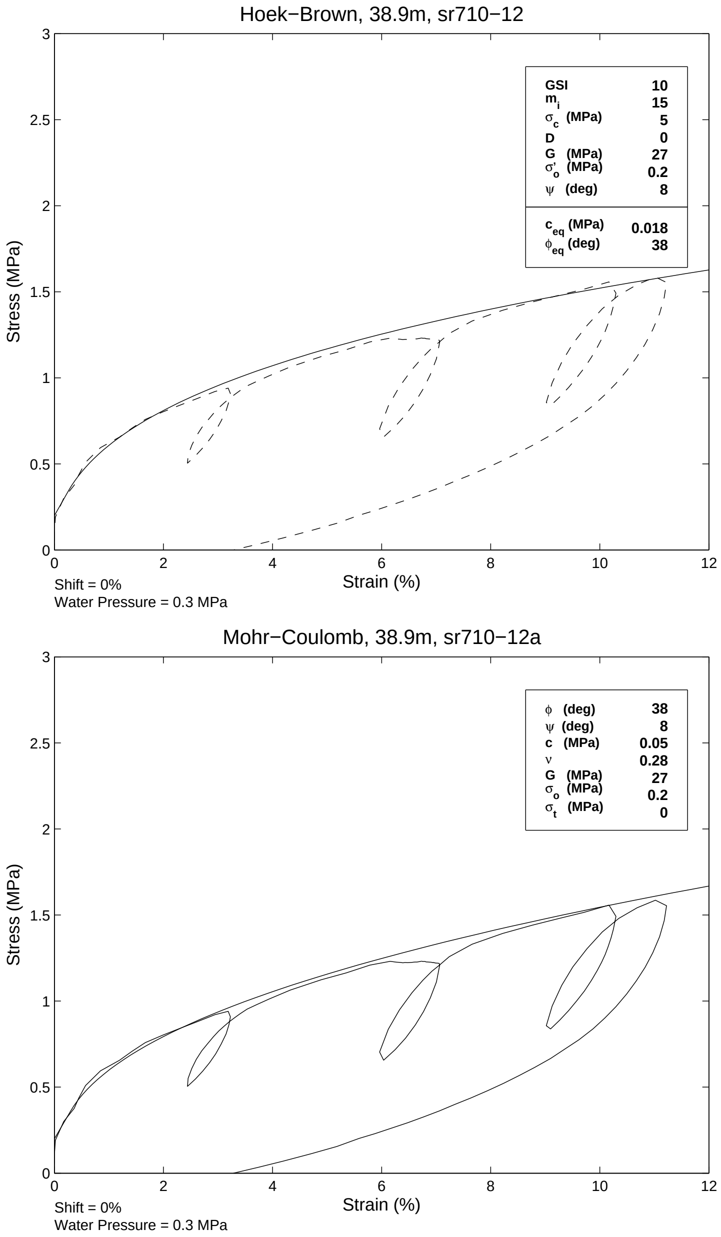

Figure 4.29: Comparison of Hoek-Brown modeling of data (top plot) versus Mohr-Coulomb modeling of data (bottom plot) for test sr710-12 in interbedded siltstone and sandstone.

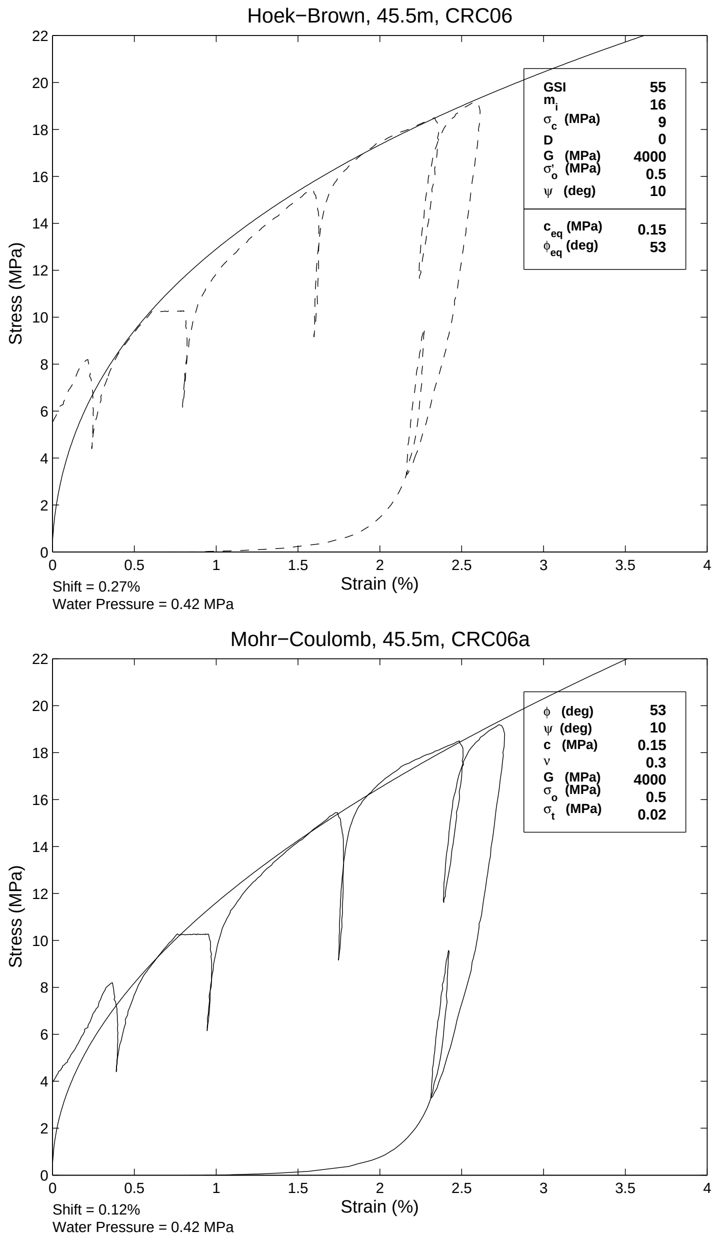

Figure 4.30: Comparison of Hoek-Brown modeling of data (top plot) versus Mohr-Coulomb modeling of data (bottom plot) for test crc06 in cemented cobbles & gravel.

The plots presented in this section were included to provide insight into the methodology used in modeling the data and show examples of how the Mohr-Coulomb model and Hoek-Brown model compared to one another for different rock formations. Typically, the equivalent $c - \phi$ values determined through the Hoek-Brown method could be used as inputs to the Mohr-Coulomb model to accomplish a reasonable fit to the data. However, some of the data, such as test kaz28, required shifts of the equivalent $c - \phi$ parameters and thus the method was not always reliable. This is likely a result of the formulation used to determine the equivalent strength values and should not suggest that the Hoek-Brown modeling parameters are invalid. The Hoek-Brown model typically was able to provide an ample fit to the data given a realistic range of inputs for each test, the results of which are presented in Appendix A. There were some tests in which the material behavior was more erratic or large amounts of disturbance was present. For these tests a poor fit was achieved with both models, however, this is an expected result as it is not realistic for an idealized pressuremeter curve to accurately model a much less than ideal data curve. Overall, the Hoek-Brown model showed much promise and performed well in modeling a large data set with many different rock formations. The Mohr-Coulomb model also performed well, but usually provided a qualitatively worse fit to the data than the Hoek-Brown model. Further discussion of the two models and possible reasons for this result are presented in the following chapter.

Chapter 5

CONCLUSIONS AND FUTURE WORK

Three models were explored for the analysis of pressuremeter data in weak to moderately weak rock. A Mohr-Coulomb model with a tensile cutoff developed by Haberfield and a Hoek-Brown model initiated by Yang *et al.* and further developed by the author were implemented and tested against a data set consisting of 5 sites and 115 pressuremeter tests. Development of a multiscale damage model established by Kondo *et al.* was begun, but requires further work. The framework for these models and methods of analysis have been laid out extensively in the previous chapters and sample plots of the Hoek-Brown model for all tests is given in the following Appendix. This section will provide some concluding remarks and thoughts on the models explored.

The main focus of this thesis was the calibration and comparison of the Hoek-Brown pressuremeter model to the Mohr-Coulomb model with a tensile cutoff. It was determined that given a realistic range of parameter input values, a good fit could be achieved between the idealized Hoek-Brown pressuremeter model and the pressuremeter data. Using an equivalent cohesion and friction angle (determined through the Hoek-Brown formulation), while keeping overlapping parameter inputs constant, a good fit between the Mohr-Coulomb model and the pressuremeter data could also be achieved. Therefore, both models could feasibly be used for pressuremeter analysis for a number of different rock types and formations. In general the Hoek-Brown model produced a qualitatively better overall fit to the data analyzed. However, there are advantages and disadvantages to each.

5.1 Discussion of Models

Mohr-Coulomb

Advantages

- The tensile cutoff provides separation between analysis as a continuum with no fracturing and analysis of a medium in which cracks form and propagate.

- Cohesion and Friction Angle are directly determined, parameters required in many engineering programs which use a Mohr-Coulomb failure criterion for modeling.

- The input of dilation angle (which is more abstract and can be difficult to determine unless other methods are used) can be replaced with the residual friction angle using Rowe's dilatancy theory or the more simple relationship proposed by Haberfield [10] of $\phi = \phi_r + \psi$, which is often known or more easily determined for different rock types.

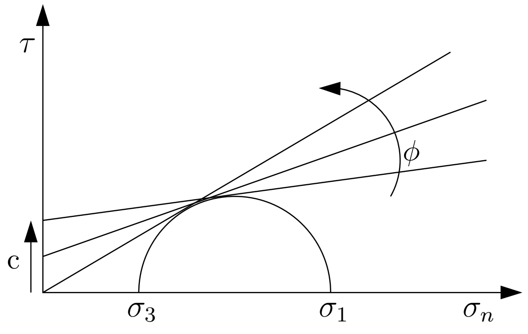

Figure 5.1: Different Mohr-Coulomb Failure Envelopes for the Same Failures Stress State.

Disadvantages

- If the tensile cutoff is reached, the empirical equation applied for modeling a fractured media did not provide a good fit for most of the data analyzed. Thus a new equation must be developed for rock types other than the mudstone analyzed by Haberfield.

- The model does not account for preexisting fractures which are almost always present in rock formations. Due to the existing fractures, it may not be realistic for the additional circumferential stress induced by the pressuremeter loading to create new fractures because the tensile stress at the preexisting fractures faces would be zero. Likely the result would be movement or further propagation of preexisting fractures, which were not considered in the development of this model.

- The Mohr-Coulomb failure criterion is linear, which is not true of rock mass behavior.

- Many possible combinations of cohesion and friction angle can produce a similar idealized pressuremeter curve. Thus, the choice of correct values for these two parameters would be difficult to determine realistically through modeling pressuremeter data. This idea is demonstrated in Figure 5.1 for a given failure stress state. This issue is reduced for a non-linear failure criterion.

Hoek-Brown

Advantages

- The Hoek-Brown failure criterion was developed for the purpose of rock analysis (unlike Mohr-Coulomb which was developed for soil analysis) and has been updated continuously as more rock data and knowledge become available.

- The failure criterion is non-linear, which is true of typical rock behavior. A result of the non-linearity is to provide a cap to potential rock strength at higher stresses.

- Some model input parameters, such as GSI and m_i, can be determined qualitatively or through use of charts for different rock types. This allows focus to be on determining other strength parameters through the modeling of pressuremeter data. Typically coring is part of the process for pressuremeter testing in rock and thus parameters such as GSI could be determined at the location of pressuremeter tests.

- Preexisting fractures are accounted for through the GSI system. Intact rock can also be considered by setting $GSI = 100$.

- Equivalent cohesion and friction angles as well as other rock mass properties (such as tensile strength) can be determined if engineering programs requires such inputs for design analysis.

- Model is valid for both weak and strong rock and has been extended to interbedded rock formations.

Disadvantages

- Determination of equivalent cohesion and friction angles is highly sensitive to the choice of σ_{3max}. Because typically low values of σ_{3max} were used in this analysis, it is likely that equivalent friction angles determined were unrealistically high and equivalent cohesion values determined unrealistically low.

- Determination of the dilation angle could be difficult unless most of the other input parameters are defined by other methods. Relations such as Rowe's dilatancy theory could be applied using the equivalent friction angle determined. However, this could have error due to the reasons listed in the bullet above.

Weighing the advantages and disadvantages of the two models, it appears the Hoek-Brown model is better suited for analyzing pressuremeter tests in rock. In particular it should be emphasized that the Hoek-Brown model can account for preexisting fractures (almost always present) through the GSI system, while the Mohr-Coulomb model cannot, which may, along with the inclusion of failure criterion non-linearity, be the reason that better modeling results were accomplished. Furthermore, determination of an equivalent cohesion and friction angle is becoming less important as a number of engineering programs have implemented the Hoek-Brown failure criterion for modeling purposes. However, challenges still exist. The level of dilation that occurs can have a significant effect on material behavior and choice of the input value for dilation angle can have a large impact on the idealized pressuremeter curve produced (see Figure 3.31). Unless extensive external analysis is performed, the dilation angle would likely always be a parameter that must be determined through analysis of pressuremeter data. This narrows the ability to model the pressuremeter data for the purpose of determining other parameters such as the lateral *in situ* stress or uniaxial compressive strength. Perhaps then it would be wise to attempt to model data with both models as was done in this study. Doing so provided a check for the equivalent cohesion and friction angle values determined by the Hoek-Brown model, while providing insight into adjustments that could be made to the input parameters. It is also possible that for certain rock formations, the Mohr-Coulomb model would provide a better fit to the data than the Hoek-Brown model and vice versa and thus both models should be checked.

The use of either model would always require that some variables are determined through external testing. For this reason, Haberfield suggested that pressuremeter data in rock should not be analyzed for strength properties and perhaps should only be used in determining the shear modulus [11]. However, it is unrealistic to expect that all strength properties can be analyzed through one form of testing, especially in working with the complexities that exist in a rock mass, where many potential fracture patterns can exist. This requires knowledge on a site by site basis. The pressuremeter is unique in that it has the capability to test rock mass strength *in situ* while considering a much larger volume of a rock formation than a laboratory test on a core sample can provide. Thus, if some strength parameters, such as GSI, can be determined through other means, the pressuremeter data can be used to then define those parameters left undetermined. In the best case, if all variables controlling rock behavior are known, pressuremeter data can be used as confirmation of those parameters.

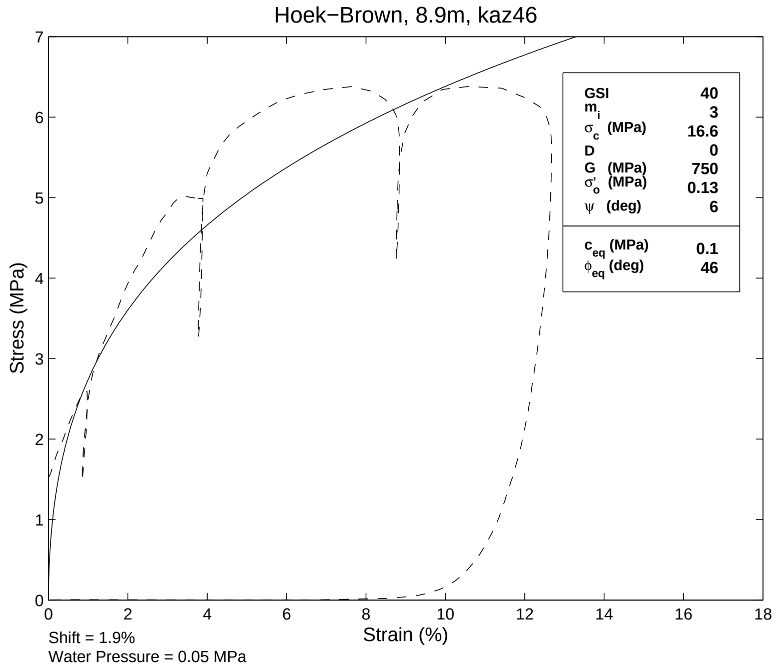

Figure 5.2: Test kaz46 Fitted with Idealized Hoek-Brown Pressuremeter Curve.

Judgment will always be required in the use of proper analysis techniques. As more knowledge is gained, techniques and models improve. There will always be pressuremeter tests in rock that are difficult to analyze or to fit a proper idealized model to as illustrated in Figure 5.2, in which rapid brittle failure occurs. However, the data collected by pressuremeter testing can be a very powerful tool for determination of material parameters if analyzed properly. These parameters can then be used as inputs into engineering and modeling programs for design. For this reason, it is important that model development and proper analysis techniques continue to be explored for pressuremeter data collected in weak rock.

5.2 Future Work

A number of different directions could be pursued for analyzing weak rock pressuremeter data. They are listed here in bullet form.

- Further exploration of the Hoek-Brown model. More data in which input parameters are determined by external methods could be used towards calibrating the model further. The Hoek-Brown model could also be implemented into a finite element program in an attempt to model different fracture patterns directly instead of modeling as an equivalent continuum.

- More research could be performed on the best choice for σ_{3max} in determining equivalent cohesion and friction angles from the Hoek-Brown parameters in regards to pressuremeter loading. The empirical equation determining σ_{3max} for tunnels was used in this research.

- Non-linear elastic behavior could be explored as opposed to the linear elastic behavior assumed here. Using a power law function, this has been employed with success by Bolton and Whittle for clay in [4].

- Development of the multiscale damage model into a pressuremeter framework. A feasibility study could be performed. The multiscale model requires a similar number of inputs, but allows for the inclusion of fractures at different orientations. There would be added complexity due to the choice of fracture orientation. Therefore the effect of the number of fractures and orientation of those fractures would have to be explored.

- Exploration of other rock models and methods not covered or discussed in this thesis. Finite element modeling and mathematical curve fitting are two such methods that could be explored. Many other constitutive rock models could be found and tested against rock data sets.

We have reached the end! Any questions regarding this thesis can be directed towards the author at dafnij@uw.edu.

Appendix A

HOEK-BROWN MODELING PLOTS FOR ALL DATA

This Appendix consists of 115 pressuremeters tests in weak to moderately weak rock. The data has been compared to an idealized pressuremeter curve to establish a best fit to the loading portion of the data. A Hoek-Brown model was used to create the idealized pressuremeter curve. Typically pressuremeter data is modeled in this way (using a chosen pressuremeter model based on the material formation) in order to determine material parameters for use in geotechnical design. The data analyzed here was used as a calibration, or test, of the Hoek-Brown model against data from a wide range of weak rock formations.

Each of the figures on the following pages represents a pressuremeter test with an idealized pressuremeter curve fit to the data. The dashed line represents the pressuremeter data, while the solid line represents the idealized pressuremeter curve. The input parameters are given in the text box in the upper right-hand corner of the figures. The equivalent Mohr-Coulomb parameters determined as described in Chapter 4 are given in the lower portion of the text box. The origin shift and shift due to water pressure are given below the graph in each figure. The test depth and test name are given in the graph title of each figure.

The data has been divided by the site in which the pressuremeter tests were performed. A summary of the test names, rock type and test depth are given for each site in each section prior to the plotted data.

A.1 Site 1

Table A.1: Test Information for Site 1

Borehole	**Test Name**	**Depth (m)**	**Rock Type**
1	CRC02	73.9	Cemented Cobble & Gravel Matrix
1	CRC01	74.4	Cemented Cobble & Gravel Matrix
2	CRC05	39.8	Cemented Cobble & Gravel Matrix
2	CRC06	45.5	Cemented Cobble & Gravel Matrix

Tests are organized by borehole and are presented from the shallowest to deepest for each borehole. Numbering of tests is according to the order in which the tests were performed. It is common that a deeper test is performed first in a given test pocket and thus the shallowest test will not necessarily correspond to the lowest test number. Note that the ordering of the tests is CRC02, then CRC01.

Expected tests not listed (such as CRC03 or CRC04 - there is a jump from CRC02 to CRC05 in the table above) were not analyzed because the data was either badly disturbed or the test pocket was too large to collect any useful data. This data therefore could not be analyzed.

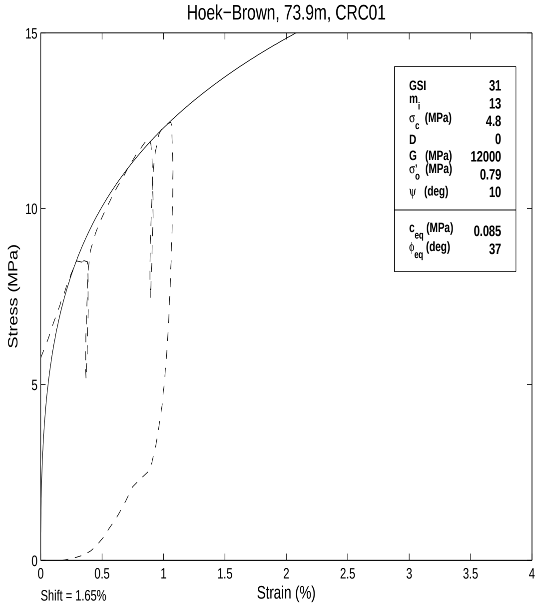

Shift = 1.65%
Water Pressure = 0.7 MPa

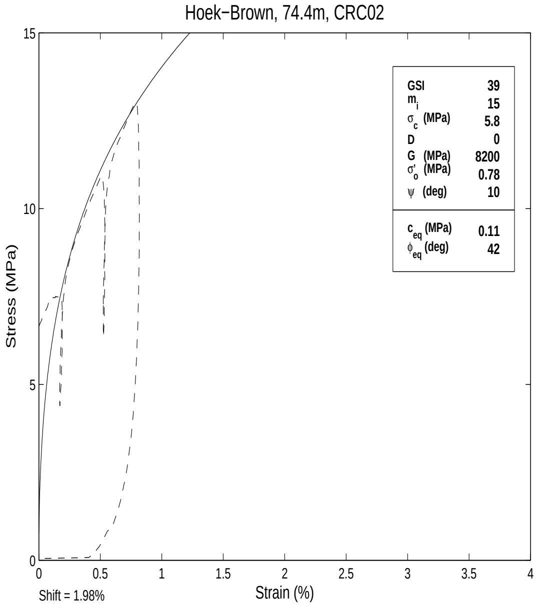

Shift = 1.98%
Water Pressure = 0.7 MPa

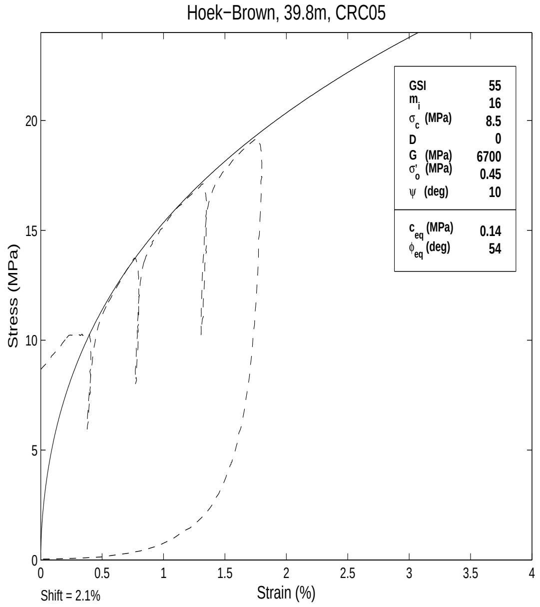

Shift = 2.1%
Water Pressure = 0.36 MPa

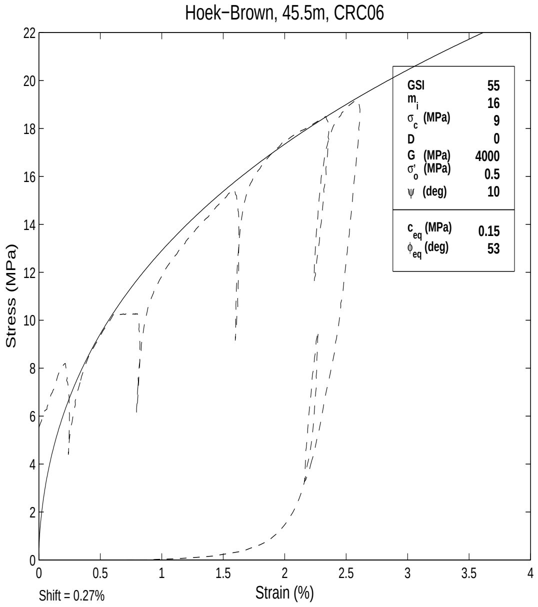

Shift = 0.27%
Water Pressure = 0.42 MPa

A.2 Site 2

Table A.2: Test Information for Site 2

Borehole	**Test Name**	**Depth (m)**	**Rock Type**
1	I-90-03	22.6	Meta Welded Lapilli Tuff
1	I-90-02	23.0	Meta Welded Lapilli Tuff
1	I-90-01	23.5	Meta Welded Lapilli Tuff
1	I-90-06	25.0	Meta Welded Lapilli Tuff
1	I-90-05	25.5	Meta Welded Lapilli Tuff
1	I-90-04	25.9	Meta Welded Lapilli Tuff
2	I-90-09	19.2	Meta Welded Lapilli Tuff
2	I-90-08	19.7	Meta Welded Lapilli Tuff
2	I-90-07	20.1	Meta Welded Lapilli Tuff
2	I-90-11	21.0	Meta Welded Lapilli Tuff
2	I-90-10	21.5	Meta Welded Lapilli Tuff
2	I-90-14	23.2	Meta Welded Lapilli Tuff
2	I-90-13	23.6	Meta Welded Lapilli Tuff
2	I-90-12	24.1	Meta Welded Lapilli Tuff
3	I-90-17	15.2	Meta Welded Lapilli Tuff
3	I-90-16	15.9	Meta Welded Lapilli Tuff
3	I-90-15	16.5	Meta Welded Lapilli Tuff
3	I-90-20	17.4	Meta Welded Lapilli Tuff
3	I-90-19	18.1	Meta Welded Lapilli Tuff
3	I-90-18	18.9	Meta Welded Lapilli Tuff
3	I-90-22	19.8	Meta Welded Lapilli Tuff
3	I-90-21	20.4	Meta Welded Lapilli Tuff

The same organization as discussed for Site 1 applies here.

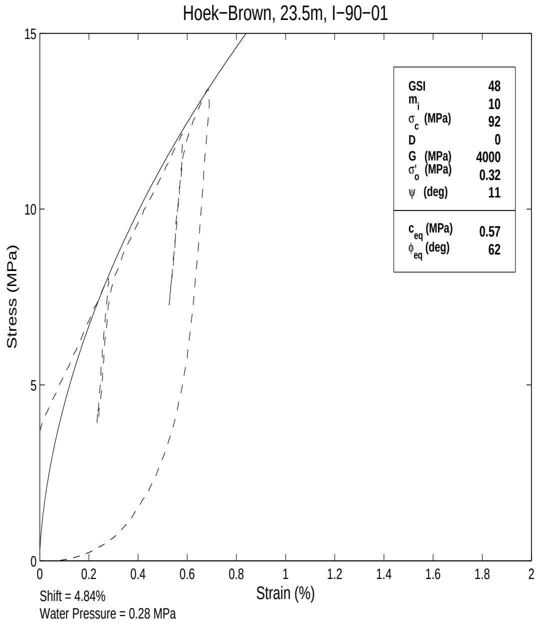
Hoek−Brown, 23.5m, I−90−01
GSI 48
m_i 10
σ_c (MPa) 92
D 0
G (MPa) 4000
σ'_o (MPa) 0.32
ψ (deg) 11
c_eq (MPa) 0.57
φ_eq (deg) 62
Stress (MPa)
0
5
10
15
0
0.2
0.4
0.6
0.8
1
1.2
1.4
1.6
1.8
2
Strain (%)
Shift = 4.84%
Water Pressure = 0.28 MPa

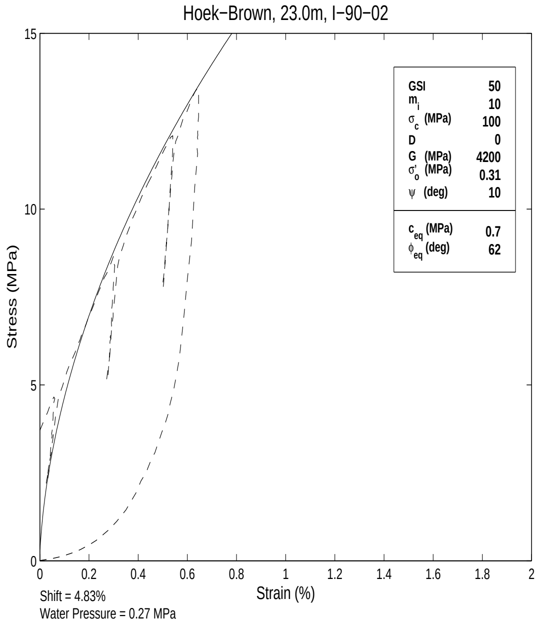
Hoek−Brown, 23.0m, I−90−02
GSI 50
m_i 10
σ_c (MPa) 100
D 0
G (MPa) 4200
σ'_o (MPa) 0.31
ψ (deg) 10
c_eq (MPa) 0.7
φ_eq (deg) 62
Stress (MPa)
0
5
10
15
0
0.2
0.4
0.6
0.8
1
1.2
1.4
1.6
1.8
2
Strain (%)
Shift = 4.83%
Water Pressure = 0.27 MPa

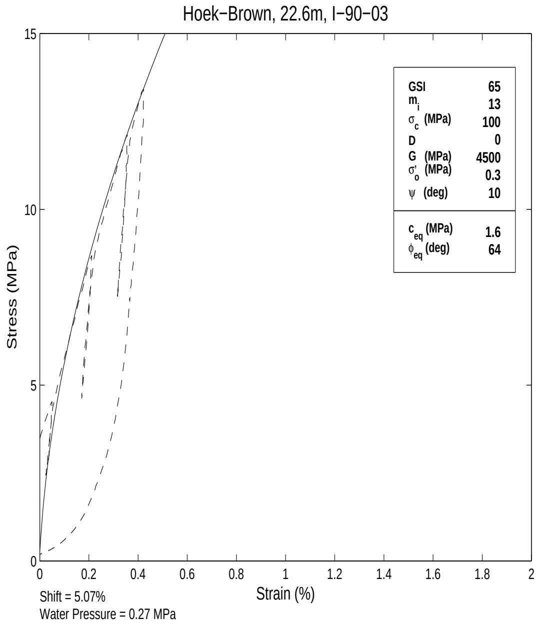
Hoek−Brown, 22.6m, I−90−03
GSI 65
m_i 13
σ_c (MPa) 100
D 0
G (MPa) 4500
σ'_o (MPa) 0.3
ψ (deg) 10
c_eq (MPa) 1.6
φ_eq (deg) 64
Stress (MPa)
0
5
10
15
0
0.2
0.4
0.6
0.8
1
1.2
1.4
1.6
1.8
2
Strain (%)
Shift = 5.07%
Water Pressure = 0.27 MPa

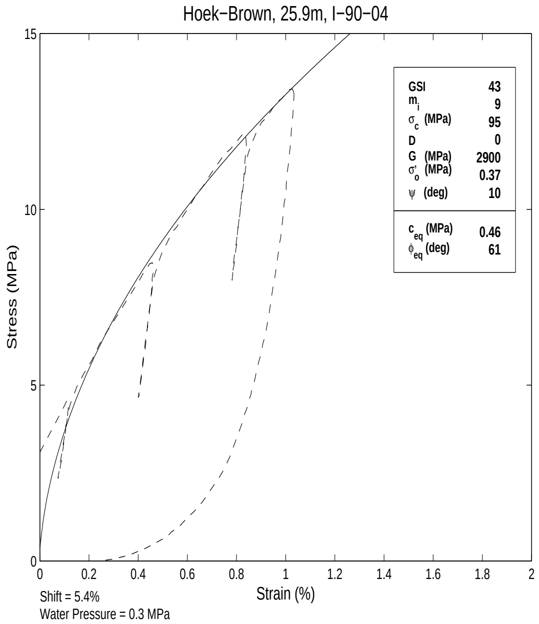
Hoek−Brown, 25.9m, I−90−04
GSI 43
m_i 9
σ_c (MPa) 95
D 0
G (MPa) 2900
σ'_o (MPa) 0.37
ψ (deg) 10
c_eq (MPa) 0.46
φ_eq (deg) 61
Stress (MPa)
0
5
10
15
0
0.2
0.4
0.6
0.8
1
1.2
1.4
1.6
1.8
2
Strain (%)
Shift = 5.4%
Water Pressure = 0.3 MPa

Hoek−Brown, 25.5m, I−90−05

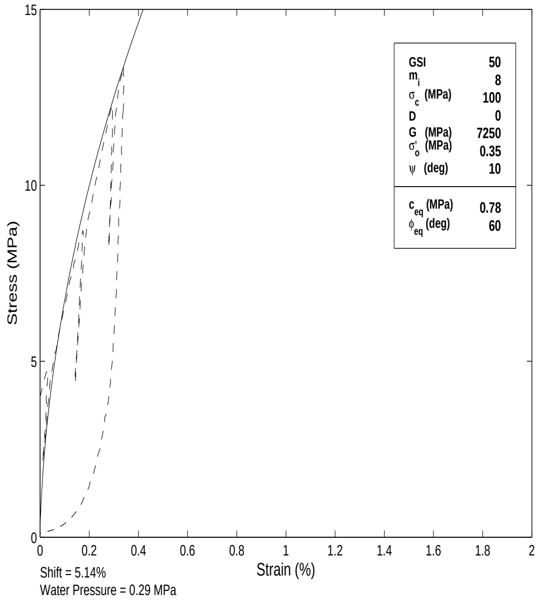

Shift = 5.14%
Water Pressure = 0.29 MPa

Hoek−Brown, 25.0m, I−90−06

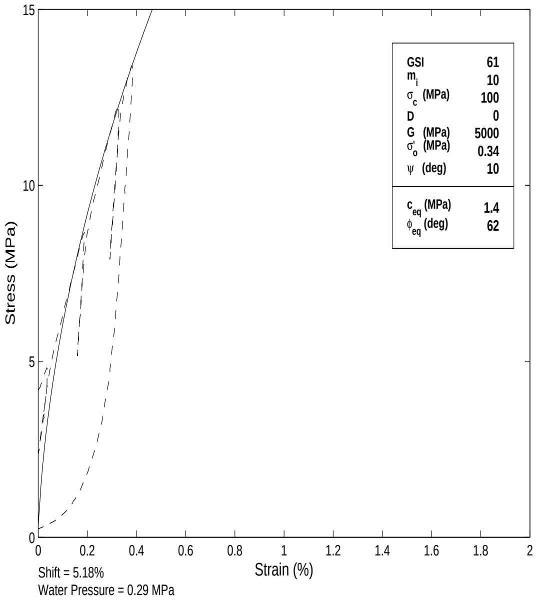

Shift = 5.18%
Water Pressure = 0.29 MPa

Hoek−Brown, 20.1m, I−90−07

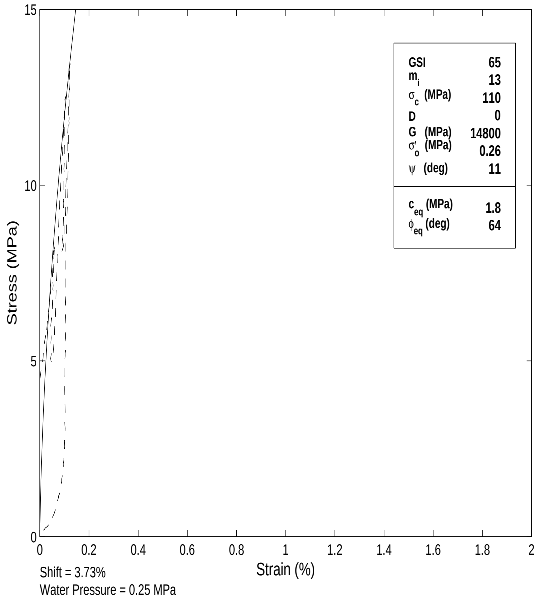

Shift = 3.73%
Water Pressure = 0.25 MPa

Hoek−Brown, 19.7m, I−90−08

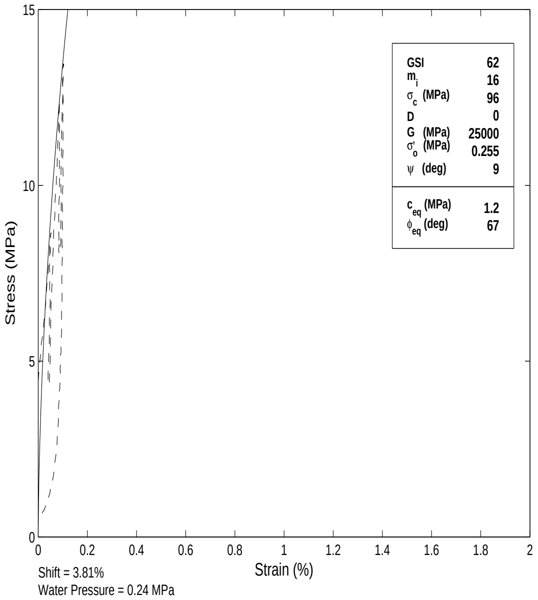

Shift = 3.81%
Water Pressure = 0.24 MPa

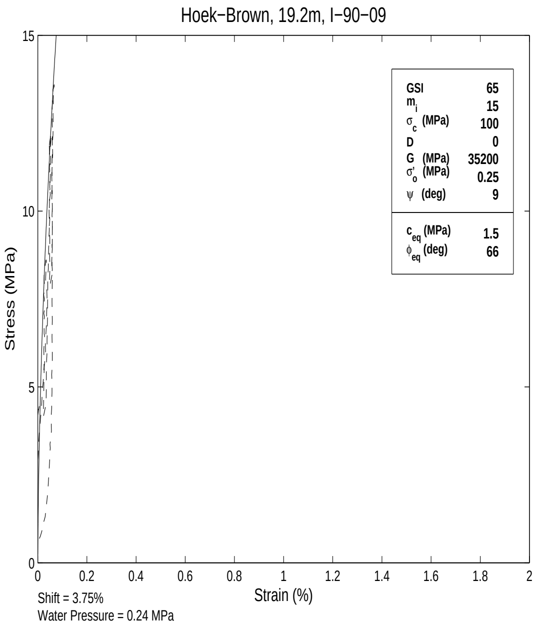
Hoek−Brown, 19.2m, I−90−09
Stress (MPa)
Strain (%)
0
5
10
15
0
0.2
0.4
0.6
0.8
1
1.2
1.4
1.6
1.8
2
GSI 65
m_i 15
σ_c (MPa) 100
D 0
G (MPa) 35200
σ'_o (MPa) 0.25
ψ (deg) 9
c_{eq} (MPa) 1.5
ϕ_{eq} (deg) 66
Shift = 3.75%
Water Pressure = 0.24 MPa

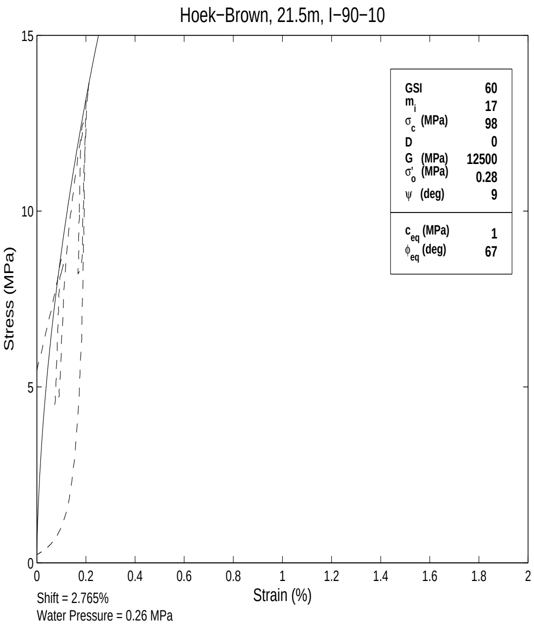
Hoek−Brown, 21.5m, I−90−10
Stress (MPa)
Strain (%)
0
5
10
15
0
0.2
0.4
0.6
0.8
1
1.2
1.4
1.6
1.8
2
GSI 60
m_i 17
σ_c (MPa) 98
D 0
G (MPa) 12500
σ'_o (MPa) 0.28
ψ (deg) 9
c_{eq} (MPa) 1
ϕ_{eq} (deg) 67
Shift = 2.765%
Water Pressure = 0.26 MPa

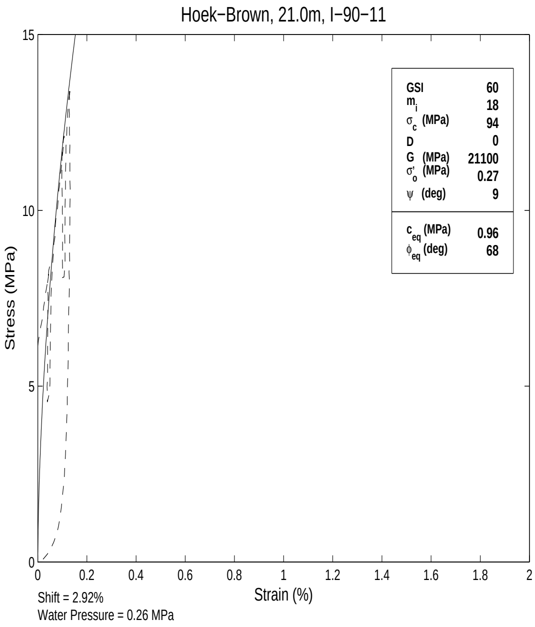
Hoek−Brown, 21.0m, I−90−11
Stress (MPa)
Strain (%)
0
5
10
15
0
0.2
0.4
0.6
0.8
1
1.2
1.4
1.6
1.8
2
GSI 60
m_i 18
σ_c (MPa) 94
D 0
G (MPa) 21100
σ'_o (MPa) 0.27
ψ (deg) 9
c_{eq} (MPa) 0.96
ϕ_{eq} (deg) 68
Shift = 2.92%
Water Pressure = 0.26 MPa

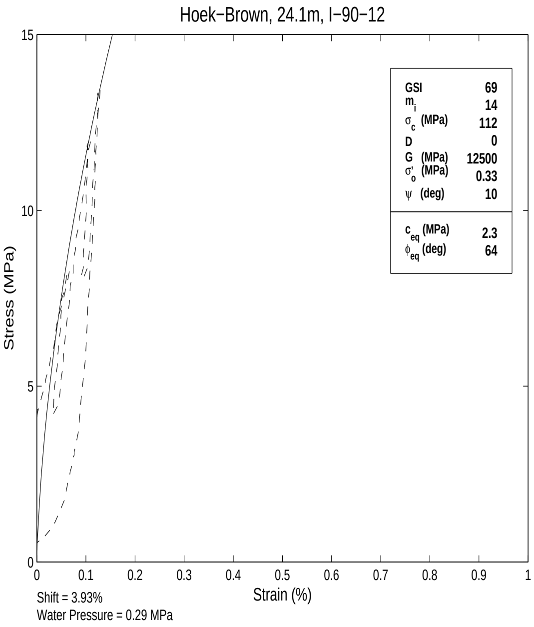
Hoek−Brown, 24.1m, I−90−12
Stress (MPa)
Strain (%)
0
5
10
15
0
0.1
0.2
0.3
0.4
0.5
0.6
0.7
0.8
0.9
1
GSI 69
m_i 14
σ_c (MPa) 112
D 0
G (MPa) 12500
σ'_o (MPa) 0.33
ψ (deg) 10
c_{eq} (MPa) 2.3
ϕ_{eq} (deg) 64
Shift = 3.93%
Water Pressure = 0.29 MPa

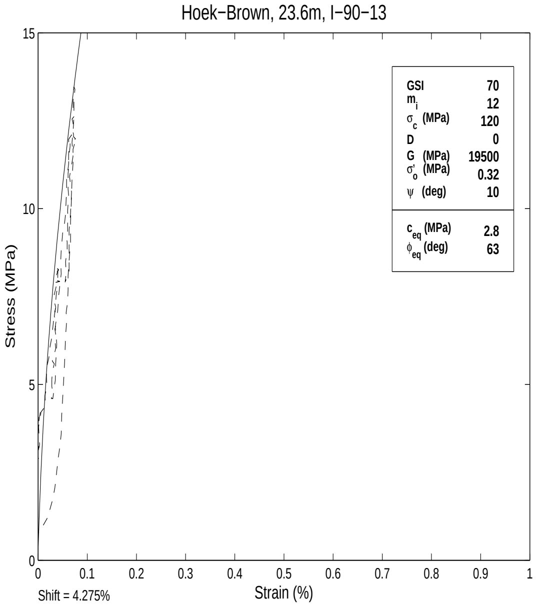

Shift = 4.275%
Water Pressure = 0.28 MPa

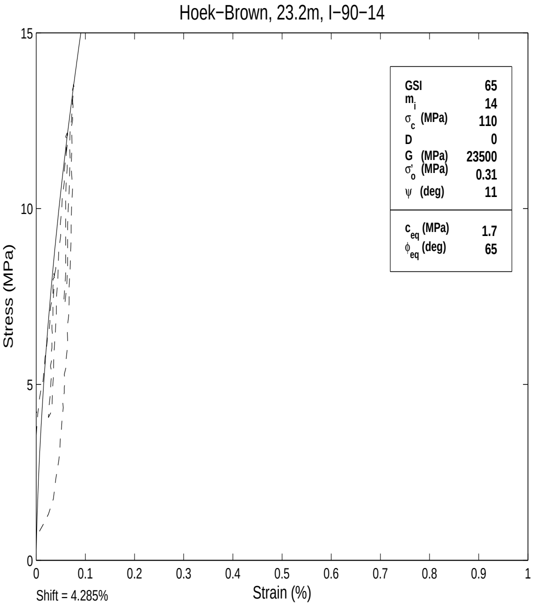

Shift = 4.285%
Water Pressure = 0.28 MPa

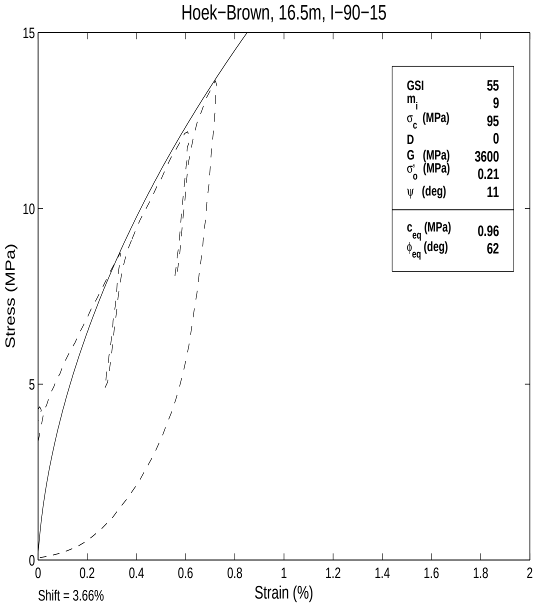

Shift = 3.66%
Water Pressure = 0.21 MPa

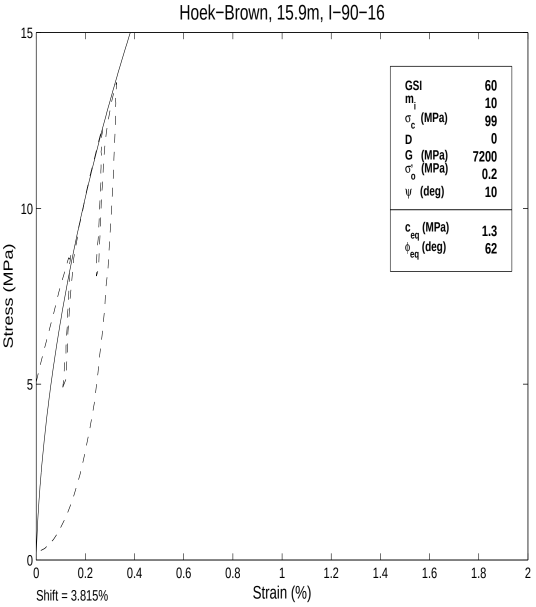

Shift = 3.815%
Water Pressure = 0.2 MPa

Hoek−Brown, 15.2m, I−90−17

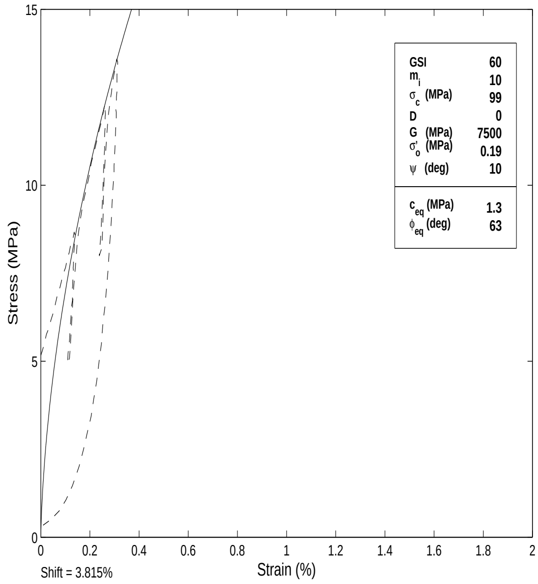

Shift = 3.815%
Water Pressure = 0.2 MPa

Hoek−Brown, 18.9m, I−90−18

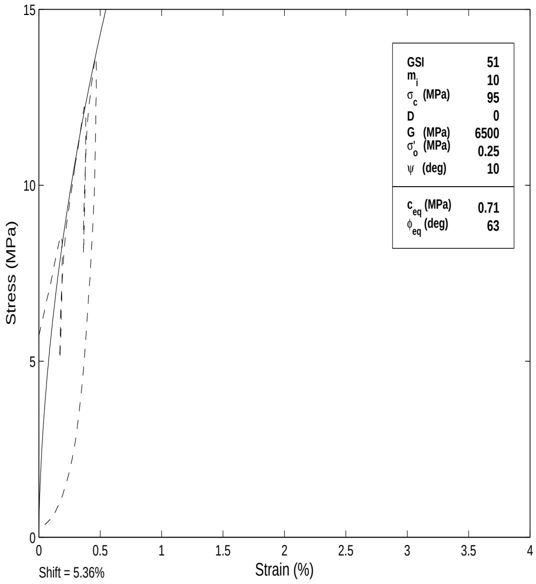

Shift = 5.36%
Water Pressure = 0.23 MPa

Hoek−Brown, 18.1m, I−90−19

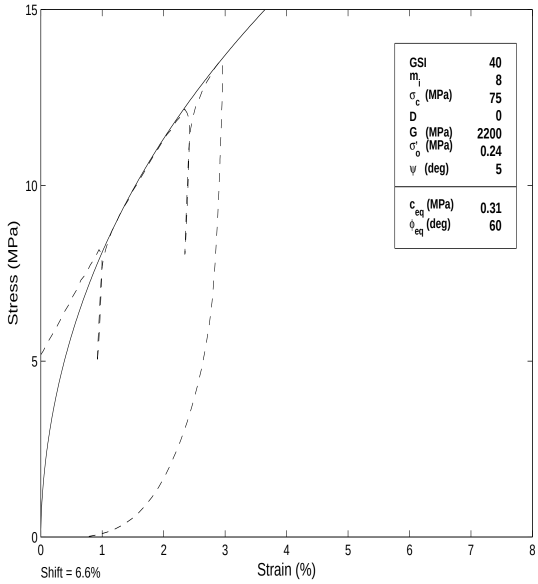

Shift = 6.6%
Water Pressure = 0.23 MPa

Hoek−Brown, 17.4m, I−90−20

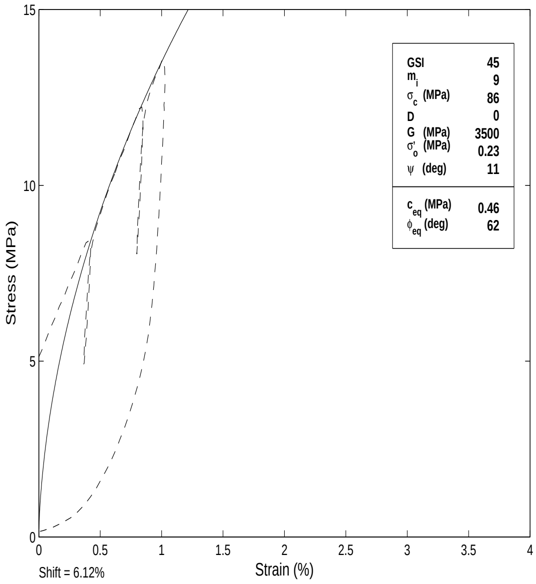

Shift = 6.12%
Water Pressure = 0.22 MPa

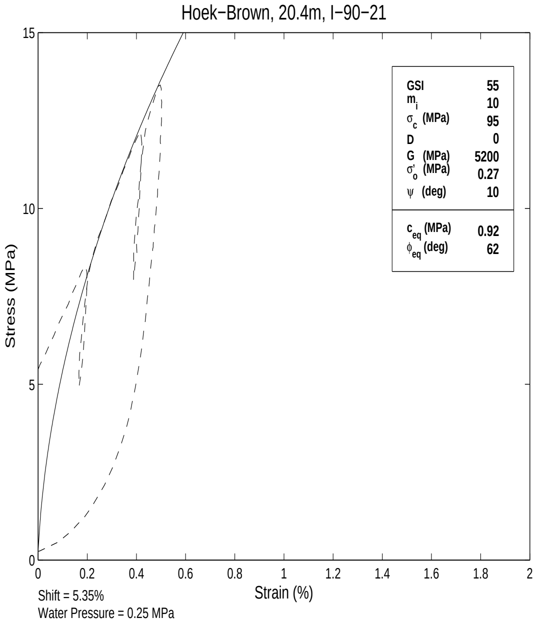

Hoek−Brown, 20.4m, I−90−21

Shift = 5.35%
Water Pressure = 0.25 MPa

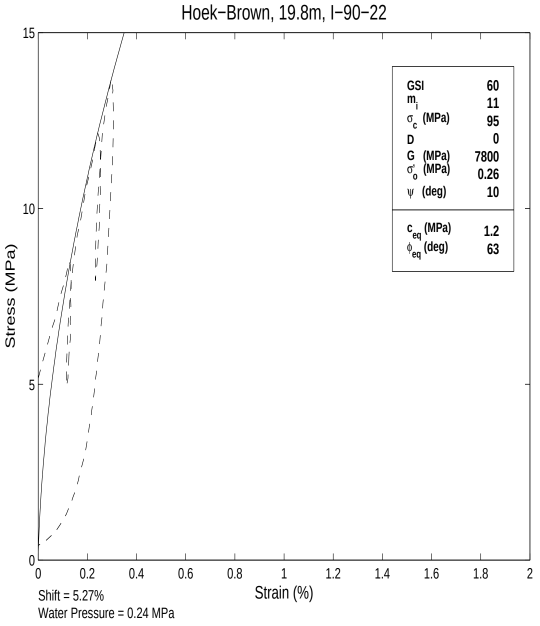

Hoek−Brown, 19.8m, I−90−22

Shift = 5.27%
Water Pressure = 0.24 MPa

A.3 Site 3

Table A.3: Test Information for Site 3 - Part I

Borehole	**Test Name**	**Depth (m)**	**Rock Type**
1	kaz01	2.0	Gruss
1	kaz03	3.0	Gruss
1	kaz02	4.0	Gruss
1	kaz05	5.0	Mudstone
1	kaz04	6.0	Mudstone
1	kaz07	7.0	Mudstone
1	kaz06	8.0	Mudstone
1	kaz08	9.0	Mudstone
2	kaz10	1.4	Gruss
2	kaz09	1.9	Gruss
2	kaz12	2.9	Gruss
2	kaz11	3.9	Gruss
2	kaz14	4.9	Gruss
2	kaz13	5.9	Gruss
2	kaz15	7.4	Crushed Stone
2	kaz17	8.4	Gruss
2	kaz16	9.4	Gruss
2	kaz19	11.3	Gruss
2	kaz18	12.3	Gruss
2	kaz21	16.4	Loam
2	kaz20	17.1	Loam

The same organization as discussed for Site 1 applies here.

Table A.4: Test Information for Site 3 - Part II

Borehole	**Test Name**	**Depth (m)**	**Rock Type**
3	kaz27	4.9	Loam
3	kaz26	5.9	Gruss
3	kaz29	6.9	Gruss
3	kaz28	7.9	Gruss
3	kaz31	8.9	Siltstone
3	kaz30	9.9	Crushed Stone
3	kaz33	10.9	Crushed Stone
3	kaz32	11.9	Siltstone
4	kaz35	1.2	Loam
4	kaz34	1.7	Loam
4	kaz38	5.9	Gruss
4	kaz41	6.9	Gruss
4	kaz40	7.4	Gruss
5	kaz47	7.9	Gruss
5	kaz46	8.9	Mudstone
5	kaz48	11.8	Mudstone
6	kaz49	6.2	Siltstone
6	kaz50	9.9	Siltstone
6	kaz51	13.5	Siltstone

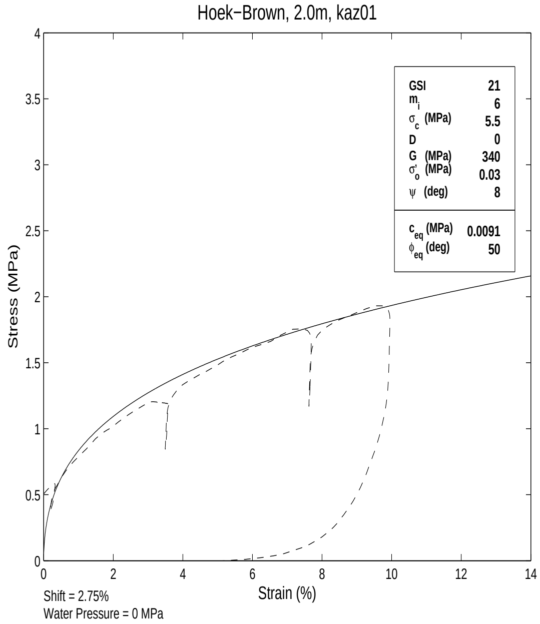
Hoek−Brown, 2.0m, kaz01
Stress (MPa)
Strain (%)
0
0.5
1
1.5
2
2.5
3
3.5
4
0
2
4
6
8
10
12
14
GSI 21
m$_i$ 6
σ$_c$ (MPa) 5.5
D 0
G (MPa) 340
σ$'_o$ (MPa) 0.03
ψ (deg) 8
c$_{eq}$ (MPa) 0.0091
φ$_{eq}$ (deg) 50
Shift = 2.75%
Water Pressure = 0 MPa

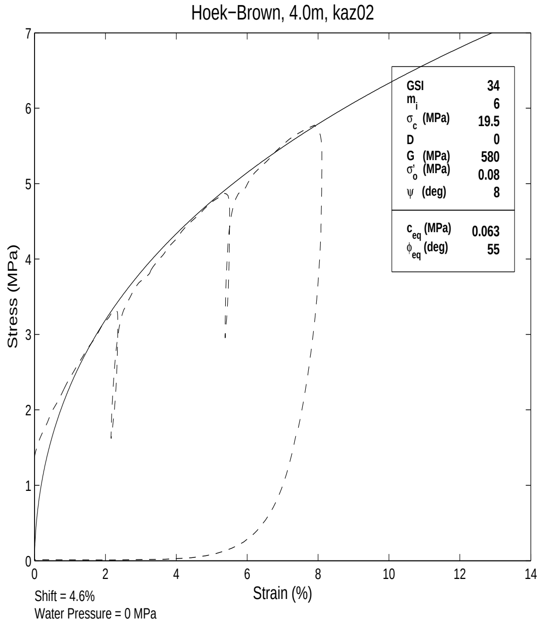
Hoek−Brown, 4.0m, kaz02
Stress (MPa)
Strain (%)
0
1
2
3
4
5
6
7
0
2
4
6
8
10
12
14
GSI 34
m$_i$ 6
σ$_c$ (MPa) 19.5
D 0
G (MPa) 580
σ$'_o$ (MPa) 0.08
ψ (deg) 8
c$_{eq}$ (MPa) 0.063
φ$_{eq}$ (deg) 55
Shift = 4.6%
Water Pressure = 0 MPa

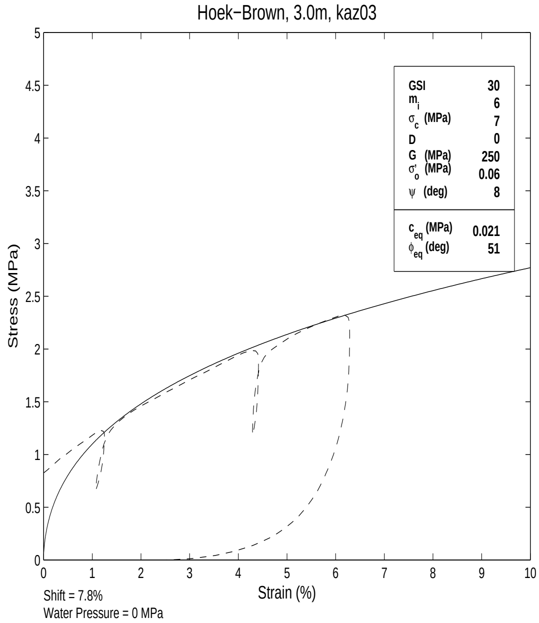
Hoek−Brown, 3.0m, kaz03
Stress (MPa)
Strain (%)
0
0.5
1
1.5
2
2.5
3
3.5
4
4.5
5
0
1
2
3
4
5
6
7
8
9
10
GSI 30
m$_i$ 6
σ$_c$ (MPa) 7
D 0
G (MPa) 250
σ$'_o$ (MPa) 0.06
ψ (deg) 8
c$_{eq}$ (MPa) 0.021
φ$_{eq}$ (deg) 51
Shift = 7.8%
Water Pressure = 0 MPa

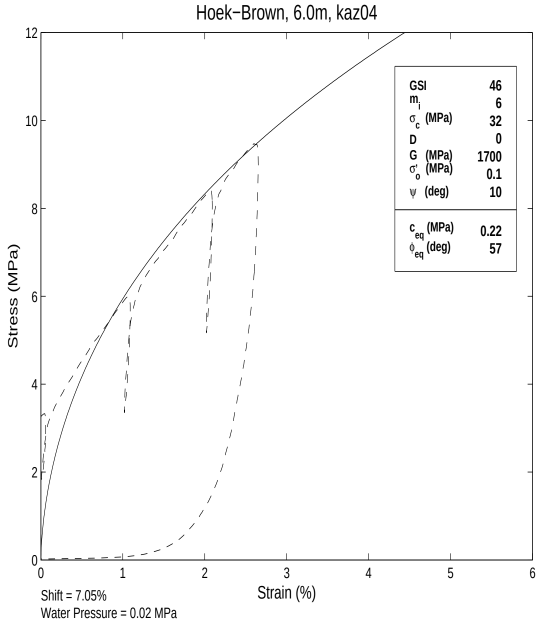
Hoek−Brown, 6.0m, kaz04
Stress (MPa)
Strain (%)
0
2
4
6
8
10
12
0
1
2
3
4
5
6
GSI 46
m$_i$ 6
σ$_c$ (MPa) 32
D 0
G (MPa) 1700
σ$'_o$ (MPa) 0.1
ψ (deg) 10
c$_{eq}$ (MPa) 0.22
φ$_{eq}$ (deg) 57
Shift = 7.05%
Water Pressure = 0.02 MPa

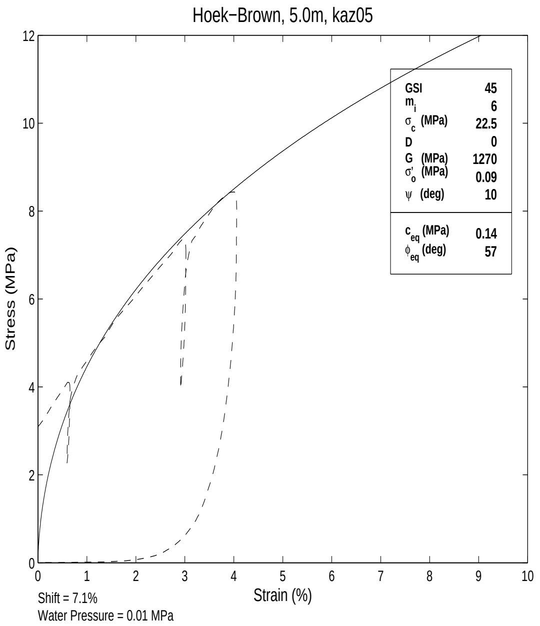
Hoek−Brown, 5.0m, kaz05
Stress (MPa)
Strain (%)
GSI 45
m_i 6
σ_c (MPa) 22.5
D 0
G (MPa) 1270
σ'_o (MPa) 0.09
ψ (deg) 10
c_{eq} (MPa) 0.14
ϕ_{eq} (deg) 57
Shift = 7.1%
Water Pressure = 0.01 MPa

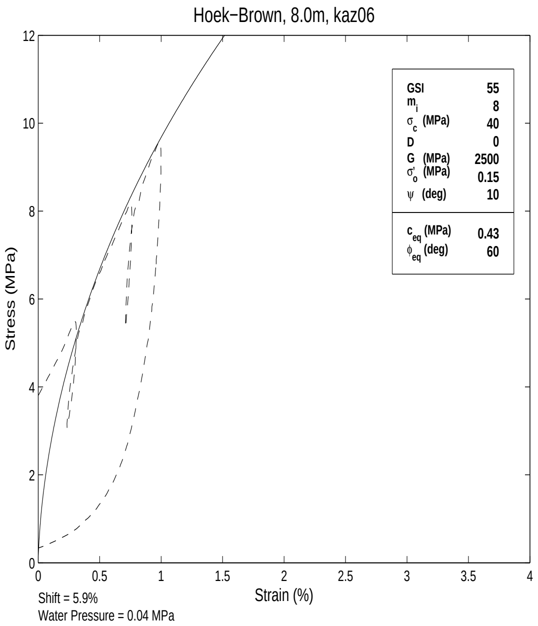
Hoek−Brown, 8.0m, kaz06
Stress (MPa)
Strain (%)
GSI 55
m_i 8
σ_c (MPa) 40
D 0
G (MPa) 2500
σ'_o (MPa) 0.15
ψ (deg) 10
c_{eq} (MPa) 0.43
ϕ_{eq} (deg) 60
Shift = 5.9%
Water Pressure = 0.04 MPa

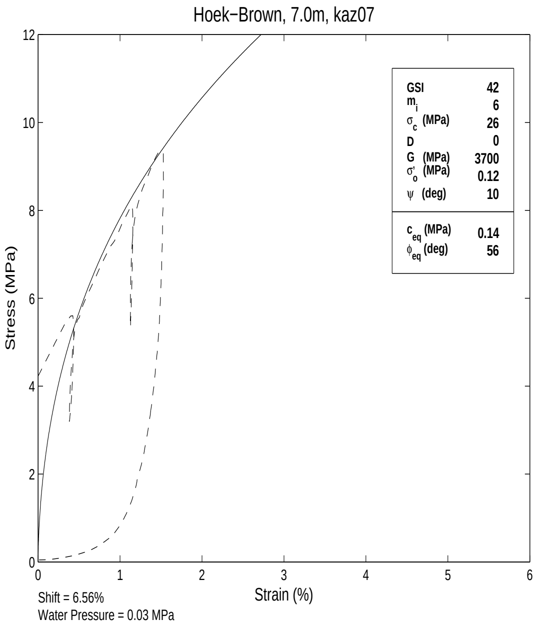
Hoek−Brown, 7.0m, kaz07
Stress (MPa)
Strain (%)
GSI 42
m_i 6
σ_c (MPa) 26
D 0
G (MPa) 3700
σ'_o (MPa) 0.12
ψ (deg) 10
c_{eq} (MPa) 0.14
ϕ_{eq} (deg) 56
Shift = 6.56%
Water Pressure = 0.03 MPa

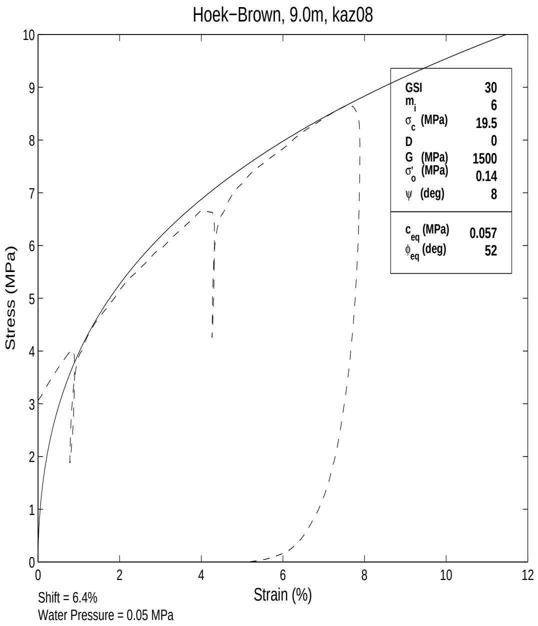
Hoek−Brown, 9.0m, kaz08
Stress (MPa)
Strain (%)
GSI 30
m_i 6
σ_c (MPa) 19.5
D 0
G (MPa) 1500
σ'_o (MPa) 0.14
ψ (deg) 8
c_{eq} (MPa) 0.057
ϕ_{eq} (deg) 52
Shift = 6.4%
Water Pressure = 0.05 MPa

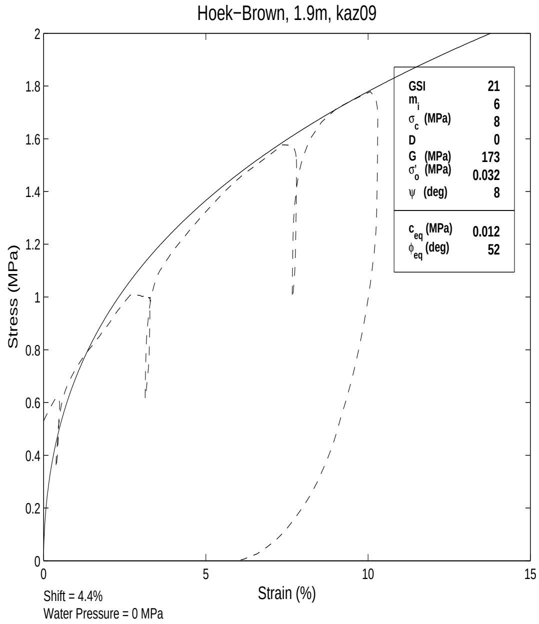
Hoek−Brown, 1.9m, kaz09
Stress (MPa)
Strain (%)
0
0.2
0.4
0.6
0.8
1
1.2
1.4
1.6
1.8
2
0
5
10
15
GSI 21
m_i 6
σ_c (MPa) 8
D 0
G (MPa) 173
σ'_o (MPa) 0.032
ψ (deg) 8
c_{eq} (MPa) 0.012
ϕ_{eq} (deg) 52
Shift = 4.4%
Water Pressure = 0 MPa

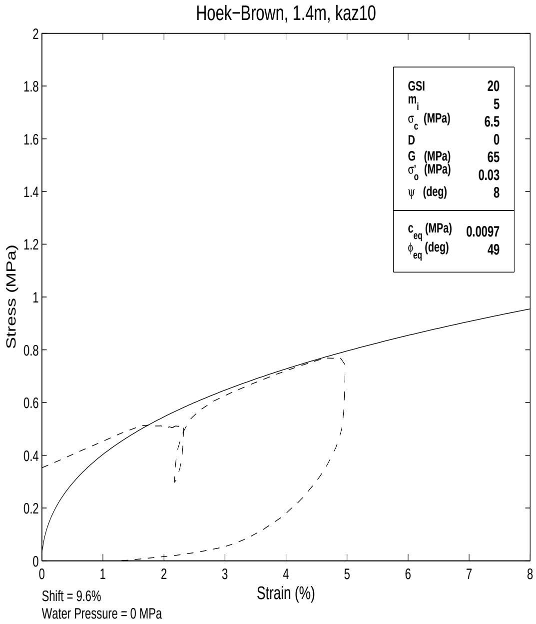
Hoek−Brown, 1.4m, kaz10
Stress (MPa)
Strain (%)
0
0.2
0.4
0.6
0.8
1
1.2
1.4
1.6
1.8
2
0
1
2
3
4
5
6
7
8
GSI 20
m_i 5
σ_c (MPa) 6.5
D 0
G (MPa) 65
σ'_o (MPa) 0.03
ψ (deg) 8
c_{eq} (MPa) 0.0097
ϕ_{eq} (deg) 49
Shift = 9.6%
Water Pressure = 0 MPa

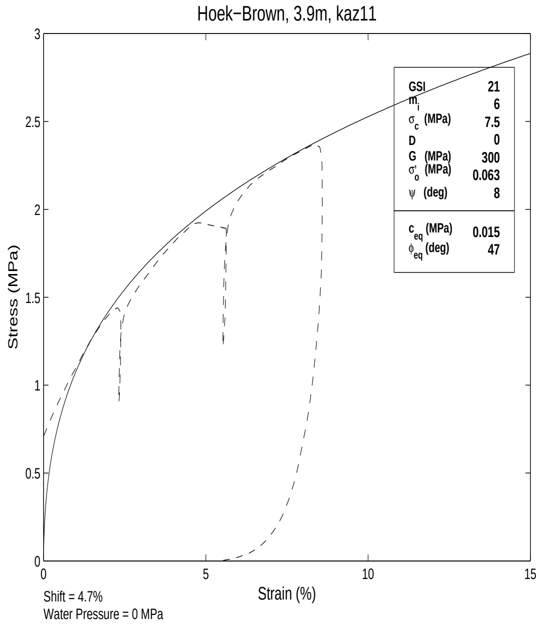
Hoek−Brown, 3.9m, kaz11
Stress (MPa)
Strain (%)
0
0.5
1
1.5
2
2.5
3
0
5
10
15
GSI 21
m_i 6
σ_c (MPa) 7.5
D 0
G (MPa) 300
σ'_o (MPa) 0.063
ψ (deg) 8
c_{eq} (MPa) 0.015
ϕ_{eq} (deg) 47
Shift = 4.7%
Water Pressure = 0 MPa

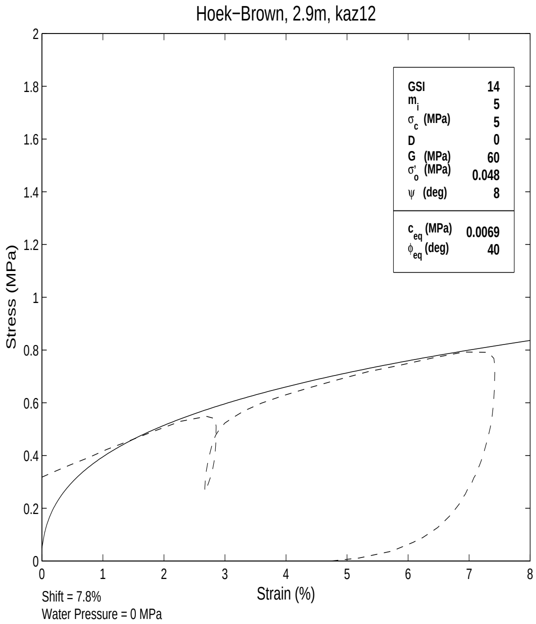
Hoek−Brown, 2.9m, kaz12
Stress (MPa)
Strain (%)
0
0.2
0.4
0.6
0.8
1
1.2
1.4
1.6
1.8
2
0
1
2
3
4
5
6
7
8
GSI 14
m_i 5
σ_c (MPa) 5
D 0
G (MPa) 60
σ'_o (MPa) 0.048
ψ (deg) 8
c_{eq} (MPa) 0.0069
ϕ_{eq} (deg) 40
Shift = 7.8%
Water Pressure = 0 MPa

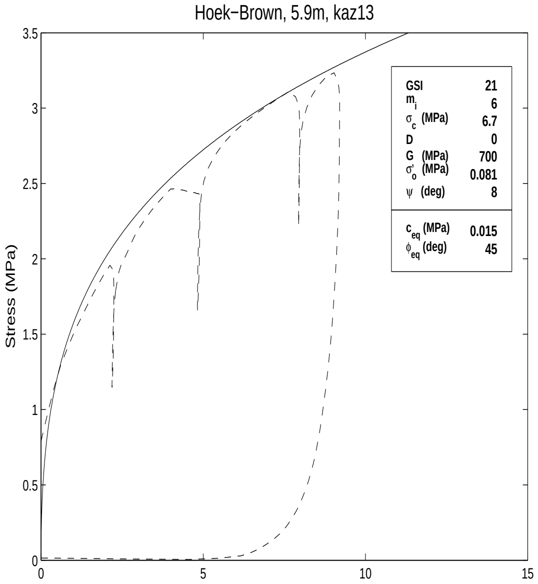

Shift = 5.85%
Water Pressure = 0.02 MPa

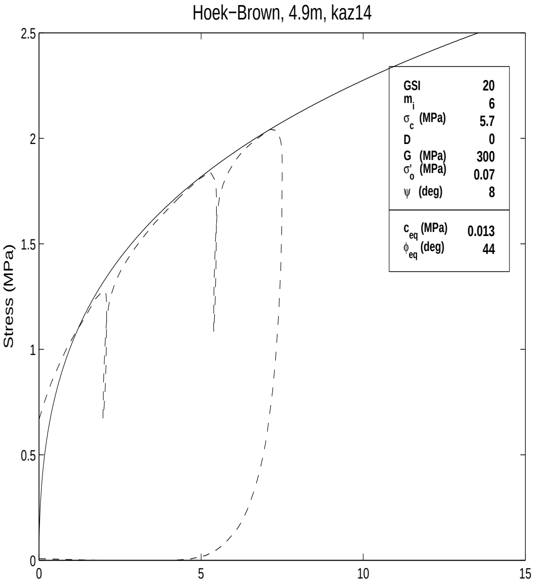

Shift = 8.1%
Water Pressure = 0.01 MPa

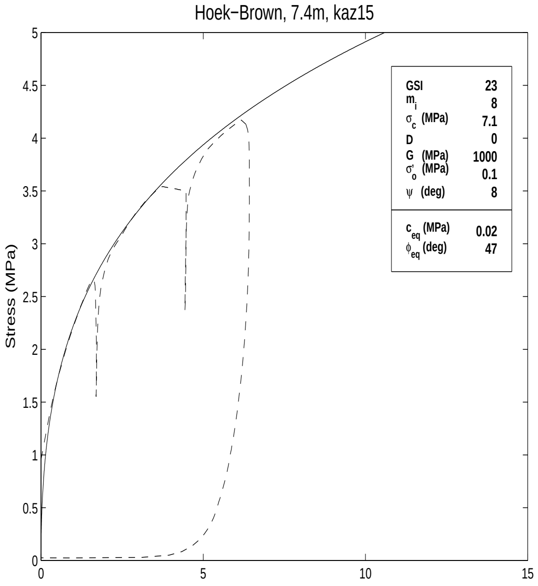

Shift = 6.6%
Water Pressure = 0.03 MPa

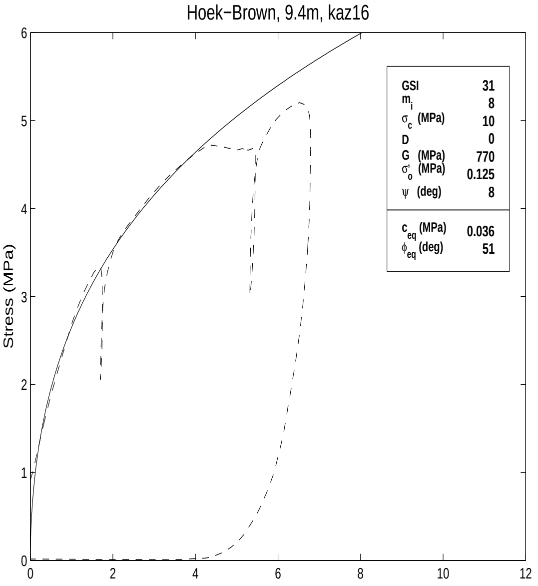

Shift = 5.7%
Water Pressure = 0.05 MPa

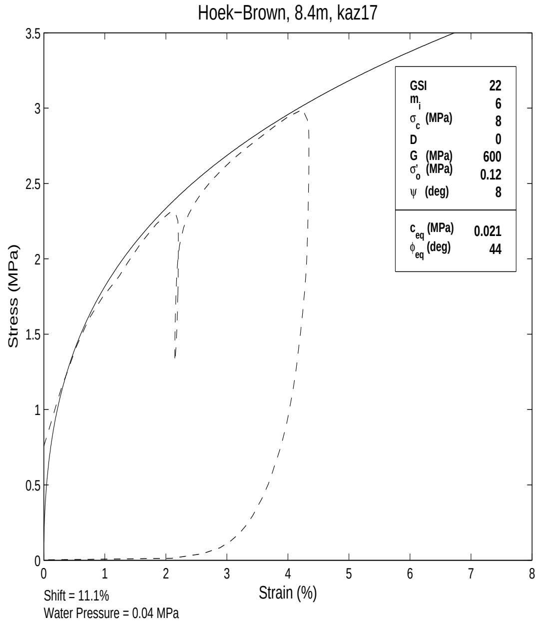
Hoek−Brown, 8.4m, kaz17

Shift = 11.1%
Water Pressure = 0.04 MPa

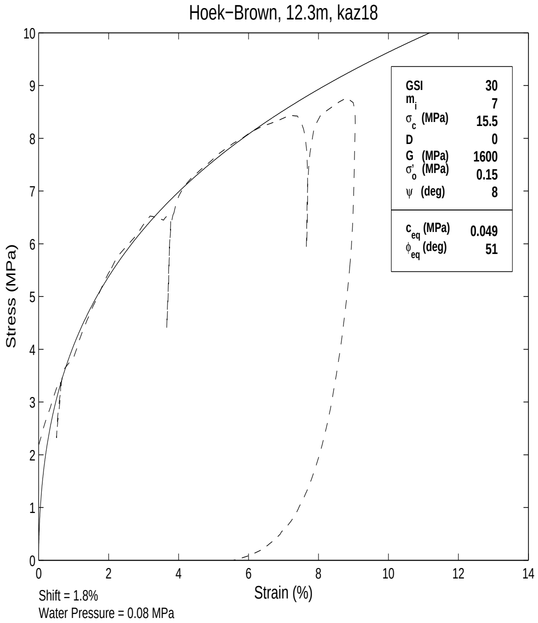
Hoek−Brown, 12.3m, kaz18

Shift = 1.8%
Water Pressure = 0.08 MPa

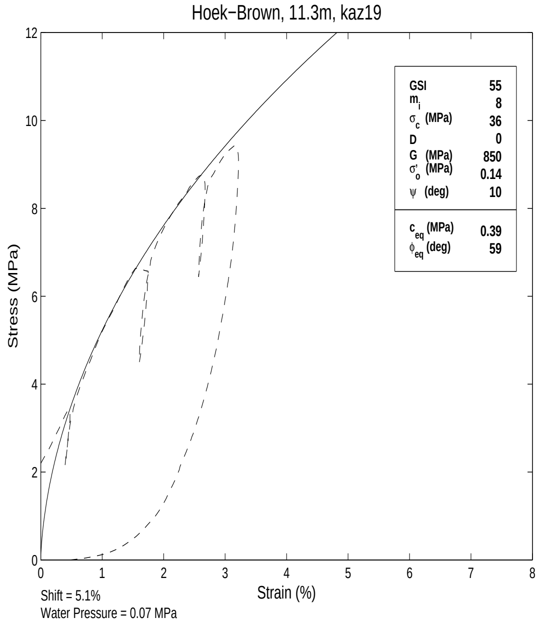
Hoek−Brown, 11.3m, kaz19

Shift = 5.1%
Water Pressure = 0.07 MPa

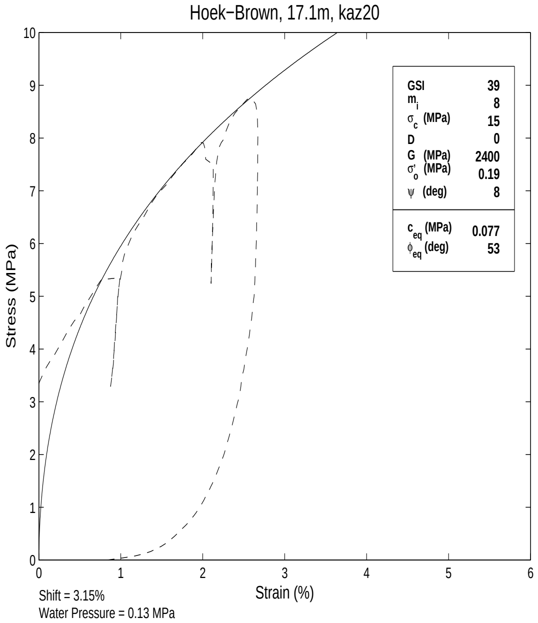
Hoek−Brown, 17.1m, kaz20

Shift = 3.15%
Water Pressure = 0.13 MPa

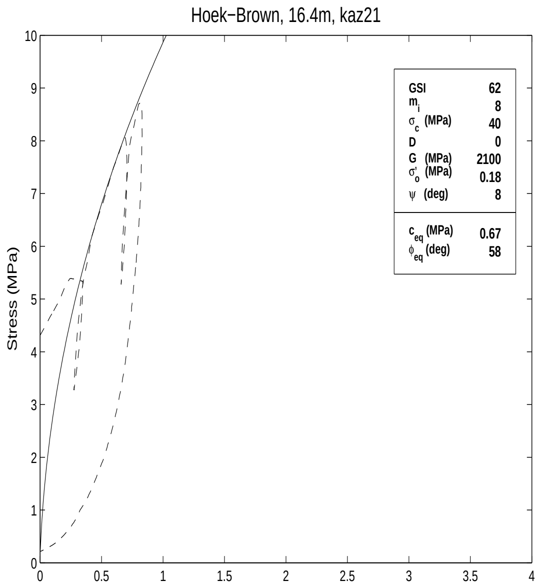
Hoek−Brown, 16.4m, kaz21

Shift = 6.8%
Water Pressure = 0.12 MPa

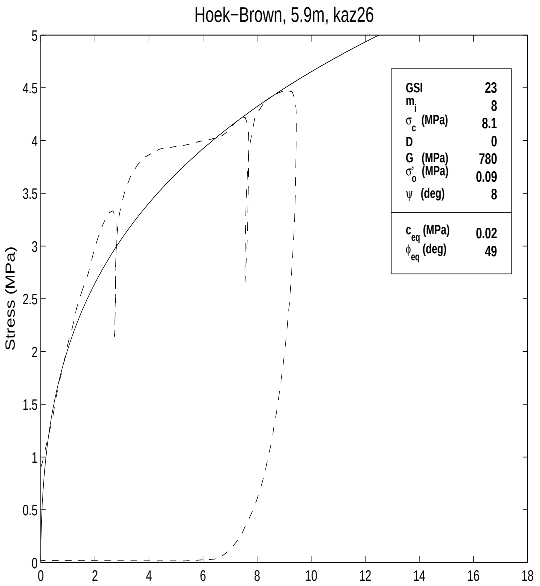
Hoek−Brown, 5.9m, kaz26

Shift = 2.6%
Water Pressure = 0.02 MPa

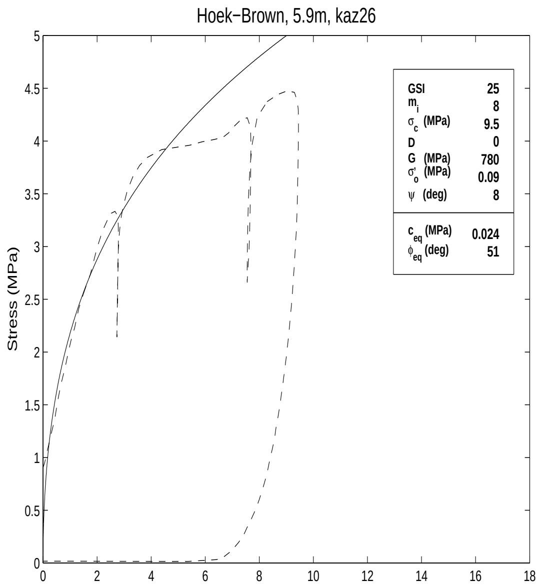
Hoek−Brown, 5.9m, kaz26

Shift = 2.6%
Water Pressure = 0.02 MPa

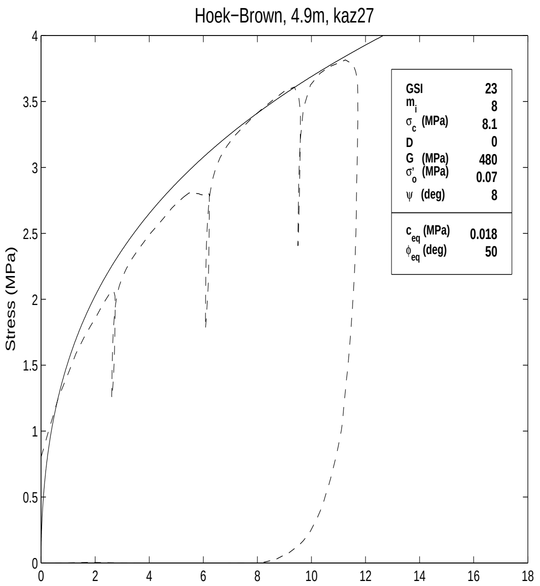
Hoek−Brown, 4.9m, kaz27

Shift = 2.4%
Water Pressure = 0.01 MPa

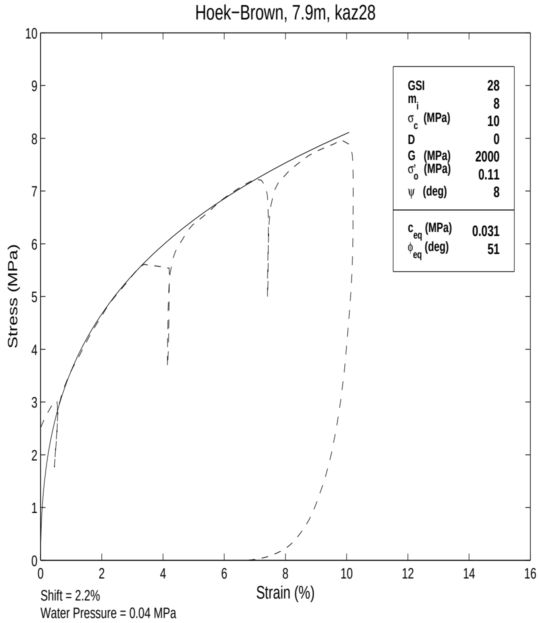

Shift = 2.2%
Water Pressure = 0.04 MPa

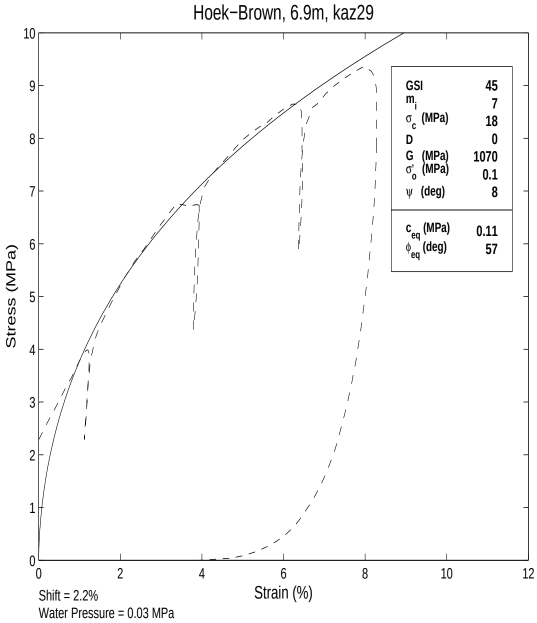

Shift = 2.2%
Water Pressure = 0.03 MPa

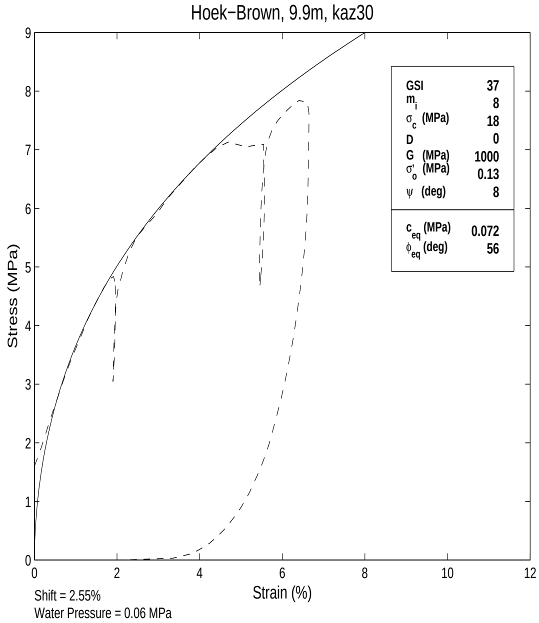

Shift = 2.55%
Water Pressure = 0.06 MPa

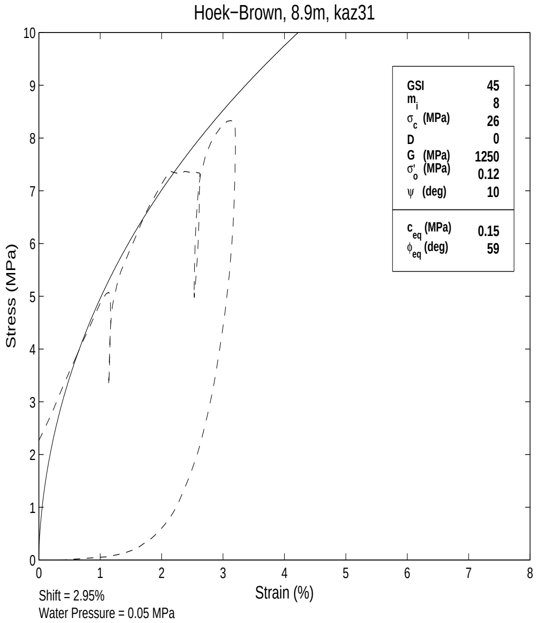

Shift = 2.95%
Water Pressure = 0.05 MPa

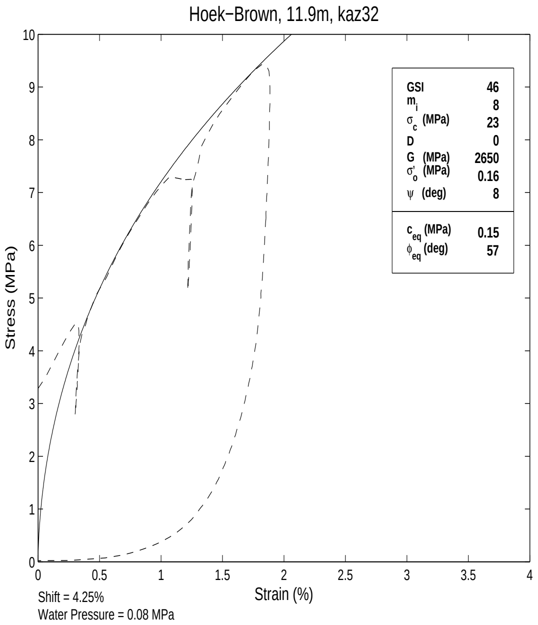
Hoek−Brown, 11.9m, kaz32
Stress (MPa)
Strain (%)
0
1
2
3
4
5
6
7
8
9
10
0
0.5
1
1.5
2
2.5
3
3.5
4
GSI 46
m_i 8
σ_c (MPa) 23
D 0
G (MPa) 2650
σ'_o (MPa) 0.16
ψ (deg) 8
c_eq (MPa) 0.15
φ_eq (deg) 57
Shift = 4.25%
Water Pressure = 0.08 MPa

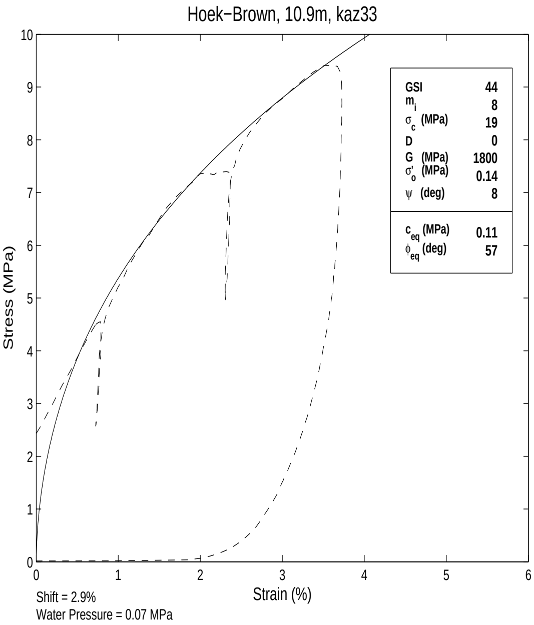
Hoek−Brown, 10.9m, kaz33
Stress (MPa)
Strain (%)
0
1
2
3
4
5
6
7
8
9
10
0
1
2
3
4
5
6
GSI 44
m_i 8
σ_c (MPa) 19
D 0
G (MPa) 1800
σ'_o (MPa) 0.14
ψ (deg) 8
c_eq (MPa) 0.11
φ_eq (deg) 57
Shift = 2.9%
Water Pressure = 0.07 MPa

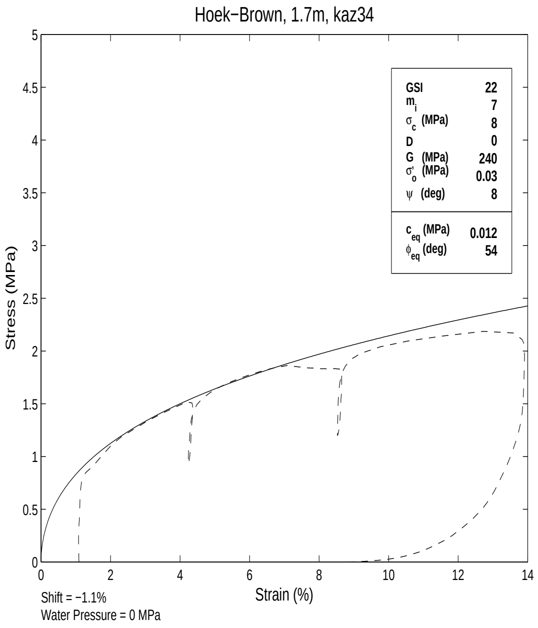
Hoek−Brown, 1.7m, kaz34
Stress (MPa)
Strain (%)
0
0.5
1
1.5
2
2.5
3
3.5
4
4.5
5
0
2
4
6
8
10
12
14
GSI 22
m_i 7
σ_c (MPa) 8
D 0
G (MPa) 240
σ'_o (MPa) 0.03
ψ (deg) 8
c_eq (MPa) 0.012
φ_eq (deg) 54
Shift = −1.1%
Water Pressure = 0 MPa

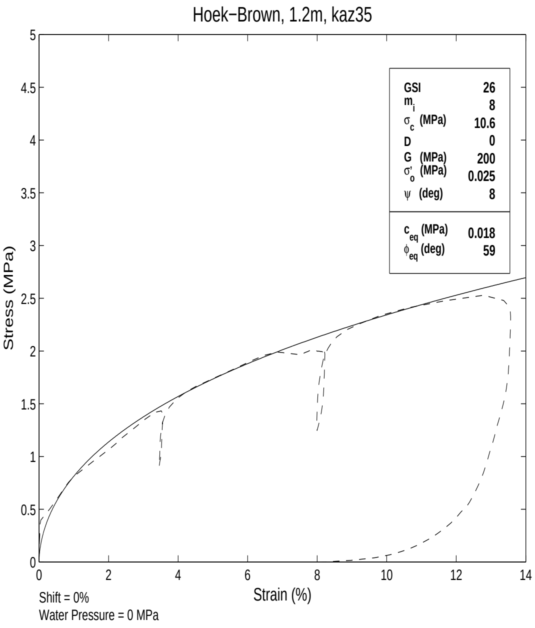
Hoek−Brown, 1.2m, kaz35
Stress (MPa)
Strain (%)
0
0.5
1
1.5
2
2.5
3
3.5
4
4.5
5
0
2
4
6
8
10
12
14
GSI 26
m_i 8
σ_c (MPa) 10.6
D 0
G (MPa) 200
σ'_o (MPa) 0.025
ψ (deg) 8
c_eq (MPa) 0.018
φ_eq (deg) 59
Shift = 0%
Water Pressure = 0 MPa

Hoek−Brown, 5.9m, kaz38

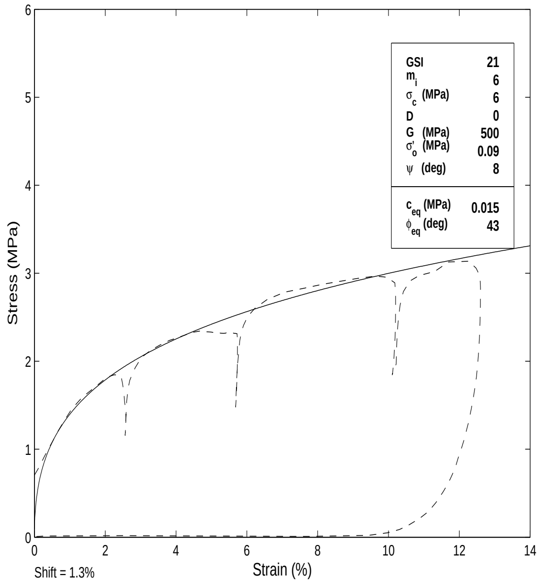

Shift = 1.3%
Water Pressure = 0.02 MPa

Hoek−Brown, 7.4m, kaz40

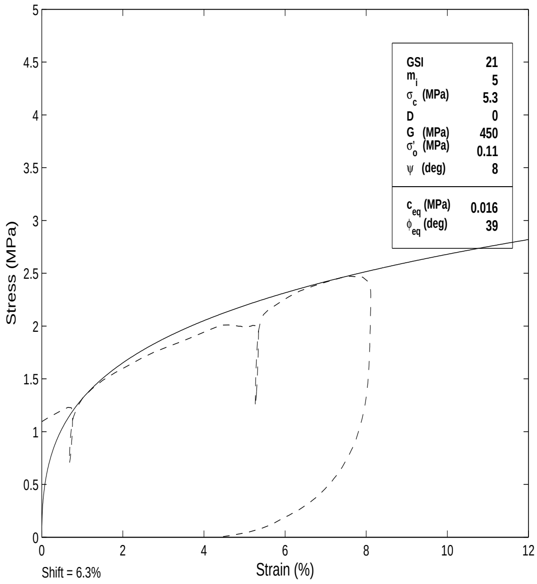

Shift = 6.3%
Water Pressure = 0.03 MPa

Hoek−Brown, 6.9m, kaz41

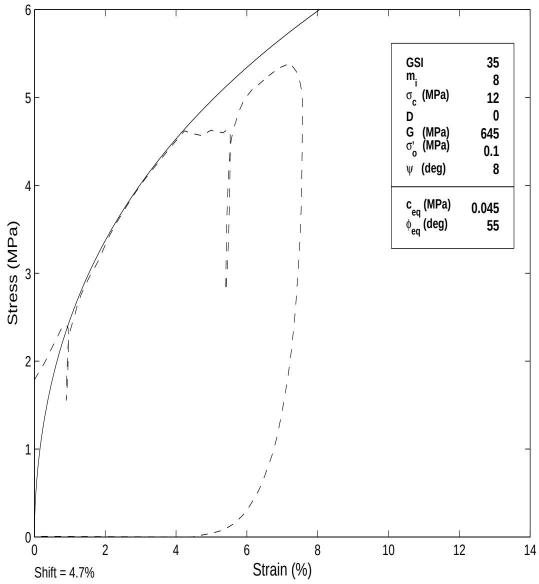

Shift = 4.7%
Water Pressure = 0.03 MPa

Hoek−Brown, 8.9m, kaz46

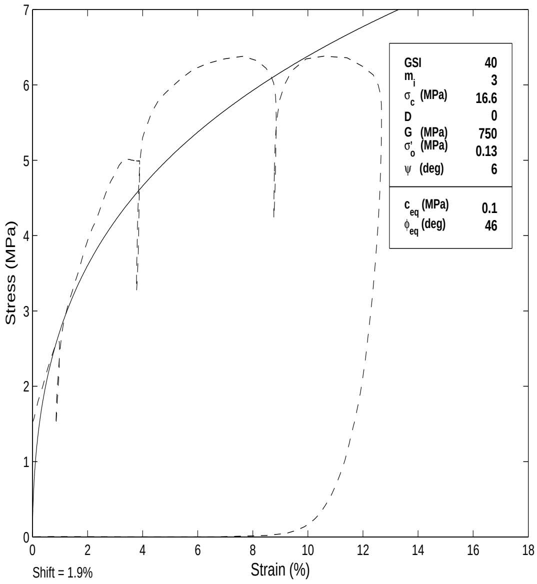

Shift = 1.9%
Water Pressure = 0.05 MPa

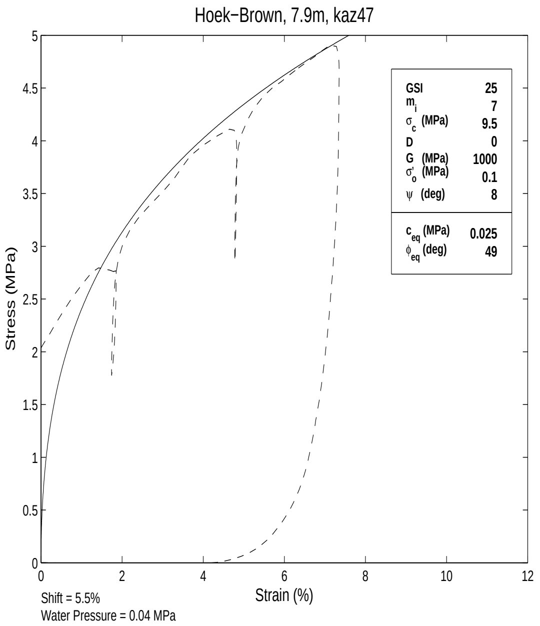
Hoek−Brown, 7.9m, kaz47

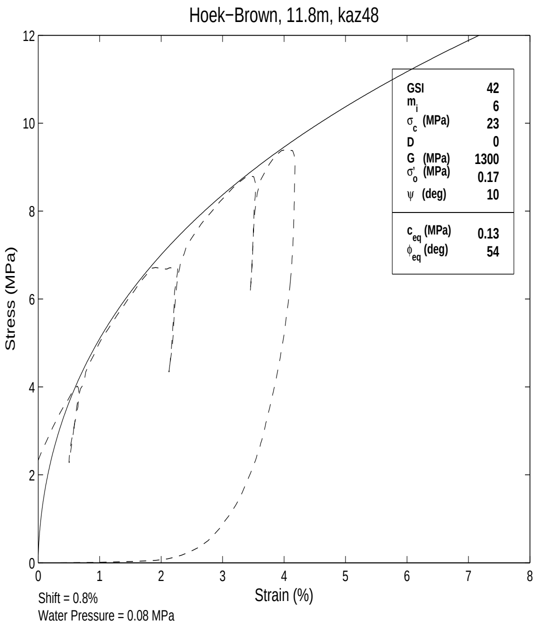
Hoek−Brown, 11.8m, kaz48

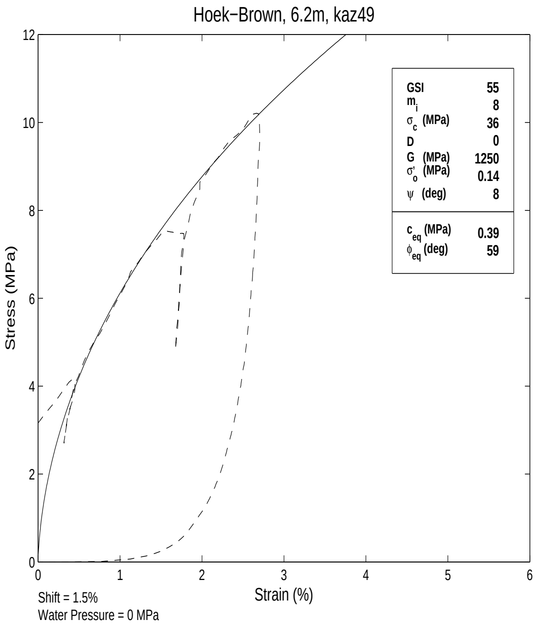
Hoek−Brown, 6.2m, kaz49

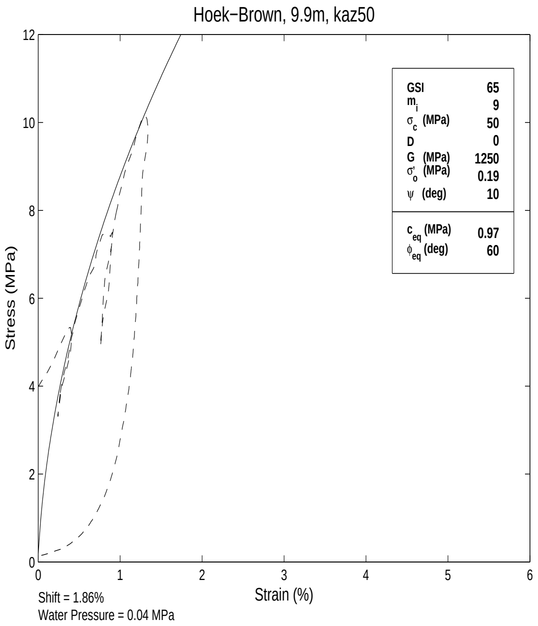
Hoek−Brown, 9.9m, kaz50

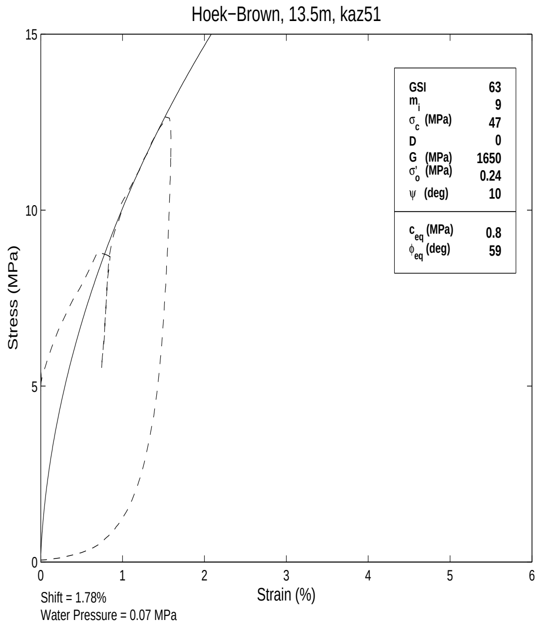
Hoek−Brown, 13.5m, kaz51
Stress (MPa)
Strain (%)
0
5
10
15
0
1
2
3
4
5
6
GSI 63
m_i 9
σ_c (MPa) 47
D 0
G (MPa) 1650
σ'_o (MPa) 0.24
ψ (deg) 10
c_{eq} (MPa) 0.8
ϕ_{eq} (deg) 59
Shift = 1.78%
Water Pressure = 0.07 MPa

A.4 Site 4

Table A.5: Test Information for Site 4 - Part I

Borehole	**Test Name**	**Depth (m)**	**Rock Type**
1	sr710-05	69.2	Quartz Diorite/Granitic Gneissic Rock
2	sr710-12	38.9	Interbedded Siltstone & Sandstone
2	sr710-11	39.3	Interbedded Siltstone & Sandstone
2	sr710-14	42.2	Interbedded Siltstone & Sandstone
2	sr710-13	42.7	Interbedded Siltstone & Sandstone
3	sr710-16	29.0	Sandy Siltstone
3	sr710-15	29.4	Sandy Siltstone
3	sr710-19	41.5	Sandy Siltstone
4	sr710-21	54.1	Sandstone
4	sr710-22	62.2	Sandstone
5	sr710-23	41.4	Sandstone
5	sr710-26	76.1	Sandstone
5	sr710-25	76.5	Sandstone
6	sr710-27	61.9	Siltstone with Interbedded Sandstone
6	sr710-28	74.7	Siltstone with Interbedded Sandstone
6	sr710-32	100.8	Siltstone with Interbedded Sandstone
6	sr710-31	101.2	Siltstone with Interbedded Sandstone

The same organization as discussed for Site 1 applies here.

Table A.6: Test Information for Site 4 - Part II

Borehole	**Test Name**	**Depth (m)**	**Rock Type**
7	sr710-30	68.4	Sandstone with Interbedded Siltstone
7	sr710-29	68.8	Sandstone with Interbedded Siltstone
7	sr710-34	76.5	Sandstone with Interbedded Siltstone
7	sr710-33	77.0	Sandstone with Interbedded Siltstone
7	sr710-36	82.3	Sandstone with Interbedded Siltstone
7	sr710-35	82.8	Sandstone with Interbedded Siltstone
8	sr710-37	84.8	Sandstone
8	sr710-42	105.3	Sandstone
8	sr710-41	105.8	Sandstone
8	sr710-44	121.3	Sandstone and Siltstone
9	sr710-40	100.8	Sandstone and Siltstone
10	sr710-43	40.2	Conglomerate
10	sr710-47	50.8	Conglomerate
10	sr710-46	51.2	Conglomerate

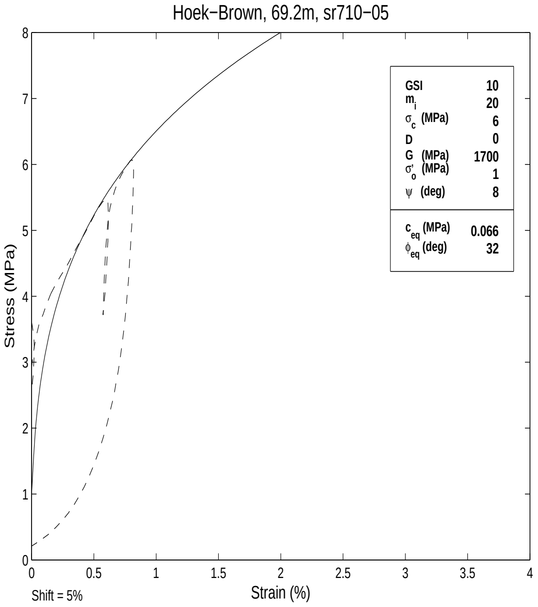

Shift = 5%
Water Pressure = 0.47 MPa

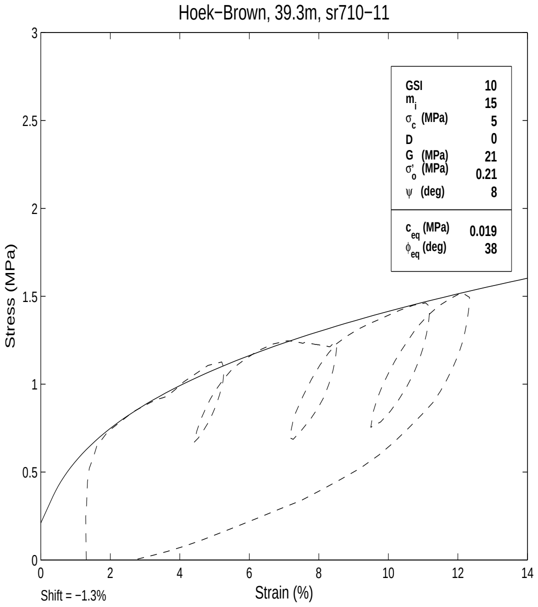

Shift = −1.3%
Water Pressure = 0.3 MPa

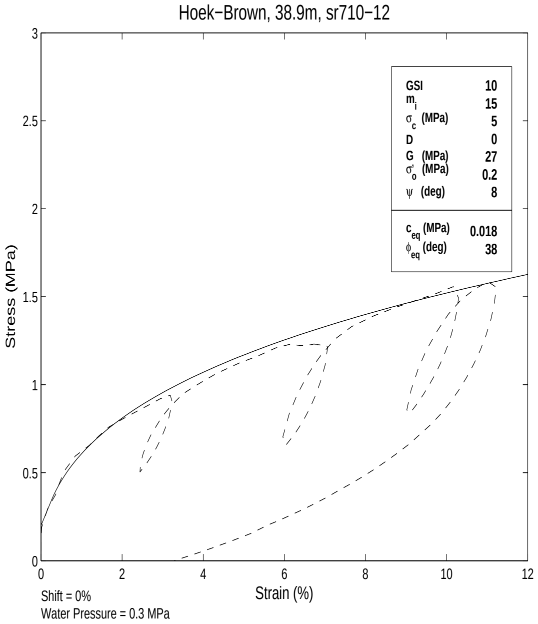
Hoek−Brown, 38.9m, sr710−12
Stress (MPa)
Strain (%)
GSI 10
m_i 15
σ_c (MPa) 5
D 0
G (MPa) 27
σ_o' (MPa) 0.2
ψ (deg) 8
c_{eq} (MPa) 0.018
ϕ_{eq} (deg) 38
Shift = 0%
Water Pressure = 0.3 MPa

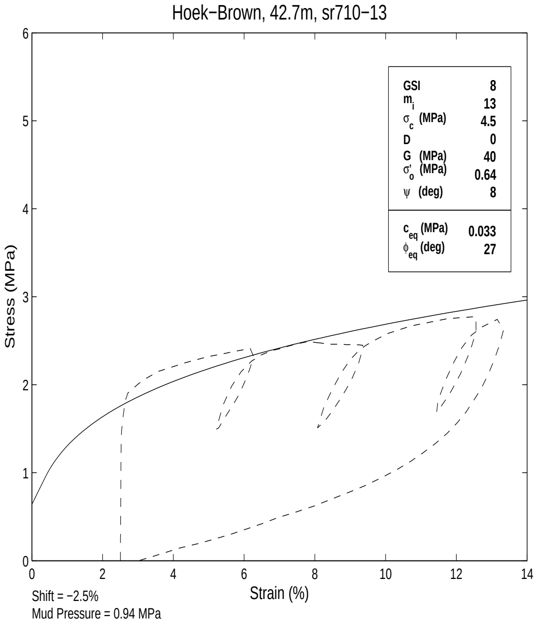
Hoek−Brown, 42.7m, sr710−13
Stress (MPa)
Strain (%)
GSI 8
m_i 13
σ_c (MPa) 4.5
D 0
G (MPa) 40
σ_o' (MPa) 0.64
ψ (deg) 8
c_{eq} (MPa) 0.033
ϕ_{eq} (deg) 27
Shift = −2.5%
Mud Pressure = 0.94 MPa

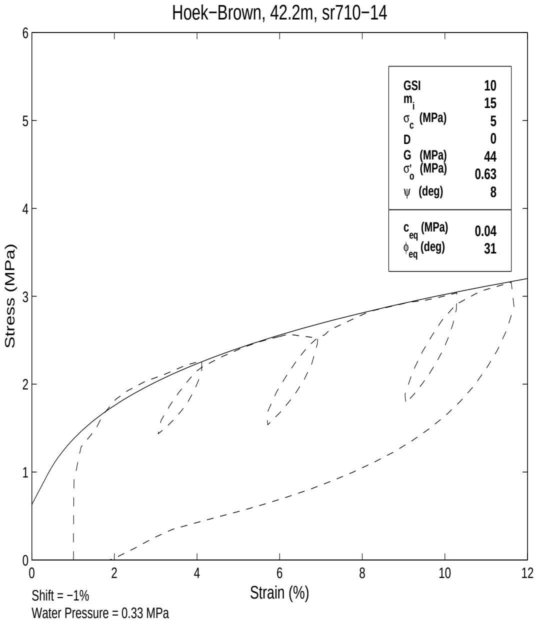
Hoek−Brown, 42.2m, sr710−14
Stress (MPa)
Strain (%)
GSI 10
m_i 15
σ_c (MPa) 5
D 0
G (MPa) 44
σ_o' (MPa) 0.63
ψ (deg) 8
c_{eq} (MPa) 0.04
ϕ_{eq} (deg) 31
Shift = −1%
Water Pressure = 0.33 MPa

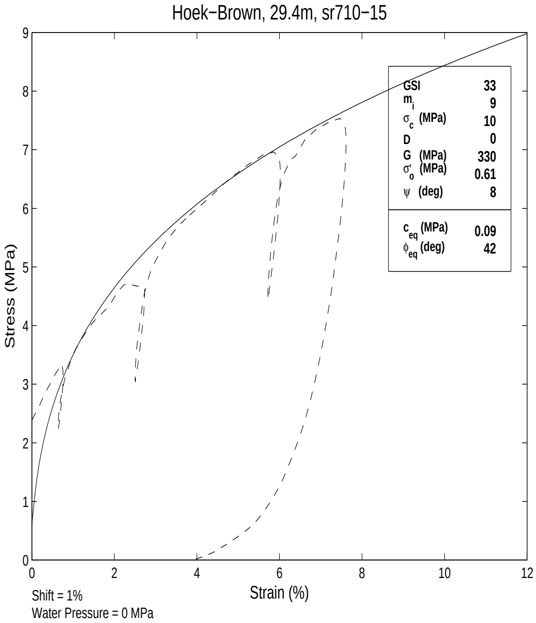
Hoek−Brown, 29.4m, sr710−15
Stress (MPa)
Strain (%)
GSI 33
m_i 9
σ_c (MPa) 10
D 0
G (MPa) 330
σ_o' (MPa) 0.61
ψ (deg) 8
c_{eq} (MPa) 0.09
ϕ_{eq} (deg) 42
Shift = 1%
Water Pressure = 0 MPa

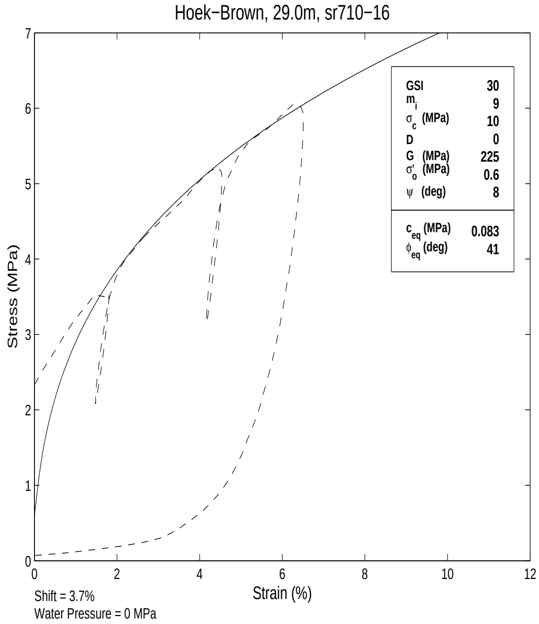
Hoek−Brown, 29.0m, sr710−16
Stress (MPa)
Strain (%)
0
1
2
3
4
5
6
7
0
2
4
6
8
10
12
GSI 30
m_i 9
σ_c (MPa) 10
D 0
G (MPa) 225
σ'_o (MPa) 0.6
ψ (deg) 8
c_eq (MPa) 0.083
φ_eq (deg) 41
Shift = 3.7%
Water Pressure = 0 MPa

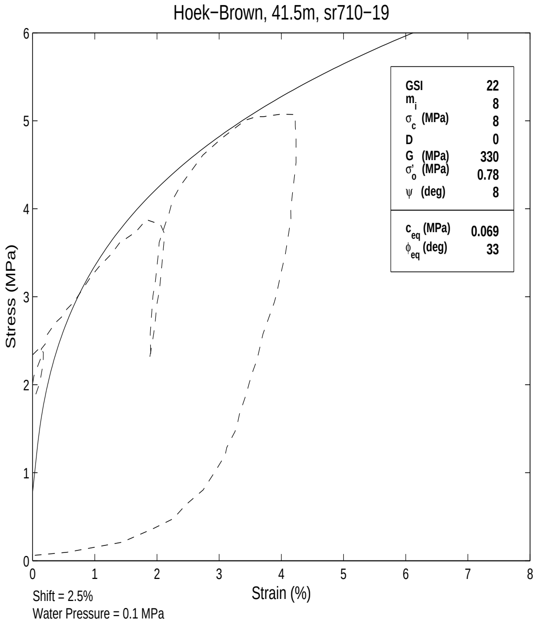
Hoek−Brown, 41.5m, sr710−19
Stress (MPa)
Strain (%)
0
1
2
3
4
5
6
0
1
2
3
4
5
6
7
8
GSI 22
m_i 8
σ_c (MPa) 8
D 0
G (MPa) 330
σ'_o (MPa) 0.78
ψ (deg) 8
c_eq (MPa) 0.069
φ_eq (deg) 33
Shift = 2.5%
Water Pressure = 0.1 MPa

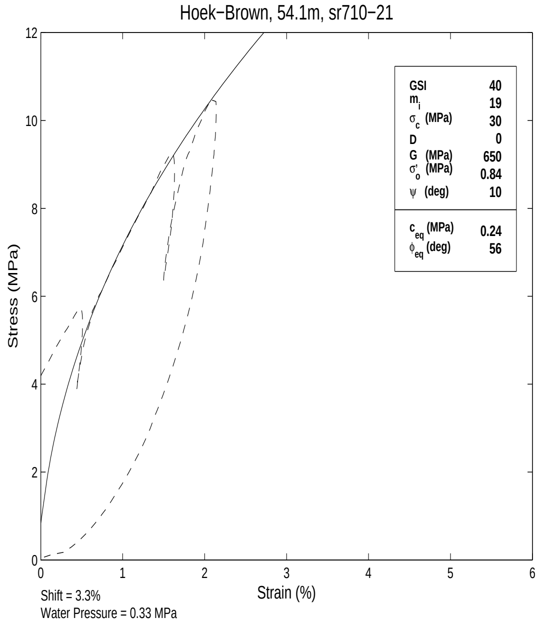
Hoek−Brown, 54.1m, sr710−21
Stress (MPa)
Strain (%)
0
2
4
6
8
10
12
0
1
2
3
4
5
6
GSI 40
m_i 19
σ_c (MPa) 30
D 0
G (MPa) 650
σ'_o (MPa) 0.84
ψ (deg) 10
c_eq (MPa) 0.24
φ_eq (deg) 56
Shift = 3.3%
Water Pressure = 0.33 MPa

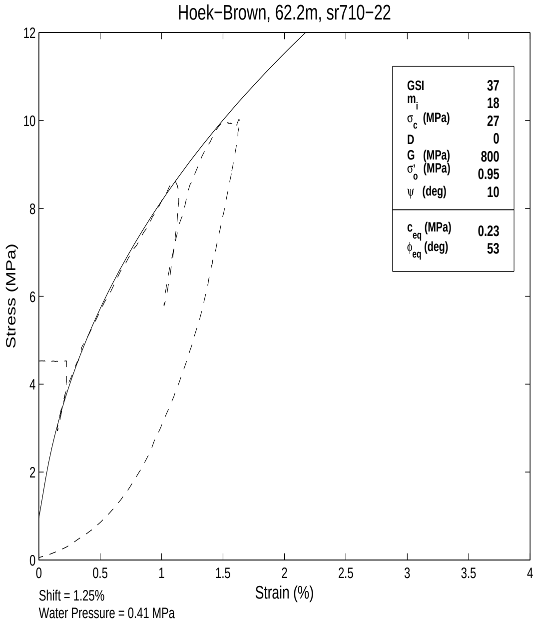
Hoek−Brown, 62.2m, sr710−22
Stress (MPa)
Strain (%)
0
2
4
6
8
10
12
0
0.5
1
1.5
2
2.5
3
3.5
4
GSI 37
m_i 18
σ_c (MPa) 27
D 0
G (MPa) 800
σ'_o (MPa) 0.95
ψ (deg) 10
c_eq (MPa) 0.23
φ_eq (deg) 53
Shift = 1.25%
Water Pressure = 0.41 MPa

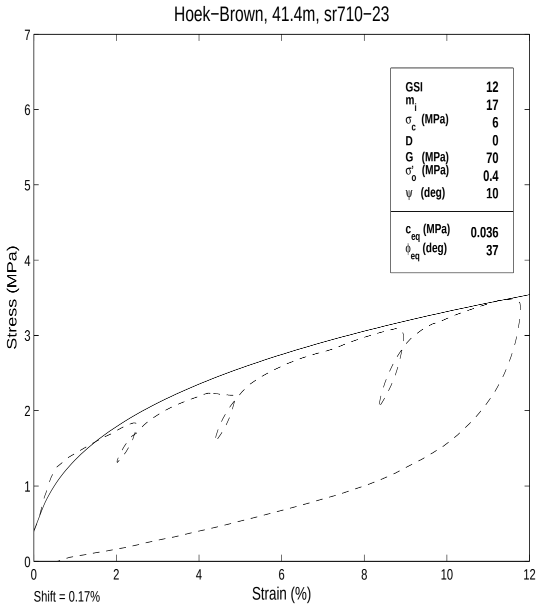

Hoek−Brown, 41.4m, sr710−23

Shift = 0.17%
Water Pressure = 0.04 MPa

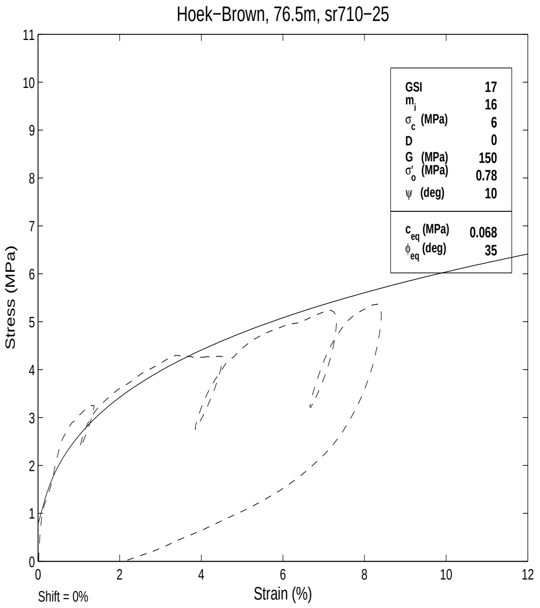

Hoek−Brown, 76.5m, sr710−25

Shift = 0%
Water Pressure = 0.38 MPa

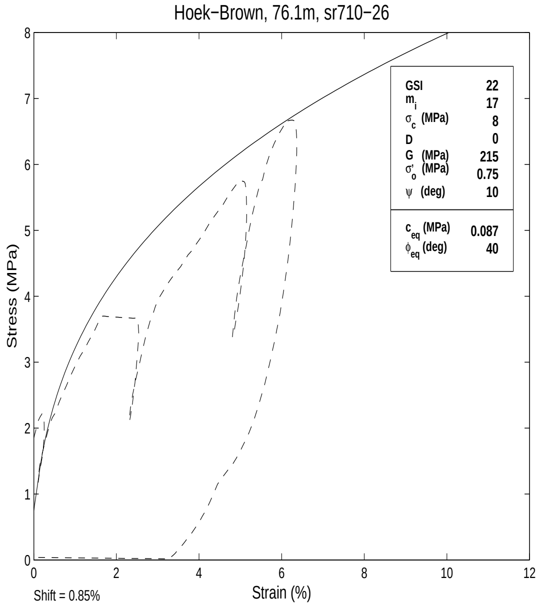

Hoek−Brown, 76.1m, sr710−26

Shift = 0.85%
Water Pressure = 0.38 MPa

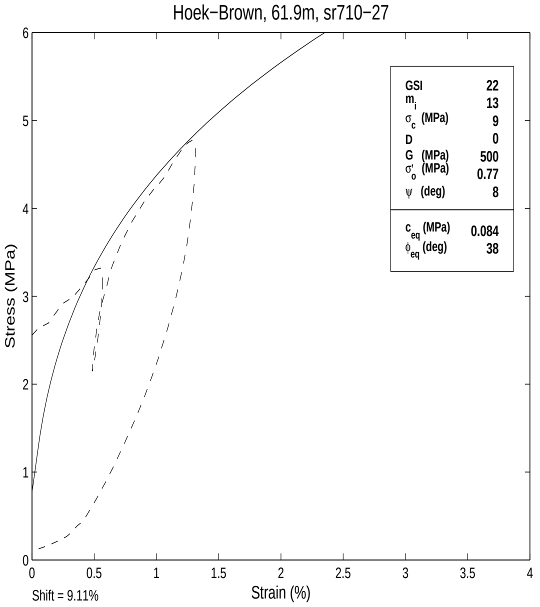

Hoek−Brown, 61.9m, sr710−27

Shift = 9.11%
Water Pressure = 0.58 MPa

Hoek−Brown, 74.7m, sr710−28

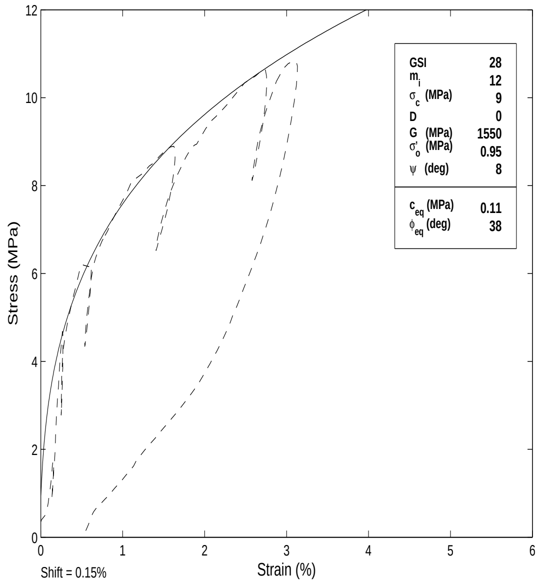

Shift = 0.15%
Water Pressure = 0.71 MPa

Hoek−Brown, 68.8m, sr710−29

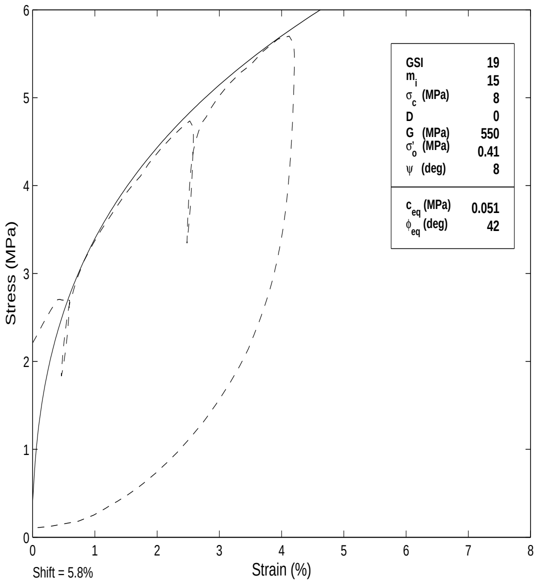

Shift = 5.8%
Water Pressure = 0.52 MPa

Hoek−Brown, 68.4m, sr710−30

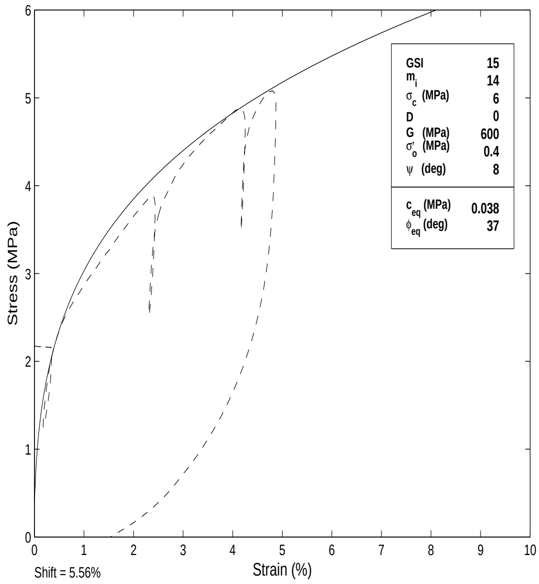

Shift = 5.56%
Water Pressure = 0.52 MPa

Hoek−Brown, 101.2m, sr710−31

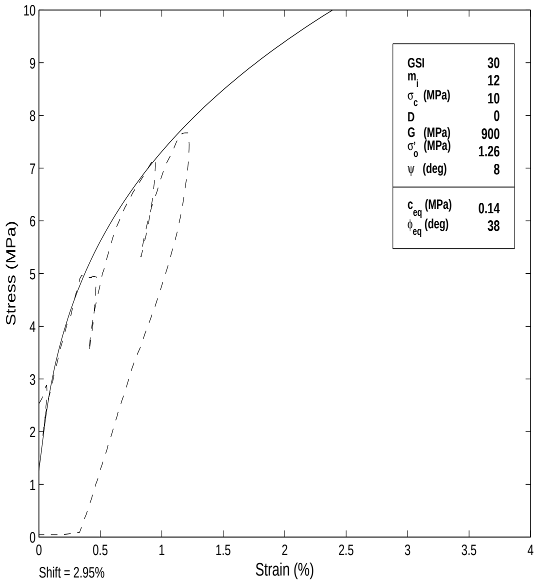

Shift = 2.95%
Water Pressure = 0.97 MPa

Hoek−Brown, 100.8m, sr710−32

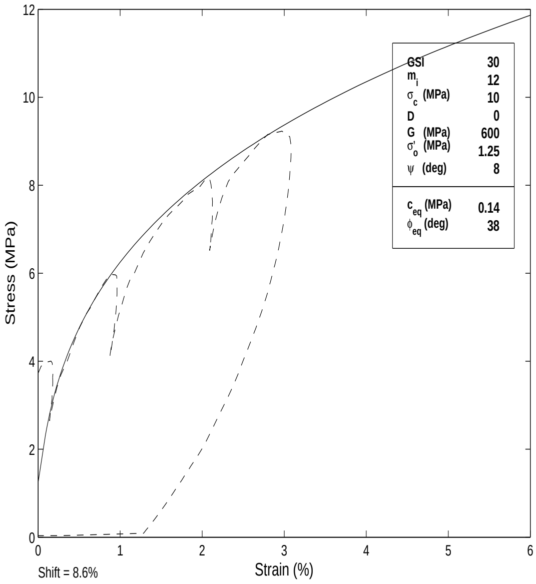

Shift = 8.6%
Water Pressure = 0.96 MPa

Hoek−Brown, 77.0m, sr710−33

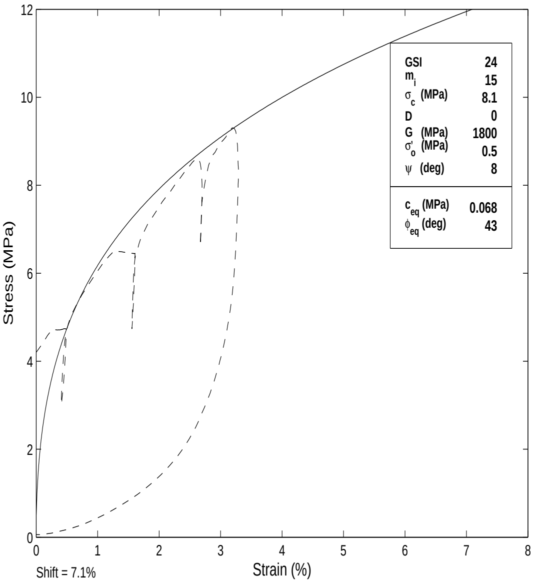

Shift = 7.1%
Water Pressure = 0.6 MPa

Hoek−Brown, 76.5m, sr710−34

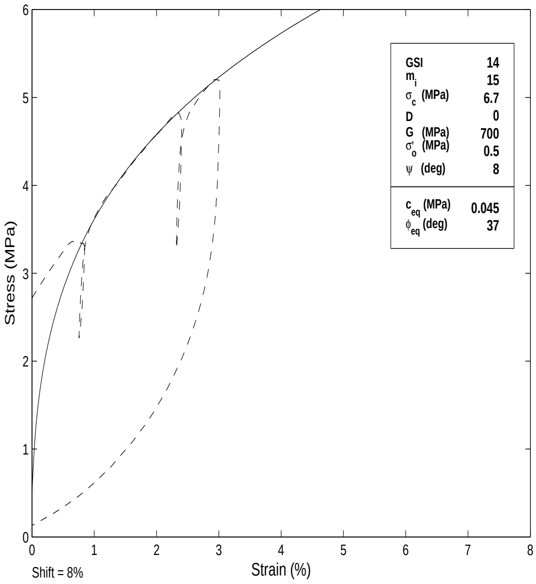

Shift = 8%
Water Pressure = 0.6 MPa

Hoek−Brown, 82.8m, sr710−35

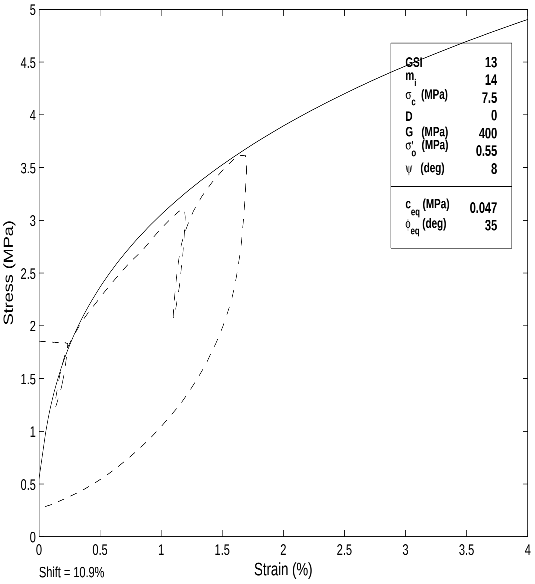

Shift = 10.9%
Water Pressure = 0.66 MPa

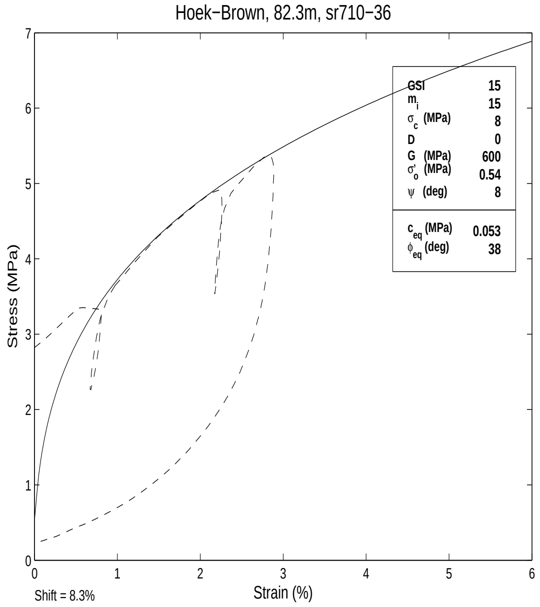

Shift = 8.3%
Water Pressure = 0.66 MPa

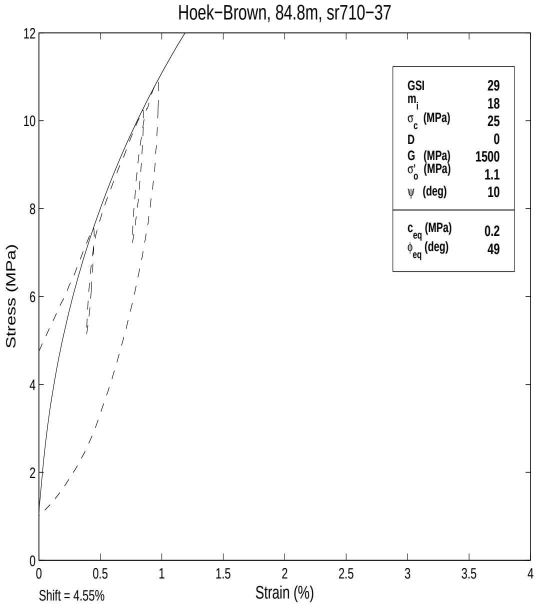

Shift = 4.55%
Water Pressure = 0.75 MPa

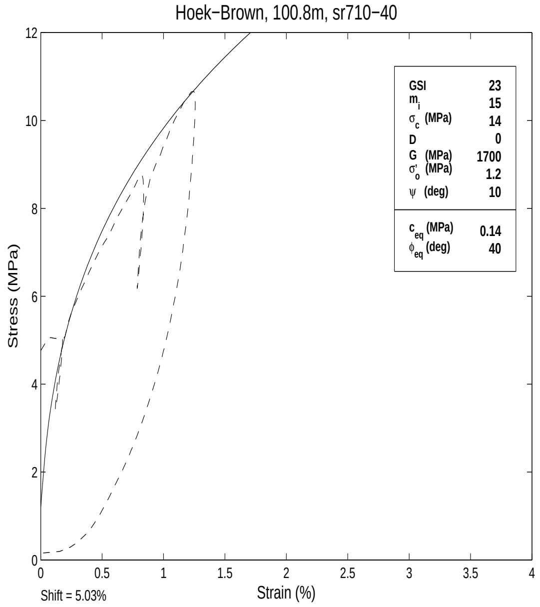

Shift = 5.03%
Water Pressure = 0.99 MPa

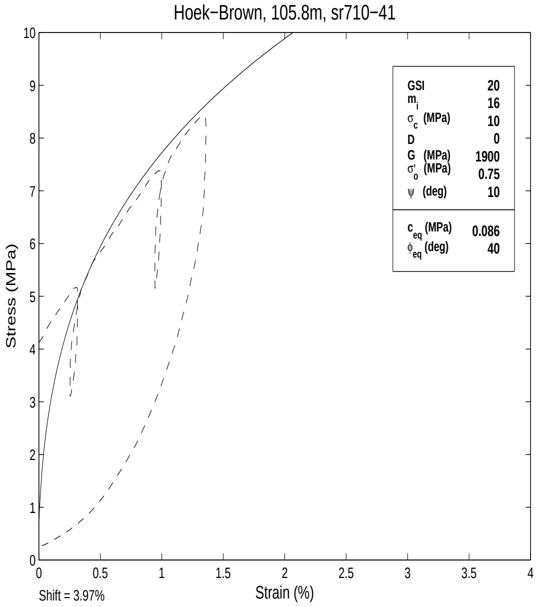

Shift = 3.97%
Water Pressure = 0.96 MPa

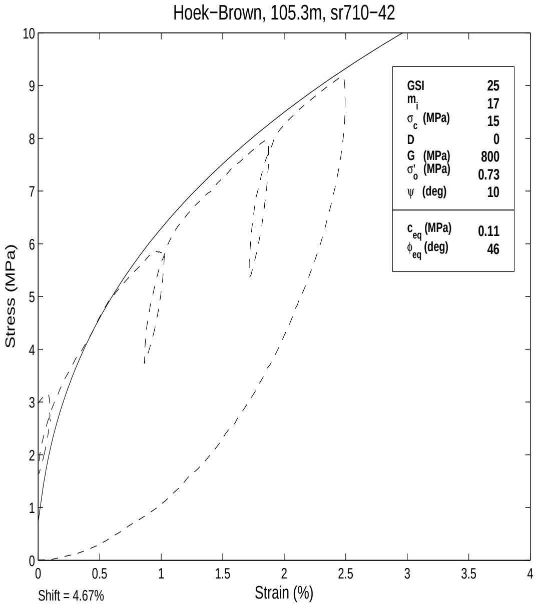

Shift = 4.67%
Water Pressure = 0.95 MPa

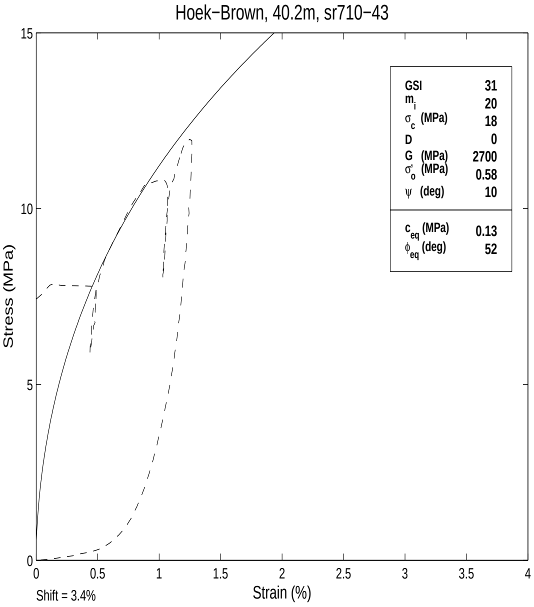

Shift = 3.4%
Water Pressure = 0.33 MPa

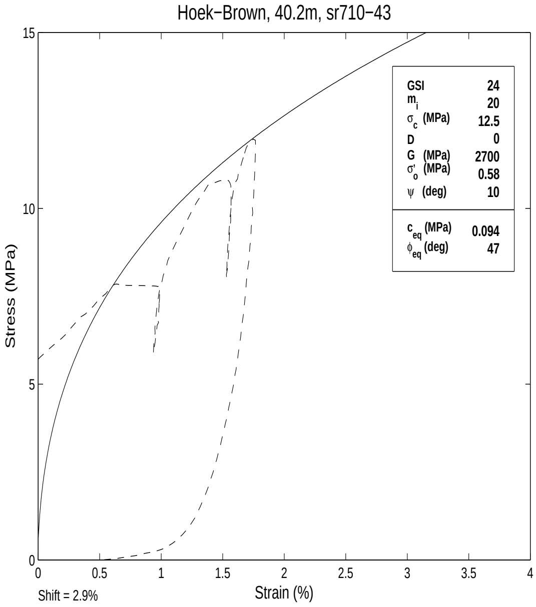

Shift = 2.9%
Water Pressure = 0.33 MPa

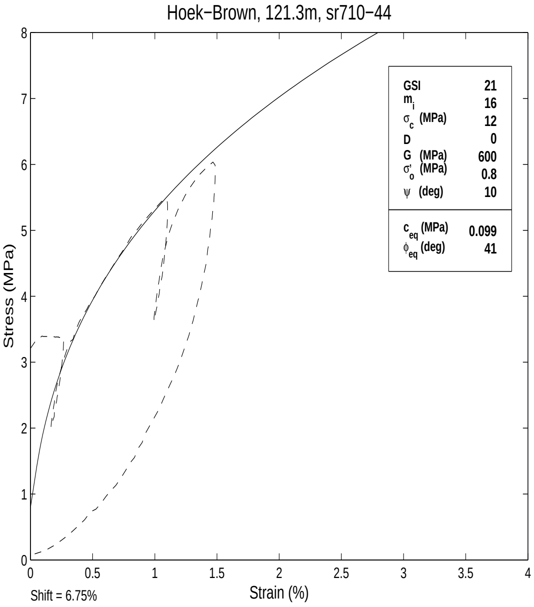

Shift = 6.75%
Water Pressure = 1.11 MPa

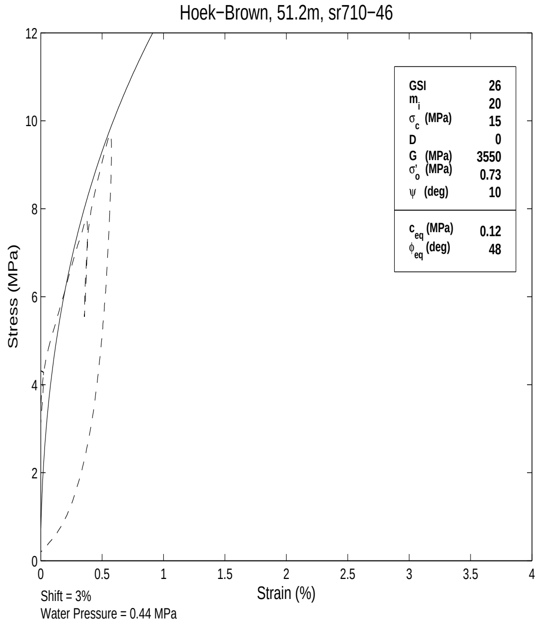
Hoek−Brown, 51.2m, sr710−46
Stress (MPa)
Strain (%)
0
2
4
6
8
10
12
0
0.5
1
1.5
2
2.5
3
3.5
4
GSI 26
m_i 20
σ_c (MPa) 15
D 0
G (MPa) 3550
σ'_o (MPa) 0.73
ψ (deg) 10
c_{eq} (MPa) 0.12
ϕ_{eq} (deg) 48
Shift = 3%
Water Pressure = 0.44 MPa

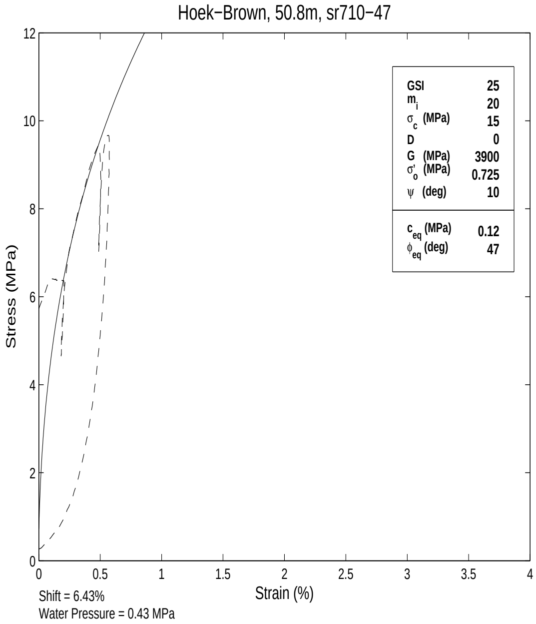
Hoek−Brown, 50.8m, sr710−47
Stress (MPa)
Strain (%)
0
2
4
6
8
10
12
0
0.5
1
1.5
2
2.5
3
3.5
4
GSI 25
m_i 20
σ_c (MPa) 15
D 0
G (MPa) 3900
σ'_o (MPa) 0.725
ψ (deg) 10
c_{eq} (MPa) 0.12
ϕ_{eq} (deg) 47
Shift = 6.43%
Water Pressure = 0.43 MPa

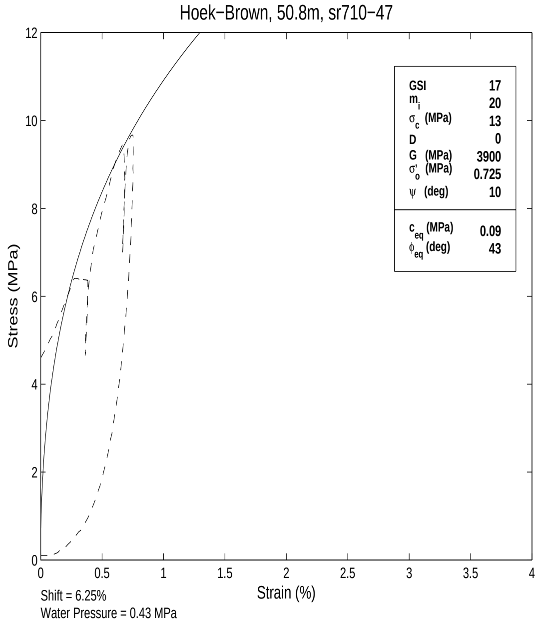
Hoek−Brown, 50.8m, sr710−47
Stress (MPa)
Strain (%)
0
2
4
6
8
10
12
0
0.5
1
1.5
2
2.5
3
3.5
4
GSI 17
m_i 20
σ_c (MPa) 13
D 0
G (MPa) 3900
σ'_o (MPa) 0.725
ψ (deg) 10
c_{eq} (MPa) 0.09
ϕ_{eq} (deg) 43
Shift = 6.25%
Water Pressure = 0.43 MPa

A.5 Site 5

Table A.7: Test Information for Site 5

Borehole	**Test Name**	**Depth (m)**	**Rock Type**
1	WALLER02	10.2	Austin Limestone
1	WALLER01	10.7	Austin Limestone
1	WALLER04	16.3	Eagle Ford Shale
1	WALLER03	16.8	Eagle Ford Shale
1	WALLER05	21.3	Limestone/Shale with Bentonite Seams
1	WALLER10	23.9	Cloice Formation
1	WALLER09	24.4	Cloice Formation
1	WALLER08	25.5	Pepper Shale
1	WALLER07	25.9	Pepper Shale
2	WALLER12	10.4	Austin Limestone
2	WALLER11	10.8	Austin Limestone
2	WALLER14	17.8	Eagle Ford Shale
2	WALLER13	18.3	Eagle Ford Shale
2	WALLER15	22.7	Limestone/Shale with Bentonite Seams
2	WALLER18	25.5	Cloice Formation
2	WALLER17	25.9	Cloice Formation
2	WALLER20	26.7	Pepper Shale
2	WALLER19	27.1	Pepper Shale

The same organization as discussed for Site 1 applies here.

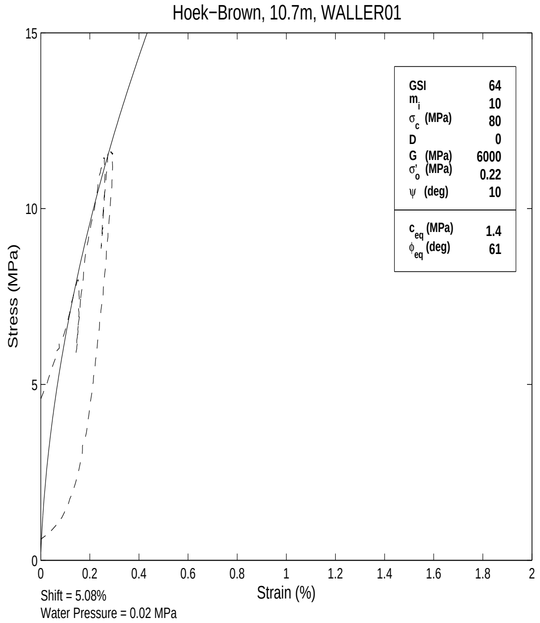

Shift = 5.08%
Water Pressure = 0.02 MPa

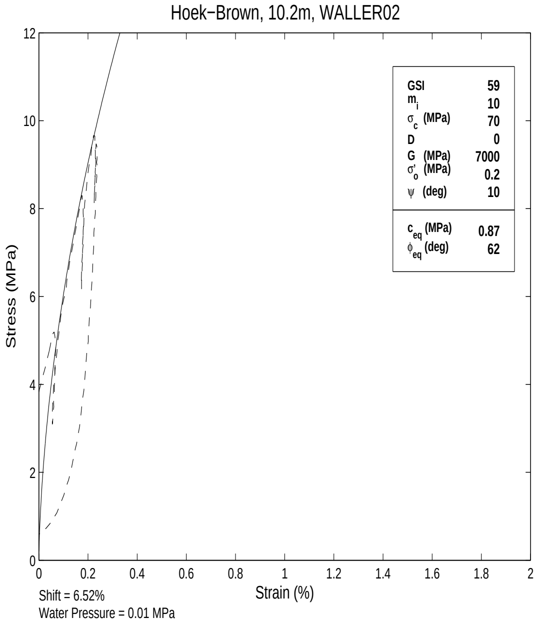

Shift = 6.52%
Water Pressure = 0.01 MPa

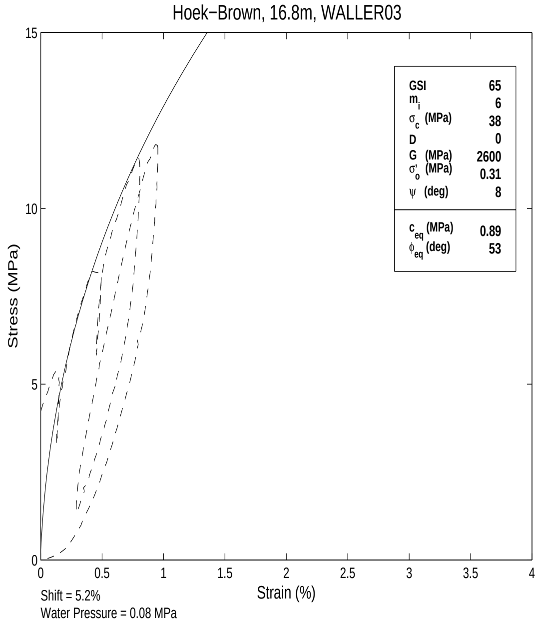

Shift = 5.2%
Water Pressure = 0.08 MPa

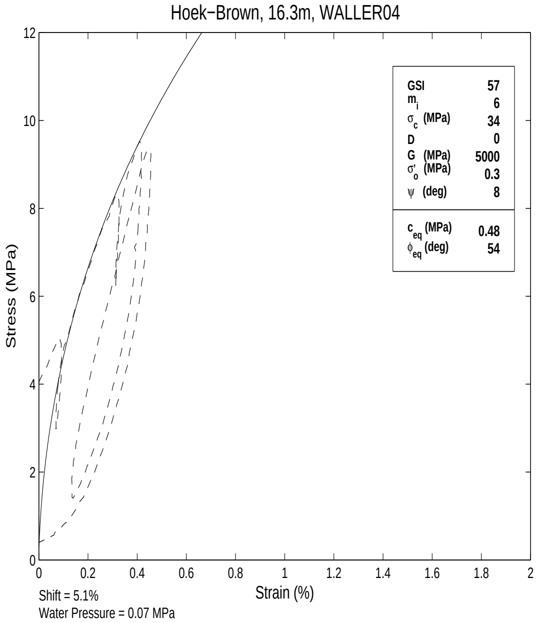

Shift = 5.1%
Water Pressure = 0.07 MPa

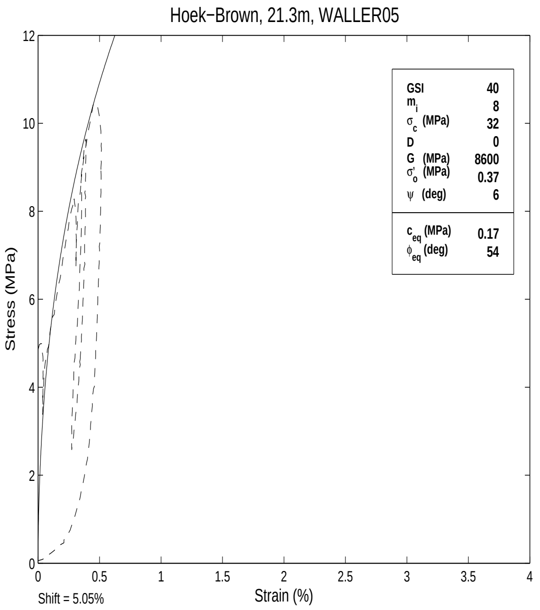

Shift = 5.05%
Water Pressure = 0.12 MPa

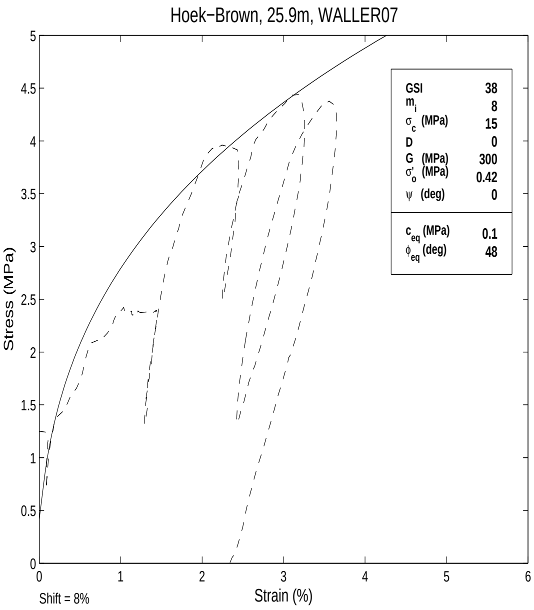

Shift = 8%
Water Pressure = 0.17 MPa

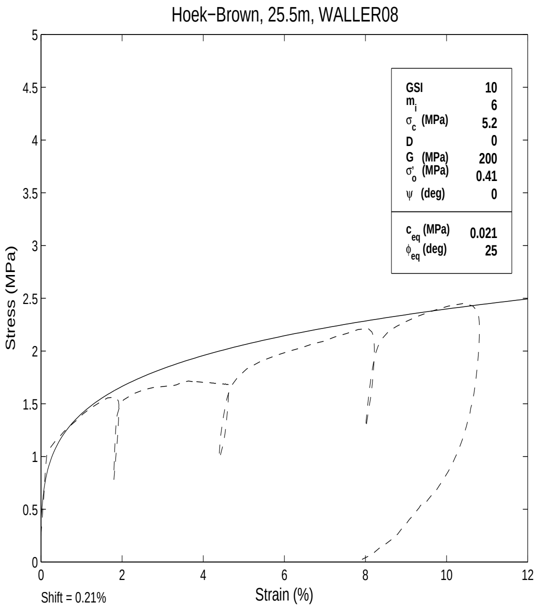

Shift = 0.21%
Water Pressure = 0.16 MPa

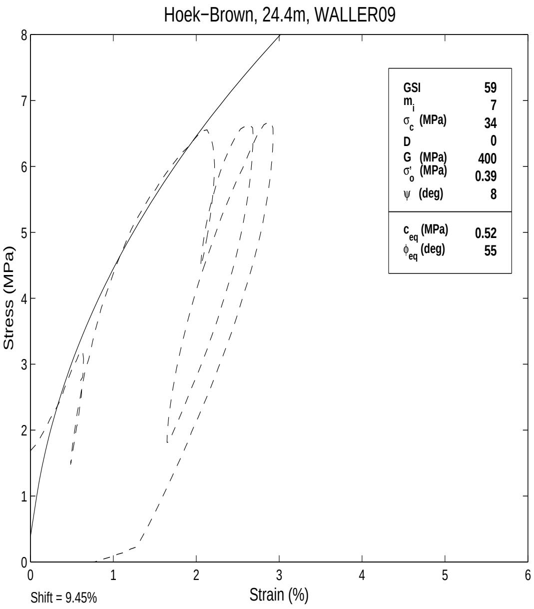

Shift = 9.45%
Water Pressure = 0.15 MPa

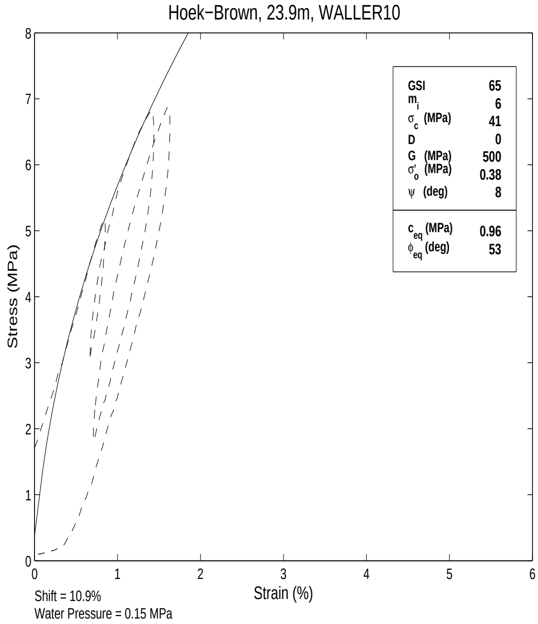
Hoek−Brown, 23.9m, WALLER10
Stress (MPa)
Strain (%)
0
1
2
3
4
5
6
7
8
0
1
2
3
4
5
6
GSI 65
m_i 6
σ_c (MPa) 41
D 0
G (MPa) 500
σ'_o (MPa) 0.38
ψ (deg) 8
c_{eq} (MPa) 0.96
ϕ_{eq} (deg) 53
Shift = 10.9%
Water Pressure = 0.15 MPa

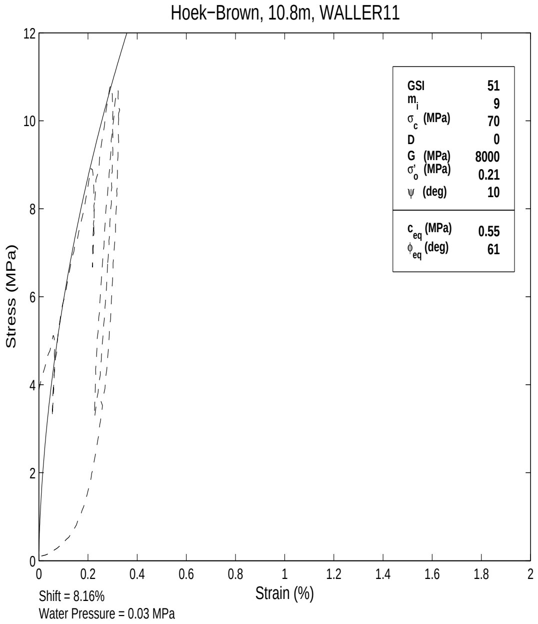
Hoek−Brown, 10.8m, WALLER11
Stress (MPa)
Strain (%)
0
2
4
6
8
10
12
0
0.2
0.4
0.6
0.8
1
1.2
1.4
1.6
1.8
2
GSI 51
m_i 9
σ_c (MPa) 70
D 0
G (MPa) 8000
σ'_o (MPa) 0.21
ψ (deg) 10
c_{eq} (MPa) 0.55
ϕ_{eq} (deg) 61
Shift = 8.16%
Water Pressure = 0.03 MPa

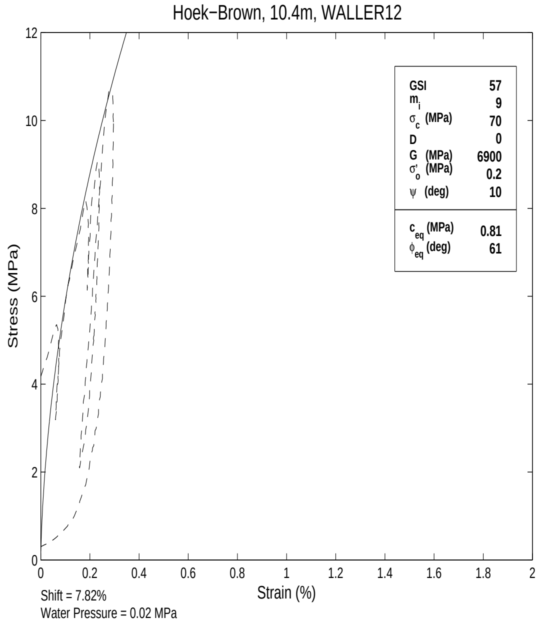
Hoek−Brown, 10.4m, WALLER12
Stress (MPa)
Strain (%)
0
2
4
6
8
10
12
0
0.2
0.4
0.6
0.8
1
1.2
1.4
1.6
1.8
2
GSI 57
m_i 9
σ_c (MPa) 70
D 0
G (MPa) 6900
σ'_o (MPa) 0.2
ψ (deg) 10
c_{eq} (MPa) 0.81
ϕ_{eq} (deg) 61
Shift = 7.82%
Water Pressure = 0.02 MPa

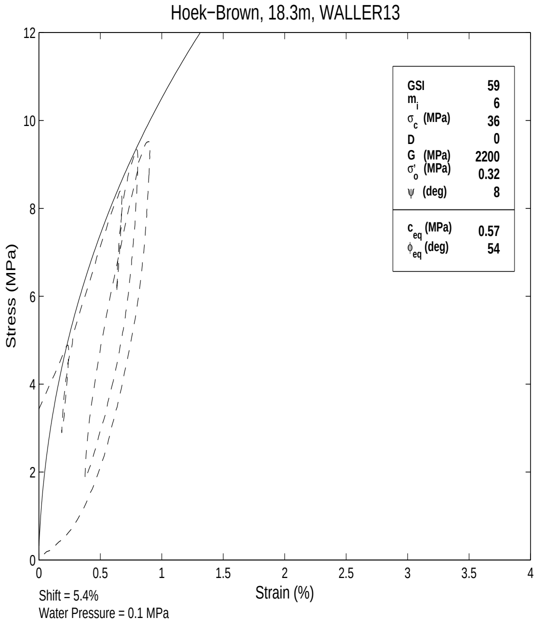
Hoek−Brown, 18.3m, WALLER13
Stress (MPa)
Strain (%)
0
2
4
6
8
10
12
0
0.5
1
1.5
2
2.5
3
3.5
4
GSI 59
m_i 6
σ_c (MPa) 36
D 0
G (MPa) 2200
σ'_o (MPa) 0.32
ψ (deg) 8
c_{eq} (MPa) 0.57
ϕ_{eq} (deg) 54
Shift = 5.4%
Water Pressure = 0.1 MPa

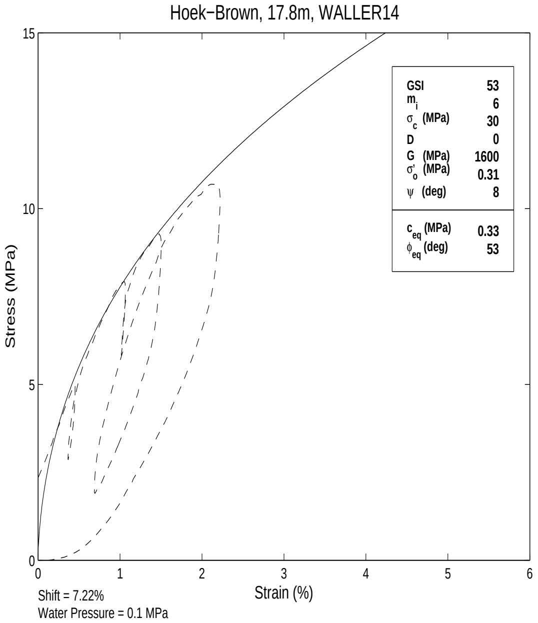
Hoek−Brown, 17.8m, WALLER14

Shift = 7.22%
Water Pressure = 0.1 MPa

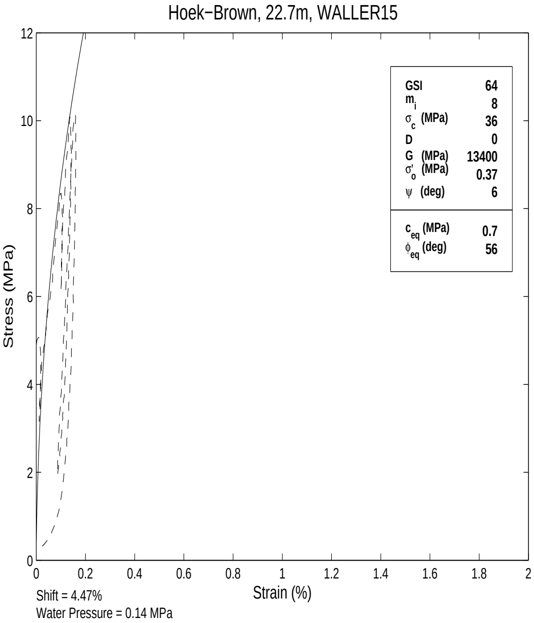
Hoek−Brown, 22.7m, WALLER15

Shift = 4.47%
Water Pressure = 0.14 MPa

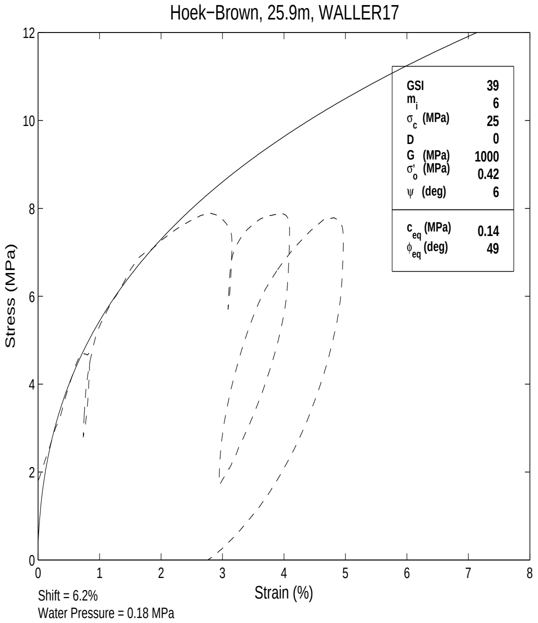
Hoek−Brown, 25.9m, WALLER17

Shift = 6.2%
Water Pressure = 0.18 MPa

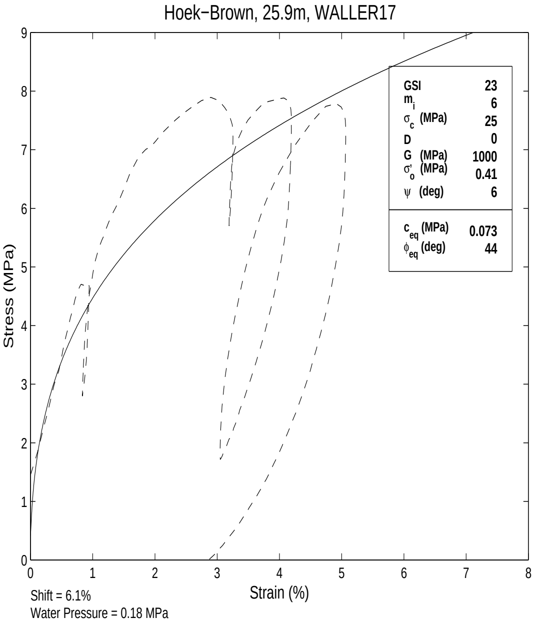
Hoek−Brown, 25.9m, WALLER17

Shift = 6.1%
Water Pressure = 0.18 MPa

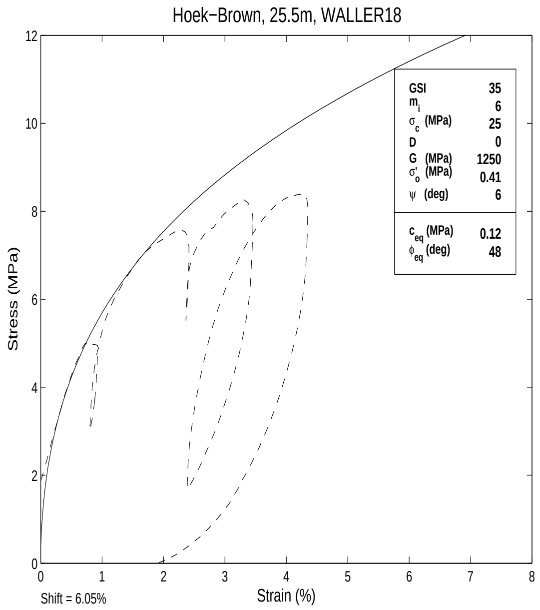

Hoek−Brown, 25.5m, WALLER18

Shift = 6.05%
Water Pressure = 0.17 MPa

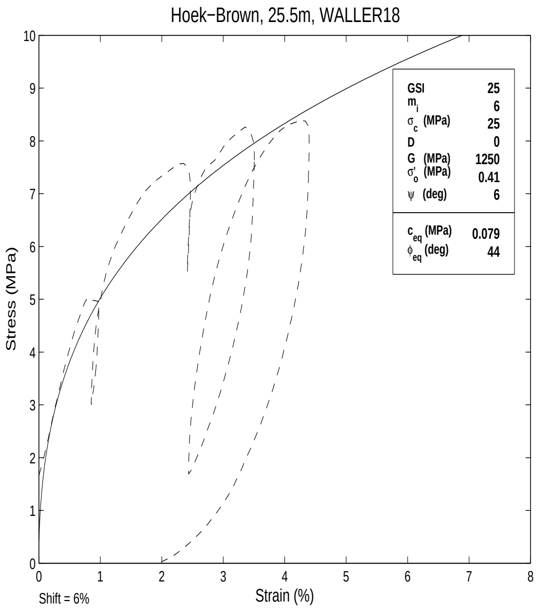

Hoek−Brown, 25.5m, WALLER18

Shift = 6%
Water Pressure = 0.17 MPa

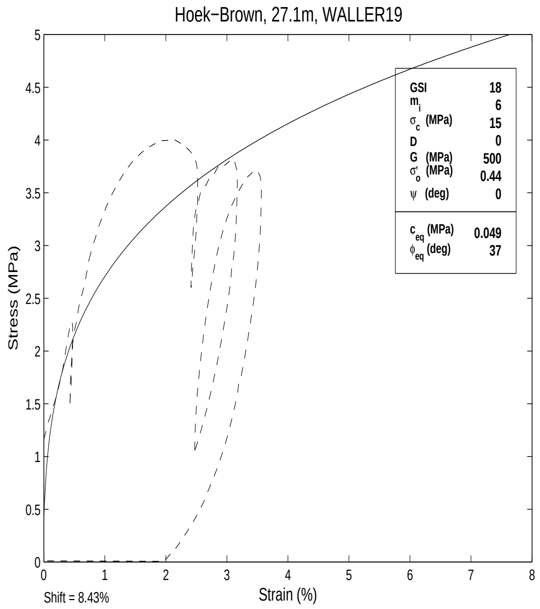

Hoek−Brown, 27.1m, WALLER19

Shift = 8.43%
Water Pressure = 0.19 MPa

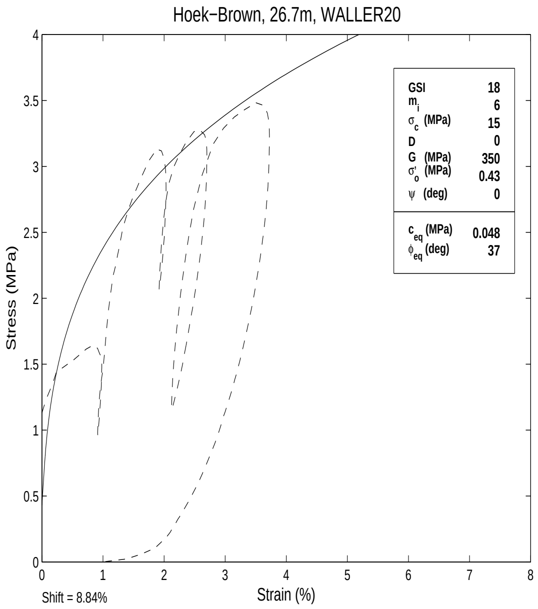

Hoek−Brown, 26.7m, WALLER20

Shift = 8.84%
Water Pressure = 0.18 MPa

BIBLIOGRAPHY

[1] T.M. Allen and T.C. Badger. Appendix e: Wsdot memorandum. Technical report, Washington State Department of Transportation, April 2009. I-90 Snoqualmie Pass East - Hyak to Kecheelus Dam Snowshed shaft foundations.

[2] George E. Andreev. *Brittle Failure of Rock Materials.* A.A. Balkema, Rotterdam/Brookfield, Netherlands, 1995.

[3] Z.P Bazant and B.H. Oh. Efficient numerical integration on the surface of a sphere. *Zamm Zangew Math. u. Mech.*, 66(1):37–40, 1986.

[4] M.D. Bolton and R.W. Whittle. A non-linear elastic/perfectly plastic analysis for plane strain undrained expansion tests. *Gẽotechnique*, 49(1):133–141, 1999.

[5] Jean-Louis Briaud. *The Pressuremeter.* A.A. Balkema, Rotterdam, Netherlands, 1992.

[6] Evert Hoek; Carlos Carranza-Torres and Brent Corkum. Hoek-brown failure criterion - 2002 edition. In *Proceedings of the Fifth North American Rock Mechanics Symposium*, volume 1, pages 267–273, Toronto, Canada, 2002.

[7] B.G. Clarke. *Pressuremeters in Geotechnical Design.* Chapman & Hall, Cambridge, England, July 1995.

[8] Djim edo Kondo; Qizhi Zhu; Jian-Fu Shao and Vincent Pensee. chapter Chapter 9 – Multiscale Modeling of Anisotropic Unilateral Damage in Quasi-brittle Geomaterials: Formulation and Numerical Applications, pages 347–376. John Wiley & Sons, Inc., Hoboken, NJ, 2008.

[9] V. Pens ee; D. Kondo and L. Dormieux. Micromechanical analysis of anisotropic damage in brittle materials. *Journal of Engineering Mechanics*, 128(8), August 2002.

[10] C.M. Haberfield. *The Peformance of the Pressuremeter and Socketed Piles in Weak Rock.* Ph.d. thesis, Monash University, 1987.

[11] C.M. Haberfield. Pressuremeter testing in weak rock and cemented sand. *Proceedings Institution of Civil Engineers, Geotechnical Engineering*, 125:168–178, July 1997.

[12] C.M. Haberfield and I.W. Johnston. A numerical model for pressuremeter testing in soft rock. *Gẽotechnique*, 40(4):569–580, 1990.

[13] E. Hoek and E.T. Brown. Practical estimates of rock mass strength. *International Journal or Rock Mechanics and Mining Sciences*, 34(8):1165–1186, 1997.

[14] Q.Z. Zhu; D. Kondo and J.F. Shao. Homogenization-based analysis of anisotropic damage in brittle materials with unilateral effect and interactions between microcracks. *International Journal for Numerical and Analytical Methods in Geomechanics*, 33:749–772, 2008.

[15] Q.Z. Zhu; D. Kondo and J.F. Shao. Micromechanical analysis of coupling between anisotropic damage and friction in quasi brittle materials: Role of homogenization scheme. *International Journal of Solids and Structures*, 45:1385–1405, 2008.

[16] B. Ladanyi. Quasi-static expansion of a cylindrical cavity in rock. In *Third Symposium on Engineering Applications of Solid Mechanics*, pages 219–240, Toronto, Ontario, 1976. University of Toronto Dept. of Mechanical Engineering.

[17] R.J. Mair and D.M. Wood. *Pressuremeter Testing–Methods and Interpretation.* CIRIA, Butterworths, London, England, 1987.

[18] Paul Marinos and Evert Hoek. Gsi: A geologically friendly tool for rock mass strength estimation. In *GeoEng2000 Conference*, Melbourne, Australia, 2000. Technomic Publishing.

[19] V. Marinos; P. Marinos and Evert Hoek. The geological strength index: applications and limitations. *Bulletin of Engineering Geology and the Environment*, 64:55–65, 2005.

[20] M. Cai; P.K. Kaiser; H. Uno; Y. Tasaka; M. Minami. Estimation of rock mass deformation modulus and strength of jointed hard rock masses using the gsi system. *International Journal of Rock Mechanics & Mining Sciences*, 41:3–19, 2004.

[21] S Nemat-Nasser and M. Hori. *Micromechanics: overall properties of heterogeneous materials.* Elsevier Science B.V., Amsterdam, The Netherlands, 1999.

[22] J.M.O. Hughes; C.P. Wroth and D. Windle. Pressuremeter tests in sands. *Gẽotechnique*, 27(4):455–477, 1977.

[23] Xiao-Li Yang and Jin-Feng Zou. Cavity expansion analysis with non-linear failure criterion. In *Proceedings of the Institution of Civil Engineers - Geotechnical Engineering*, volume 164, pages 41–49. ICE Publishing, February 2011.

[24] Hai-Sui Yu. *Cavity Expansion Methods in Geomechanics.* Kluwer Academic Publishers, Dordrecht, Netherlands, 2000.

[25] P.J Sabatini; R.C. Bachus; P.W. Mayne; J.A. Schneider; T.E. Zettler. Geotechnical engineering circular no. 5: Evaluation of soil and rock properties. Technical Report FHWA-IF-02-034, U.S Department of Transportation Office of Bridge Technology, Federal Highway Administration, Washington D.C, April 2002. FHWA COTR: Chien-Tan Chang, FHWA Technical Consultant: Jerry A. DiMaggio.